# Caliste-MM : a new spectro-polarimeter for soft X-ray astrophysics

Paul Serrano

NNT : 2017SACLS594

# Thèse de doctorat de l'Université Paris-Saclay préparée à l'Université Paris-Sud

École doctorale n°127
Astronomie et Astrophysique
Spécialité de doctorat : Astronomie et Astrophysique

par

**M. Paul Serrano**

## Caliste-MM: a new spectro-polarimeter for soft X-ray astrophysics

Thése présentée et soutenue au CEA Saclay, le 26/10/2017.

Composition du Jury :

| | | | |
|---|---|---|---|
| Mme. | Esther Ferrer Ribas | Ingénieur-chercheuse<br>CEA | (Co-directrice) |
| M. | Olivier Limousin | Ingénieur-chercheur<br>CEA | (Co-directeur) |
| M. | Fabio Sauli | Professeur<br>CERN | (Rapporteur) |
| M | Denis Bernard | Directeur de recherche<br>CNRS | (Rapporteur) |
| Mme. | Margarita Hernanz | Professeure<br>Institut de Ciencies de l'Espai | (Examinatrice) |
| M. | Ioannis Giomataris | Directeur de recherche<br>CEA | (Examinateur) |
| M. | Ezio Caroli | Directeur de recherche<br>INAF Bologna | (Examinateur) |
| M. | Alain Abergel | Professeur<br>Institut d'Astrophysique Spatiale | (Président du jury) |

Dans une thèse, les remerciements sont normalement la dernière partie écrite, après la soutenance, une fois le manuscrit validé et le titre de docteur décerné (et toujours grandement mérité, cela va sans dire). Pour les écrire, on m'a dit, je cite « tu peux te lâcher ». Dans le doute j'ai fait valider cette assertion plusieurs sources indépendantes, qui normalement n'ont pas pu se concerter avant de me répondre et n'ont en théorie pas pu me tendre un piège. Je suis donc légitimement parti du principe qu'elle était vraie, et je dois maintenant me faire un devoir de l'appliquer. Je me suis bridé sur tout le reste du manuscrit qui va suivre, histoire de ne pas passer pour un clown aux yeux des gens qui ne me connaissent pas (pour ceux qui me connaissent, c'est déjà trop tard), alors vous pensez bien que sur les remerciements je suis en roue libre. Puis, entre vous et moi, je sais pertinemment que pour 99% d'entre vous ce sont les seules pages que vous lirez, alors autant qu'elles sortent un minimum du lot.

J'espère que chacun va y trouver son compte et que je n'oublierai personne. Personne d'important sur le projet, ni personne parmi les gens qui m'ont demandé une dédicace pour pouvoir à jamais avoir leur nom associé à ce manuscrit et ce travail d'une qualité extraordinaire (c'est pas moi qui l'ai dit, c'est le jury ; et le fait que chaque jury dise ça pour chaque thèse n'a aucun rapport). Allez : sortez les trompettes, les tambours, les cors anglais, les clarinettes et les triangles, et lançons-nous gaiement dans ces remerciements que vous attendez tous.

Je vais évidemment commencer par les deux personnes les plus importantes, sans qui il n'y aurait pas eu de projet ni de sujet (et faire une thèse sans sujet aurait nécessairement apporté une contrainte difficile à surmonter), et grâce à qui cette thèse a été une expérience extraordinaire. Pas la peine de faire un faux suspens, il s'agit bien sûr de mes deux directeurs de thèse.

Tout d'abord Esther, la madre du projet. Je ne vais pas faire un paragraphe entier en espagnol pour te remercier, ma maîtrise de la langue est encore beaucoup trop bancale (honte à moi). Mais je vais

faire un effort sur quelques phrases, parce que je te dois au moins ça. Esther, muchas gracias para todo. Son simples palabras, pero importantes para mi, y vienen de lo profundo de mi corazón. Sans toi, ta gentillesse, tes conseils, tes connaissances sur tout le milieu des détecteurs gazeux et de toute la communauté, sans ton aide précieuse dans les moments de galères, j'aurais été incapable de sortir ne serait-ce que le spectre le plus moche. Sans ta bienveillance je ne serais pas venu au labo tous les jours avec la même envie. Et c'est grâce à tout ça que j'ai pris autant de plaisir à faire cette thèse avec toi. Je pourrais écrire sans aucune difficulté 50 pages juste pour te remercier pour tout ce que tu as fait pour moi pendant ces 3 ans. Mais ça deviendrait légèrement trop long, et je vais m'arrêter là, en te disant sincèrement une fois de plus : merci du fond du coeur.

Au tour d'Olivier (Limousin) maintenant. Trop de choses ont déjà été dites sur toi dans les remerciements de tes thésards précédents, et pour garder mon esprit vierge de toute subjectivité je ne les ai pas lus : donc si ici je répète certaines choses écrites par tes étudiants précédents, c'est un hasard ! Il y a un peu trop de choses à dire donc forcément je vais en oublier 90%. Chaque discussion avec toi était une surprise (et le sera toujours, car je sais qu'on sera amené à se revoir) : impossible en commençant de savoir dans quelle direction ça allait partir et où ça allait se terminer, et que ce soit pour des anecdotes sur des yeux de poisson japonais ou pour parler de science. Parler avec quelqu'un d'aussi vif que toi est une expérience terriblement stimulante. Et je ne peux pas compter les fois où je suis resté coincé pendant des heures sur un problème que tu m'as aidé à résoudre en moins de 5 minutes. Grâce à toi j'ai pu découvrir le karaté, et j'ai maintenant l'objectif de devenir le plus grand ninja de France (mais la route sera longue, vu à quel point je suis loin d'être le meilleur ninja de juste Villebon-sur-Yvette). Olivier : merci. C'était au début un honneur de connaître quelqu'un comme toi, c'est maintenant une véritable joie de t'avoir comme ami.

Ensuite, c'est ma famille que je tiens à remercier. Mes parents d'abord, ma mère et mon père. Rentrer chez eux le week-end de temps en temps est une sensation toujours réconfortante, que l'on a tous connu. Se retrouver l'espace de quelques jours dans cet état d'enfant qui se goinfre comme un pachyderme sans avoir grand-chose à faire permet clairement de déconnecter de la semaine et de se ressourcer pour en démarrer une nouvelle avec entrain et énergie. Merci maman, merci papa (toute ressemblance avec une chanson de Pierre Perret est purement fortuite). Merci aussi à mon frère,

toujours aussi mauvais à FIFA et Mario Kart : ne perds pas espoir, un jour tu progresseras. Je te souhaite bon courage pour la thèse que tu viens d'entamer. Merci à mes grands-parents, que j'ai l'immense chance d'avoir au complet. Clairement je ne vous vois pas autant que je le voudrais ; chaque moment passé avec vous est toujours un grand plaisir, et je suis fier d'être votre petit fils. Et enfin merci aussi à Michel et Garménick, toujours là pour me soutenir et m'encourager à continuer.

J'aimerais maintenant remercier mes collègues, sans qui clairement ma thèse n'aurait pas eu la même saveur. Que ce soit à travers une aide précieuse sur le projet ou simplement grâce des discussions divertissantes qui m'ont permis de me changer les idées et d'avoir des pauses plus efficaces (et parfois plus longues que nécessaires, mais aussi beaucoup plus drôle), vous m'avez beaucoup aidé. J'espère n'oublier personne dans la liste qui suit, et qui n'est absolument pas rangée par ordre d'importance mais plutôt dans l'ordre absurde et arbitraire choisi par mon cerveau au fur et à mesure que j'écris cette page.
Merci à Aline, la mère et spécialiste des Caliste et récente maman d'un garçon tout choupinou. Merci à Claire, à qui je souhaite une retraite aussi remplie que sa carrière. Merci à la troupe Diana, Sophie, Pierre-Anne, David (Baudin) et Daniel pour les afterworks, soirées, conf et autres joyeuseries. Merci à Olivier (Gevin) pour ton aide sur Idef-X, et surtout pour m'avoir remotivé à me remettre sérieusement au piano : c'était certainement involontaire de ta part, mais c'est grâce à toi que je m'y suis remis. Merci à David (Attié), d'abord pour ton aide sur tout ce qui concerne les détecteurs et la physique des particules, et ensuite merci de m'avoir aidé à me mettre au sport : au moment de démarrer la course, savoir que quand j'aurais le niveau je pourrais t'accompagner le midi m'a aidé à garder le rythme des entraînements ; c'est en fait indirectement grâce à toi que j'ai pu te traîner sous une pluie battante à courir un semi en 1h45 ! Merci à Fabien et Thomas pour vos questions pointues qui m'ont clairement permis de progresser sur la compréhension de mon détecteur, et des détecteurs gazeux de manière générale. Merci à Mariam sans qui le détecteur ne marcherait clairement pas vu que j'aurais été incapable d'y mettre du gaz. Merci à Daniel (Desforges) sans qui la chambre du détecteur n'existerait pas. Merci à Pierre-Henri, à qui j'en ai fait voir des belles avec mon insouciance chronique (que j'essaie toujours de régler). Merci à Philippe (Bourgeois) et à Nathalie de m'avoir aidé dès que j'avais une galère admin-

istrative. Merci à Stefan, qui m'a aidé à plusieurs moments clés et qui a clairement une part de responsabilité dans la simplicité de mise en place du détecteur à Soleil. Merci à Eric pour ton accueil au sein du SEDI (qui a maintenant changé de nom mais je me rappelle plus du nouveau), et tes remarques sur les phénomènes de diffusion dans les couches résistives. Côté DAp, merci à Pascale (Delbourgo) pour ton sourire permanent et ton aide sur toutes les procédures. Merci à Philippe (Ferrando) pour tes relectures et ton aide sur tout ce qui concerne l'astrophysique. Merci à Philippe (Laurent), spécialiste de la polarisation haute énergie, grâce à qui j'ai pu comprendre tous les enjeux scientifiques du domaine. Merci à Dominique (Monvoisin) et son efficacité incroyable reconnue par tout dans le service. Merci à Isabelle et sa bonne humeur qui semble inébranlable (et que je compte bien revoir régulièrement maintenant que je suis en poste à 3D Plus). Je souhaite bon courage à Geoffrey qui vient de démarrer sa thèse (et qui au vu des débuts fracassants devrait rendre un travail qui sera difficile à égaler). Et enfin je souhaite remercier l'université d'Orsay (ou Paris XI ou Paris Sud ou Paris Saclay, je sais plus quel est le terme officiel) qui m'a financé pendant ces 3 ans, et sans qui par conséquent je n'aurais rien pu faire.

Merci à Fabio et Denis, mes deux rapporteurs, qui avec leurs remarques ont amené le manuscrit à un niveau largement supérieur. Et merci aux autres membres du jury pour leurs remarques et leurs questions : c'est peut-être surprenant à dire, mais j'ai passé un excellent moment, très stimulant, pendant vos questions lors de ma soutenance.

J'aimerais consacrer un paragraphe entier à 3 personnes : Fabienne, Paulo et Pascal, membres de la ligne Métrologie du synchrotron Soleil. Grâce à vous, j'ai pu avoir accès à un faisceau synchrotron qui semblait avoir été fait sur mesure pour ma manip. Grâce à vous j'ai pu avoir des données incroyables, dans des conditions optimales et avec une aide à toute heure du jour et de la nuit pendant les 4 jours où vous m'avez permis de squatter le faisceau (4 jours incluant le week-end). Grâce à vous, tout le dernier chapitre de ce manuscrit existe. On va pas se mentir, la courbe obtenue est vraiment classe et sans vous, elle n'aurait jamais pu exister. J'ai eu l'occasion de vous remercier pendant ma soutenance, mais 1) vous ne pouviez malheureusement pas tous être là, et 2) je voulais qu'il soit écrit noir sur blanc (au sens propre et figuré) à quel point l'aide que vous m'avez apporté est précieuse. Merci encore à vous trois.

Et enfin vient le tour des amis (calmez-vous, c'est pas que vous

passez après tous les autres, c'est un hasard). Tout le troupeau dit « de Supélec » (même si vous ne venez pas tous de Supélec, c'est là que je vous ai connu donc c'est comme ça que je vous appelle) : Louis, Victoire, Alois, Baptiste, PM, Ambre, Quentin, Inès, Nico, Léa, Gaétane, Audrey, Gurvan, Sandra, Clémence, David, Iris, Rémi, Lucile. J'ai eu l'occasion de vous voir plusieurs fois pendant ces 3 ans, et avec toujours autant de plaisir. Merci à Bréna pour ton soutien pendant les derniers mois, les plus intenses de la rédaction du manuscrit et loin dêtre les plus faciles. Merci à mes deux journalistes préférés Kocila et Milly (d'accord, vous êtes les deux seuls journalistes que je connaisse, mais je suis presque sûr que même si j'en connaissais d'autres vous seriez mes préférés) pour les bières et pizzas qu'on a pu partager ensemble. Merci au groupe dit « de Sicile » (là encore, vous n'êtes pas siciliens, mais c'est là que je vous ai connu), Clémence, JB, Morgane et Hannah : j'ai aussi eu l'occasion de vous retrouver à plusieurs reprises, et je suis sidéré d'à quel point les soirées passent vite avec vous (et Hannah, toutes mes félicitations pour tes fiançailles : on se voit à ton mariage !).

J'espère n'avoir oublié personne, même si j'ai parfaitement conscience que ma mémoire de poisson rouge m'a forcément fait passer à côté de personnes que j'aurais voulu remercier. Et je m'en excuse sincèrement.

Il est d'usage commun de finir cette page en citant un scientifique important, et Einstein dans la mesure du possible. Cependant : comme je l'ai précisé au début, on m'a encouragé à me lâcher. J'aimerais pouvoir citer en toute humilité une phrase de Pierre Gringoire du roman Notre-Dame de Paris « J'ai le bonheur de passer toutes les journées avec un homme de génie qui est moi, et c'est fort agréable ». Mais cette phrase est fausse sur un point précis (que je vous laisse trouver : attention les possibilités sont nombreuses) et je suis comme vous le savez d'une modestie légendaire. Je ne peux donc pas l'utiliser ici.
À la place je vais citer le poète français du XVIIe siècle Nicolas Boileau (et la phrase qui suit est souvent à tort attribuée à Einstein) : " Ce que l'on conçoit bien s'énonce clairement, Et les mots pour le dire arrivent aisément " (Nicolas Boileau, Canto I, l. 153). Ce qui me permet de réaliser qu'il y a un peu trop de choses que je conçois mal.

Mon blabla est maintenant terminé, et je vous invite à la lecture du manuscrit qui suit, dans un style beaucoup plus conventionnel, pour découvrir mon travail de thèse. Je vous souhaite en le lisant

(si vous le lisez) d'éprouver autant de plaisir que moi pendant mes 3 ans de travail.
*Encore merci à tous, c'était vraiment marrant.*

# Contents

# Introduction

The objective of astrophysics is the study of the various celestial bodies: their formation, evolution, interaction and death. Several ways exist to get information from these objects, but the more ancient and uberous is the observation of the light they emit. Here, light is to be understood in the broad sense of electromagnetic waves, covering the whole electromagnetic spectrum from radio waves to gamma-rays. From the observation of light, it is possible to perform four different sciences in order to get information on the physical processes at work in the source.

The first one is to measure precisely the position of the emitting source in the sky and, when possible, its shape or structure. The science dedicated to this measurement is called *imaging*, and it allows to locate the source in the sky and to make high resolution images of extended objects. The second science, called photometry, consists in the measurement of the intensity of the light. Photometry is almost always associated with the measurement of the time variation of the intensity, so we generally speak more of timing science than of photometry. The timing measurement is ideal for the study of a lot of objects. It is the favorite method used to find new exoplanets, and it allows the measurement of the rotating frequency of pulsars for instance. The third science is spectrometry: it is the precise measurement of the frequency of light (or of its energy if we look at it with the photon point of view). Spectrometry allows to get information such as the chemical composition of the interstellar dust, stars temperature or the rotation speed of accreting disks. The last possible science is polarimetry. It is the study of the wave behavior of the electric field of the electromagnetic wave. Depending on the emitting process, on the surrounding geometry or on the geometry of the various objects encountered by the light on its travel to the observer, the undulation of the electric field will be different. Performing polarimetry is ideal to get information on the magnetic field in the source or on the geometry of small objects like

pulsars accretion disks.

Those four sciences give great results for each band of the electromagnetic spectrum. There is only one missing piece: polarimetry in the soft X-ray band ranging from 1 keV to 20 keV. Intents to perform those measurements have been made in the 60's by using the Bragg diffraction phenomenon. But the efficiency of this technique is extremely low. This low efficiency was coupled with the absence of X-ray telescopes at that time, making the whole instrument very inefficient. Moreover, the Bragg diffraction can be performed at only one energy, with an energy range of just a few eV for a given crystal. Those two obstacles of low efficiency and very narrow energy band made the measurement too challenging to give proper results. Some results have still been obtained, like the polarization of the Crab nebula. But the precision obtained when using the Bragg technique was too low to be used on other more challenging astrophysical sources.

Because of these instrumental problems, soft X-ray polarimetry missions have been abandoned, despite the information that they could bring. In fact, it could allow measurements which would validate or discard some theoretical models in various astrophysical applications. Thanks to soft X-ray polarimetry, it is possible to measure the direction of the magnetic field in the source by the measurement of the synchrotron radiation emitted by the electrons, and this would be useful to validate theoretical models of magnetic field distribution in pulsar wind nebulae. It could also help the measurement of black holes spins: up to now several models describe the same phenomenon of Doppler shift of the K_alpha Fe line at 6.4 keV in the black holes accretion disk, but they all give a different value of polarization of the line. Hence measuring the polarization of this line would help to chose between the various theoretical models and then obtain the proper value of the black holes spin. Soft X-ray polarimetry could serve other purposes like the study of magnetic birefringence thanks to the gamma ray bursts observations.

Because of this wide range of possible applications of soft X-ray polarimetry, there is a high interest from the astrophysical community. This interest is reinforced by the recent development in gaseous detectors which allows to use the photoelectric effect to perform polarimetry in the soft X-ray band. During the photoelectric effect, the ejection direction of the photoelectron is linked to the polarization direction of the detected light. Thus a soft X-ray polarimeter

has to be able to recover the ejection direction for each photoelectron.

This manuscript is dedicated to the fabrication, characterization and test of a new concept of gaseous detector aiming at performing spectro-polarimetry in the soft X-ray band. It uses the piggyback detector, derived from the Micromegas bulk technology, to convert photons into photoelectrons and amplify the signal. In gas a photoelectron created by a 6 keV photon has a mean free path which ranges from few 100 $\mu$m to few millimeters, and it leaves a track of ionization electrons behind. By recovering this track it is possible to reconstruct the ejection direction of the photoelectron, hence to perform polarimetry. The breakthrough of this detector is its novel architecture: the anode of the piggyback consists of a resistive layer spread on a ceramic plate. The detector is placed in a chamber filled with gas, and the ceramic plate acts as a chamber wall, making the chamber leak tight. There are no readout electronics nor strips or pixels inside the gaseous chamber. The readout is to be placed outside, facing the ceramic, and reading the signal thanks to capacitive coupling. The electronics used is the space-qualified Caliste electronics, developed at CEA and on which the laboratory has an enormous expertise. The association of the piggyback detector and the Caliste readout forms the detector called Caliste-MM.

This work presents the results obtained with the novel Caliste-MM detector. The first light and shape of events detected are shown. Characterizations with different gain, gases and other tunable parameters are presented, such as the spectroscopic capability. Simulations using analytical calculations have been performed to understand the detector behavior with the various parameters. I got the possibility to bring the Caliste-MM detector at the Soleil synchrotron facility which produces a 100% polarized monochromatic soft X-ray beam. Thanks to this experiment, the polarimetric capability of the detector has been studied deeply. A reconstruction method of the photoelectrons tracks is proposed in order to recover their ejection direction. Measurements of the modulation factor of the detector at different energies are presented. Results are then put into perspective and further axis of improvements are proposed to go to the next generation of Caliste-MM detector, with the best possible performance.

# Chapter 1

# Introduction: polarimetry in astrophysics

# Contents

## Contents



## 1.1 Introduction

Astronomy is a science which studies the objects of the universe and tries to understand the physical phenomena that drive them. It can be split into two distinct worlds: theory and observation, observation confirming (or discarding) some theories, and theories explaining observations which were up to now not understood. The experimental method is then critical in astronomy by being essential to theory. Several methods exist to study the universe. The direct study of solid elements in space is one of those, and we can cite the

well know european space mission Rosetta and its lander Philae [1] which studied very closely the comet 67p Churyumov-Gerasimenko, or the no less famous Curiosity rover from NASA [2] which, since August 2012, studied the ground of Mars.

The observation and study of neutrinos, still mysterious particles [3], or of the gravitational waves (detected for the first time in 2015 by the american interferometer LIGO [4]) would allow, once mastered, to get brand new information about hot and dense regions of the universe, from where light has troubles to get out. But those two methods, even if they already gave very promising results, are for now at the beginning of their development and their use is currently marginal.

The study of cosmic rays and astroparticles is a third way to recover information from the universe. The discovery of cosmic rays goes back to the beginning of the $20^{th}$ century. At that time, the state of the art electroscopes all registered an ionizing radiation coming from an unknown source. The prevailing theory was that this radiation came from Earth. In 1909, the German physicist Theodor Wulf measured the rate of radiation at the top of the Eiffel tower, expecting it to decrease with height. But the rate did not decrease significantly. In 1911, Victor Hess made experiments at an altitude of more than 1000 meters thanks to a balloon flight, and found no significant decrease in the ionization rate, showing that the Earth was not the source of this ionization. The Sun being one other possible source, Hess made an other experiment in 1912, in his balloon, at an altitude of 5300 meters and during a near total eclipse of the Sun. Here again, the ionization rate did not decrease despite the high altitude and the eclipse, and Hess reasoned that the Sun could not be the source of radiation: it had to be coming from further out in space. With this experiment, Hess discovered the existence of cosmic rays, discovery for which he got the Nobel Prize in 1936. Their study is still a topic of current interest, and the Pierre Auger observatory [5] and the soon-to-be launched JEM-EUSO [6] experiment are missions dedicated to the study of cosmic rays, which gives a lot of information about very high energetic objects such as black holes, supernovae or gamma ray bursts.

The last technique to explore the universe, and by far the most used, is the observation of the light emitted by the various celestial bodies. In astronomy, the word "light" is to be understood as the whole electromagnetic spectrum, going from radio waves to gamma rays, of which we can find a representation in fig. 1.1. Observing

light at all energies gives access to full information and is essential in astronomy, and we give in the following a few examples. The use of radio waves has for instance allowed the (accidental) discovery of pulsars [7]. The infrared light is used, among other things, to study the cold dust weakly heated by neighboring stars, or to observe new born stars yet in formation thanks to their emission in near infrared which exits molecular clouds. The use of visible wavelengths, the oldest observational method, gave way to the detailed observations of planets, galaxies and other celestial bodies, which we can admire on the wonderful pictures of the Hubble space telescope. The Ultraviolets can be used to observe very hot objects such as galaxy's dust heated to several tens of thousand degrees by massive stars, allowing us to estimate the number of those stars. X-rays allow the study of phenomena of several millions of degrees, or of synchrotron emission produced by electrons spinning at a very high speed in high magnetic fields. And thanks to the use of gamma rays we discovered the existence of mysterious phenomena like gamma ray bursts or pevatrons (astrophysical objects accelerating particles at energies up to PeV), still not well understood.

## 1.2 The four ways of observing light in astrophysics

As we just explained, the observation of light is essential in astronomy, and we are still far from having completely used the wealth of information it can provide. Four types of measurements can be made from the observation of light.

The first is imaging. It is the science which consists in the precise localization of the observed source, and of the various details of this source. The quality of an imaging telescope is expressed in term of angular resolution. Among the most relevant imaging telescopes we can mention the Hubble space telescope [8] (visible imaging detector) or the Very Large Array [9], radio-telescope which uses interferometry techniques to reach impressive spatial resolutions up to 10 ms of arc.

The second way is spectroscopy. It is the capability to measure the energy of the incoming photons, not just by simply making the difference between UV and IR, but by being more precise than this and being able to separate precisely the energy bands. This is

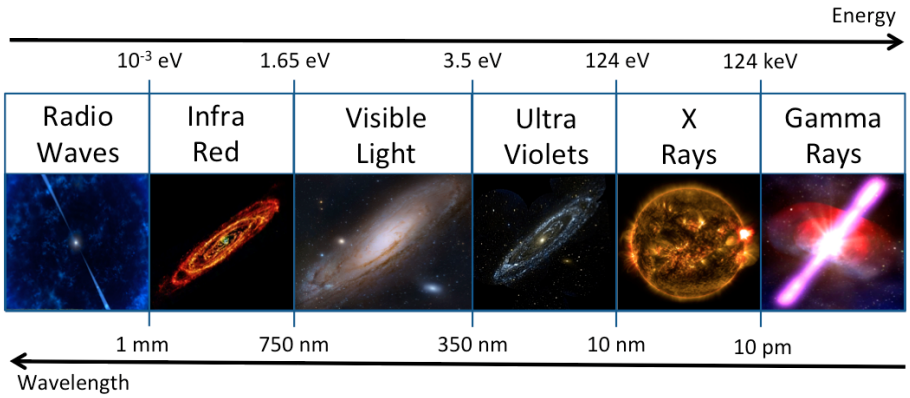


Figure 1.1: *Electromagnetic spectrum and examples of observation at various energies. Radio waves allowed the discovery of pulsars (artist's view). Infrared is used to observe the cold dust of galaxies, weakly heated by forming stars, and allow the estimate of the number of those forming stars in the observed galaxy. Visible light gives information on the number of stars in the observed galaxy, and UV on the number of hot and massive stars doomed to end their life in supernovae. X-rays are used for the observation of very hot phenomenon or of synchrotron emission of electrons accelerated in a high magnetic field. The most energetic phenomena in the universe emit gamma rays, which are then perfectly suited to understand still mysterious events such as gamma ray bursts (artist's view).*

what gives the possibility, in submillimeter radio observations, to measure the hydrogen quantity in molecular gases, by being able to look closely to the 21 cm emission line of hydrogen caused by the transition between the two hyperfine states of the fundamental state of the atom. Moreover it allows to measure the speed of celestial objects by measuring the Doppler shifts in their spectrum. A lot of missions in various energy domains gave pioneer and fundamental results in spectroscopy, like XMM-Newton [10] or Chandra [11] (X-ray observation satellites), the HARPS spectrograph [12] installed on the VLT [13], or the SPI instrument [14] on board the INTEGRAL satellite [15] which observes gamma rays.

The third way is timing. It is the precise study of variable signals in time, in order to characterize their time development. This science allows the precise measurement of the rotation speed of pulsars, or the classification in two different categories of gamma ray bursts depending of their duration. The RXTE satellite [16] is for instance dedicated to the study of time variation of X-ray astrophysical sources.

The last technique is polarimetry. It is the study of light as an electromagnetic wave and consists in the characterization of the electric field (and the magnetic field) carried by the light: is the field rotating (circular polarization) ? Does it oscillate in a specific direction (linear polarization) ? And if yes with which amplitude ? Is the field oscillating randomly (no polarization) ? *etc...* A strong magnetic field influences the motion of charged particles, and then the polarization state of the light they emit. The polarization state is also influenced by the interaction of the light with matter. Polarimetry is then used to study the magnetic field in the observed sources, the geometry of the source or even the interstellar medium by its interaction with the light which crosses it. A strong example of application of polarimetry is the study of the Cosmic Microwave Background (CMB). In fact, the anisotropy of temperature shown by the CMB creates a polarization of the light emitted during the epoch of recombination by Thomson scattering: the measurement of the CMB polarization, coupled to the measurement of temperature anisotropy, allows the validation of some theories of cosmology [17]. A more detailed measurement would give access to the so-called B-modes of the CMB, in theory caused by gravitational waves, which may validate the cosmic inflation hypothesis and strengthen our knowledge of the early phases of our universe. Among the existing polarimeters, we can quote the PhotoPolarimeter on board the Pi-

oneer 11 probe which measured the polarization of radio galaxies. Or the WMAP [18] and Planck [19] satellites, which measured not only the temperature anisotropy of CMB with a great accuracy, but also its polarization.
In this PhD, we will focus on spectroscopy and polarimetry, and this for X-rays.

## 1.3 The X-rays in the universe

The study of X-rays in astronomy is a field which has been developed quite recently. In fact, the terrestrial atmosphere absorbs the X-rays emitted by astrophysical sources, and it is then essential to put into orbit the X-ray instruments in order to get rid of the negative effects of the atmosphere. In a time where radio, visible and even infrared astronomy were possible, X-ray astronomy had to wait for the space race to start its development.

A lot of objects emit X-rays: some binary systems, accretion disks of black holes, pulsars, or supernovae remnants. X-rays are mostly emitted by synchrotron emission. A schematic figure is given on fig. 1.2. In the presence of a magnetic field, charged particles have their path diverted and then follow a non linear trajectory. This curvature of the trajectory of particles comes along with an emission of light. The light will be emitted in continuous spectrum, the general shape of which can be found in fig. 1.3. The flux of emitted photons increases up to a critical energy which depends on the speed of the emitted particle: the faster the particle, the greater the emitted energy. The best candidates as charged particles are then electrons, whose lightness allows them to reach very high speeds: they can then emit synchrotron radiation extending from radio waves to gamma rays.

The observation of X-rays gives then important information about energetic phenomenon (fast charged particles) in a high magnetic field. But in addition of being quite recent, X-ray astronomy faced two other problems. First of all X-ray sources have a relatively low intensity: in order to collect enough photons, it is necessary to have long exposure times, or a way to focus the incident light. Unfortunately, the wavelength of X-rays is of the order of the interatomic distance, and it is then hard to build mirrors adapted to focus X-rays on a focal plane, which is the second problem. Focusing X-rays

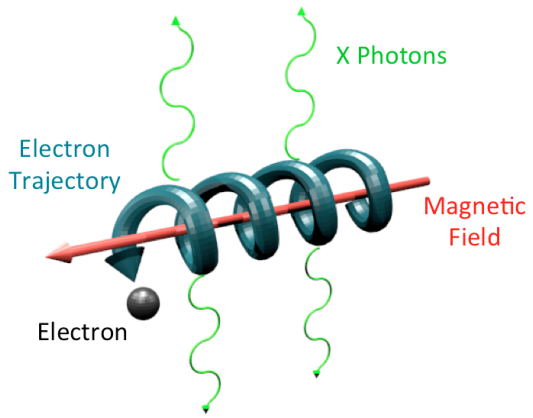


Figure 1.2: *Schematic of a synchrotron emission for an electron. The curvature of the trajectory comes along with an emission of light in the radial direction. If the electron is fast enough, emitted photons will go up to X-rays.*

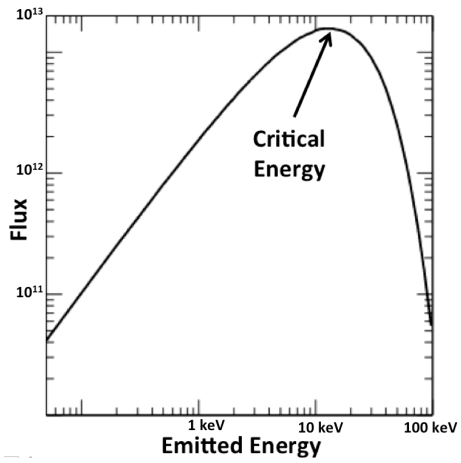


Figure 1.3: *Synchrotron Spectrum. The emitted spectrum is a continuum. The flux of emitted photons increase with the energy up to a critical energy which depends on the speed of the emitting particle. After this critical energy, the flux drops drastically.*

is still possible at low X-ray energies (up to few keV) thanks to grazing incidence mirrors, and a lot of efforts have been made in this direction. It allowed the launch in 1978 of the Einstein Observatory [20], the first fully imaging X-ray telescope (sensitive up to 4.5 keV). Since then, thanks to space missions like XMM-Newton, Chandra or RXTE, results obtained in imaging, spectroscopy and timing are outstanding. But X-ray polarimetry is still almost nonexistent. To understand this absence, we will detail in the next paragraph the various methods of polarimetry in the other energies, in order to see why their application to X-rays is not possible. But before we will go a bit deeper into the notion of polarimetry.

## 1.4 Polarimetry

Polarimetry is the study of the behaviour of the electric field oscillations created by the light propagation: its polarized fraction and its oscillation direction. This electric field is orthogonal to the propagation direction of light, and then oscillates in the plane perpendicular to this propagation direction. An observer placed in the light's propagation direction would observe different cases: a randomly oscillating electric field (unpolarized light), a rotating field which describes an ellipse (left or right elliptical polarization), a rotating field which describes a circle (left or right circular polarization), a field oscillating in a specific direction (linear polarization), or a combination of those states.
As the field oscillates in a plane, it is possible to represent it as the combination of two orthogonal components. The most intuitive orthogonal base simply consists in the expression of the electric field as the sum of the two orthogonal spatial components $\overrightarrow{E} = \overrightarrow{E_x} + \overrightarrow{E_y}$ as shown in fig. 1.4.

Let us take the example of a light linearly polarized and monochromatic (meaning that its carried electric field has a unique and well defined frequency), and oscillating in a direction making an angle $\theta$ with the vertical axis as represented in fig. 1.5.
In this case, if we call $A$ the amplitude of the electric field, $\lambda$ its wavelength, $z_0$ the observer's coordinate, $c$ the speed of light, $\omega$ the oscillation frequency ($\omega = \frac{2\pi}{\lambda}c$) and $k$ the wave vector ($k = \frac{2\pi}{\lambda}$), we have:
$\overrightarrow{E_x} = A.\sin(\theta).\cos(\omega t - kz_0)\overrightarrow{e_x}$ and $\overrightarrow{E_y} = A.\cos(\theta).\cos(\omega t - kz_0)\overrightarrow{e_y}$ and then $\overrightarrow{E}(t,z_0) = A.\sin(\theta).\cos(\omega t - kz_0)\overrightarrow{e_x} + A.\cos(\theta).\cos(\omega t - kz_0)\overrightarrow{e_y}$.
In the case of circular polarization, the two components $\overrightarrow{E_x}$ and $\overrightarrow{E_y}$ will have the same module $\frac{A}{\sqrt{2}}$ and one will be delayed by $\pm\pi/2$ compared to the other, the sign of the delay giving a right (resp. left) handed circular polarization if the field rotates in the direct (resp. indirect) direction around the propagation direction of light, giving then $\overrightarrow{E}(t) = \frac{A}{\sqrt{2}}\cos(\omega t - kz_0)\overrightarrow{e_x} + \frac{A}{\sqrt{2}}\cos(\omega t - kz_0 \pm \pi/2)\overrightarrow{e_y}$.
The general case of unpolarized light is $\overrightarrow{E}(t,z_0) = E_x\cos(\omega t - kz_0)\overrightarrow{e_x} + E_y\cos(\omega t - kz_0 + \phi(t))\overrightarrow{e_y}$, with $\phi(t)$ varying in an unpredictable way. It is also possible to express the electric field in a different base

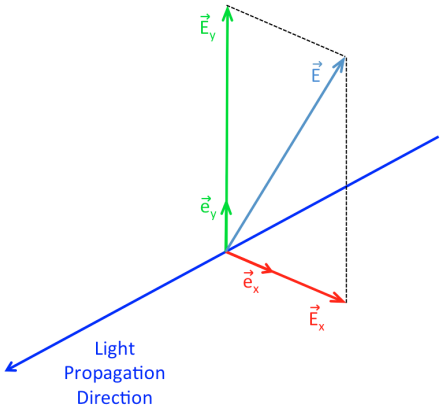


Figure 1.4: *The electric field oscillates in the plane orthogonal to the propagation direction of the light. It is then possible to express it at every moment as the sum of two perpendicular components:* $\vec{E} = \vec{E_x} + \vec{E_y}$.

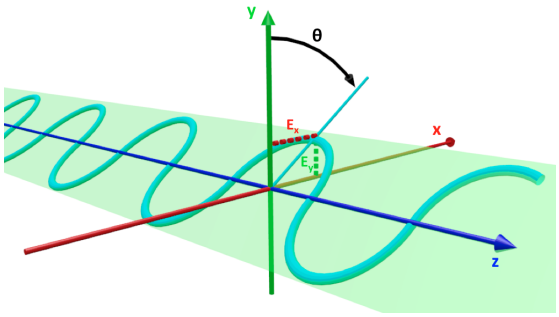


Figure 1.5: *Expression of a linearly polarized light with the two orthogonal components* $\vec{E_x}$ *and* $\vec{E_y}$

than $(\overrightarrow{e_x},\overrightarrow{e_y})$, the orthonormed base $(|L\rangle,|R\rangle)$, where $|L\rangle$ (resp. $|R\rangle$) is the state of left (resp. right) handed circular polarization.

It is common to express the electric field by using the complex representation of a wave: $\overrightarrow{E_x} = E_x e^{j(\omega.t - k.z_0)}\overrightarrow{e_x}$ and $\overrightarrow{E_y} = E_y e^{j(\omega.t - k.z_0 + \phi(t))}\overrightarrow{e_y}$. We recover the expression of the electric field by using the real part of each component: $\overrightarrow{E} = \Re(E_x e^{j(\omega.t - k.z_0)})\overrightarrow{e_x} + \Re(E_y e^{j(\omega.t - k.z_0 + \phi(t))})\overrightarrow{e_y}$. From those expressions, we can express what is called the Stokes vector $S = \begin{pmatrix} I \\ Q \\ U \\ V \end{pmatrix}$

with:
$I = ||E_x||^2 + ||E_y||^2$ which is the total measured intensity
$Q = ||E_x||^2$ - $||E_y||^2$
$U = 2\Re(E_x E_y^*)$

$V$ = -2$\Im(E_x E_y^*)$, called the "circular polarization intensity". $V = 0$ in the case of a linearly polarized light, $V = 1$ (resp. -1) in the case of a right (resp. left) handed circular polarization.
The coefficient $L = Q + jU$ is called the linear polarization intensity. $|| L || = 1$ in the case of a linear polarization, and $|| L || = 0$ in the case of a circular polarization. We can note that $U$ represents the polarization state at 45 degrees: $|| U || = 1$ if the light is polarized in the direction $\pm 45^o$.
The knowledge of the Stokes vector is enough to fully characterize the polarization state of light.

An horizontally polarized light has a Stokes vector: $S = \begin{pmatrix} 1 \\ 1 \\ 0 \\ 0 \end{pmatrix}$.

Vertically $S = \begin{pmatrix} 1 \\ -1 \\ 0 \\ 0 \end{pmatrix}$.

At an angle $\theta = 45^o$ $S = \begin{pmatrix} 1 \\ 0 \\ -1 \\ 0 \end{pmatrix}$.

Left handed circular $S = \begin{pmatrix} 1 \\ 0 \\ 0 \\ -1 \end{pmatrix}$.

Right handed circular $S = \begin{pmatrix} 1 \\ 0 \\ 0 \\ 1 \end{pmatrix}$.

And unpolarized $S = \begin{pmatrix} 1 \\ 0 \\ 0 \\ 0 \end{pmatrix}$. It is also possible to express the Stokes vector with the components $|L\rangle$ and $|R\rangle$ of the electric field.
More complex cases of partially polarized light can also be characterized with a Stokes vector, by considering the light wave as the sum of a polarized and an unpolarized wave. The Stokes vector gives then every important information for polarimetry, and we can define the polarization degree $P = \frac{\sqrt{Q^2 + U^2 + V^2}}{I}$. However, in most

cases, it is the linear polarization degree $P_{lin} = \frac{\sqrt{Q^2+U^2}}{I}$ which is interesting, the measurement of the circular polarization intensity $V$ is then optional. To recover the direction of polarization $\theta$ of the incoming wave we use the formula $\theta = \frac{1}{2}\arctan(\frac{U}{Q})$.

## 1.5 Polarimetry: some techniques, from radiowaves to UV

Classical techniques are based on the measurement of the Stokes vector. As we saw, it is fully calculable from the two orthogonal components $\overrightarrow{E_x}$ and $\overrightarrow{E_y}$, which are the values measured by the instruments. If we take the case of radiowaves, most of current radio telescopes are arrays of radio antennas separated by several meters (even kilometers) of distance, like the Very Large Array in New Mexico, or the Atacama Large Millimeter Array [21] in Chile which can be seen in fig. 1.6. Such a configuration allows the telescope to perform interferometry, and then to reach incredible spatial resolution up to 10 marcsec. In order to perform polarimetry, the various antennas of the radio telescope are not all sensitive to the same polarization: by positioning carefully the feeding antenna, it is possible to make it sensitive only to the horizontal component $\overrightarrow{E_x}$ or the vertical component $\overrightarrow{E_y}$ (or only to the left handed circular component $|L\rangle$ or right handed circular component $|R\rangle$). Thanks to the interferometry principle, it is possible to have a direct access to the amplitude and phase (or more precisely phase difference) of the measured waves, and then to express them completely under their complex form $\overrightarrow{E_x}$ and $\overrightarrow{E_y}$ (or $|L\rangle$ and $|R\rangle$). From those measurements, the Stokes vector can be calculated, and polarimetry is then easy to measure [22].

The way to perform polarimetry in the IR, visible and UV energies is based on the same principle of measurement of the components $\overrightarrow{E_x}$ and $\overrightarrow{E_y}$. However, as a telescope in those energies is rarely constituted of an array of antennas, it is impossible to measure directly the amplitude and phase of the wave, and we have only access to the intensity $I$. But this measurement $I$ can be enough if it is repeated under different conditions, and several methods of

(a) *The Very Large Array radio telescope is an array of 27 antennas of 25 m each.*

(b) *The ALMA radio telescope. Placed at more than 5000 m height in the chilean desert of Atacama, it is constituted by 66 antennas of a diameter varying from 7 m to 12 m.*

Figure 1.6: *The Very Large Array and ALMA telescopes.*

polarimetry exist in the energies from IR to UV [23].

The first method consists in the use of a linear polarizer: this optical instrument transforms the incident light of a random polarization into a light linearly polarized in a known direction. The schematic of such a linear polarizer forming an angle $\theta$ with the vertical direction is shown in fig. 1.7. To understand the idea behind performing polarimetry with a polarizer we express the Stokes vector of the output field $\overrightarrow{E'}$ as a function of the incoming field $\overrightarrow{E}$. For this, we express the polarizer under the form of a Mueller matrix [26], which models the action of the polarizer on the Stokes vector of the incoming wave. In the case of a linear polarizer forming an angle $\theta$ with the vertical (positive angle when going from the axis $\overrightarrow{e_y}$ to the axis $\overrightarrow{e_x}$), its Mueller matrix is:

$$\mathrm{M}(\theta) = \frac{1}{2}\begin{pmatrix} 1 & \cos(2\theta) & \sin(2\theta) & 0 \\ \cos(2\theta) & \cos^2(2\theta) & \sin(2\theta)\cos(2\theta) & 0 \\ \sin(2\theta) & \sin(2\theta)\cos(2\theta) & \sin^2(2\theta) & 0 \\ 0 & 0 & 0 & 0 \end{pmatrix}$$

To get $S' = \begin{pmatrix} I' \\ Q' \\ U' \\ V' \end{pmatrix}$ the Stokes vector of the output wave, we multiply

the Stokes vector of the incoming wave $S = \begin{pmatrix} I \\ Q \\ U \\ V \end{pmatrix}$ with the Mueller matrix $M$: $S' = M(\theta).S$, giving the equations:

$$\begin{pmatrix} I' \\ Q' \\ U' \\ V' \end{pmatrix} = \begin{pmatrix} I + \cos(2\theta)Q + \sin(2\theta)U \\ \cos(2\theta)I + \cos^2(2\theta)Q + \sin(2\theta)\cos(2\theta)U \\ \sin(2\theta)I + \sin(2\theta)\cos(2\theta)Q + \sin^2(2\theta)U \\ 0 \end{pmatrix} \tag{1.1}$$

Only the intensity can be measured without interferometry, so the only useful equation is $I' = I + \cos(2\theta)Q + \sin(2\theta)U$. If we perform the measurement of the intensity $I'$ for 3 different values of the angle $\theta$, we get the system of 3 equations with 3 variables:

$$I_{\theta_1} = I + \cos(2\theta_1)Q + \sin(2\theta_1)U \tag{1.2}$$
$$I_{\theta_2} = I + \cos(2\theta_2)Q + \sin(2\theta_2)U \tag{1.3}$$
$$I_{\theta_3} = I + \cos(2\theta_3)Q + \sin(2\theta_3)U \tag{1.4}$$

which can be solved in order to get the coefficients $I$, $Q$ and $U$. It can be noted that with this method we have absolutely no information about the intensity of circular polarization $V$. However, we are only interested in the degree of linear polarization $P_{lin} = \frac{\sqrt{Q^2+U^2}}{I}$, which does not involve $V$. It is this principle which is used by instruments such as NICMOS [24] (near IR camera) on board the Hubble space telescope. However, this method has a limitation: to keep a linearly polarized wave at its output, the polarizer absorbs a great part of the intensity of the incoming wave, which lowers the efficiency of the instruments and thus requesting longer exposure times.

This is the reason why a majority of instruments use a second method, which uses a Wollaston prism [25] which schematic can be seen in fig. 1.8. The Wollaston prism is made of two prisms attached side by side. A randomly polarized light coming into the prism goes out under the form of two rays, polarized linearly and

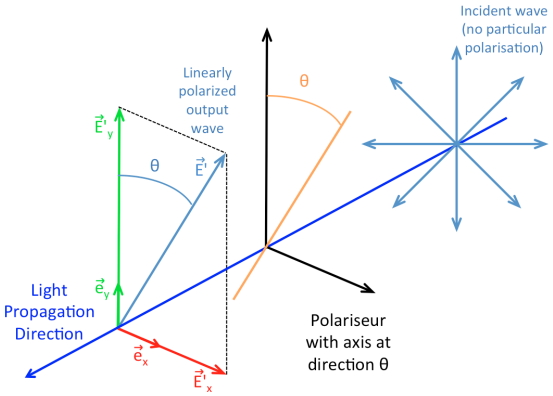


Figure 1.7: *Principle of a linear polarizer. The output light is linearly polarized in a specific direction given by the main axis of the polarizer.*

perpendicularly to each other. If the prism is turned by an angle $\beta$ around the light's propagation direction, the two output waves will have as polarization direction $\beta$ and $90^o+\beta$.

It is possible to express the Stokes vector of the incoming wave as a function of the intensity measured at the output. By calling $I_0$ and $I_{90}$ the intensity of the two output waves in the configuration $\beta$=$0^o$, and $I_{45}$ and $I_{135}$ the intensity of the two output waves in the configuration $\beta$=$45^o$, we have

$$S = \begin{pmatrix} I \\ Q \\ U \\ V \end{pmatrix} = \begin{pmatrix} I_0 + I_{90} = I_{45} + I_{135} \\ I_0 - I_{90} \\ I_{45} - I_{135} \\ \text{not measurable} \end{pmatrix} \tag{1.5}$$

With two different measurements, it is then possible to get all the necessary information about the incoming wave and determine its polarization degree. The first solution would be to simply turn the prism and to make two measurements. But this has the effect of modifying the direction of the two output waves as shown in fig. 1.8: a larger detection plane would then be needed, and all pixels of the detection plane would have to be precisely calibrated. On top of that, if turning a polarizer does (almost) not modify the path of light inside the detector, turning the prism has an influence on the optical path and can then distort the measurement of the intensity. And if instead of rotating the prism it is decided to rotate the whole instrument, the entrance slit will rotate too: if the observed source is broad, the observed part won't be exactly the same after the ro-

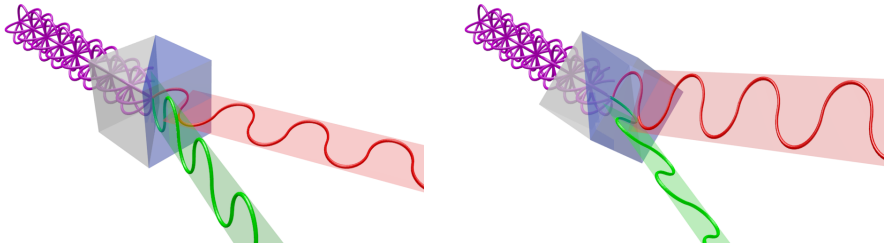

(a) *Incident angle $\beta$=0º. Both output waves are polarized in directions $\theta$=0º (red) et $\theta$=90º (green).*

(b) *Incident angle $\beta$=45º. Both output waves are polarized in directions $\theta$=45º (red) et $\theta$=135º (green).*

Figure 1.8: *Schematic of a Wollaston prism. The randomly polarized incoming wave (purple) goes out as two perpendicular linearly polarized waves (red and green), whose directions depend on the orientation angle of the prism.*

tation of the slit, and the measured Stokes parameters will be those of a different incoming wave.

To overcome this problem, the idea is to use a half waveplate which will be placed just before the prism. The half waveplate will change the polarization direction of the incoming wave by mirroring it through the plane formed by the fast axis of the plate and the propagation direction of light, as shown in fig. 1.9. In fact, in a half waveplate, the component aligned with the fast axis will experience no change, while the component perpendicular to the fast axis will have its phase shifted by $\pi$. We then have $\overrightarrow{E'_x} = \overrightarrow{E_x}$ and $\overrightarrow{E'_y} = \overrightarrow{E_y} e^{j\pi}$ $= -\overrightarrow{E_y}$, the output polarization state is then the mirror of the incoming one compared to the fast axis. We also have the following effect: rotating the half waveplate by an angle $\theta$ will rotate the polarization direction of the output wave by an angle $2\theta$. The Mueller matrix of a half waveplate forming an angle $\theta$ with the vertical axis (angle positive with the same convention than for the polarizer) is

$$M(\theta) = \begin{pmatrix} 1 & 0 & 0 & 0 \\ 0 & \cos(4\theta) & \sin(4\theta) & 0 \\ 0 & \sin(4\theta) & -\cos(4\theta) & 0 \\ 0 & 0 & 0 & -1 \end{pmatrix}$$

We can note the coefficient $-1$ at the fourth line of the matrix:

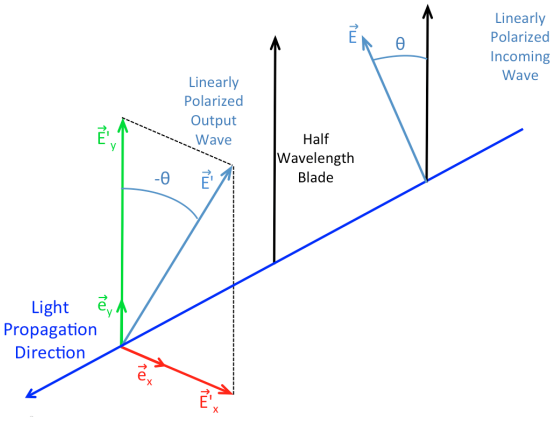


Figure 1.9: *Principle of a half waveplate. The polarization direction of the incoming wave is mirrored through the plane defined by the fast axis and the propagation direction, giving an output wave with a polarization direction of* $-\theta$.

this coefficient will act on the sign of $V$ (the intensity of circular polarization), which means that it will modify a left handed circular polarization into a right handed one (and vice versa).

The half waveplate is used as follow: it is placed in a first configuration used as a reference, at an angle $\theta$ defined as $0^o$. The output wave goes through the Wollaston prism and is analyzed. Then the half waveplate is turned by an angle of $22.5^o$: the output wave which enters into the prism has a linear polarization oriented at $2\times22.5^o = 45^o$ compared to the configuration $\theta = 0^o$. We then recover the system of equations (1.5). The advantage of using a half waveplate is that turning it does not change the optical path of the wave or requires a rotation of the instrument. It also does not modify the direction of the two waves going out of the prism, which will arrive at the same place on the detection plane: the plane can then be smaller, and the calibration of the various pixels is easier. This technique is thus often used, and it is the one used by the instruments FORS1 [27] (installed on the VLT until 2009) or LRISp [28] (still installed on the Keck observatory).

## 1.6 Hard X-ray and Gamma polarimetry

All the techniques described above cannot be used for X and gamma energies. In fact, the wavelength associated to those energies are close to interatomic distances or are even smaller, and optical instruments like polarizers, prisms or waveplates have no effect on them, so other methods have to be used. Depending on the considered energy, the interaction between light and matter is different, implying a different way to perform polarimetry. We will first describe the Hard X-rays and Gamma energies. For very high energies of more than tens of keV, there are two types of interaction between photons and matter, and it is possible to recover polarimetry information from both of them.

The first type of interaction is for energies between ≈20 keV and few MeV and is called Compton scattering. It is an elastic collision between a photon and an electron. The schematic of a Compton interaction is shown in fig. 5.8. If we consider the phenomenon from the particle point of view (where we represent light under the form of photons instead of the form of a wave), the Compton interaction consists of an incoming photon of energy $E_1$ colliding with an electron at rest. The electron will be ejected in some direction and have the energy $E_e$, while the photon will be scattered in the direction ($\theta$,$\phi$) (angles defined on the fig. 5.8) and will have the energy $E_2$. The energies $E_1$ and $E_2$ are linked by the equation:

$$E_2 = \frac{E_1}{1 + \frac{E_1}{m_e c^2}\left(1 - \cos(\theta)\right)} \tag{1.6}$$

The only useful angle to determine the energy is $\theta$. An interesting aspect for polarimetry is the differential cross section, which consists in the probability that the interaction happens in a solid angle $\mathrm{d}\Omega$ [29]:

$$\frac{\mathrm{d}\sigma_{Compton}}{\mathrm{d}\Omega} = \frac{1}{2} r_0^2 \frac{E_2^2}{E_1^2}\left[\frac{E_1}{E_2} + \frac{E_2}{E_1} - 2\sin^2(\theta)\cos^2(\phi)\right] \tag{1.7}$$

where $E_1$, $E_2$, $\theta$ and $\phi$ are the angles defined in fig. 5.8, and $r_0 \approx 2.82\ 10^{-15}$ m is the classical electron's radius. This formula has been

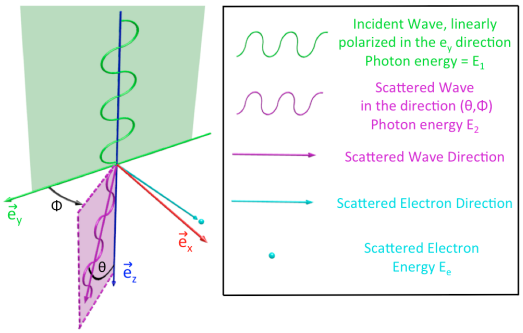


Figure 1.10: *Compton scattering. An incoming wave corresponding to photons of energy $E_1$ arriving on a electron at rest is diffused on the direction ($\theta$,$\phi$) defined from the direction of the incoming wave and its polarization direction. The diffused photons have the energy $E_2$. The electron is ejected in a second direction with the energy $E_e$.*

derived by Heitler in 1954 from the Klein-Nishina formula which expresses the differential cross section of the Compton effect in relation to the energy of the diffused photon $\frac{\mathrm{d}\sigma_{KN}}{\mathrm{d}E_2}$. The interesting point in the Heitler formula is the apparition of the coefficient $\cos^2(\phi)$: the probability of the interaction is modulated by the polarization direction of the incoming wave, and the scattered photon has more chances to be emitted in the direction $\phi = 90^o$. For a fixed angle $\theta$ which, according to (1.6) is the same than fixing the energy $E_2$, it is possible to make a statistical distribution of the number of photons received for different azimuthal angles $\phi$, and according to equation (1.7) this distribution will be asymmetric. The shape of this asymmetry depends on the polarization direction of the incoming wave, and on its polarization degree. fig. 1.11a shows the shape of this asymmetry for different polar angles $\theta$ and fig. 1.11b [30] shows real data taken in a 100% polarized beamline. The instrument ISGRI and PICsIT of the gamma observing satellite INTEGRAL have been used to perform polarimetry of observed sources thanks to this method, and the polarization of the Crab supernova remnant has been measured and the best upper limit on Lorentz invariance could be obtained.

The second type of interaction happens for energies higher than the MeV. In this case, the incoming photon is converted into an electron-positron pair. For such an interaction to happen, the in-

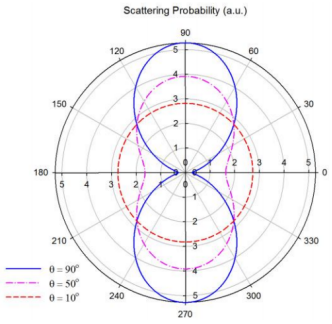


(a) *Theoretical normalized histogram of the azimuthal directions of diffused photons for an incoming light linearly polarized in the azimuthal direction $\phi$=0º (greatest ejection probability at $\phi$=90º).*

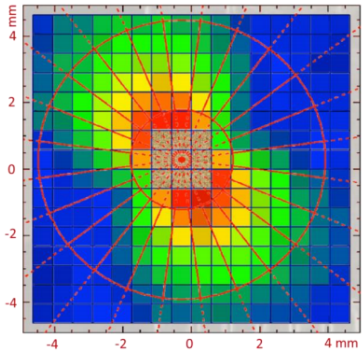


(b) *Counts distribution of events at $\theta$ = 90º ($E_2$ = 139-148 keV) from a 200 keV incoming beam with linear polarization oriented at 30º, giving a maximum probability of azimuthal ejection of diffused photon at $\phi$ = 90º + 30º = 120º.*

Figure 1.11: Figures from [30]

coming photon needs to have at least twice the rest energy of the electron $m_e c^2 = 511$ keV, meaning 1.022 MeV. The excess of energy $E - 1.022$ MeV is distributed under the form of kinetic energy between the created electron and positron. Here again, it is possible to recover polarimetry information of the incoming light thanks to the study of the interaction. In fact, the two ejection directions (the one of the electron and the one of the positron) define a plane which forms a definite azimuthal angle $\phi$ in relation to the polarization angle $\phi_0$. And this angle modulates the differential cross section of the interaction:

$$\frac{\mathrm{d}\sigma}{\mathrm{d}\phi} \propto (1 + AP\cos(2(\phi - \phi_0)) \tag{1.8}$$

where $P$ is the polarized fraction of the incoming wave, and $A$ a factor called "polarization asymmetry" [31]. Here again, by performing a statistical distribution of the azimuthal angles of the interaction on a sufficient number of photons, it is possible to perform polarimetry. Up to now, there are no space telescopes able to perform polarimetry above the pair creation threshold, despite the interest of such measurements. They could for instance allow a precise localization

of the emission region of the non thermic pulsed radiation of a pulsar. At the moment several models exist, and only a polarization measurement could discard the invalid ones). This is why several projects are under development like HARPO [32] or AdEPT [33].

## 1.7 Soft X-ray polarimetry: Thomson scattering and Bragg reflection

We now focus on the so called "soft" X-rays, those having an energy between 1 keV and few tens of keV. Until now, only two polarimetric methods have been used [34].
The first method is the use of the Thomson scattering. It is a process very close to Compton scattering, but for lower energies (of the order of few tens of keV). The photon is 'deviated' by the charged particle and this happens without any energy transfer from the photon to the charged particles. In the case of Thomson scattering, the scattered waves in the direction perpendicular to the direction of the incoming wave are linearly polarized in the scattering plane, as seen in fig. 1.12. This scattering in the orthogonal plane is not isotropic, and like for the Compton scattering there is a preferred azimuthal angle $\phi_0$. This preferred direction is linked to the fraction of linear polarization of the incident wave, and to its polarization direction. By making a measurement of the intensity of the scattered wave for several azimuthal angles $\phi$, it is possible to get the necessary information for polarimetry. A polarimeter based on the Thomson scattering has the advantage of working on a large energy band (from 1 keV to several tens of keV, where Compton scattering becomes the preferred mechanism). However the polarimetry measurement is not very precise. Also, because only waves scattered at 90 degrees are measured, all the other are rejected: only a small part of the scattered wave is then measured, which makes the instrument not efficient. Finally, such an instrument is hard to build, because the scattering material has to be chosen carefully: it has to be thick enough to diffuse the incoming wave, but thin enough not to absorb it too much. Because of this scattering material, the instrument loses even more efficiency. The instrument also needs several measurements for different scattering angles $\phi$: several detection planes are needed (which increases the background noise of the instrument, or one detection plane that needs to be turned. Because of all these problems, only one polarimeter using this principle has flown, on

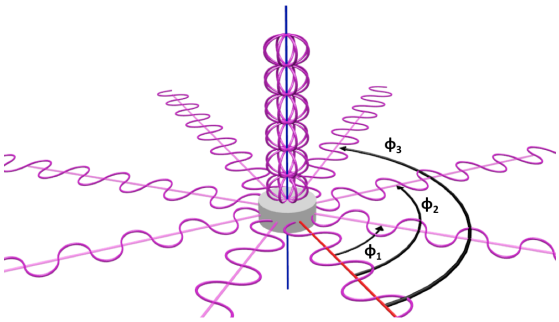


Figure 1.12: *Thomson scattering at 90 degrees. The scattered wave in the plane perpendicular to the incoming wave are linearly polarized. The scattering is not isotropic, and some azimuthal angles $\phi$ are preferred. Those preferred directions are directly linked to the polarization state of the incoming wave.*

three different experiments, and only on board sounding rockets in 1968, 1969 and 1971 ([35, 36, 37]).

The second method is the use of the Bragg reflection. The incoming wave arrives on a crystal under an angle of 45°, and is reflected with the same angle. Such a configuration of the crystal makes the output wave 100% polarized in the direction perpendicular to the direction of the incoming plane and parallel to the plane formed by the crystal lattices. If this output wave is 100% polarized it is because only the linearly polarized fraction of the incoming wave is reflected by the interference phenomenon. The crystal, under this configuration, acts like a linear polarizer. As seen before in this chapter, by making a measurement for several orientation angles of the crystal, it is possible to get the polarimetry information of the incoming wave. Fig. 1.13 shows the effect of two different orientations of the crystal, which each one giving a linear polarization in the same plane, but not in the same direction and with the same intensity.

This method is extremely precise and the error on the measurement of the polarization parameters is very small (the measured modulation factor can reach 93% [38]. However, it is also very inefficient for two reasons. First, like for a linear polarizer, it absorbs a great part of the incoming wave to reflect only the part which is polarized in the good direction. This was already a problem for energies from IR to UV, but it is even worse for X-ray sources as they

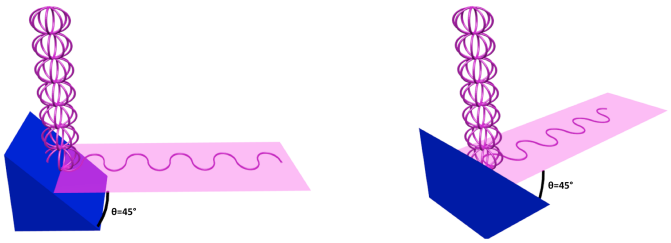


Figure 1.13: *Polarization direction of the output wave in function of the crystal orientation. The output waves are polarized in the same plane perpendicular to the incoming wave, but in different directions, parallel to the lattices of the crystal.*

are usually not intense: an inefficient instrument implies a very long exposure time. The second problem is the very narrow energy band on which this instrument works. For a given crystal placed in the Bragg configuration as presented in fig. 1.14, only 3 different energies come out, given by the 3 orders of constructive interferences. In fact, the reflection on the crystal, lattices of which are spaced by a distance $d$, of a wave with an incoming angle $\theta$, is ruled by the grating equation $2 \times d \times \sin(\theta) = n \times \lambda$ . Only energies of wavelength $\lambda = \dfrac{2 \times d \times \sin(\theta)}{n}$ (with $n$ integer) are then reflected by the crystal. For $\theta = 45^o$, if we take the case of $2d = 4.27$ Å (corresponding to a Lithium Fluoride 200 crystal), we get $\lambda \approx \dfrac{1.51}{n}$Å, corresponding to energies for the output wave of $\approx 4$ keV, 8 keV et 12 keV for $n$ equals 1, 2 and 3. Above these energies, Bragg reflection does not happen anymore (because the wavelengths are too low to be reflected by the crystal as they reach the interatomic distances). And the variation of the energies of the output wave around those given by the grating formula are of the order of eV. So the dynamic energy range of such a polarimeter is very weak which represents an enormous problem. This is why only two polarimeters using Bragg reflection have been used, one on a sounding rocket [39], and the other on board the OSO-8 satellite [40].

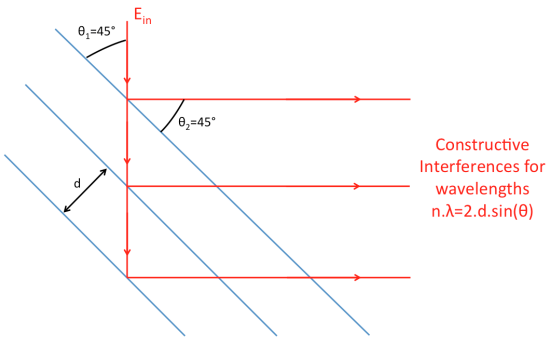


Figure 1.14: *Interference phenomenon in a crystal. Here, the case $\theta_1$=45° is represented, but the phenomenon is available for every angle $\theta_1$. The output wave in the direction $\theta_2$=$\theta_1$ is the result of interferences between the reflected waves by the various lattices of the crystal. Only the constructive interferences give an output wave, which wavelength $\lambda$ is defined by the grating formula $2\times d\times sin(\theta) = n\times\lambda$ with n integer.*

## 1.8 Soft X-ray polarimetry: the interest of the astrophysics community

The experiments of soft X-ray polarimetry we just mentioned were conducted in the 70's, and since then no polarimeter for soft X-rays has been launched, neither Bragg or Thomson, because of the reasons we mentioned: the great progress in term of imaging, spectroscopy and timing in those energies made the soft X-ray polarimeters and their low efficiency completely behind in terms of scientific results. X-ray polarimetry has in fact been discarded for instrumental reasons. Yet the astrophysics community is very interested in it, and we will detail a few examples of applications of soft X-ray polarimetry, of which an exhaustive list can be found in [41].

A first application is about **pulsar nebulas**. A pulsar is a magnetic dipole in a very fast rotation (making a complete turn around its axis in few milli-seconds in some cases): this rotation creates a magnetic field of intensity proportional to the rotation speed and to its derivative. The created magnetic field is then very intense. Charged particles, mostly electrons (the lightest charges particles) follows the magnetic field lines and emit synchrotron radiation up to X-rays. Two zones can be identified. The first is very close to the pulsar. In this zone, it is possible to measure polarization, but the

very low angular precision of X-ray instruments makes it impossible to know if the polarization is aligned with the rotation axis of the pulsar, or with its magnetic axis. Being able to chose one of those two cases would allow to discard or validate some theories. The second zone is far from the pulsar, in the nebula. Here the polarization seems to be random, but the low precision of the polarimeters which performed the measurement does not allow to say more than this. Yet three different models of magnetic field creation inside the pulsar nebula exist (polar cap, outer cap and slot gap), each giving a different topology of magnetic field [42]. A measurement of polarimetry would allow to chose the right model. It is important for such a measurement to be able to separate the different energies, as it allows to separate the various emitting zones of the pulsar despite the low angular resolution.

A second example of application of X-ray polarimetry is the **X-ray binary systems** study [43]. In these systems, a dense body absorbs the matter of its companion via an accretion disk and re-emit it under the form of a jet, and the physics underlying this jet is still unknown. Because this emission of matter can come along with a high emission of X-rays, these energies can be used to probe the phenomenon and to complete our knowledge of binary systems. The study of the energy-dependent X-ray polarization properties could bring a lot of crucial information to study these systems [50].

The study of **black holes** would also benefit of X-ray polarimetry. When a black hole is isolated, it is impossible to detect it. However, when the black hole is in a binary system, as for instance Cygnus X1 which has a supergiant star as companion, the matter from the companion wind falls into it. This constitutes a binary system, and the above-mentioned phenomenon applies and can be studied with X-ray polarimetry. On top of that a black hole in a binary system has an accretion disk around it. This disk emits a thermal spectrum in soft X-rays, and a line at 6.4 keV (K$\alpha$ emission line of neutral iron). The theory says that this emission is polarized. A measurement of the polarization of the spectrum would not just confirm the theory, but also give access in an indirect way to two essential properties of a black hole: its mass and its spin.
Up to now, the measurement of black holes masses is done by Kepler's laws. It is the same method used to measure the mass of the black hole at the center of our galaxy. For black holes in binary systems, we measure the transit of the black hole by looking at the drop of the brightness of the companion star, allowing a measurement of

the orbit time, and then of the black hole mass. However, those measurements are affected by uncertainties, and are very dependent of the orbit inclination of which measurement is not accessible by usual methods. Because the polarization is influenced by the geometry of the system, a polarimetry measurement would give information about the inclination angle of the accretion disk (a disk seen from the top would give a polarization of 0%, and a disk viewed from the side would give a higher polarized fraction [47]). These systems being usually X-ray binaries, they mostly emit in X-rays, and only a polarimetric measurement of X-rays would give enough information to measure the black hole's orbit inclination, and then its mass.
The strong gravity near the Black Hole is responsible for several processes such as relativistic aberration or gravitational lensing. These effects can combine to give a measurable signature on the polarization of the light coming from the accretion disk [48]. The level of polarization depends on the Black Hole spin and the inclination angle of the accretion disk. Measuring the polarization of the accretion disk can then give information about the Black Hole spin and its inclination [49].

A last example of X-ray polarimetry is the study of **Gamma Ray Bursts** (GRB) [44, 45]. These phenomena are a prompt and very intense emission of gamma rays, and are detected by hard X-rays and gamma observatories which have a field of view wide enough to capture this signal without having to look directly at the source. These are followed by a second type of signal called the afterglow. The afterglow is caused by bremsstrahlung radiation and is not polarized. So even if measurements have never been performed on it there are almost no doubts on this fact. However the prompts are very polarized, but soft X-ray polarimetry measurements have never been done on the prompts. The reason is that GRBs are almost never in the low field of view of previous soft X-ray polarimeters. Such a measurement would complete the polarimetry measurements done on gamma energies and improve our knowledge and understanding of GRBs.
The study of GRB polarimetry would also allow a measurement of a more fundamental physics phenomenon, called the Vacuum Magnetic Birefringence (VMB) [46]. It is a phenomenon that would violate the Lorentz invariance by making the speed of light propagation in vacuum energy dependent. So if the VMB is true, two adjacent energies emitted by the same source would see their polar-

ization direction rotate on their path in a different way. The waves going out of the source with the same polarization direction would be detected with a different polarization direction. However, this phenomenon is difficult to measure as it is supposed to be quite weak: the emitting sources then need to be as far as possible, to let the time to the two energies to have their polarization plane rotated in a different way. This is the case of GRBs, which are extra galactic sources. By looking at two adjacent energy bands of a GRB and by comparing their polarization state, it is possible to test the theories which go beyond the standard model and predict VMB. Here again, the polarimetry measurement needs to be associated to the spectroscopy measurement of the observed light, and it is a spectro-polarimeter which is needed.

## 1.9 The photoelectric effect for polarimetry: the solution ?

Those examples are some among many. The interest of the astrophysics community for soft X-ray spectro-polarimetry is here, despite the instrumentation problems. And since the early 2000's, thanks to the development of micro-pattern gaseous detectors, this interest has been renewed.
In fact, these detectors make it possible the use of a dominating effect at energies between 1 keV and few tens of keV: the photoelectric effect. During this phenomenon, presented fig. 1.15.a, an electron is ejected from the detecting atom. This electron is called photoelectron, and its energy is the one of the detected photon minus the energy needed to eject the electron from the atom. The electron is ejected in a direction ($\theta$,$\phi$) (here $\theta$ is the polar angle and $\phi$ the azimuthal angle). Similarly to the Compton scattering, Heitler expressed the differential cross section of the photoelectric effect [29]:

$$\frac{\mathrm{d}\sigma_{ph}}{\mathrm{d}\Omega} = r_0^2 \alpha^4 Z^5 \left[\frac{m_e c^2}{E}\right]^{\frac{7}{2}} \frac{4\sqrt{2}\sin^2\theta\cos^2\phi}{(1-\beta\cos\theta)^4} \tag{1.9}$$

where $r_0$ is the classical radius of the electron and $\beta$ its speed expressed in units of speed of light, $\alpha$ the fine structure constant, $m_e$ the electron's mass at rest, $E$ the energy of incoming photon, $Z$ the atomic number of the absorbing atom, $c$ the speed of light and $\theta$ and $\phi$ the polar and azimuthal angle defined in fig. 1.15a.

The probability of the interaction is then modulated by $\cos^2\phi$: there is a preferred azimuthal ejection direction, which depends on the direction of polarization of the incoming light which carries the absorbed photon. By looking at the angular distribution of the azimuthal ejection direction of the photoelectrons, it is then possible to estimate the polarization direction of the incoming wave and its fraction of linear polarization. In fact, according to the equation (1.9), it is possible to fit the angular distribution of azimuthal direction of the photoelectrons by the function $M(\phi) = A + B \times \cos^2(\phi - \phi_0)$, where $A$, $B$ and $\phi_0$ are free parameters [52]. Here $A$ is the standar notation commonly used and is not to be confounded with the parameter of eq. (1.8).

The polarized fraction $P$ of the incoming light is proportional to the amplitude of the modulation curve $a = \dfrac{M_{max} - M_{min}}{M_{max} + M_{min}} = \dfrac{B}{2A + B}$. $a$ is called modulation amplitude. In theory, for a 100% polarized source, $A$=0 and $a$=1.

However, a detector is never perfect and will not give $a = 1$ even for a completely polarized source. So we introduce a coefficient $\mu$ called the modulation factor: $\mu$ corresponds to the measured value of $a$ for a 100% polarized source. For a measurement of a given source, the measured polarized fraction is then $a_p = \dfrac{a}{\mu}$. We can see that for a 100% polarized beam we have $a_p = 1$ as expected. So $\mu$ represents the "efficiency" of the detector: $\mu = 1$ means that the detector will give a measurement of $a = a_p$. The modulation factor $\mu$ of a polarimeter is then a very important parameter as it allows to measure the real polarized fraction of the observed source.

Another important point is the Minimum Detectable Polarization (MDP). It is the factor $a_{MDP}$ which determines the minimum value of measured $a$ which can be associated without doubts to a polarization of the observed source, and not associated to a statistical effect. In presence of noise, which we describes as a Poisson distribution with a total number of measured counts $N$, the probability p($a$,$\phi$) to measure a modulation $a$ in a direction $\phi$ is given by [53, 54]:

$$p(N, a, \phi) = \frac{Na}{4\pi} \exp\left[-\frac{N}{4}\left[a^2 + a_0^2 - 2aa_0\cos(\phi - \phi_0)\right]\right] \quad (1.10)$$

where $a_0$ is the true amplitude and $\phi_0$ the true orientation of polarization. In the case of the observation of a non polarized source ($a_0$ = 0) we then have:

$$p(N, a) = \frac{Na}{4\pi} \exp\left[-\frac{N}{4}a^2\right] \tag{1.11}$$

We can integrate equation (1.11) to find the probability of measuring the amplitude $\alpha$ in the case of $a_0$=0 :

$$P(N, a = \alpha) = \int_0^\alpha p(N, a)\, \mathrm{d}a \tag{1.12}$$

We note $a_{1\%}$ the value of the amplitude which gives $P(N, a_{1\%}) = 1\%$. $a_{1\%}$ is called the Minimum Detectable Amplitude (MDA). It is the measured amplitude which has less than 1% chance to be caused accidentally by noise or statistical fluctuations inside the detector. From the equation (1.12) we get $a_{1\%} = MDA = \frac{4.29}{\sqrt{N}}$. The Minimum Detectable Polarization is $MDP = \frac{MDA}{\mu} = \frac{4.29}{\mu\sqrt{N}}$, where $\mu$ is the modulation factor defined earlier and $N$ the number of counts recorded by the detector. The $MDP$ corresponds to the minimum polarized fraction that can be detected if we recorded $N$ counts in the detector, with less than 1% of chance than this measurement is caused by statistical fluctuations. The $MDP$ then depends on the number of counts in the detector, and on the modulation factor $\mu$. If $\mu$ is close to 1, less counts would be needed in the detector to reach the $MDP$.

## 1.10 Gas and photoelectric effect

In order to reach the best modulation factor, the detector needs to be able to recover properly the azimuthal ejection direction of the photoelectron. So the photoelectron has to recoil far enough with respect to the pixel size in the detector to be able to be detected by the readout electronics that must be pixelated accordingly. The photoelectron energy is equal to the difference between the energy of the incoming photon and the electron binding energy of the absorbing atom. The interacting material must then have a low electron binding energy for the photoelectron to get as much energy as possible from the incoming photon. The photoelectron then propagates inside the material and ionize it on its path, leaving a track of several electrons.
This track must be long enough to be detected, so the material must

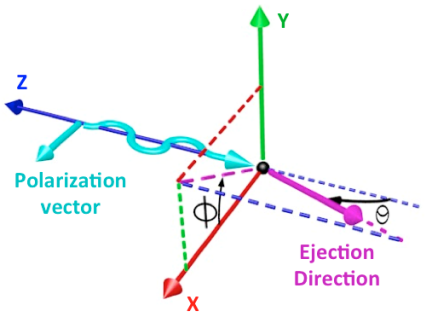


(a) *Photoelectric effect. The emission probability is modulated by* $\cos^2(\phi)$.

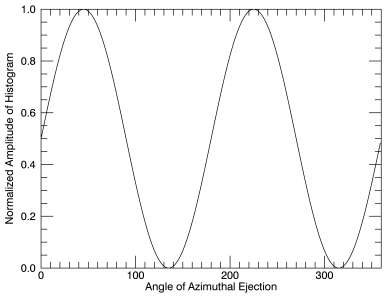


(b) *Theoretical histogram of the azimuthal angle of ejection of photoelectron, for an incoming wave with linear polarization oriented at 45º (maximum of emission for* $\phi$ *= 45º.*

Figure 1.15

have a low ionization energy, and have the lowest density possible: in this case the photoelectron will lose its energy by ionization on a distance long enough to be measured by the electronics. However, equation (1.9) tells that it is important to have a high $Z$ absorbing material, to have a large probability for the photoelectric effect to happen and then have an efficient detector. Unfortunately, a high $Z$ solid material is often a dense one.

Some attempts have been made using silicon as absorbing material. The photoelectron crosses several pixels of the readout electronics, and the anisotropy of emission of the photoelectric effect creates an excess of events in pixels close to the interaction point, which would give an image as the one in fig. 1.11b. However, in silicon, the photoelectron range is too short for energies of less than 15 keV as it is of the order of 50 $\mu$m. In fact, for "slow" electrons (meaning the ones having energies between 1 keV and 40 keV), an empirical formula gives the practical range of an electron of energy $E$ in a material: $R(\mu\text{g.cm}^{-2}) = 10.0{*}E^{1.7}$ (with $E$ in keV) [51], so for a material of a bulk density $\rho$, the practical range of the photoelectron is $\dfrac{R}{\rho}$. In Silicium, we have $\rho_{Si} \approx 1.1$ g.cm$^{-3}$, giving for a photoelectron of 10 keV $R_{Si} \approx 4.5$ $\mu$m, much too low to be observed by pixelated detectors, with pixels of the order of several hundreds of $\mu$m.

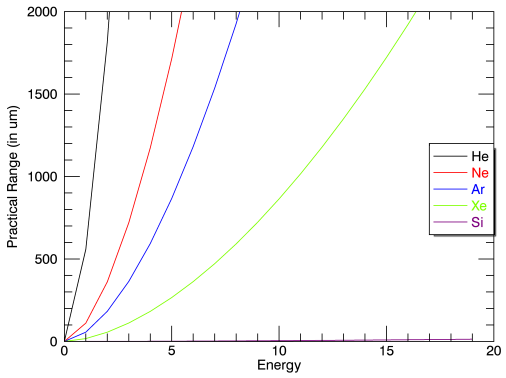


Figure 1.16: *Several values of practical range vs energy for several gases. The gas is clearly more adapted than semi-conductor detectors for soft X-ray polarimetry, as they allow the photoelectron to recoil far enough to leave a track that can be measured by a readout electronics.*

So for the soft X-ray energy range (between 1 keV and $\approx$ 20 keV) it is necessary to use another material, with a low bulk density. Gas is a perfect candidate. The gas acts like any other material: by photoelectric effect an incoming photon transfers its energy to a photoelectron which ionizes the gas on its path. Thanks to the low density of gas, even at low energies the recoil of the photoelectron can be long enough to be observed by a pixelated detector. Then, in argon under standard conditions for temperature and pressure (NTP: 1 atm, 25 Celsius) of bulk density $\rho = 1.78\times10^{-3}\text{g.cm}^{-3}$, we get $R_{Ar} \approx 1.2$ mm for a photoelectron of 6 keV, and $\text{R}_{Ar} \approx 2.8$ mm for a photoelectron of 10 keV. In a gas with a lower density such as helium of bulk density $\rho_{He} = 1.78\times10^{-3}\text{g.cm}^{-4}$ at NTP, $R_{Ar} \approx$ 11 mm for a 6 keV photoelectron. Practical range curves as a function of the energy at NTP and for various materials are presented in fig. 1.16. We clearly see the advantage of a gaseous medium compared to semi-conductors: their low values of bulk densities allow the photoelectron to recoil far enough to be able to recover its ejection direction in a readout electronics. This concept of gaseous polarimeters is used by the projects XIPE [50], IXPE and PRAXyS [56].

However, a polarimeter using gas as an interacting medium will experience several problems. The first one is the reliability of the

detector: as we will see in chapter 2, gaseous detectors are very sensitive to localized high energy deposition which can damage them. On earth, these high energy depositions are caused by muons. In space, it would be caused by cosmic hadrons. A gaseous polarimeter in space would then be exposed to a high flux of energetic particles. It is then imperative to think about reliable solutions to protect the detector and its readout electronics. The second problem is the necessity to have a spectro-polarimeter, because a polarimeter does not give all possible information on the observed sources if it is not able to separate the various energies. In a gaseous detector, a good spectroscopic capability needs a "heavy" gas (argon or xenon), which comes along with a lower photoelectron range (as shown in fig. 1.16). A trade-off has to be made in order to perform spectroscopy with a satisfying energy resolution, and still having good conditions to do polarimetry. Several obstacles have then to be overcome and my PhD work falls within the context of instrumentation of soft X-ray spectro-polarimetry.

## 1.11 Summary

Observational astrophysics has experienced enormous developments in every energy bands, from radio waves to gamma rays, in spectroscopy, imaging and timing.
In polarimetry, X-rays are missing: for instrumental reasons, missions in X-ray spectro-polarimetry have been discarded despite all the scientific information it could bring, and no results have been obtained since the early 1970's.
Thanks to the recent development of micro pattern gaseous detectors at the early 2000's, the use of the photoelectric effect for X-ray spectro-polarimetry has become possible, and the interest of the astrophysics community has been renewed. For those reasons, the XIPE (ESA) and IXPE (NASA) X-ray polarimetry missions have been selected for phase A study.
However, before using gaseous detectors in space, several problems have to be overcome. Moreover, most of the proposed polarimeters do not perform spectroscopy, which reduces the number of sources which can be observed.

It is in this context that the work of this thesis started. I explore a new concept of soft X-ray gaseous spectro-polarimeter overcoming the major issues of the use of gaseous detectors.

# Bibliography


[1] http://sci.esa.int/rosetta/

[2] https://mars.nasa.gov/msl/

[3] J. G. Learned and K. Mannheim, *High-Energy Neutrino Astrophysics*, Annual Review of Nuclear and Particle Science; **50**, 679-749

[4] B. P. Abbott et al., *Observation of Gravitational Wavesfrom a Binary Black Hole Merger*, Phys. Rev. Lett. **16**, 061102

[5] https://www.auger.org/

[6] http://jem-euso.roma2.infn.it/

[7] S. J. Bell, A. Hewish et al., *Observation of a Rapidly Pulsating Radio Source*, Nature **217**, 709-713 (1968)

[8] https://www.nasa.gov/mission_pages/hubble/main/index.html

[9] http://www.vla.nrao.edu/

[10] http://sci.esa.int/xmm-newton/

[11] https://www.nasa.gov/mission_pages/chandra/main/index.html

[12] https://www.eso.org/public/france/teles-instr/lasilla/36/harps/

[13] http://www.eso.org/public/france/teles-instr/paranal-observatory/vlt/

[14] https://integral.cnes.fr/fr/INTEGRAL/Fr/GP_instrument.htm

[15] http://sci.esa.int/integral/

[16] https://heasarc.gsfc.nasa.gov/docs/xte/XTE.html

[17] J. Delabrouille et al., *CMB polarization as complementary information to anisotropy*, C. R. Physique 4 (2003), 917-924

[18] https://map.gsfc.nasa.gov/

[19] http://sci.esa.int/planck/

[20] https://heasarc.gsfc.nasa.gov/docs/einstein/heao2.html

[21] http://www.eso.org/public/france/teles-instr/alma/

[22] F. Mantovani and A. Kus, *The Role of VLBI in Astrophysics, Astrometry and Geodesy*, NATO Science Series II: Mathematics, Physics and Chemistry, pp191-204

[23] J. Vernet, *Etude Spectropolarimétrique des premières phases de l'évolution des galaxies les plus massives*, PhD Thesis

[24] http://hubblesite.org/the_telescope/nuts_.and._bolts/instruments/nicmos/

[25] https://spie.org/samples/PM200.pdf

[26] http://photonics.intec.ugent.be/education/IVPV/res_handbook/v2ch22.pdf

[27] http://www.eso.org/sci/facilities/paranal/instruments/fors.html

[28] https://www2.keck.hawaii.edu/inst/lris/polarimeter/polarimeter.html

[29] W. Heitler, *The Quantum Theory of Radiation*, Oxford University Press, 1954 (p.206)

[30] S. Antier et al., *Hard X-ray polarimetry with Caliste, a high performance CdTe based imaging spectrometer*, Experimental Astronomy 39 (2015) 233-258

[31] P. F. Bloser, *Gamma-Ray Polarimetry in the Pair Production Regime*, X-ray Polarimetry Workshop, February 9-12, 2004

[32] P. Gros et al., *HARPO - TPC for High Energy Astrophysics and Polarimetry form the MeV to the GeV*, TIPP 14 3rd Technology and Instrumentations in Particle Physics conference, 2-6 June 2014 Amsterdam, Proceedings

[33] S. D; Hunter, *A pair production telescope for medium-energy gamma-ray polarimetry*, Astroparticle Physics **59** July-August 2014, pp18-28

[34] M. C. Weisskopf et al., *The prospects for X-ray polarimetry and its potential use for understanding neutron stars*, **357** Astrophysics and Space Science Library, pp.589-619

[35] Angel et al., *Search for X-Ray Polarization in SCO X1*, Physical Review Letters, **22**, 1969

[36] R. S. Wolff et al., *Search for Polarization in the X-Ray Emission of the Crab Nebula*, Astrophysical Journal Letters; **160**, L21-L25, 1970.

[37] Novick et al., *Detection of X-Ray Polarization of the Crab Nebula*, Ap.J, **174**, 1972

[38] R. Novick et al., *The OSO-8 mosaic graphite stellar X-ray polarimeter*, New instrumentation for space astronomy, Proceedings of the symposium, Tel Aviv, Israel, June 7-18, 1977

[39] Weisskopf et al., *A Graphite Crystal Polarimeter for Stellar X-Ray Astronomy*, Rev. Sci. Instrum., **43** (1972)

[40] Weisskopf et al., *Measurement of the X-Ray Polarization of the Crab Nebula*, Ap.J, **208**, L125-L128 (1976)

[41] Bellazzini et al., *X-ray Polarimetry, A New Window in Astrophysics*, Cambridge University Press, ISBN: 9780521191845

[42] A. K. Harding, *Polarization of pulsar wind nebulae*, in X-ray Polarimetry, A New Window in Astrophysics

[43] K. Wu, *X-ray polarization from accreting white dwarfs and associated systems*, in X-ray Polarimetry, A New Window in Astrophysics

[44] D. Lazzati, *X-ray polarization of gamma-ray bursts*, in X-ray Polarimetry, A New Window in Astrophysics

[45] N. Produit, *POLAR: an instrument dedicated to GRB polarization measurement*

[46] R. Gambini and J. Pullin, *Nonstandard optics from quantum space-time*, Phys. Rev. D, **59** 124041 (1999)

[47] M. Dovciak et al., *Polarization of thermal emission from accreting black holes*, in X-ray Polarimetry, A New Window in Astrophysics

[48] P. A. Connoes and R. F. Stark, *Observable gravitational effects on polarised radiation coming from near a black hole*, Nature, **269**

[49] J. Schnittman and J. H. Krolik, *X-Ray Polarization from Accreting Black Holes: the Thermal State*,ApJ, **701** 1175-1187 (2009)

[50] P. Soffitta et al., *XIPE: the X-ray Imaging Polarimeter Explorer*, *Experimental Astronomy* **36** 523-567 (2013).

[51] F. Sauli, *Gaseous Radiation Detectors, Fundamentals and Applications*, Cambridge University Press, ISBN: 9781107043015

[52] F. Muleri, *On the Operation of X-Ray Polarimeters with a Large Field of View*, ApJ **728** (2014)

[53] M. C. Weisskopf et al., *On understanding the figures of merit for detection and measurement of x-ray polarization*, in proceedings of SPIE, Space Telescopes and Instrumentation 2010: Ultraviolet to Gamma Ray

[54] T. E. Strohmayer and T. R. Kallman, *On the statistical analysis of X-ray polarization measurement*, ApJ, **773** (2013)

[55] M. C. Weisskopf et al., *An Imaging X-ray polarimeter for the study of galactic and extragalactic X-ray sources*, in proceedings of SPIE, Space Telescopes and Instrumentation 2008: Ultraviolet to Gamma Ray

[56] http://asd.gsfc.nasa.gov/praxys/

# Chapter 2

# Gaseous detectors: from Cloud Chambers to Micro Pattern Gaseous Detectors

# Contents

## Contents

# 2.1 Introduction

This chapter is dedicated to generalities of gaseous detectors. After a brief historical overview of the cloud and bubble chambers, the principle of gas ionization by detected particles (charged particles, photons and neutrons) is explained. The motion of created electron-ion pairs (diffusion and drift under an electric field) and the various regions of operations of a gaseous detectors are then developed. The chapter continues with the presentation of the Multi-Wire Proportional Chamber and its evolutions, and ends with the presentation

of Micro Pattern Gaseous Detectors, mainly the Gas Electron Multiplier and the Micromegas architecture.

## 2.2 Historical background: cloud and bubble chambers

### 2.2.1 The cloud chamber

As it has been explained in the previous chapter, a detector using gas as a detection medium is needed to recover the track of the photoelectron and perform soft X-ray polarimetry. The use of gaseous based detectors as tracking detectors is old and started with the invention of the cloud chamber by Charles Wilson in 1911, invention for which he received the Nobel Prize in 1927. It consists of a sealed chamber filled with oversaturated alcohol vapor. Because of this state of oversaturation, vapor condensates when a perturbation occurs. The passage of a charged particle creates a perturbation that condensate vapor along its trajectory, leaving a track of alcohol droplets that can be analyzed to get information about the detected particles.
But the first cloud chamber could not count more than 2 events per minute. The concept was improved over the years to give good pictures of the events tracks, or better counting rate, but not both at the same time. Despite those problems, it still allowed the discovery of the positron [1], the first image ever left by a positron in a detector, made by Anderson in 1932, is shown in fig. 2.1. It can be added that Anderson also discovered the muon in 1936 thanks to the cloud chamber [2].

### 2.2.2 The bubble chamber

In 1952, Donald Glaser invented the bubble chamber [3], and got the Nobel Prize in 1960 for this invention. The concept is similar to the cloud chamber: here the chamber is filled with a heated liquid, just below its boiling point. When a charged particle enters the detector, a piston is triggered and suddenly decreases the pressure inside the chamber, which puts the liquid in a superheated phase. The crossing particle perturbs this phase, and vaporize the liquid along its track. The study of this track (bubble density and curvature under a magnetic field) gives information on the energy and

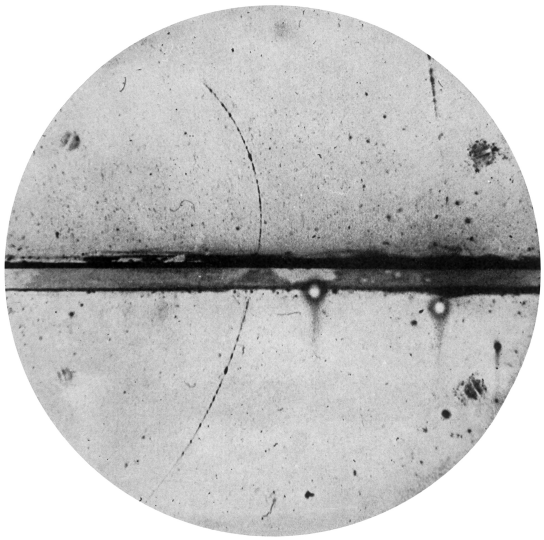

Figure 2.1: *First positron image, made with a cloud chamber by Anderson in 1932 [2].*

momentum of the detected particle. The advantages of the bubble chamber over the cloud chamber are its simplicity, and its spatial precision (down to few $\mu$m) which allows a better identification of the detected particles.
But there are several drawbacks when using a bubble chamber. Like the cloud chamber, the counting rate is very low, as after each interaction the bubbles have to be compressed back to vapor, and this process takes time. And most of all, both for cloud and bubble chambers, the identification of events was visual: for each event, a picture was taken, and analyzed by eye by the scientists to detect "interesting" events.

### 2.2.3 The need for readout electronics

Those problems of very low count rate and heavy event analysis were very limiting to study deeply the new field of particle physics, but there were no other solutions, until the invention of the Multi-Wire Proportional Chamber (MWPC) by Georges Charpak in 1968 [4]. This new instrument marked an enormous step forward in the development of particle physics: first, after an interaction there was no need to wait for several minutes for the detector to be ready again, and then the tracks of the particles were no longer recorded on a

photographic plate, but on a fast readout electronics. The invention of MWPCs was a cornerstone in the field of particle physics, as it brought it in the electronics era. For his invention, G. Charpak was awarded with the Nobel prize in 1992.
MWPCs use the same detection principle than modern gaseous detectors, so before entering into details, we first describe the principles of interaction between charged particles and gas, and charges motion in a gas under an electric field.

## 2.3 Interaction of particles with matter

Gaseous detectors can be used to detect different type of particles: charged particles, photons and neutrons. In the following we explain briefly the different physical processes at work.

### 2.3.1 Detection of charged particles

The main use of gaseous detectors is to detect charged particles. These particles can interact with the gaseous medium through the strong, weak or electromagnetic interaction, but the electromagnetic interaction being many orders of magnitude most probable than the two others, it is the only interaction used for the detection. The electromagnetic interaction of a charged particle in a medium has been extensively studied, here only the main properties will be mentioned.
The charged particle can interact directly with the nucleus of the atom. Using the approximation of non-relativistic kinematics and energy-momentum conservation, the maximum energy transfer of a particle of mass $m$ with a nucleus of mass $M$ is

$$\Delta E_{max} = \frac{1}{2} m v^2 \left[ \frac{4mM}{(m+M)^2} \right] \tag{2.1}$$

So, in the case of a particle interacting with a heavy nucleus ($m \ll M$), we get

$$\Delta E_{max} \approx \frac{1}{2} m v^2 \left( 4 \frac{m}{M} \right) \tag{2.2}$$

Which is close to 0 in the case of high mass nucleus. So in most cases, in a collision with a nucleus, the charged particle has its direction changed, but it loses little energy in the collision. This interaction is

called *multiple scattering*. At energies of the order of keV, it occurs often when the charged particle is an electron.

The charged particle then loses energy through *Bremsstrahlung* radiation, which is an electromagnetic radiation emitted by any accelerated charged particle. The energy loss through Bremsstrahlung radiation is very low for "heavy" charged particles (such as alpha particles or protons), but quite important for electrons.

The particle can also lose energy through the *Cerenkov effect* if its speed in the detecting material is greater than $\frac{c}{n}$, where $c$ is the speed of light and $n$ the refractive index of the material, but this is an effect negligible in gaseous detectors.
It can also lose energy through *transition radiation* when crossing the interface between the detector and the outside, but here again this effect is excessively small and can be neglected.

Most of the energy loss of the particle occurs with its *Coulomb interaction* with the electrons of the medium. The particle excites and ionizes the atoms on its way, leaving behind it a trail of excited atoms, ions and free electrons. The expression for the average differential energy loss (loss per unit length) due to these interactions with the electrons has been derived by Bethe in 1930 for non-relativistic particles, and corrected in 1932 for the relativistic case [5]:

$$\frac{\mathrm{d}E}{\mathrm{d}x} = -\frac{4\pi n Z^2}{m_e c^2 \beta^2}\left(\frac{e^2}{4\pi\epsilon_0}\right)^2\left[\ln(\frac{2m_e c^2\beta^2}{I(1-\beta^2)}) - \beta^2\right] \qquad (2.3)$$

where
$E$ = particle energy
$x$ = traveling distance of the particle
$v$ = particle speed
$c$ = speed of light
$\beta = \frac{v}{c}$
$e$ = elementary charge
$Z$ = atomic number of the detecting medium
$m_e$ = rest mass of the electron
$n$ = electron number density of the detecting material
$I$ = mean excitation potential of the material
$\epsilon_0$ = vacuum permittivity.

The electron number density is given by $n = \frac{N_A Z \rho}{A M_u}$, where $N_A$ is the Avogadro number, $Z$ the atomic number of the detecting medium, $A$ its mass number, $\rho$ its density and $M_u$ the molar mass constant

$= 1$ g/mol.
We rewrite this equation in the electrostatic unit system (CGS system), in which $4\pi\epsilon_0 = 1$, and we get:

$$\frac{\mathrm{d}E}{\mathrm{d}x} = -\frac{2\pi N_A z^2 e^4}{m_e c^2}\frac{Z}{A}\frac{\rho}{\beta^2}\left[\ln\frac{2m_e c^2\beta^2 E_M}{I^2\left(1-\beta^2\right)} - 2\beta^2\right] \tag{2.4}$$

where $E_M = \dfrac{2m_e c^2\beta^2}{1-\beta^2}$ is the maximum energy transfer allowed in each interaction between the particle and one electron.
The ionization potential $I$ is usually measured, but Bloch derived a good approximation [6] with $I = I_0 Z$, where $I_0 \approx 12$ eV.
It is important to note that this equation is not valid if the detected charged particle is an electron, as an electron will lose a great part of its energy through Bremsstrahlung radiation, as explained above. But for the detection of other charged particles it is very important because it shows how energy is deposited inside the detector.

### 2.3.2 The detection of photons

The detection of charged particles is the main application of gaseous detectors. But they can also be used to detect photons. Photons being the gauge boson of the electromagnetic interaction, they are also detected thanks to the electromagnetic interaction. In gaseous detectors, it is possible to detect photons from UV to gamma energies, thanks to the photoelectric effect, Thomson and Compton scattering, or pair production.

In the photoelectric absorption, the photon undergoes an interaction with an atom of the medium, and completely disappears. It is a quantum process in which one (or more) energy transition(s) of the electron shells of the detecting atom occurs. If we note $E_j$ the binding energy of an electron of the shell $j$, the photoelectric effect in the shell can take place for photons with energy $E_X \geq E_j$. The binding energy of a shell of an atom depends on its atomic number $Z$: the higher $Z$ is, the higher the binding energy is. Fig. 2.2 [7] presents the binding energy of the K, L and M of an atom as a function of its atomic number.

Because a photon cannot be absorbed by a free electron (which will only diffract it), we can expect the probability for the photoabsorption to be the highest for strongly bounded electrons. As fig. 2.2 shows, this is the case for the electrons of the K-shell. If the

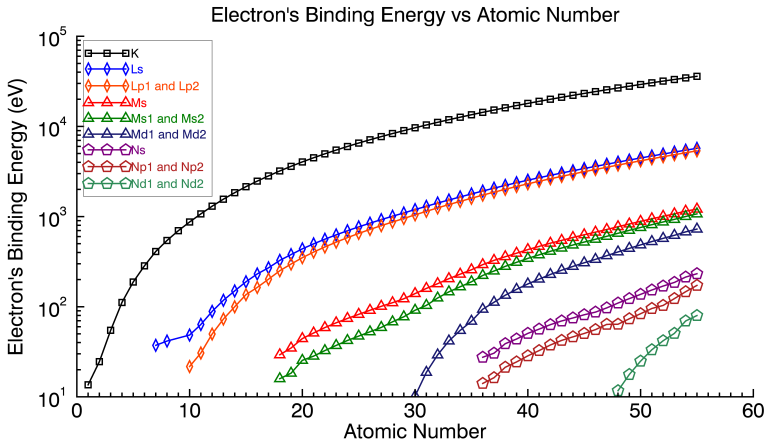


Figure 2.2: *Binding energy of electrons as a function of the atomic number of the atom [7]. The K shell requires more energy to be ionized than the L, M or N shell.*

incoming photon has enough energy to ionize the K-shell, it will then preferentially ionize it. This effect can be illustrated through the measurement of the absorption coefficient $\mu$. If we take a beam of light of intensity $I_0$, in a medium of density $\rho$, we have, after crossing the thickness $X$, an intensity of $I = I_0 \mathrm{e}^{-\mu\rho X}$ where $\mu$ is the mass attenuation coefficient, or absorption coefficient in $\mathrm{cm}^2.\mathrm{g}^{-1}$. Fig. 2.3 presents the calculated values of $\mu$ from the transmission curves of a thickness of 1 cm, at atmospheric pressure and 20°C, for different gases commonly used in gaseous detectors. In the case of a gaseous mixture of $n$ gases of absorption coefficient $\mu_i$, each one in proportion $p_i$ (in %), we can assume that the mass attenuation coefficient of the mixture is $\mu = \sum_{i=1}^{n} p_i \mu_i$. In the soft X-ray energy domain (from $\approx$ 2 keV to $\approx$ 20 keV), the K-shell absorption dominates for most gases, so we can limit our study to this phenomenon.

An incoming X-ray photon of energy $E_X$ arriving on a K-shell of ionization energy $E_K$ will result in the emission of an electron from the K-shell, called photoelectron, with an energy $E_e = E_X - E_K$. This electron will have enough energy to ionize the gas like described for the case of charged particles in the previous paragraph. It will also be emitted in a preferential direction, as explained in chap.I, which is essential to perform polarimetry. The ionized atom is left in an excited state, with a vacancy in its K-shell. An electron

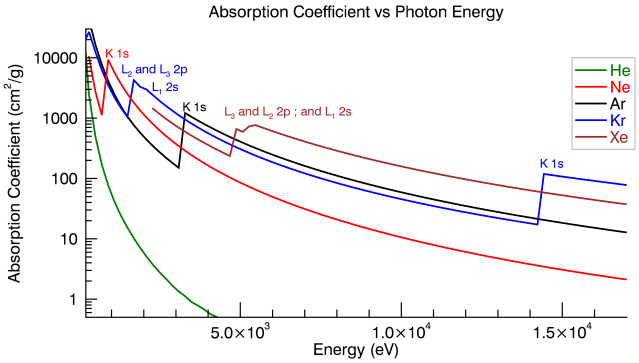


Figure 2.3: *Values of the absorption coefficient as a function of the energy of the incoming photon, for several gases [4]. A sharp increase in the absorption happens when the photon has enough energy to ionize one shell. There is only one energy possible to ionize the K shell, but 3 possibilities for the L shell (ionization of its sub-shell s, and 2 ways to ionize its sub-shell p because of electron's spin effects).*

from an outer shell (mainly L shell) fills the vacancy left by the photoelectron, which results in the emission of energy. This energy can result in mainly two mechanisms.

The first mechanism is called the Auger effect. The transition energy is transmitted to an electron of the outer shell (which has a very low binding energy): the electron is then ejected, and is called an Auger electron. Its kinetic energy is the difference between the transition energy of the initial electronic transition (which is very close to the binding energy of the K-shell), and the binding energy of the most outer shell (which is very low). So the kinetic energy of the Auger electron is $E_A \approx E_K$. The Auger electron also ionizes the medium, like the photoelectron does, and we can recover in the detector the energy $E_e + E_A \approx E_X$ - $E_K + E_K \approx E_X$, which is the energy of the incoming photon.

The second mechanism is called fluorescence. Here, the transition energy is emitted under the form of a photon of energy $E_p = E_K$ - $E_i$ where $E_i$ is the binding energy of the shell where the transition electron comes from. Because $E_p \leq E_K$, this fluorescence photon will have a low probability of being absorbed by an atom of the medium, and will often escape the detector without being detected. Only the energy $E_e = E_X$ - $E_K$ of the photoelectron can be recovered, and it results in spectrometry in a secondary peak, centered at the energy $E_e$, called *escape peak*.

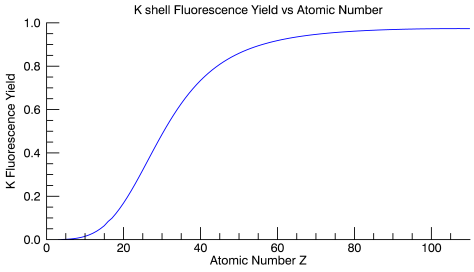


Figure 2.4: *Fluorescence yield as a function of the atomic number [11]. The fluorescence increases with Z.*

Those two mechanisms of de-excitation of the ionized atom can happen, and the proportion of fluorescence is called fluorescence yield. Fig. 2.4 shows the fluorescence yield as a function of the atomic number of the absorbing atom, from measured data in [9], and shows that it increases with the atomic number. For argon ($Z$=18), the fluorescence yield is of roughly 15%: for 15% of the detected photons, an argon based detector will only recover the energy of the photo electron $E_X$ - $E_K$.

It must be insisted that the detection of a photon inside the gaseous detector results in the creation of one photoelectron (and possibly an Auger electron). And those electrons will interact with the gaseous medium the same way as other charged particles do, described in the previous paragraph.

### 2.3.3 Other particle detection

A gaseous detector can also be used to detect neutrons or try to detect dark matter candidates called WIMPs (for Weakly Interactive Massive Particles). Their detection is different than the one of charged particles and photons interacting with the gas through the electromagnetic force. A neutron or WIMP having no electric charge and not being the gauge boson of the electromagnetic interaction, it does not interact by leaving a track of ions in the detector. But it undergoes nuclear interactions with one atom of the gas, which creates charged reaction products (such as recoil ions) that can be observed in the gaseous detectors.

| Gas | Z | W (eV) | F (theory) | F (exp) |
|---|---|---|---|---|
| He | 2 | 41 | 0.17 | |
| Ne | 10 | 36.2 | 0.17 | $\leq 0.17$ |
| Ar | 18 | 26.2 | 0.17 | |
| Xe | 54 | 21.5 | | |
| Ar+0.8% $CH_4$ | 18 | 26.0 | 0.17 | 0.19 |

Table 2.1: Atomic number, average energy per ion pair and Fano factor for pertinent gases for this work [11, 18].

## 2.4 Drift of charges in gases and electric field influence

This section presents how the signal can be amplified and transmitted to a readout electronics. Charge motion in gaseous detectors is described in more detail in [11].

### 2.4.1 Number of electron-ion pairs created

As explained in the previous section, a charged particle loses its energy following equation (2.4). This loss of energy comes from the ionization of the atoms of the gas, which results in the formation of electron-ion pairs. This is called primary ionization. If the electrons created through primary ionization have enough energy, they further ionize the gas: they are called $\delta$-electrons. Primary and secondary ionization result in the creation of a number of electron-ion pairs $N$, which can be expressed by $N = \frac{\Delta E}{W}$, where $\Delta E$ is the total energy loss and $W$ the energy needed to create an electron-ion pair in the medium. For the detection of a photon, $\Delta E = E_X$ - $E_K$ as defined in the previous section. For a particle depositing energy in the detector, $\Delta E$ can be expressed with the loss per unit length $\frac{\mathrm{d}E}{\mathrm{d}x}$ of (2.4): $\Delta E = \frac{\mathrm{d}E}{\mathrm{d}x}x$ where $x$ is the pathlength of the particle in the medium. Values of $W$ have been measured and tabulated, and can be found in [12] . Table 2.1 gives the value of $W$ for various gases and gaseous mixtures.

### 2.4.2 Energy resolution: the Fano limit

The number of electron-ion pairs created by a particle is important as it will define the *energy resolution* of the detector. The energy resolution is the capability of the detector to measure precisely the energy deposited by the particle inside the detector, and depends on various parameters related to the construction of the detector, but also on statistical effects due to the electron-ion pairs creation: no matter how accurate the detector is, these statistical fluctuations will limit the energy resolution of the detector.

In a first approximation, we can estimate that the number of electron-ion pairs created follows a Poissonian statistics, as it is constituted of a number of independent events (collisions between the particle and one atom) happening in a finite time. So if a particle passes through the detector, it creates an average number of pairs $n_0 = \frac{\Delta E}{W}$ (where $\Delta E$ is the energy deposited in the detector), and the probability to have a number $k$ of pairs created by the particle is $p_{n_0}(\mathrm{k}) = \frac{n_0^k}{k!}\mathrm{e}^{-n}$. The mean of such a distribution is $\mu = n_0$ and the standard deviation is $\sigma_{n_0} = \sqrt{n_0}$. This represents the deviation from the perfect case, where $N = \frac{\Delta E}{W}$ charges are always created by the particle. The Full Width at Half Maximum (FWHM) of the distribution of the number of charges created, if the primary ionization is considered as a Poisson process, can be approximated by FWHM $= 2\sqrt{2ln(2)}\sigma_{n_0} \approx 2.35\sigma_{n_0}$. The energy resolution of the detector is defined by $R = \frac{FWHM}{\mu} = 2.35\sqrt{\frac{W}{\Delta E}}$.

This would give an energy resolution of 15.6% FWHM for 6 keV photons detection in a detector using argon. However, the assumption of a Poisson-like phenomenon is not accurate, as the different ionizations generated by the particle are not independent from each other. First the particle has a definite energy which imposes a maximum number of electron-ion pairs that can be created, and it loses energy at each ionization, which has a direct influence on the next ionization. This has been demonstrated by the physicist Ugo Fano in 1947 [17], who introduced the Fano factor $F$ in order to correct the standard deviation from the Poisson statistics $\sigma_{n_0} = \sqrt{Fn_0}$, giving an energy resolution

$$R = 2.35\sqrt{\frac{F.W}{\Delta E}} \tag{2.5}$$

| Gas | F | Energy (keV) | Particle |
|---|---|---|---|
| He | 0.17 | | $\beta$ |
| Ne | 0.17 | | |
| Ar | $0.23 \pm 0.05$ | 5.9 | $\gamma$ |
| | $0.23 \pm 0.05$ | 5305 | $\alpha$ |
| Xe | $0.170 \pm 0.007$ | 1.49 | $\gamma$ |
| | $0.13 \pm 0.01$ | 5.9 | $\gamma$ |
| $C_4H_{10}$ | 0.26 | 1.49 | $\gamma$ |
| $CO_2$ | 0.33 | 1.49 | $\gamma$ |
| Ar + 0.8% $CH_4$ | 0.19 | 5.9 | $\gamma$ |
| Ar-DME (50%-50%) | 0.244 | 5.9 | $\gamma$ |
| Ar-DME (80%-20%) | 0.202 | 5.9 | $\gamma$ |
| Ar-DME (90%-10%) | 0.177 | 5.9 | $\gamma$ |
| Ne-DME (50%-50%) | 0.273 | 5.9 | $\gamma$ |
| Ne-DME (80%-20%) | 0.245 | 5.9 | $\gamma$ |
| Ne-DME (90%-10%) | 0.215 | 5.9 | $\gamma$ |
| He-DME (50%-50%) | 0.289 | 5.9 | $\gamma$ |
| He-DME (80%-20%) | 0.297 | 5.9 | $\gamma$ |
| He-DME (90%-10%) | 0.294 | 5.9 | $\gamma$ |

Table 2.2: *Measured Fano Factor for different gases and with different particles and energies [20, 5].*

The Fano factor $F$ depends on the gas used for the detection, and on the detected particle. The different values of $F$ as a function of the detecting medium and detected particle can be found in table 3.1 of [19]. Some values of Fano factors can be find on table 2.2 [20, 5]. We will quote the case of detection of 6 keV photons in a mixture of argon-methane (90% - 10%) which gives a Fano factor of $\approx 0.21$, resulting in an energy resolution of $R \approx 7\%$ at 6 keV, which is better than the 15.6% found in the purely Poissonian approximation. This correction found by Fano implies a statistical limit on the detector called the Fano limit, which depends on the gas and the energy of the particle to detect. No matter how perfect the detector is, it will always be limited by the Fano limit. It is then an important fact to take into account when developing a spectrometer.

Now that the ionization processes and the electron-ion pairs creation have been described, it is essential to understand how the charges are collected.

### 2.4.3 Diffusion and drift under an electric field

A gaseous detector always uses at least two electrodes: the cathode which collects the positive charges, and the anode which collects the negative charges. A bias voltage between the anode and the cathode is applied. This creates an electric field $\overrightarrow{E}$ that acts on the charges through the Lorentz force $\overrightarrow{F} = Q\overrightarrow{E}$ where $Q$ is the charge of the particle. The charge of electrons and ions being opposite, both carriers move in opposite direction: the electrons toward the anode and the ions toward the cathode. This electric field, if strong enough, prevents the recombination of electrons and ions, and allows the collection of the charges by the detector. The motion of the charges through the influence of the electric field is called *drift motion*. The drift of the charges (ions and electrons) has been extensively studied, and we will focus on the electrons drift.

Under an electric field $E$, the electrons will acquire a drift velocity $v_d$ given by $v_d = \frac{e}{2m}E\tau$ [13], where $e$ is the elementary charge, $m$ the mass of the electron and $\tau$ the time between collisions of the electron and the gas molecules. It has been found that $\tau$, which is directly linked to the cross-section of the collisions, depends strongly on the electric field $E$. When $E$ varies, $\tau$ goes through maxima and minima, in what is called the Ramsauer effect [14]. So the variation of the drift velocity with $E$ is not linear: it has been measured for various gaseous mixtures and values can be found in [15]. For instance in pure argon, under an electric field of $10^4$ V/cm, $v_d = 40$ $\mu$m/ns.

During this drift motion toward the anode, the electrons experience a diffusion phenomenon. This diffusion has two components: in the direction of the applied electric field, called longitudinal diffusion, and in the plane perpendicular to the electric field, called transverse diffusion. If we call $n$ the number density of electrons, the space and time repartition of $n$, for an electric field $\overrightarrow{E} = E\overrightarrow{e_z}$ is given by

$$n(x,y,z,t) = \frac{N}{4\pi D_T t\sqrt{4\pi D_L t}} \exp\left(-\frac{x^2+y^2}{4D_T t}\right) \exp\left(-\frac{(z+v_d t)^2}{4D_L t}\right) \tag{2.6}$$

where *x, y, z, t* are the space and time coordinates ($z$ being the coordinates of the electric field direction), $N$ is the number of electrons, and $D_T$ and $D_L$ are respectively the transverse and longitudinal diffusion coefficients. The diffusion coefficients depend on the strength

of the applied electric field in a complex way. The values of the diffusion coefficients impact directly the shape of the electrons cloud arriving on the anode, and this deformation is expressed through the standard deviations $\sigma_L = \sqrt{2D_L t}$ and $\sigma_T = \sqrt{2D_T t}$ usually expressed in $\mu\text{m}/\sqrt{\text{cm}}$. Simulations and measurements of the values of the drift velocity $v_d$, of $\sigma_T$ and of $\sigma_L$ in several gas mixtures have been performed extensively. The reader can find a large data base of those values on the website of the ILC-TPC project [1]. In pure argon, under a field of $10^3$ V/cm, $\sigma_L = 500$ $\mu\text{m}/\sqrt{\text{cm}}$ and $\sigma_T = 1000$ $\mu\text{m}/\sqrt{\text{cm}}$.

Ions being much heavier than electrons, they drift slower and diffuse less. For a given electric field, the drift velocity of ions is approximately 1000 times lower than the one of electrons.

Understanding this diffusion phenomena when the charge are migrating towards the anode is essential, because the initial goal of gaseous detectors is to measure the trajectory of the ionizing particle: the reconstruction process relies on a good knowledge of drift and diffusion physical processes.

### 2.4.4 Working at low electric fields: the recombination and ion chamber regions

One use of the electric field is to separate the electrons from the ions, and to bring the electrons on the anode in order to collect them. But there is another interest on the electric field, which is its strong influence on the intensity of the signal generated. In fact, depending on the intensity of the electric field, the number of charges collected at the anode varies, as shown schematically on fig. 2.5, and it is possible to identify different regimes.

The first region, concerning low electric fields, is the recombination region. At those fields, recombination between ions and electrons dominates: the charges are not all collected. As the field increases, recombination decreases, so more charges can be collected at the anode.

At one point, the electric field is high enough to fully separate the electrons and the ions and prevent any recombination. The charges created by the ionizing particle are all collected, and the signal created on the anode is constant for increasing electric fields. This is the *ionization chamber region*, as it is the region used by the

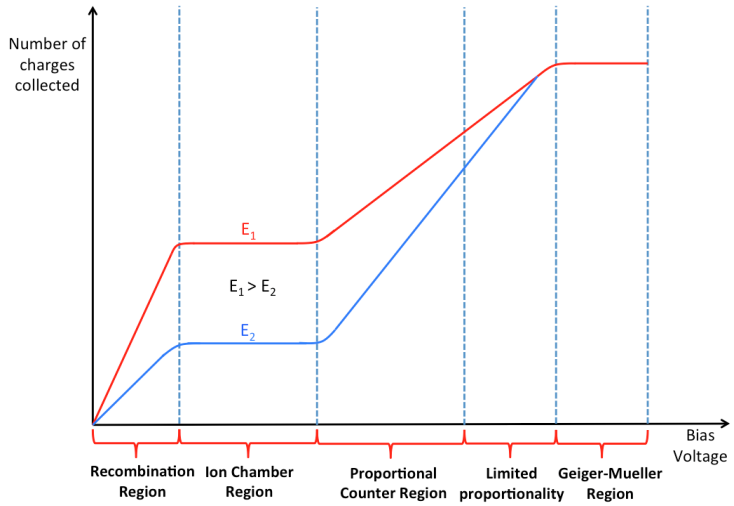


Figure 2.5: *Gain - Voltage characteristics for two particles of energy $E_1$ and $E_2$ [11]. Depending on the strength of the electric field, the behavior of the detector is different, and we can identify 5 different operating regions. Depending on the goal of the detector, the field will be chosen to operate in the desired region.*

ionization chambers. An ionization chamber is a gas filled detector which collects the charges created by an ionizing particle without any amplification in the medium. Smoke detectors used in common houses are good examples of ionization chambers.

### 2.4.5 Working at moderate electric fields: the avalanche phenomenon

When the bias voltage is increased above a threshold value of few kV.cm$^{-1}$, the detector enters in the *Proportional Counter Region*. In this region, a phenomenon called avalanche multiplication occurs. Under the high electric field created by the bias voltage, the electrons quickly gain energy thanks to the acceleration provided by the Lorentz force $\overrightarrow{F} = -e\overrightarrow{E}$. If their increase in energy before a collision with a gas atom is higher than the ionization potential of the gas, they will ionize it and create other electron-ion pairs. The change in number of pairs per unit path length is given by the equation:

$$\frac{\mathrm{d}N}{\mathrm{d}z} = \alpha N \quad \text{or} \quad \mathrm{d}N = \alpha N \mathrm{d}z \tag{2.7}$$

where $N$ is the number of electron-ion pairs, $\mathrm{d}z$ is the path length (we assume here that the electric field is oriented in the direction $z$), and $\alpha$ is the Townsend coefficient.

$\alpha$ is the number of collisions which create an electron-ion pair per unit length. If $\lambda$ designs the mean free path of ionization, i.e. the mean length that an electron can cover before entering in a collision and ionize a gas atom, $\alpha$ is given by the relationship $\alpha = \frac{1}{\lambda}$. $\lambda$ depends on the energy gained by the electron between the collisions (and then depends on the applied electric field), and on the ionization potential of the gas.
If the field is uniform, the Townsend coefficient is constant, and solving equation (2.7) gives

$$N = N_0 e^{\alpha z} \quad \text{or} \quad M = \frac{N}{N_0} = e^{\alpha z} \tag{2.8}$$

where $N_0$ is the number of primary charges created by the impinging particle. $M$ is called the multiplication factor. This creation of secondary charges by acceleration of the electrons is called *avalanche multiplication*. If the field is not uniform, the Townsend coefficient is a function of $z$ and the multiplication factor becomes:

$$M = \frac{N}{N_0} = e^{\int_{z_1}^{z_2} \alpha(z)\,\mathrm{d}z} \tag{2.9}$$

Because of the difference of drift velocity between electrons and ions and their charge of opposite sign, at a given instant all electrons are located at the front of the charges (electrons and ions) distribution, closer to the anode, while the ions are at the tail. Because electrons are much lighter than ions, their drift velocity is higher, typically by a factor of around 1000. This gives a drop-like shape to the charge distribution, as shown in fig. 2.6. At the tail, the ions decrease in number, and in lateral extension. Most of them are produced in the last mean free path because this is where the number of electrons is higher. So half of the ions are contained in the front part near the electrons.

This repartition of the charges is very important, as it modifies quite importantly the electric field around the charge distribution, modifying locally the Townsend coefficient $\alpha$. Understanding the repartition of the charges and computing the corresponding $\alpha$ coefficient is a topic of main interest since the creation of gaseous

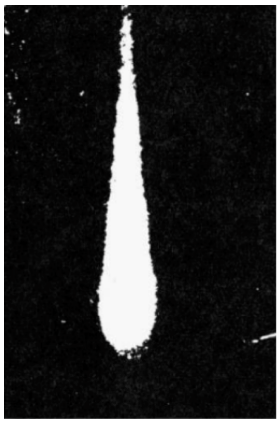

Figure 2.6: *Drop-like shape of the charge distribution. On the left, a photograph of an actual avalanche as observed in a cloud chamber [22]. On the right a model showing the repartition of ions and electrons in the charge distribution.*

detectors, and a lot of efforts have been dedicated to it. Many approximated analytic expressions exist for $\alpha$ for different strength and geometry of the electric field. One of the most used expression was proposed by Korff [23], and gives

$$\frac{\alpha}{P} = A\mathrm{e}^{-\frac{BP}{E}} \tag{2.10}$$

$P$ is the pressure of the gas, $A$ and $B$ are parameters accounting for the dependence of $\alpha$ on the electric field. This formula is mostly valid for low $\alpha$ values (low amplification). The parameters $A$ and $B$ depend on the applied electric field and on the gas used. They have been experimentally measured and some values can be found in [18]. This approximation quicly reaches its limits, but gives a rough idea of the dependence of $\alpha$ with the electric field, allowing to compute its value under any field configuration.

### 2.4.6 Limit on the multiplication factor: the Raether's limit

An important fact about the multiplication factor $M$ is that it cannot be increased at will. Secondary processes happen in the gas, such as photon emission which can create undesired avalanches. This process will be explained in more details when talking about the choice of gas filling. Also the distortion of the electric field around the charge distribution becomes too important if too many charges are

created. Near the electrons the electric field can become too important, resulting in a spark breakdown: a channel of electrons is created between the cathode and the anode, resulting in a current between both electrodes which prevents the bias voltage from being maintained. This spark breakdown has several undesired effects for the detector: the electric field is not maintained, the detector can be damaged by the excess of charges, and a dead time for the detector operation is generated. A phenomenological limitation has been given by Raether [24]. The Raether limit is $\alpha L \approx 20$, or $M \approx 10^8$. (where $L$ if the length covered by the accelerated electrons). According to Raether, this limit comes from the above-mentioned distortion of the electric field around the space charge distribution.

But in a practical case, all electrons created by primary ionization do not have the same energy: this statistical distribution of the energy of electrons prevents the detector from operating at gains higher than $M \approx 10^6$, the highest possible energy possible for an electron, although not the most probable, preventing the gain from being higher).

At this point the interest of the avalanche phenomenon and high gain of gaseous detectors must be stressed out. The number of charges created by primary ionization is usually around few hundreds electron-ion pairs: this is way to low to be measured by any readout electronics. The avalanche amplifies the signal sufficiently to allow the use of electronic devices to read it. This is extremely important: understanding this avalanche phenomenon brought the particle detection from visual identification, as in cloud and bubble chambers, to electronic readouts. This implies more precise measurements, and most of all extremely short deadtime between the reading of two events: from several minutes with bubble chambers to milli/micro seconds with gaseous detectors.

### 2.4.7 Signal induction on electrodes: the Ramo theorem

The electric field is used to collect the charges and amplify them, but it is also responsible of the signal creation on the electrodes. In fact the signal detected is produced by the motion of the charges between the two electrodes explained by the Shockley-Ramo's theorem [25, 26], which allows to determine the amplitude of the signal induced on an electrode by moving charges. This theorem states that the

current induced on an electrode is

$$I(t) = q.E_w.v_d(t) \tag{2.11}$$

where $t$ is the time, $q$ the charge of the moving electron or ion, $v_d$ the drift velocity of the considered charge and is counted negatively if the charge drifts away from the electrode, and $E_w$ is the parameter called the *weighting field*. The weighting field is the component of the electric field in the direction of the drift velocity at the instant $t$, calculated with the condition that the charge is not here and the considered electrode is at 1 V and all other are grounded.
The induced charge on the electrode is

$$Q = I_e t_e + I_i t_i \tag{2.12}$$

where $I_e$ (resp. $I_i$) is the current induced by electrons (resp. ions), and $t_e$ (resp. $t_i$) is the transiting time of electrons (resp. ions).

Electrons and ions have opposite charges, but because they move in opposite directions, they will both induce a positive current on the anode and then both participate on the charge induction. The electrons being lighter, they have a faster drift velocity than the ions, and they will then create a much more intense current on the anode than ions. They are also created close to the anode, and will be collected rapidly: the current they induce is short. On the contrary, ions are slow, but created far from the cathode so there drifting time will be very long compared to the electrons: they will then induce a weaker current than electrons on the anode, and a longer signal.

## 2.5 The Proportional Counter

The electric field on a gaseous detector is used to separate the charges and collect them, to amplify the signal by avalanching the electrons, and to induce the signal on the electrode. As shown on fig. 2.5, depending on its value, the behavior of the detector will be different.

If the electric field is high enough for avalanches to appear, but not too high to keep the gain under the Raether limit, the detector operates in the region called *the proportional counter region*, as it is used by a type of detectors called proportional counters. The idea is to collect a number of charges which depends, in a proportional way, on the energy deposited by the detected particle, for a better identification.

### 2.5.1 The parallel plate design

The simple idea of a parallel plate detector can be considered. It consists of two conductive plates separated by a gap of few hundreds $\mu$m, with a bias voltage applied in order to create a strong electric field of few kV.cm$^{-1}$ and filled with a gaseous detection medium. An incoming particle will create electrons and ions by primary ionizations, those charges will drift toward the electrodes and the signal will be amplified by the avalanche phenomenon. The level of amplification will depend on the path length of the charges, which means that the intensity of the created signal will depend on where the incoming particle creates the primary ionizations. Another problem comes from the Raether condition. For such a plane architecture, the electric field is uniform. At a constant electric field, $\alpha$ is constant over the detector, so the Raether limit is $\alpha x \approx 20$, where $x$ is the drift length of electrons. At a gain too high, Electrons created close to the anode, with a small drift length $x$, validates the condition $\alpha x < 20$, while electrons created close from the cathode and drifting all the length $L_{tot}$ toward the anode reach the Raether limit if $\alpha L_{tot} < 20$. Thus operating such a detector at high gain is not possible.
Moreover, the gain being $e^{\alpha x}$, the fluctuation of the position of the interaction in the detector is responsible of a bad energy resolution.

### 2.5.2 The proportional counter

Those difficulties are overcome when considering a cylindrical geometry, as shown in fig. 2.7. In such a detector, the anode is a thin wire, surrounded by a conductive cylinder acting as a cathode. A bias voltage is applied between the two electrodes. Because of the cylindrical geometry, the electric field created between the electrodes is not constant. It is very strong at the surface of the anode wire, and quickly decreases as $r^{-1}$, where $r$ is the distance from the center of the anode wire.

Because of this fast decrease of the electric field, the charges created by primary ionization will experience a low field, not strong enough to start an avalanche, and will simply drift toward the anode. At a distance of few anode's radii from the wire's center, the electric field is strong enough for the avalanche phenomenon to start. Thanks to this, all primary electrons will be avalanched starting from the same distance of the anode, in the same way and along the same length. The intensity of the detected signal depends only on

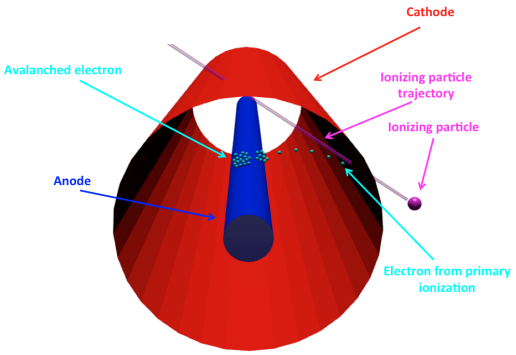


Figure 2.7: *Detail on a proportional counter. The detected particles create primary electrons through primary ionization. Under the electric field the electrons migrate toward the anode. When close to the anode, the electric field is high enough to start the avalanche. Thanks to this method, the number of charges created does not depend on the position of primary ionizations.*

the energy deposited by the ionizing particle, in a proportional manner, hence the name. It is then very good for particle identification. It also has the advantage of being able to operate at high gains: the electrons all start the avalanche at the same distance $L$ of the wire and $L$ being quite small, it is possible to get a high amplification factor of around $M \approx 10^4$ before reaching the Raether limit $\alpha L \approx 20$.

### 2.5.3 The limited proportionality region

On fig. 2.5 it can be seen that when the electric field increases, the proportionality between the detected signal and the applied voltage is lost, as for two different energies deposited by an incoming particle the two signals end up by being the same. This loss of proportionality is a consequence of the cylindrical geometry. In fact, when the electric field increases, more and more electron-ion pairs are created during the avalanche. The electrons are quickly collected, thanks to their high drift velocity and to the fact that they are created close to the anode. The ions drift toward the cathode, but slowly because of their high mass. Because they are created near the anode and move slowly, they start to build a positive space charge around the anode, which distorts the electric field locally.

If the deposited energy increases, the electric field distortion be-

comes more important: the signal of a high energy ionizing particle will then be less amplified than it should be, and the proportionality of the measured signal is lost. This region of high electric field is called *region of limited proportionality*, as the detected signal is no longer proportional anymore to the deposited energy in the detector.

### 2.5.4 The saturated and breakdown regions

When the electric field increases even further, the region of limited proportionality ends up in a saturated region. In this region, the detected signal will always have the same intensity, regardless of the energy deposited in the detector. This region is called the Geiger Müller region, as it is how Geiger counters operate: the number of particles crossing the detector can be counted, but without any energy measurement.

If the field is increased even more, the detector enters in the continuous discharge region. In this region, continuous channels of charges can be created between the electrodes, resulting in short circuits and electrical arcs between them, which can damage the detector by burning the electrodes or the readout electronics. The passage between the Geiger Müller region and the continuous discharge region is called breakdown.

## 2.6 The Choice of the gas

Getting high gain in a gaseous detector such as the proportional counter is important as it allows the detection and identification of low energy particles. But the proportional counter has to stay into the proportional region, otherwise its interest is lost. The maximum gain that can be achieved for a detector before entering another region of operation or going into breakdown depends on the gas used. The choice of the gas filling is extremely important, and depends on the goal of the detector.

Avalanche multiplication occurs in all gases, so technically any gas or gas mixture can be used in a proportional counter. However, in the experiments that uses these detectors there are some important requirements: low working voltages, high gain operation, high rate capabilities, good proportionality (for better identification), long lifetime etc... which are often conflicting. For instance,

it is not possible to have the highest gain in the detector, with the highest possible rate. These requirements restrict the choice of gas to few possibilities.

### 2.6.1 The use of noble gas as the main component

First of all, avalanches multiplication occur in noble gases at much lower voltages than in any other gas. In fact, in a noble gas, the only way for an electron to lose energy is by ionization of other atoms, whereas in other gases there are several ways for the electron to lose energy such as the vibration or the rotation of the molecule, especially when using polyatomic molecules. Thus using a noble gas allows operation at the lowest possible values of the electric field. The noble gases that can be used are helium, neon, argon, krypton and xenon. Helium is extremely light and leaks easily from the detectors, quite transparent to X-rays or high energy particles, and has a high Fano factor and a degraded energy resolution, which is why it is not commonly used except for specific reasons or for UV detection. Krypton is radioactive and then rarely used because of the background noise it induces in the detector. Xenon is very expensive and is often discarded in non-sealed detectors. Neon, cheaper than xenon, is still more expensive than argon, on which the choice falls then naturally.

However pure argon-based detectors cannot operate at gains higher than $10^2$- $10^3$. First, during the avalanche, excited atoms are formed. Those atoms return to their ground state by emitting a photon. The minimum energy of the emitted photon in argon is 11.6 eV. This energy is above the ionization potential of the metal constituting the cathode (copper, commonly used as cathode, has an ionization potential of 7.7 eV): the photon can then extract a photoelectron from the cathode, and initiate a new avalanche almost instantly after the primary avalanche, which can lead to breakdown if the gain is too high as the avalanches added up. The argon ions are also responsible for the limitation of the gain: they migrate toward the cathode, and when they reach it they are neutralized by extracting an electron from it. The excess of energy is radiated as a photon, or as secondary emission (extraction of a second electron from the cathode), which both result in a new avalanche. Here again, even at moderate gain, the probability of the process is high, which quickly

causes breakdown and bring the detector into continuous discharge.

### 2.6.2 The interest of quencher gases

Using only a noble gas prevents the detector from operating at high gain. The solution is to add a polyatomic gas in small proportions to the argon. In a polyatomic gas an electron can lose energy through non-radiative mechanisms: the addition of a polyatomic gas then slightly increases the threshold voltage, i.e the voltage needed in order to enter into the proportional region. But those non-radiative mechanisms have a large advantage: they allow the absorption of low energy photons in a relatively wide energy band. For instance, in methane, the photo absorption is very efficient between 7.9 eV and 14.5 eV, which covers the energy range of secondary photons emitted by excited argon atoms, or by photo-emission from the cathode. Polyatomic molecules absorb those photons and enter in a non-radiative excited state, where they dissipate the excess of energy through elastic collisions or dissociation to simpler molecules. Another advantage is that an ionized polyatomic molecule is absorbed at the cathode with a very low probability of secondary emission, as during the neutralization the excess of energy is dissipated in dissociation (creation of simpler molecules) or polymerization (formation of more complex molecules).

The addition of polyatomic gases to argon reduces greatly the creation of secondary avalanches, and the drawback of increasing the voltage needed to start an avalanche is widely compensated by the possibility to reach gains of $10^6$ (which is 2 or 3 order of magnitude greater than in a pure noble gas detector). Polyatomic gases are called quenchers, as they prevent the continuous discharge region to be reached too soon. The more atoms in the molecule, the more efficient the quenching is. For this reason, isobutane ($iC_4H_{10}$) is often used for high gain operation. Adding a few % of quencher is enough to reach very high gains. The major drawback of using a polyatomic organic gas is that the lifetime of the detector is reduced. In fact, the polymerization mentioned earlier is responsible for deposition of polymers on the cathode which can substantially modify the operation of the detector. This phenomenon is called aging of the detector, and depending on the organic quencher and its proportion, the detector will cease to operate properly after a certain number of counts in the detector, typically $10^8$ [18]. The use of

inorganic quenchers such as $CO_2$ avoids aging, but as a counterpart the maximum reachable gain before breakdown is lower.

It is also possible to add electronegative gases (freon for instance) to reach the highest possible gain before discharge (or before the Geiger Müller region). Those gases capture the free electrons that are emitted from the cathode after the argon's (or other noble gas) ions neutralization. The addition of a small quantity of such a gas allows stable operation at gains up to $10^7$, but the detector is sensitive to the aging effect.

## 2.7 The Multi-Wire Proportional Chamber and its upgrades

The invention of proportional counters has been a great step in particle detection, as it brought the detectors into the electronics era, implying better identification and most of all very high rate compared to cloud and bubble chambers. But the simple proportional counter does not allow any spatial localization: it cannot give the trajectory of an ionizing particle. And being able to recover this trajectory is important in particle detection: if a magnetic field is applied, the curvature of the trajectory of the particle allows the measurement of the momentum of the detected particle, which is, with the energy, the second most important parameter to be measured.

### 2.7.1 The MWPC

To overcome this problem, G. Charpak invented the Multi-Wire Proportional Chamber in 1968 [4]. A schematic can be found in fig. 2.8. It consists of thin parallel anode wires disposed in a plane, and symmetrically sandwiched by two cathode planes. The electric field lines are parallels far from the anode, and converge to the anode wires. An ionizing particle creates a cloud of primary electrons that drift to the anode wires under the influence of the electric field. As in the proportional counter, when the electrons are close enough to the anode they enter in a high field region where they can start an avalanche phenomenon. The number of charges created is then high enough and can be read by an electronics. The electronics captures the number of charges created, directly linked to the deposited en-

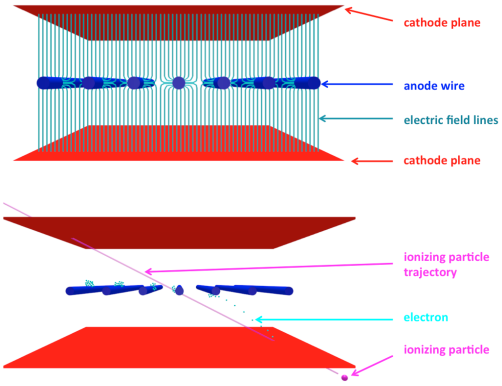


Figure 2.8: *MultiWires Proportional Chamber Schematic. Anode wires are disposed horizontally and sandwiched by two cathode planes. The top image shows the electric field lines on the detector. The bottom shows the detection of an ionizing particle. In an MWPC it is possible to measure the deposited energy, and the 1D trajectory of the ionizing particle.*

ergy in the detector, and the 1D projection on the anode plane of the ionizing particle trajectory. By putting the detector in a transverse magnetic field, with the magnetic field lines parallel to the anode wire, and looking at the bending of the trajectory of the particle, it is possible to measure partly its momentum.

The MWPC gives then access to the deposited energy, and to the momentum of the detected particle, and this with a fast rate and identification time of a detector using electronic readouts. The spatial resolution of an MWPC is governed by the spacing between the anode wires. Reducing the distance between the wires increases the spatial resolution. Unfortunately, the wires present a capacitive coupling between them, strongly influenced by their spacing, which plays an important role on the electric field. Without entering into the details, the idea is that by bringing the wires closer to one another, the voltage applied on the wires has to be increased in order to keep the same value of the electric field, which is often an enormous drawback in experiments. For this reason, classical MWPCs usually have anode spacing larger than 2 mm, with a typical value for the spacing of about 6 mm.

An MWPC will often be used in the proportional or limited proportional region, but can be used in the other regions presented for the proportional counter. For a deeper study of MWPCs, the operational regions, the field inside, the mechanical constraints, the effect of electrostatic forces on the wire etc... the reader can refer to [27].

### 2.7.2 The Drift Chamber and the Time Projection Chamber

An improvement of the MWPC is the *drift chamber*, which gave access to a second spatial coordinate (the one perpendicular to the anode plane). In such a device, a scintillator is used to detect the ionizing particle when it leaves the detector. Because the particle is quicker than the created electrons in the chamber, it will arrive at the scintillator almost immediately after having created the first electron-ion pair. The signal of the scintillator corresponds then almost to the entry of the particle inside the detector. By comparing this to the time of the first detected signal, and comparing also the time of the detected signals on the various anode wires, it is possible to compute the 2D trajectory of the detected particle. This computation is quite challenging as it implies to know perfectly the drifting mechanisms of electrons, and the electric field geometry and strength in the detector. But it is still possible, and early work on simple structures of drift chamber gave spatial resolution of $\approx 100$ $\mu$m [28].

Drift chambers often use a more complex geometry than classical MWPC, because the low electric field in MWPC when far from the anode results in a strong non-linearity in the relationship between the coordinate of origin of the created electron and its drifting time. For more information about the various geometry of drift chambers to get a suitable electric field the reader can refer to [28] and [29].

The last improvement of this kind of detector consisted in getting the third space coordinate and is called a Time Projection Chamber (TPC). It has been invented by David Nygren in 1974 [30] and mentioned for the first time in an internal report at Berkeley university where he was working. The idea to get the third spatial coordinate is to build one of the two cathode plane in a printed circuit suitably stripped to provide a coordinate measurement thanks to the induction of the signal by the moving charges. If the strips of the cathode are not parallel to the anode wires, it is possible to reconstruct the 2D projection of the track of the detected particle on the anode plane, the third coordinate (orthogonal to the anode and cathode plane) being recovered thanks to time measurement as in drift chambers. The particularity of the first used TPC is the use of a magnetic field parallel to the electric field lines, in order to limit the lateral diffusion of electrons and to reach a better spatial reso-

lution. Since then, several other configurations have been used such as no magnetic field [31], cylindrical [32] or spherical configuration [33].

## 2.8 The Micro Patterned Gaseous Detectors

The introduction of the MWPC and its rapidly coming improvements provided for the first time a fine space resolution on top of allowing a good energy measurement. Those detectors were the best (but also only) trackers for good space resolution for several years, until the invention of solid state trackers. Solid state trackers are much more precise, but they are also extremely expensive. MWPCs being cheap and relatively easy to use, they remained the best solution for experiments needing large detection surfaces.

Despite being an option, their spatial resolution needed to be improved. So was their rate capability as the luminosity of particle accelerators was increased constantly. Those two requests can be solved by reducing the size of the detectors basic cells (meaning the miniaturization of the pixels or strips of the readout plane). Thanks to the development of photolithography techniques, this miniaturization became possible, starting the era of the so-called Micro Pattern Gaseous Detectors (MPGDs).

### 2.8.1 The MSGC

The first MPGD was the Micro-Strip Gas Chamber (MSGC), invented in 1988 [34]. In such a detector, the readout plane consists of an insulating material on which cathode and anode strips are deposited alternatively. Classical parameters for such a detector are 200 $\mu$m spacing, 100 $\mu$m width for cathode strips and 10 $\mu$m width for the anode strips. The alternation of cathode and anode strips is here to ensure that the geometry of the electric field is different from what can be found in a simple plane detector. The electrons created by primary ionization drift toward the anodes of the readout plane under the influence of a low electric field created by the top electrode. Thanks to the alternation of cathode and anode strips, and to the small size of the anodes, the electric field close to them is

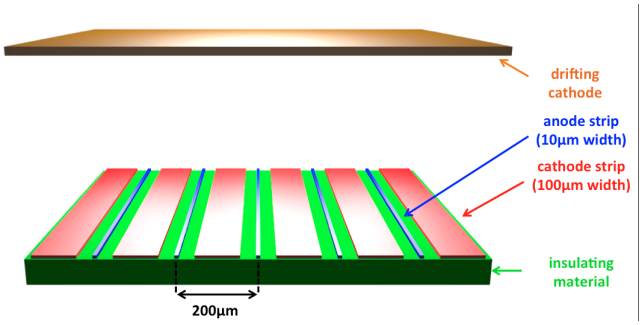


Figure 2.9: *MicroStrip Gas Chamber. The readout plane (bottom) is an insulating material on which are deposited alternatively cathode and anode strips. The charges created by primary ionization drift toward the readout plane thanks to a low electric field created by the drifting electrode. The alternation of cathode and anode strips on the readout plane, and the small width of the anode, create an electric field very strong at the anode's surface, allowing electrons to start an avalanche when they get close to the anode.*

very high, so when electrons get close enough they start to avalanche and create a signal high enough to be read by the electronics.

Thanks to their very small pitch of 200 $\mu$m, MSGCs exhibit spatial resolutions down to 30 $\mu$m and high rate capability, this by keeping a very good energy resolution ($\approx$ 12% FWHM at 6 keV in argon) and an acceptable gain of $10^4$ [44]. Unfortunately, in an MSGC the high electric field at the edges of the anode strips rapidly cause damages on the detector, and charge accumulation at the surface of the insulator is responsible for important variations of the gain over time.

At the end of the 90s, two other technologies for MPGDs were introduced: the GEM and the MicroMegas, which were both more stable in time than the MSGC.

### 2.8.2 The Gas Electron Multiplier

GEM stands for Gas Electron Multiplier, and was invented by Fabio Sauli in 1997 [35]. The reader can find a complete description of GEM detectors and their application in [36]. The schematic of a GEM detector is presented in fig. 2.10. The main part of the GEM is a thin dielectric foil metalized on both sides, on which a pattern of holes is produced by photolithography. The anode plane is a

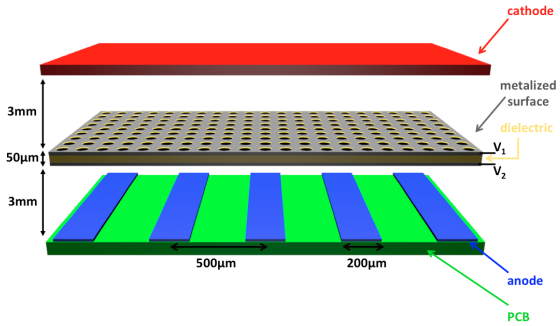


Figure 2.10: *Schematic of a GEM detector. The GEM consists in a thin dielectric foil, typically 50 µm thick, with metalized surface on both sides. A pattern of holes is produced by photolithographic techniques. Hole parameters are typically 100 µm pitch and 70 µm in diameter. The anode plane are strips or pixels readout deposited on PCB with a fine pitch for good spatial resolution.*

Printed Circuit Board, or other insulator, on which thin and fine pitch anode strips (or pixels) are deposited, allowing to obtain a good spatial resolution down to few tens of $\mu$m.

The principle of a GEM is shown in fig. 2.11 and is as follows: a bias voltage of few 100 V is applied on the metalized surfaces of the foil. It creates a moderate electric field between the cathode and the foil: the electrons created by primary ionization by the detected particle drift toward the foil. Because of the bias voltage applied on both sides of the foil, the field lines go through the holes, and electrons are then guided inside the holes. In the holes, the electric field is very strong and above 10 kV/cm, so the electrons start an avalanche. When going out of the holes, the cloud of avalanched electrons is guided thanks to a low electric field toward the anode, where they are collected.

Compare to MSGC, GEMs have a big advantage: there is no strong electric field on the anode plane, so the detector is not damaged. Also, for the same reason, and because the density of metal on the anode plane is lower than in MSGCs, charge depositions on the insulator are rare and do not degrade the gain of the detector. Finally, because the anode is not an active electrode, it does not need to be perfectly planar to get a good energy resolution. Hence it is possible to use PCB-kind structures for the anode.

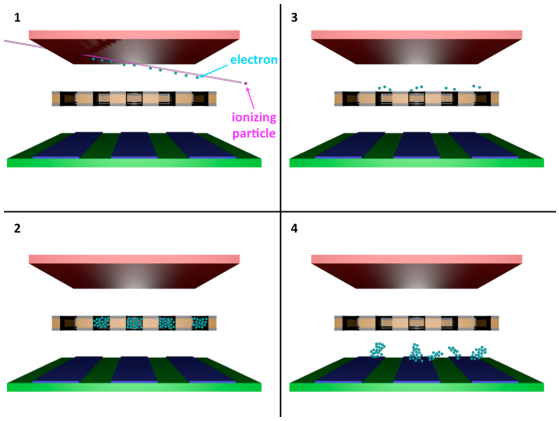


Figure 2.11: *GEM detection principle. 1) The ionizing particle creates a cloud of primary electrons. 2) Under the influence of a moderate electric field, the electrons drift toward the holes and are guided into them. 3) In the holes, the electric field is very strong, so the electrons are accelerated and gain enough energy to start an avalanche. 4) The clouds of avalanched electrons go out of the holes and drift toward the anode where they are collected.*

### 2.8.3 The GEMs derivatives and their applications

The main problem with GEM detectors are their low gain of the order of ten when using a single foil. They were initially used as a preamplification stage for MWPCs or MSGCs. But quick developments introduced the use of detectors using 2 or 3 stacked GEM foils in detectors, as represented in fig. 2.12. In such a detector, the electrons from primary ionization will experience three different avalanches before they reach the anode where they are collected. Each GEM foil usually has an amplification factor of few 10, allowing the total gain of the detector to reach easily values up to $10^5$.

The success of GEM detectors was such that many different architectures based on the same concept have been proposed. Resistive-GEMS (Re-GEMS) are GEMs using electrodes made of a resistive material [37], which reduces the damages caused by discharges in the detector and allows operations at a higher rate and a higher gain. Thick GEMs (THGEMs) [38] use a different technology to produce the GEM foil: the standard coated foil is replaced by a PCB, and holes are produced by drilling. This production technique allows

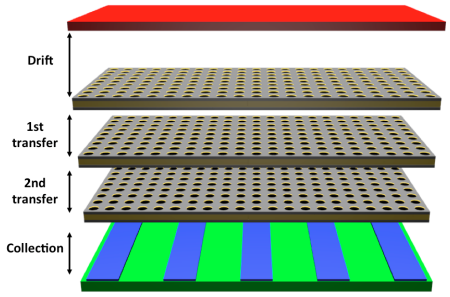


Figure 2.12: *Triple GEM detector scheme. The electrons created by primary ionization are guided toward the GEMs and undergo 3 successive amplifications before being collected at the anode. GEM foils each having a gain of ≈20, the total gain of the detector are typically ≈ 8000.*

fast and cheap production of a large quantity of detectors. The thickness of THGEMs are around one order of magnitude higher than classical GEMs, which make them mechanically robust and can then be produced in large size. The gain of a single-THGEMs is up to $10^5$, and they resist to damages caused by discharge. This robustness can be improved further by using Resistive Thick GEMs (RTGEMs) [39].

All those developments and study on GEMs quickly made them ready to be used in several experiments, mostly in high energy particle physics experiments. GEMs are used as the amplification system of the tracker in the COMPASS experiment at CERN [40], or in the LHCb [41] and TOTEM [42] experiments on the LHC. They have also been selected to be the forward muon spectrometer of the CMS experiment on LHC (installation planned during the 2nd long shutdown in 2019), where they will cover a surface of 300 $m^2$. GEM detector is also the baseline of the IXPE polarimetric experiment mentioned in chapter 1 [43], which has been selected by NASA for a launch in 2021. For an exhaustive list of experiments using GEM-based detectors, the reader can refer to [44].

We will not enter here into more details on the characteristics (gains, rate, resolution, etc..) of the various types of GEM detectors, but the reader can refer to [36] for a recent and quite complete overview of characteristics and current (and future) applications.

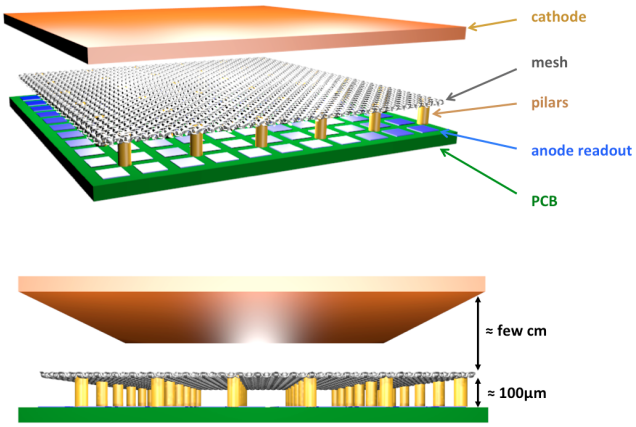


Figure 2.13: *The Micromegas detector architecture. A micromesh is stretched between the two parallel electrodes. The mesh parameters depend on the technology used, but the thickness varies between 5 µm and 36 µm, with a standard pitch of 50 µm. The anode plane is the same than for GEMs.*

## 2.9 The Micro Pattern Gaseous Detectors: Micromegas

### 2.9.1 The Micromegas architecture

The second main architecture of MPGD is the Micro-MEsh GAseous Structure detector, or Micromegas (MM) detector [45] invented by Ioannis Giomataris in 1996. The MM detector is a parallel plate structure, the scheme of which can be found in fig. 2.13. A micromesh is stretched between the cathode and the anode, and fixed at a distance of typically 100 $\mu$m from the anode thanks to supporting pillars made of an insulating material. The mesh can be made of thin conducting wires of 18 $\mu$m diameter woven to form a grid of 36 $\mu$m thickness with a typical pitch between the holes of 50 $\mu$m, or an electroformed mesh of any conducting material. Like for GEMs, the anode plane is a PCB or other insulator on which are deposited thin anode strips or pixels with a small pitch.

The working principle of a Micromegas is shown in fig. 2.14. The MM detector consists of two volumes: the conversion volume and the amplification volume. Voltages are applied on the electrodes and on the mesh in order to create a low electric field of the order of

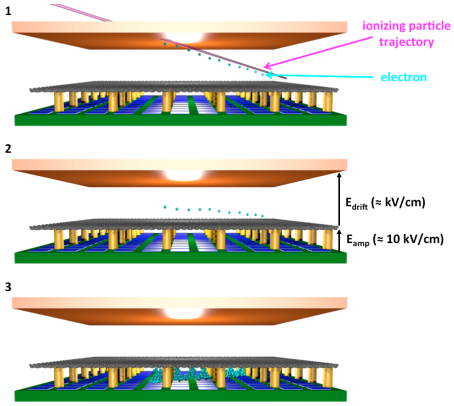


Figure 2.14: *Detection principle of a Micromegas detector. 1) The ionizing particle creates a cloud of primary electrons. 2) Thanks to a low electric field, the electrons drift toward the mesh and are guided through the holes into the second part of the detector. 3) In the second part of the detector, the electric field is high enough for electrons to create an avalanche, creating a signal strong enough to be read out at the anode.*

few kV.cm$^{-1}$, called drift field, in the conversion region and a high electric field of the order of few 10 of kV.cm$^{-1}$, called amplification field, in the amplification region. With the optimal field ratio, the field lines go through the holes of the mesh.

The ionizing particle enters the detector in the conversion region where it creates a cloud of primary electrons. Those primary electrons drift toward the mesh under the influence of the drift field, and are guided through the holes of the mesh into the amplification part of the detector. There, under the influence of the high amplification field, the electrons start an avalanche when drifting toward the anode, where the amplified signal is collected.

### 2.9.2 Amplification factor of a Micromegas

Except at the surrounding of the mesh where the field lines are difficult to estimate, the electric field in a Micromegas in each volume is homogenous, and can be easily estimated with $\overrightarrow{E} = -\overrightarrow{grad}(V)$. It gives the field absolute values: $E_{drift} = \frac{|V_{mesh} - V_{cathode}|}{d_{drift}}$ and $E_{amp} = \frac{|V_{mesh} - V_{anode}|}{d_{amp}}$.

The gain of a Micromegas depends on its amplification gap. In fact, when looking at equation (2.8) and equation (2.10), replacing

$E_{amp}$ by $\frac{\Delta V}{d}$ (where $\Delta V = |V_{mesh}$ - $V_{anode}|$ and $d$ is the thickness of the amplification gap) gives:

$$M = \exp\left(APd \times \mathrm{e}^{-BP\frac{d}{\Delta V}}\right) \tag{2.13}$$

with $A$ and $B$ parameters that depend on the gas used.
At a fixed gap thickness $d$, the gain reaches a maximum for $\Delta V = BPd$. This allows to understand that for high pressure operations with a given gas ($B$ fixed), small gaps are better, and for low pressure operation high gaps are better [46].

### 2.9.3 Mesh transparency

Another important parameter to take into account in a Micromegas detector is the electronic transparency of the mesh. This mesh transparency has a great influence on the transmission of the detector. For Micromegas detectors, the transmission is defined by

$$T = \frac{n_a}{n_d} \tag{2.14}$$

where $n_a$ is the number of primary electrons reaching the anode, and $\mathrm{n}_d$ is the number of primary electrons crossing the mesh. The transmission is hard to measure experimentally as estimating $n_a$ is difficult. For high drift fields the transmission is low as the electric field lines end up in the mesh, preventing primary electrons from being guided through the holes of the mesh and entering the amplification region: the mesh is not transparent. For low drift fields, the transmission is close or equal to 1 as most field lines goes through the mesh holes and guide the primary electrons correctly: the mesh is transparent. It is the drift fields aimed at when using a Micromegas, in order to bring each primary electron to the amplification region. At lower fields, the transmission sharply decreases, not because of the mesh transparency, but because the electrons drift too slowly and recombination becomes more important (see fig. 2.5).
Even for good ratios of fields, creating electric field lines going through the mesh, a fraction of electrons can be lost due to transverse diffusion. This depends on the optical transparency of the mesh, of which parameters has to be chosen carefully.

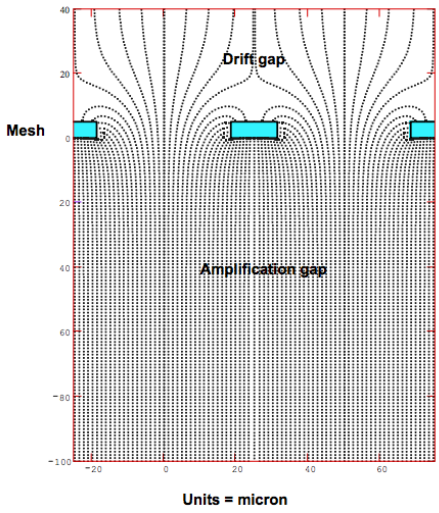


Figure 2.15: *Simulation of electric field lines in a micromegas detector [47]. If the ratio of drift and amplification field is chosen properly, the field lines go through the hole of the mesh and electrons are guided from the drifting region toward the amplification region. Hence the electron transparency is good despite the use of a mesh with low optical transparency.*

The transmission depends then greatly on the drift field. Usually, the anode plane has a fixed and low voltage because this is where the readout electronics are, and it operates at voltages of the order of 1 V, so the amplification field is almost fully controlled by the value of $V_{mesh}$, which also controls the drift field. For this reason the parameter to study the transmission is often the ratio of drift and amplification field instead of simply the drift field. Fig. 2.15 [47] shows a simulation of electric field lines in a Micromegas detector when a transparency of 1 is achieved. The field lines coming from the drift regions go through the holes of the mesh into the amplification region and guide the electrons through the holes of the mesh.

### 2.9.4 Energy resolution

The third important parameter, with gain and transparency, is the energy resolution of the detector. Equation (2.5) gives the best achievable resolution in any gaseous detector by $R = 2.35\sqrt{\frac{F.W}{\Delta E}}$. For a micromegas detector, the equation can be modified to take into account the statistical effect of the avalanche and of the transparency into:

$$R = 2.35\sqrt{\frac{(F+b).W}{\Delta E}} \tag{2.15}$$

where $b$ takes into account the avalanche and transmission contribution [48]. The parameter $b$, and then the energy resolution, depends on the transmission and on the gain, so depends on the ratio of field and on the amplification field. Those parameters values have to be chosen carefully in order to minimize $b$ and optimize the energy resolution. The energy resolution is also degraded by non-uniformities inside the detector which is responsible of non-uniform electric fields, and by the mesh thickness. In fact, a standard mesh of 36 $\mu$m thickness has field lines not perfectly going through the holes: the transmission is then close but not equal to 1. A standard mesh is not flat due to the woven wires. Consequently the amplification field is not uniform, which degrades the energy resolution. Thinner and flatter meshes can improve the resolution. Tests performed on Microbulk and InGrid Micromegas exhibit a resolution of 11% FWHM at 6 keV in an argon mixtures, which is close to the theoretical resolution of 7% given by eq.(2.5).

### 2.9.5 The Micromegas family

Several adaptations have been performed on Micromegas and like for GEMs, there are now several existing families of Micromegas detectors. In the first Micromegas generation, the anode was made of strips deposited on a PCB, and the pillars between the anode and the mesh were small cylinders in a photo-imaging resin, an insulating material. The pillars were deposited on the anode thanks to PCB manufacturing technique. The mesh, consisting on electroformed nickel, was deposited on top of it and screwed manually on a supporting frame. A bias voltage was applied to create a strong electric field and pulled the mesh toward the anode, allowing to get a good flatness and parallelism. Efforts have been made towards the development of thin meshes to improve the energy resolution, and high accuracy etching techniques allow the use of 5 $\mu$m copper mesh with holes of diameter of 25 $\mu$m and pitch of 50 $\mu$m [49].

The second technology of Micromegas detectors is the *bulk* family [50]. It consists of detectors where the mesh and the anode are in one single entity. The electroformed mesh is replaced by a woven wire mesh: it is cheap, commonly produced in high quantity on market, and several materials are available. The anode plane is covered by a photo-resistive film of the thickness of the wanted gap, and the mesh is added on top of the film. The three pieces are

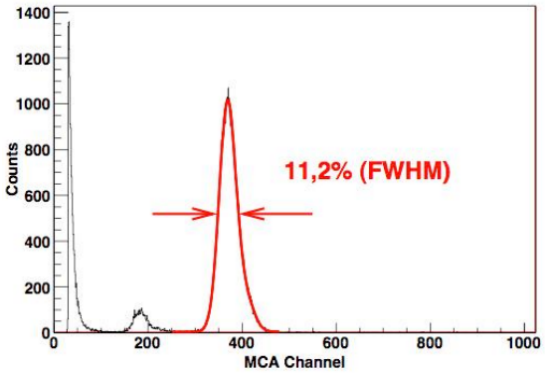


Figure 2.16: *Spectrum obtained with a Microbulk micromegas [52]. An energy resolution of 11% is obtained.*

laminated together to form a single piece. Photo-lithography is used in order to etch the photo-resistive film and to form the pillars of the gap. The full detector is made by simply adding a cathode at the desired distance. Bulk Micromegas are robust, can be produced in large area, and can even be curved like in the CLAS12 tracker [51]. They exhibit an acceptable energy resolution of around 18% FWHM at 6 keV, mostly limited by the use of the woven mesh which is responsible for an imperfect uniformity of the amplification field and which limits the transparency of the detector.

The third technology is the MicroBulk family [52]. The idea is still the same than for the simple bulks: having the anode and mesh in one piece, but the production techniques are different as here it is based on Kapton photolithography. First the strips are directly etched on the detector, and not deposited like for the bulk. Then the mesh used is not a woven mesh, but is a thin copper film of 5 $\mu$m etched to get the required holes pattern. This allows to reach energy resolution of 11% FWHM at 6 keV as shown in fig. 2.16. Another important point of the Microbulk is the fact that the amplification gaps can be reduced down to 12.5 $\mu$m, which is ideal for high pressure applications. They are also low mass detectors, and radiopure, which make them perfect for rare events experiments such as neutrinoless double beta decay or dark matter search.

The fourth technology is the InGrid family. Here again the mesh and the anode will be one single entity. For bulk and microbulk the fabrication processes were to progressively etch the detector and the mesh into the desired shape from a Kapton foil. In the InGrid technology, the various parts of the detector are progressively deposited

on a silicon wafer: the detector is grown on the wafer. This allows to get meshes as flat as 1 $\mu$m, giving almost a 100% transmission, and a resolution of 11% FWHM at 6 keV in an argon-based mixture, which is the best resolution ever obtained with any kind of gaseous detectors [53].

Like for GEMs with the RGEMs, Micromegas using resistive anodes have been developed. Initially they were developed to improve the spatial resolution by spreading the signal on several strips for a better spatial reconstruction. But it conveniently appeared that resistive anodes absorbed the excess of energy during a discharge and protected the readout electronics.

The last family of micromegas is the Piggyback Micromegas [1]. It is a bulk Micromegas, but the anode plane is a simple resistive layer made in ruthenium oxide, and spread on a ceramic plate of desired thickness. The readout layer is to be put in the other side of the ceramic, completely isolating the readout from the gaseous medium. The resistive layer will absorb the excess of energy released during discharges, protecting the detector. The fact that the readout is outside the gaseous medium also protects it from discharges and makes it easy to change.

Here again, thanks to very good performance, the Micromegas detectors have been selected to equip several major scientific experiments. The Micromegas technology have been selected to serve as muon inner-forward tracker on ATLAS at the LHC, needing the production of 1200 $m^2$ of detector surface [55]. They also equip the COMPASS experiment at CERN, the T2K neutrino experiment [56] in Tokai (Japan) or in the Axion search experiment CAST at CERN [57]. For a more exhaustive list of the different experiments using Micromegas technology, the reader can refer to [44].

### 2.9.6 Brief sum up of MPGDs

All the specificities of these gaseous detectors are summed up in fig. 2.17, 2.18 and 2.19. It shows the incredible developments of gaseous detectors, mostly since the end of the 90s with the invention of GEMs and Micromegas architectures. The invention of these two types of detectors is responsible for the renewed interest for soft X-ray polarimetry at the beginning of the 21st century. As explained in the previous chapter, using the photoelectric effect for soft X-ray polarimetry can be done only in gaseous detectors, as a high

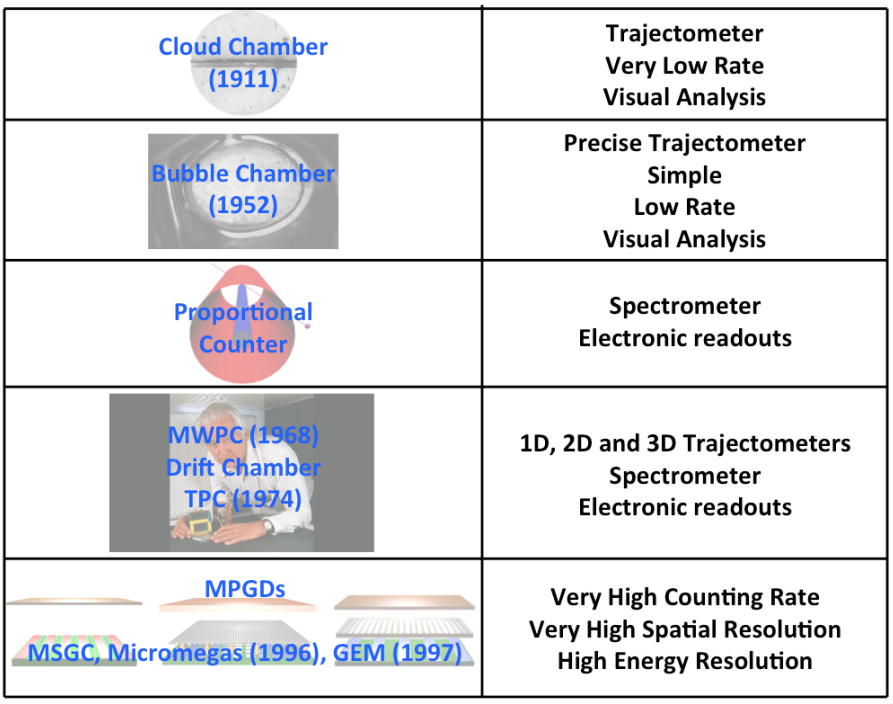


Figure 2.17: *A brief history of gaseous detectors for particle physics. It started at the beginning of the 20th century with the Cloud Chamber invented by Wilson, and is still a topic of main interest more than a hundred years later with continuous developments of MPGDs detectors.*

spatial resolution is needed in order to recover properly the photo-electron's track. And GEMs and Micromegas are gaseous detectors with high spatial resolution. For this reason, the IXPE (NASA) and XIPE (ESA) projects use a GEM architecture, and the Caliste-MM project is based on a Micromegas architecture. The next chapter will be focused on the Caliste-MM detector, presenting in more details the above mentioned Piggyback concept, the readout electronics, and the various characterizations performed on this new concept of detector.

## 2.10 Summary

Gaseous detectors are used since more than 100 years, with the invention of the Geiger Müller counter and the cloud chamber.

The invention of the MultiWires Proportional Chamber by Charpak

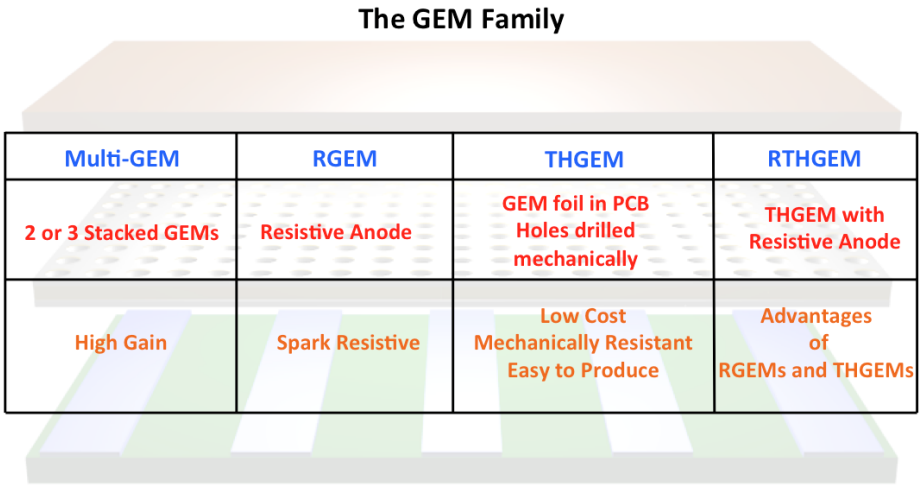


Figure 2.18: *The GEM architecture family.*

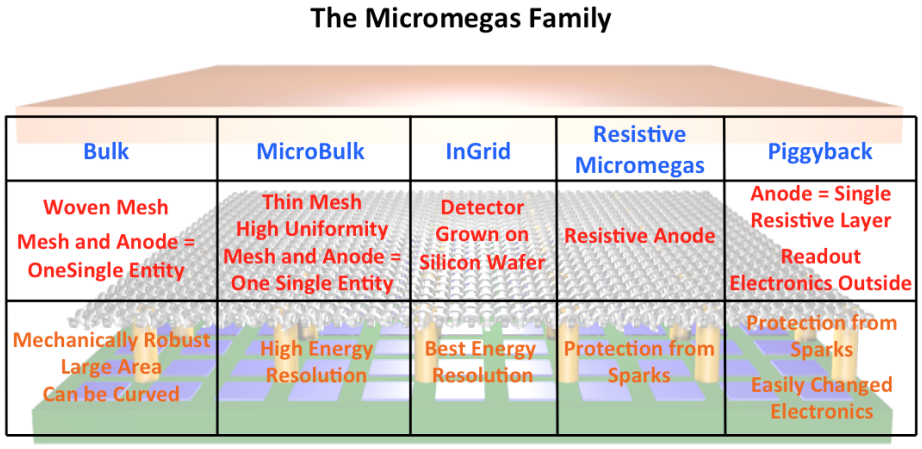


Figure 2.19: *The Micromegas architecture family.*

in 1968 marked a turn in particle physics detector, as it brought them to the electronics era.

In the last 90s, Ioannis Giomataris and Fabio Sauli invented respectively the Micromegas and the GEM, two different detector architectures allowing good energy and spatial resolution, and a high rate capability.

Thanks to those two detectors, performing soft X-ray spectro-polarimetry by using the photoelectric effect became possible, which renewed the interest for this science at the beginning of the years 2000.

The IXPE and XIPE projects use a GEM architecture in their detector, while the Caliste-MM detector, which is presented in the next chapter, uses a Micromegas architecture.

# Bibliography


[1] C. D. Anderson, *The Positive Electron*, Phys. Rev. **43** 491-494 (1933)

[2] S. H. Neddermeyer and C. D. Anderson, *Note on the Nature of Cosmis-Ray Particles*, Phys.Rev. **51**, 884

[3] D. A. Glaser, *Some Effects of Ionizing Radiation on the Formation of Bubbles in Liquids*, Phys. Rev. **87** (1952)

[4] G. Charpak et al., *The Use of MultiWires Proportional Counters to Select and Localized Charged Particles*, Nucl. Instrum. Methods, **62**, 262 (1968)

[5] H. Bethe, *Bremsformel für Elektronen relativistischer Geschwindigkeit (Braking Formula for Electrons of Relativistic Speed)*, Zeitschrift für Physik, **76**, 293 (1932)

[6] F. Bloch, *Bremsvermögen von Atomen mit mehreren Elektronen*, Z. Phys. **16** (1933)

[7] C. D. Wagner and G. E. Muilenberg, *Handbook of X-Ray Photoelectron Spectroscopy*, Perkin-Elmer Corp. (1979)

[8] http://physics.nist.gov/cgi-bin/Xcom/xcom2

[9] W. Bambynek, *A New Evaluation of K-Shell Fluorescence Yields*, in Proceedings of the X-84 X-Ray and Inner-Shell Processes in Atoms, Molecules and Solids, Leipzig, Aug.20-23, 1984

[10] http://xdb.lbl.gov/

[11] F. Sauli, *Gaseous Radiation Detectors: Fundamentals and Applications*, Cambridge University Press, 2014

[12] G. F. Knoll, *Radiation Detection and Measurement*, John Wiley and Sons, third edition, 2000

[13] J. Townsend, *Electrons in gases*, Hutchinson, London, 1947

[14] C. Ramsauer, *Über den Wirkungsquerschnitt der Gasmoleküle gegenüber langsamen Elektronen*, Annalen der Physik **Vol. 369, Issue 6**, pp.512-540 (1921)

[15] A. Breskin, G. Charpak, F. Sauli, M. Atkinson and G. Schultz, *Recent observations and measurements with high-accuracy drift chambers*, Nucl. Instr. Methods, **124** (1975)

[16] http://www-hep.phys.saga-u.ac.jp/ILC-TPC/gas/

[17] U. Fano, *Ionization Yield of Radiations. The Fluctuations of the Number of Ions*, Phys. Rev., **72**, 26-29 (1947)

[18] F. Sauli, *Principles of operation of multiwire proportional and drift chambers*, Lectures given in the Academic Training Program of Cern (1977)

[19] M. Chefdeville, *Development of a Micromegas-like gaseous detectors using a pixel readout chip as collecting anode*, Ph.D, University of Amsterdam

[20] F.J. Iguaz., *Development of a time projection chamber prototype with micromegas technology for the search of the double beta decay of 136Xe*, phD thesis, Universidad de Zaragoza, Zaragoza, Spain, February 2010

[21] S.F Biagi, D. Duxbury and E. Gabathuler, *E*xperimental results from a microdot detector overcoated with a semiconducting layer, Nuclear Instruments and Methods In Physics Research A, **419**, 438-443 (1998), 594-601

[22] L. B. Loeb, *Basic processes of gaseous electronics*, University of California Press, Berkeley (1961)

[23] S. A. Korff, *Electrons and Nuclear Counters*, Van Nostrand (1946)

[24] H. Raether, *Electron avalanches and breakdown in gases*, Butterworths (1964)

[25] W. Shockley, *Currents to Conductors Induced by a Moving Point Charge*, Journal of Applied Physics, **9** (1938)

[26] S. Ramo, *Currents Induced by Electron Motion* in Proceedings of the Institute of Radio Engineers, **27** (1939)

[27] G. Charpak and F. Sauli, *Multiwire Proportional Chambers and Drift Chambers*, Nuclear Instruments and Methods, **162**, 405-428 (1979)

[28] G. Charpak, *La Détection des Particules au Moyen des Décharges dans le Gaz*, J. Phys. Colloques, **30** (1969)

[29] W. Blum et al., *Particle Detection with Drift Chambers*, Springer-Verlag Berlin Heidelberg (2008)

[30] D. R. Nygren, *Proposal to investigate the feasibility of a novel concept in particle detection*, LBL internal report, Berkeley, February 1974

[31] P. Gros et al., *HARPO - TPC for High Energy Astrophysics and Polarimetry form the MeV to the GeV*, TIPP 14 3rd Technology and Instrumentations in Particle Physics conference, 2-6 June 2014 Amsterdam, Proceedings

[32] H. Fenker et al., *BoNus: Development and use of a radial TPC using cylindrical GEMs*, Nuclear Instruments and Methods A, **592** (2008) 273-286

[33] A. L. Fard, *Étude d'un détecteur sphérique gazeux pour la recherche d'événements rares à bas seuil en énergie*

[34] A. Oed *Position Sensitive Detector with Microstrip Anode for electron Multiplication with Gases*, Nuclear Instruments and Methods, **263** (1988)

[35] F. Sauli, *GEM: A new concept for electron amplification in gas detectors*, Nuclear Instruments and methods A, **386** (1997)

[36] F. Sauli, *The gas electron multiplier (GEM): Operating principles and applications*, Nuclear Instruments and Methods A, **805** (2016) 2-24

[37] A. Yoshikawa et al., *Development of Resistive Electrode Gas Electron Multiplier (Re-GEM)*, JINST, **7** C06006

[38] A. Breskin et al., *A Concise review on THGEM detectors*, Nuclear Instruments and Methods A, **598** (2009)

[39] R. Oliveira, V. Perkov, F. Pietropaolo and P. Picchi, *First tests of thick GEMs with electrodes made of a resistive kapton*, Nuclear Instruments and Methods A, **576** (2007)

[40] B. Ketzer et al., *Performance of triple GEM tracking detectors in the COMPASS experiment*, Nuclear Instruments and Methods A, **535** (2004) 314.

[41] M.Alfonsi et al., The LHCb Triple-GEM Detector for the Inner Region of the First Stationof the Muon System: Construction and Module-0 Performance 0-7803-8700-7/04 (C)2004IEEE.

[42] M.G. Bagliesi et al., *The TOTEM T2 telescope based on triple-GEM chambers* Nuclear Instruments and Methods A, **617** (2010) 134.

[43] M. C. Weisskopf et al., *An Imaging X-ray polarimeter for the study of galactic and extragalactic X-ray sources*, in proceedings of SPIE, Space Telescopes and Instrumentation 2008: Ultraviolet to Gamma Ray

[44] S. Dalla Torre, *MPGD developments: historical roadmap and recent progresses in consolidating MPGDs*, JINST, **8** C10020 (2013)

[45] Y. Giomataris, P. Rebourgeard, J. Robert and G. Charpak, *MicrOMEGAs: A High granularity position sensitive gaseous detector for high particle flux environments*, Nuclear Instruments and Methods A, **376** (1996)

[46] Y. Giomataris, *Development and prospects of the new gaseous detector Micromegas*, Nuclear Instruments and Methods A, **419** (1998) 239

[47] G. Charpak et al. *MICROMEGAS, a multipurpose gaseous detector*, Nuclear Instruments and Methods A, **478** (2002)

[48] L. Segui Iglesia, *Pattern Recognition in a high pressure time projection chamber prototype with a Micromegas readout for the 136Xe double beta decay*, Ph.D, Universidad de Zaragoza

[49] A. Delbart et al, *New Developments of micromegas detector*, Nuclear Instruments and Methods A, **461** (2001)

[50] Y. Giomataris, *Micromegas in a bulk*, Nuclear Instruments and Methods A, **560**, 405-408 (2006)

[51] S. Aune et al., *Micromegas tracker project for CLAS12*, in proceedings of the 8th International Conference on Position Sensitive Detectors, Glasgow (2008)

[52] T. Papaevangelou et al., *Development and performance of microbulk micromegas detectors*, Journal of Instrumentation, **5** (2010)

[53] M. Chefdeville et al., *An electron-multiplying 'Micromegas' grid made in silicon wafer post-processing technology*, Nuclear Instruments and Methods A, **556**, (2006) 490-494

[54] D. Attie et al., *Piggyback resistive Micromegas*, Journal of Instrumentation **8** C11007 (2013)

[55] Fabien Jeanneau (ATLAS Coll.), *Design and Construction of Large Size Micromegas Chambers for the ATLAS Upgrade of the Muon Spectrometer*, IEEE Transactions on Nuclear Science, **63** (2016) no.4, 2336-2342

[56] N. Abgrall et al., *Time Projection Chambers for the T2K Near Detectors*„ Nuclear Instruments and Methods A, **637** (2011) 25-46.

[57] S. Aune et al., *Low background x-ray detection with Micromegas for axion research*, JINST, **9** 2014, 01, P01001.

# Chapter 3

# The Caliste-MM concept: setup and modelization

# Contents

## Contents

## 3.1 Introduction

This chapter presents the Caliste-MM detector: its components, its new concept of detection and the first results obtained with the detector. First I present the two main parts of the detector: the piggyback gaseous detector and the Caliste readout electronics. Then the parts are put together to form the Caliste-MM detector and I present the first registered events. I perform a characterization and an analytical simulation to prove the understanding of the physical phenomena underlying the detection of photons with this new concept of detector.

## 3.2 The Piggyback detector

### 3.2.1 Parameters description

The piggyback detector [1] is a bulk micromegas, with the particularity that the anode plane is a single resistive layer made of a screen printed ruthenium oxide paste spread on a ceramic plate, as shown in fig.3.1. The size of the amplification gap between the mesh and the anode is controlled by the height of the holding pillars and is typically of 128 $\mu$m. Fig.3.2 presents pictures of the mesh and holding pillars of a piggyback detector. The mesh wires, 18 $\mu$m thick, are woven to form a grid with 45 $\mu$m holes width. The holding pillars are made in photoresist and have a diameter of $\approx$ 300 $\mu$m.

The resistance of the resistive layer can be adjusted, depending on its composition and on the number of deposited layers. For the Caliste-MM application I used resistivity between 6 M$\Omega/\square$ and 100 M$\Omega/\square$. The $\Omega/\square$ unit is used for thin film characterization. For a material of resistivity $\rho$, width $L$, length $l$ and thickness $t_R$, the

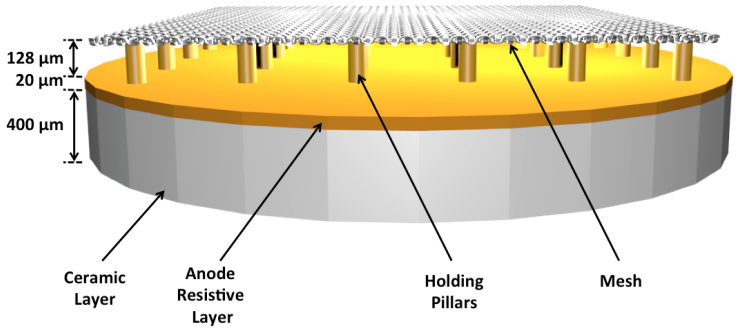


Figure 3.1: *Piggyback detector scheme. It is based on a bulk micromegas concept: the mesh and the anode are grouped in one single mechanical entity. The anode is a resistive layer spread on a ceramic plate of few 100 µm thickness, and there are no readout electronics inside the detector. The resistance of the anode layer can take values up to 100 MΩ/□.*

resistance is $R = \rho\frac{l}{t_R L}$. If the piece of material is a square (l = L), we get $R = \frac{\rho}{t_R}\times 1$. The coefficient $R_\square = \frac{\rho}{t_R}$ is called sheet resistance and is often preferred as a value because it is measured directly when making a 4-point probe measurement.

### 3.2.2 Gain and energy resolution

Even without readout electronics on the anode, it is still possible to study the piggyback detector in terms of gain and energy resolution by studying the signal created on the mesh by the moving charges. To perform this measurement, a charge preamplifier is connected to the mesh. The charge measured on the mesh is converted into voltage which value linearly depends on the measured charge. This voltage is then usually converted into a digital value by a Multi Channel Analyzer (MCA) for data treatment.

Fig.3.3 presents the curve of energy resolution and gain of a piggyback detector for a signal read directly on the mesh [1].
The process to calculate the gain is the following. I plug a capacitor of known capacitance at the input of the acquisition chain constituted of the charge preamplifier, a classical amplifier and the Multi Channel Analyzer. I apply a pulse voltage at the input of the capacitor, in order to generate a known charge at the entry of the

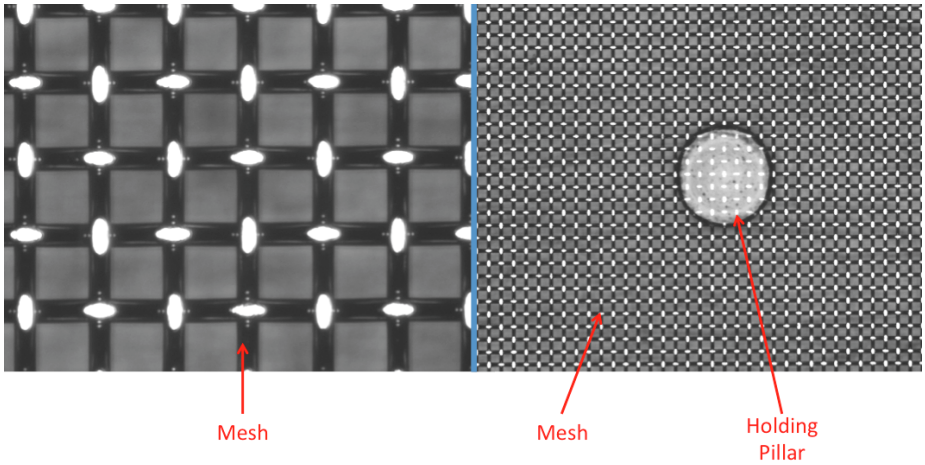


Figure 3.2: *Top view of the piggyback components. Top: woven mesh. Wire thickness = 18 µm, hole width = 45 µm. Bottom: woven mesh and holding pillar. Pillar diameter = 300 µm.*

acquisition chain. By looking at the digital output of the MCA created by the known input charge, it is possible to convert the data from Arbitrary Digital Units into electronic charge. From this it is possible to know the electronic charge deposited in the piggyback by a detected photon and thus the total number of electrons created after amplification $n_t$. Using a $^{55}$Fe source producing 5.9 keV photons in a gaseous mixture using argon and isobutane, it is possible to estimate quite precisely the number of charges created by primary ionization in the detector $n_i$. The gain of the detector $M$ is given by $M = \frac{n_t}{n_i}$.
The absolute gain of the detector in a mixture of argon-isobutane (95%-5%) is high and ranging from $10^3$ to $10^5$, which are typical values for a detector using the bulk technology. An energy resolution of 18% FWHM at 6 keV can be achieved, and this is also a typical result when using the bulk technology for a micromegas. Fig. 3.4 shows a typical spectrum obtained in a piggyback detector at 6 keV in argon-isobutane (95%-5%).

### 3.2.3 The main interest of the piggyback

The main interest of the piggyback detector is to try to read the signal through the ceramic layer with a readout electronics. The piggyback is placed in a gaseous chamber, with the ceramic layer acting as one of the side of the box and making the detector tight,

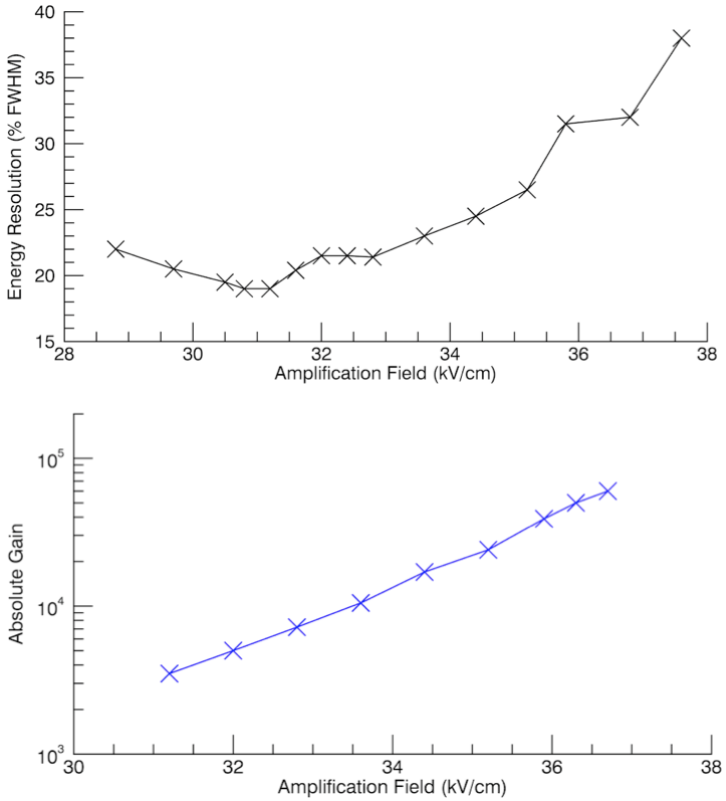


Figure 3.3: *Piggyback characteristics for the signal read on the mesh. The gas used is a mixture of argon-isobutane (95% - 5%). The piggyback tested has a resistive layer of 100* $\mathrm{M}\Omega/\square$.
*Top: energy resolution curve at 6 keV as a function of the amplification field. The resolution can go down to 18% FWHM at 6 keV, which is a typical result for a micromegas using a bulk technology and a woven mesh. Bottom: Absolute gain curve. The gain is found to be between* $10^3$ *and* $10^5$ *which is standard for a micromegas based gaseous detector.*

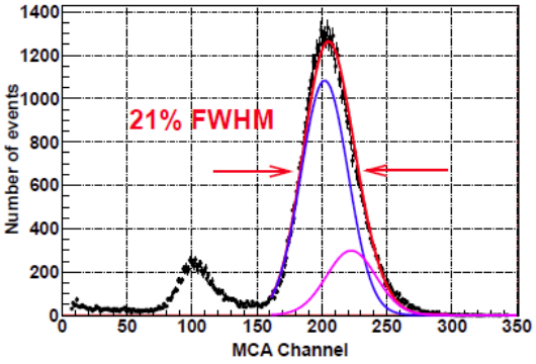


Figure 3.4: *Spectrum obtained with a piggyback [1]. The detected photons are 6 keV photons produced by a $^{55}Fe$ source in a mixture of argon-isobutane (95%-5%). The argon escape peak is visible. The main peak is fitted using a double Gaussian fit corresponding to the $K_\alpha$ and $K_\beta$ line of $^{55}Fe$.*

as presented in fig.3.5. The readout electronics is outside the gaseous medium, facing the ceramic layer, to read the signal at the anode thanks to a contactless capacitive coupling in the air.

This allows to have a completely outer and independent readout electronics, as it is not integrated to the detector. The electronics is protected from the sparks thanks to the resistive layer of the piggyback, which acts as a resistive anode, and this without being spread on the pixels. It also means that the electronics can be easily changed: there is a high flexibility for substitution of electronics if other parameters are needed such as channel gain or pixels size. The electronics can be changed without changing the gaseous part, then all the characterizations of the piggyback remain.
Another advantage of such a detector architecture is the mechanical protection of the electronics: the readout has to be put in front of the electronics, without necessarily touching it as adding an air layer still allow to read the signal. The fact that the pixels do not even touch the ceramic permits a very easy coupling between the electronics and the piggyback: the electronics can then be developed completely independently as its integration to the detector is more convenient.

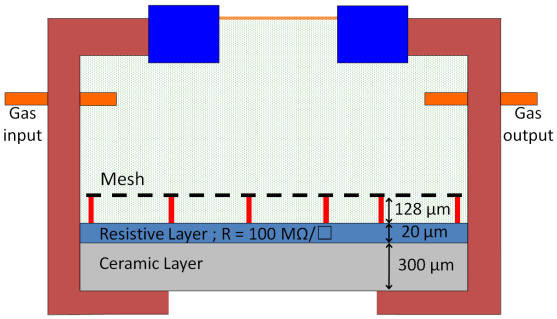


Figure 3.5: *Piggyback configuration in a gaseous chamber. The entrance window is made of 20 µm thick Kapton film. The ceramic layer acts as one side of the box and make the detector leak tight. The readout electronics is to be put in front of the ceramic, outside the gaseous medium, to read the signal through the ceramic thanks to capacitive coupling.*

## 3.3 The Caliste readout electronics

### 3.3.1 The requirements of the electronics readout

The readout electronics requires some characteristics in order to read properly the signal, and to perform spectro-polarimetry. First the electronics must be sensitive enough to be able to read the signal through the ceramic and an air layer, which necessarily attenuates the signal. It also must be low noise in order to perform spectroscopy in a correct way where the electronics noise will be negligible. Its pixels, or strips must be small enough in order to be able to recover the photoelectrons tracks and enable to perform polarimetry.

A last point to keep in mind is that the final goal of such a detector is to be sent into space: its goal being to study X-ray characteristics, and X-rays being absorbed completely by the atmosphere, it must be put on a satellite. So even at an early R&D stage it is important to consider the use of space qualified electronics.

### 3.3.2 The Caliste

As readout electronics, it has been decided to use the Caliste electronics [2, 3]. It is a 3-dimension electronics, initially designed to read semi-conductor space detectors. Several versions of the Caliste electronics exist, and for this project it is the version Caliste HD

(HD is standing for High Dynamic) that has been used. A picture of the Caliste-HD and one of its readout chains can be found in fig.3.6. Its characteristics are presented in table 3.1.

Caliste-HD has 256 pixels, each of them using the analogic architecture presented in fig.3.6 (left). The incoming charge is converted into voltage by the charge preamplifier. Then the signal is shaped in order to optimize the signal to noise ratio. The maximum of the shaped signal is recorded and converted into a digital value that can be treated by software. The important point is that the pixels are self triggered: when an incoming charge arrive on a pixel, the acquisition is automatically triggered. The threshold on each pixel can be set independently, varying from 0 to 14400 electrons for the highest threshold.

The electronics was built by taking care of having a very low noise. The electronic noise is represented by the Equivalent Noise Charge (ENC). The ENC is expressed in electrons root mean square (rms), and is the charge that needs to be present at the entry of the electronics to produce a Signal to Noise Ratio of 1. The $SNR$ is then expressed by the formula $SNR = \frac{Q}{ENC}$. An ENC of 50 $e^-$ rms as the one of Caliste means that to get an SNR greater than 1, more than 50 electrons have to be presented at the entrance of the electronics. During measurements, it is good to use a threshold of 3×ENC or 4×ENC to be sure to not trigger on electronic noise. The minimum threshold to use on the pixels is then 200 electrons. This value is low, and it allows a good reading of the signal through the ceramic, even if it is attenuated.
The pixel pitch of 580 $\mu$m is relatively small, especially for an electronics initially made for semi-conductor reading with independent chanels.
It is important to remark the Caliste triggering strategy. After a trigger due to at least one channel detection, a latency time larger or equal to the shaper peaking time is set. After this time, the analog chains are frozen and the communication starts with the digital chain. All channels which have been triggered are readout. Consequently it is possible to readout multiple events, which is necessary in the Caliste-MM detector.

Finally, it must be noted that the Caliste readout was initially developed for space applications. Being already space qualified, it is radiation hard and it has a low power consumption.

Several parameters can be tuned, such as the threshold on each pixel or the shaping time of the signal, in order to get the best com-

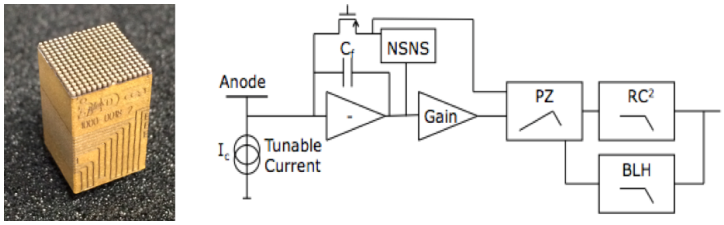


Figure 3.6: *The Caliste readout electronics. Left: The Caliste electronics. It is an auto-trigged electronics of 256 pixels. Right: electronic chain of one channel. The incoming charge is converted into voltage and shaped into a specific form to reduce the noise.*

| | |
|---|---|
| 3D block: | $10 \times 10 \times 16.5$ mm$^3$ |
| 16x16 pixels: | 8 ASICs IDeF-X [4] of 32 channels |
| Pixel diameter: | 500 $\mu$m |
| Pixel Pitch: | 580 $\mu$m |
| Consumption: | 850 $\mu$W/channel |
| Low Noise: | ENC = 50 e$^-$ rms |
| Threshold tunable on each pixels | Between 0 and 14400 electrons |
| Dynamic: | 10 fC to 40 fC |
| Peaking time: | 1 $\mu$s to 10 $\mu$s |

Table 3.1: Caliste's main characteristics.

bination of parameters to minimize the ENC. It is extremely useful when trying to read the faint signal of a semi-conductor, as getting the best energy resolution requires a fine tuning of those parameters [5]. For the Caliste-MM application it is less important because the noise mostly comes from the gaseous part of the detector. Being able to tune the threshold independently on each pixel is still interesting for our application.

It is also important to note that the Caliste is a 3D electronics device: the ASICs are molded in a resin and connected and multiplexed thanks to laser etching on the edge. This 3D architecture is important for the Caliste-MM application, as it allows to get the pixels close to the ceramic. Moreover, Caliste is abuttable on four sides and allows to consider a large detector area with the same technology.

## 3.4 The Caliste-MM detector: setup and acquired events

### 3.4.1 Setup

The innovation of the Caliste-MM detector is to use the Caliste readout electronics to read the signal developed in the piggyback micromegas detector. A scheme of the whole setup can be found in fig.3.7, and pictures of the real setup in fig.3.8.

The air layer has several uses. First it protects the electronics mechanically: the gaseous part can be moved, removed or aligned without damaging the Caliste pixels as they are not in direct contact with the ceramic. It has also the great interest of limiting the influence of the different heights of the pixels: the height of a pixel can vary from $\pm$ 15 $\mu$m, creating a difference up to 30 $\mu$m. If I try to approach the ceramic closer to the pixels, some might touch it and some will be quite far from the ceramic, which creates a high gain difference between the various signal read on the pixels: by letting an air layer of few 100 $\mu$m, this height difference is smoothed and the pixels read a signal with the same gain.
Moreover the distance between the Caliste and the ceramic plays an important role on the gain of the detector. If the readout is too close from the ceramic, the range in term of amplification field that can be used will be lower, as the electronics will enter into a saturation mode quicker. It is also the case if the detected photons have an energy too high.

### 3.4.2 Detecting 6 keV photons

This concept of detection used by the Caliste-MM detector is new and had to be tested. To make the various characterization of the detector, I used an $^{55}$Fe source producing 5.9 keV X-ray photons. The standard tests were performed with a standard gaseous mixture for Micromegas characterization: using argon as the main component and isobutane as the quencher, in the proportion 95% - 5%.

Fig.3.9 and 4.22 show typical events that are registered in the detector and read by the electronics. By event, I mean here the following process: a photon produced by the $^{55}$Fe source enters the piggyback detector through the entrance window made in a 20 $\mu$m thick Kapton film, and is converted in the gas into a photoelectron

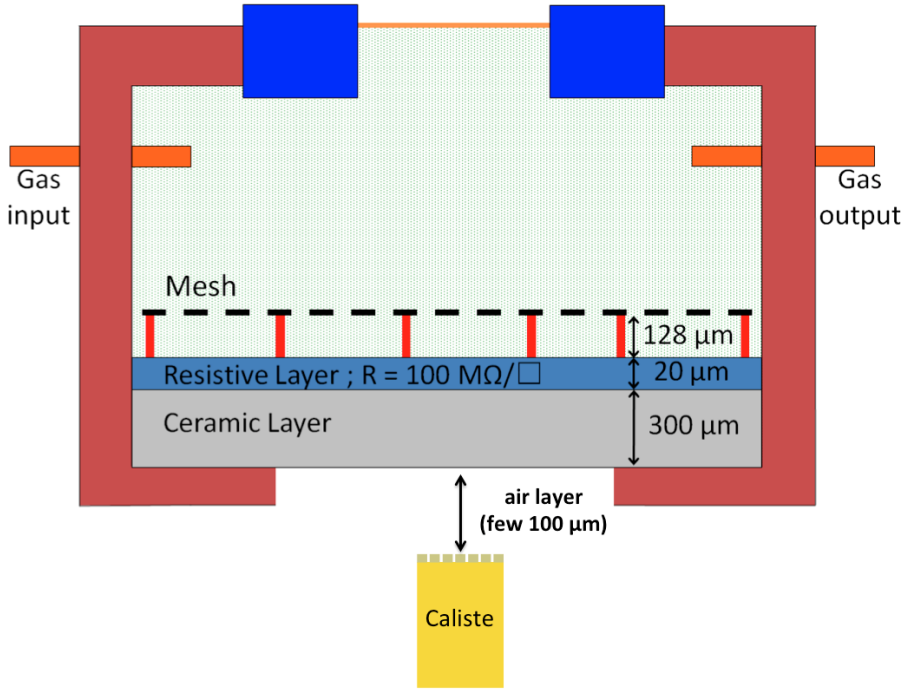


Figure 3.7: *Caliste-MM scheme. The Caliste is placed outside the gaseous medium, facing the ceramic to read the signal developed inside the piggyback through the ceramic. The resistive layer ensures a protection against the various discharges that can happen in the detector in case of high energy deposition (by a cosmic ray for instance). The air layer ensures mechanical protection of the electronics, as well as a smoothen distance between the top of each pixel and the ceramic layer. The detection and readout part of the setup are completely uncoupled and can be changed easily, depending on the requirements.*

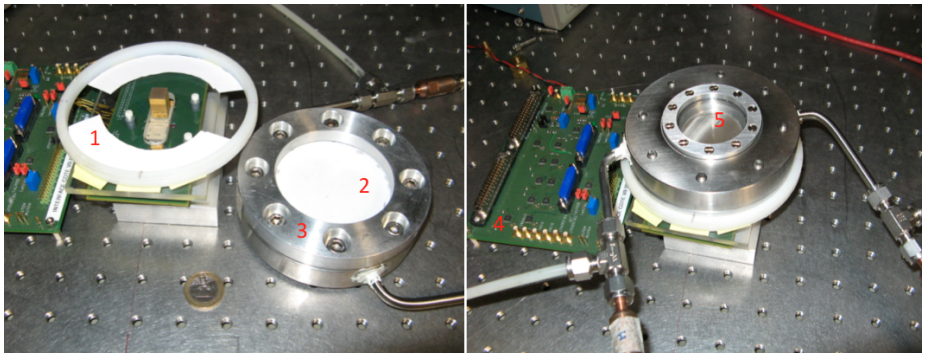


Figure 3.8: *The Caliste-MM setup. Left: The two parts separated. 1: Spacers to control the distance between the ceramic and the pixels. 2: Ceramic of the piggyback. 3: Gaseous detection chamber. Right: the Caliste-MM setup: the piggyback is simply placed on top of the Caliste electronics. 4: Digital to analog conversion card. 5: Entrance window transparent to X-ray photons.*

thanks to the photoelectric effect. The photoelectron ionizes the gas and creates a cloud of primary electrons which migrates toward the amplification gap of the detector, where it is amplified thanks to the avalanche process. The charge cloud created diffuses inside the resistive layer. The Caliste electronics, outside of the gaseous medium, reads the signal through the ceramic and an air layer and registered a signal such as the ones shown in fig.4.22.

## 3.5 Diffusion process in the resistive layer: the case of single infinitely extended resistive layer.

### 3.5.1 Comments on event topology

It is important at this point to comment on the shape of the detected events. The width of the events presented in fig.4.22 is of around 8 pixels. The pixel pitch being 580 $\mu$m, it makes a width of around 4.5 mm. The data coming from [1] gives a size of cloud charge of around 250 $\mu$m in an argon-isobutane mixture (95% - 5%) for an amplification field of 38 kV.cm$^{-1}$ (typically used in our application) and an amplification gap of 128 $\mu$m. The events registered by the electronics are then more than 4 times wider than the size of the cloud charge reaching the resistive anode.

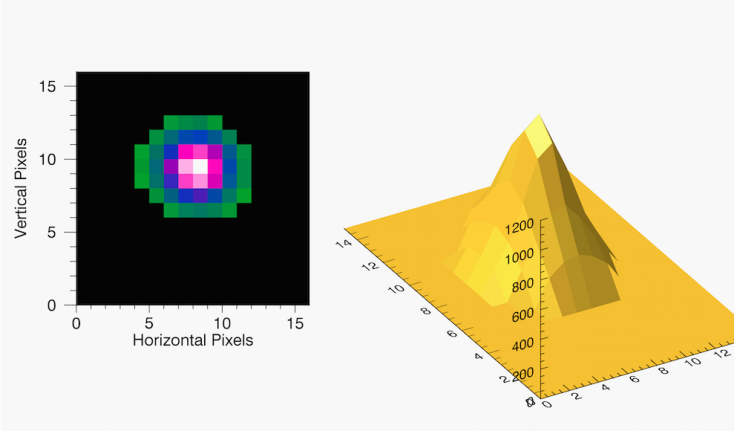


Figure 3.9: *Typical event as acquired by the Caliste electronics when the detector is illuminated with a $^{55}Fe$ source, in a mixture of argon-isobutane (95%-5%). Left: colormap. The color represents the intensity of the signal on each pixel. The horizontal and vertical lines represent respectively the horizontal and vertical pixel numbers. Right: Surface map. The vertical axis gives the gain registered by the pixels (in ADU).*

### 3.5.2 The model of infinitely extended resistive layer

To understand the physical processes happening when a point charge arrives on a resistive layer, I first start with the simple case of a single infinitely extended thin resistive layer presented in fig. 3.11. It consists in a 2D resistive layer of infinite size surrounded by air. At $t$=0, a point charge is placed at the coordinate ($x$=0, $y$=0, $z$=0). The objective is to look at the potential time variation of such a system, and this on a surface corresponding to the size of a pixel of the Caliste readout. This will not give a precise measurement of the signal developed on the Caliste, but it allows me to understand the physics of the charge dispersion in the resistive layer.

The surface charge density on the resistive layer created by the point charge at the origin is [7]:

$$\rho(r,t) = \frac{Q_0}{2\pi} \frac{vt}{\sqrt{(r^2 + v^2t^2)^3}} \tag{3.1}$$

where $r = \sqrt{x^2 + y^2}$ is the radial coordinate. $v = \dfrac{1}{2\epsilon_0 R}$ has the dimensions of a velocity, but it does not correspond to the speed of

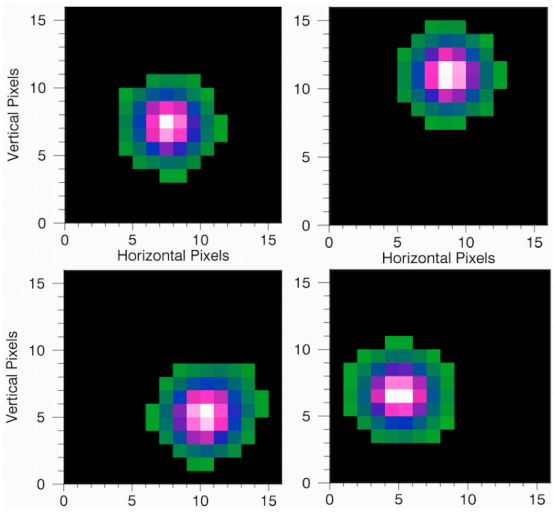


Figure 3.10: *Several 6 keV events acquired by the Caliste electronics in a mixture of argon-isobutane (95%-5%). Each event represents a photon conversion in the gas, the migration of the primary charges into the amplification gap of the piggyback, the amplification of the primary charges, the diffusion of the charges in the resistive layer, and the reading of the signal through the ceramic and an air layer. The center of each event gives information on the location of the photon conversion in the gas. The intensity of the signal carries the information of the energy of the detected photon.*

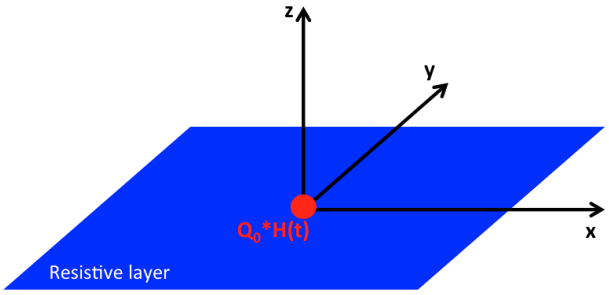


Figure 3.11: *Infinitely extended thin resistive layer. The resistive layer of square resistivity R is located at z =0 and infinitely extended in the plane (x,y). The surrounding medium is a material of dielectric permittivity $\epsilon_0$. A point charge is located at the coordinate (x=0,y=0,z=0). H is the Heaviside step function: H(t<0) = 0 and H(t≥0) = 1. $Q_0$*H(t) indicates that the point charge is placed at the time t=0 and does not exist at t < 0.*

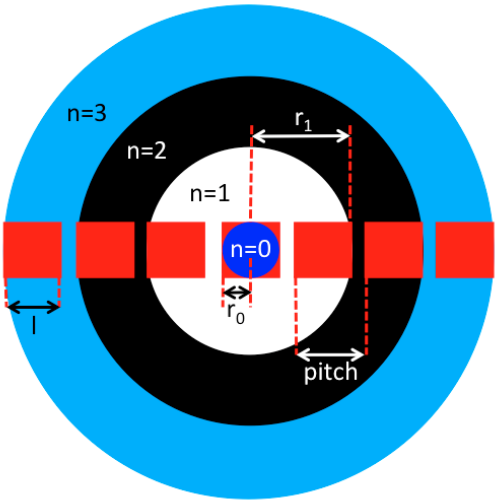


Figure 3.12: *Drawing of the surfaces for charge calculations. pitch = 580 $\mu$m, $l$ = 500 $\mu$m, $r_n = n \times pitch + \frac{l}{2}$. The red squares indicate the pixels position. The colored rings indicate the surface on which I calculate the surface charge density.*

the charge $Q_0$ in the resistive layer.
The charge on a disk of radius $r_0$ is obtained by integrating $\rho$ between 0 and $r_0$:

$$\begin{aligned} Q(r_0,t) &= \int_0^{2\pi}\int_0^{r_0} \rho(r,t)\mathrm{d}r.r\mathrm{d}\theta \\ &= \int_0^{r_0} rQ_0vt \times (r^2+v^2t^2)^{-\frac{3}{2}}\mathrm{d}r \\ &= Q_0\left(1-\frac{vt}{(v^2t^2+r^2)^{\frac{1}{2}}}\right) \end{aligned} \tag{3.2}$$

From this total charge, I evaluate the mean surface charge density at the vertical of a Caliste pixel. Fig. 3.12 presents the scheme of calculation for the surface charge density at the vertical of a pixel. First I consider that at the coordinate ($x$=0,$y$=0) is at the vertical of the center of one pixel. Then I calculate the total charge on the disks of radius $r_n = n \times p + \dfrac{l}{2}$ where $n$ is an integer, $p$ = 580 $\mu$m is the pixel pitch of the Caliste and $l$ = 500 $\mu$m is the length of a pixel. The total charge on a disk of radius $r_n$ is then:

$$Q_n(t) = Q_0\left(1-\frac{vt}{(v^2t^2+r_n^2)^{\frac{1}{2}}}\right) \tag{3.3}$$

Hence, the charge on the ring $n$ of surface $S_n$ is

$$\begin{aligned} Q_{S_n}(t) &= Q_n(t) - Q_{n-1}(t) \\ &= Q_0 \times \left[ \frac{vt\left(v^2t^2 + (np + \frac{l}{2})^2\right)}{\sqrt{\left(v^2t^2 + (np + \frac{l}{2})^2\right)^3}} - \frac{vt\left(v^2t^2 + \left((n-1)p + \frac{l}{2}\right)^2\right)}{\sqrt{\left(v^2t^2 + \left((n-1)p + \frac{l}{2}\right)^2\right)^3}} \right] \end{aligned}$$

The surface of the ring $n$ is

$$S_n = \pi r_n^2 - \pi r_{n-1}^2 \tag{3.4}$$

Considering the approximation $p = l$, eq.(3.4) gives

$$S_n = 2p^2\pi n \tag{3.5}$$

The surface charge density in the ring $n$ is then

$$\rho_{S_n}(t) = \frac{Q_{S_n}}{S_n} \tag{3.6}$$

$\rho_{S_n}$(t) is the surface charge density at the vertical of the pixel $n$ which center is located at the distance $n \times p$ from the point charge $Q$. In the Caliste-MM detector the incoming charge is not a point charge but assumes a Gaussian shape. $\rho_{S_n}$(t) is then convoluted with a Gaussian function in order to take this fact into account. The convolution is handled numerically.
Using the fact that the resistive layer has a thickness of $t = 20$ $\mu$m, the volume charge density at the vertical of the pixel n is:

$$\begin{aligned} \rho_V(n,t) &= \frac{\rho_{S_n}(t)}{d} \\ &= \frac{Q_0}{2p^2\pi nd} \times \left[ \frac{vt\left(v^2t^2 + (np + \frac{l}{2})^2\right)}{\sqrt{\left(v^2t^2 + (np + \frac{l}{2})^2\right)^3}} - \frac{vt\left(v^2t^2 + \left((n-1)p + \frac{l}{2}\right)^2\right)}{\sqrt{\left(v^2t^2 + \left((n-1)p + \frac{l}{2}\right)^2\right)^3}} \right] \end{aligned} \tag{3.7}$$

From eq.(3.8) the potential at the vertical of the pixel $n$, $V_n(t)$, can be calculated thanks to the Poisson equation:

$$\Delta V_n(t) = -\frac{\rho_V(n,t)}{\epsilon_0} \tag{3.8}$$

### 3.5.3 The finite difference method

The calculation of the Laplace equation eq.(3.8) can be done numerically by a finite difference method [8]. It is based on the discretization of the differential operators. The spatial second derivatives are here approximated by finite differences thanks to the second order of the Taylor formula.
The Taylor formula approximates the value of a function $U$ near the coordinate $(x,y)$ by

$$\begin{aligned} U(x+h,y) &= U(x,y) + h\frac{\partial U}{\partial x}(x,y) + \frac{h^2}{2}\frac{\partial^2 U}{\partial x^2}(x,y) + o(h^2) \\ U(x-h,y) &= U(x,y) - h\frac{\partial U}{\partial x}(x,y) + \frac{h^2}{2}\frac{\partial^2 U}{\partial x^2}(x,y) + o(h^2) \end{aligned}$$

which gives the finite differences

$$\begin{aligned} \frac{U(x+h,y)-U(x,y)}{h} &= \frac{\partial U}{\partial x}(x,y) + \frac{h}{2}\frac{\partial^2 U}{\partial x^2}(x,y) + o(h) \quad (3.9) \\ \frac{U(x-h,y)-U(x,y)}{h} &= -\frac{\partial U}{\partial x}(x,y) \\ &\quad + \frac{h}{2}\frac{\partial^2 U}{\partial x^2}(x,y) + o(h) \quad (3.10) \end{aligned}$$

These equations are both an approximation of the partial derivative $\frac{\partial u}{\partial x}$ at the first order in $h$. Adding (3.9) and (3.10) gives:

$$\frac{\partial^2 U}{\partial x^2} = \frac{1}{h^2}(U(x+h,y) + U(x-h,y) - 2U(x,y)) + o(h) \quad (3.11)$$

Using, in 2D and in cartesian coordinates

$$\Delta U(x,y) = \frac{\partial^2 U}{\partial x^2}(x,y) + \frac{\partial^2 U}{\partial y^2}(x,y)$$

eq.(3.11) allows to write an approximation of the Laplacian of the function $U$:

$$\Delta U \approx \frac{1}{h^2}\Big[U(x+h,y)+U(x-h,y)+U(x,y+h)+U(x,y-h)-4U(x,y)\Big] \quad (3.12)$$

I use eq.(3.8) to replace $\Delta V$ by $-\frac{\rho_V(i,j,t)}{\epsilon_0}$, where $\rho_V(i,j,t)$ is given by eq.(3.8) and depends on the pixel at the vertical of the

coordinate ($i$,$j$) considered. Combining this with eq.(3.12) gives:

$$V(x,y) = \frac{1}{4}\Big[V(x+h,y)+V(x-h,y)+V(x,y+h) + V(x,y-h)+h^2\frac{\rho_V(i,j,t)}{\epsilon_0}\Big] \quad (3.13)$$

It is then possible to calculate for several time $t$ the potential by an iterative method. For this I designed a simple 2D model presented in fig.3.13. This model is meshed with mesh elements of 20 $\mu$m length. Hence in this model the thickness of the resistive layer is of only one element. The width of the model uses 150 elements, resulting in a size of 2980 $\mu$m. This size allows to calculate the potential variation on 5 pixels.
The point charge $Q$ is located at ($x$=0,$y$=0) at the vertical of the center of one pixel. The voltages are standard voltages used in the Caliste-MM detector. The distances are the one used in the Caliste-MM detector. The resistivity of the resistive layer is 100 M$\Omega/\Box$.
The boundary conditions are fixed at the top and bottom by the potential on the mesh, the pixels and the interpixel. The boundary conditions at the side are periodic conditions.
The potential $V$ is calculated by iteration. At each iteration, the whole mesh is calculated and the value of the potential $V^k(i,j)$ is calculated by using $V^{k-1}(i\text{-}1,j)$,$\mathrm{V}^{k-1}(i+1,j)$, $\mathrm{V}^{k-1}(i,j\text{-}1)$ and $\mathrm{V}^{k-1}(i,j+1)$. After a sufficient number of iterations, the calculated potentials converge toward their real values.

Several iterative methods exist to solve the system of eq.(3.13). I used the Gauss-Seidel method [8], which is:

$$V^{k+1}(i,j,t) = \frac{1}{4}\Big[h^2\frac{\rho_V(i,j,t)}{\epsilon_0} + V^k(i+1,j,t)+V^k(i,j+1,t) + V^{k+1}(i-1,j,t)+V^{k+1}(i,j-1,t)\Big] \quad (3.14)$$

In this method, when the calculations are performed on the nodes with increasing values of $i$ and $j$, the value of the potential $V(i,j,t)$ at the iteration $k$ uses the values $V(i\text{-}1,j,t)$ and $V(i,j\text{-}1,t)$ calculated during the same iteration. This method has a fast converging time compared to the direct method of eq.(3.13).
I combined it with a Successive Over Relaxation (SOR) [8] method,

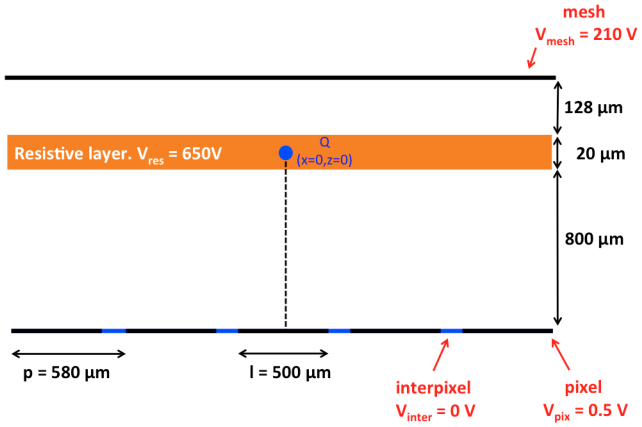


Figure 3.13: *Modelization of part of the detector to calculate the potential on the resistive layer. The point charge Q is located at (x=0,y=0). The resistivity of the resistive layer is 100* MΩ/□*. The parameters are standard parameters used in the Caliste-MM detector*

which gives

$$\begin{aligned} V^{k+1}(i,j,t) &= (1-w)V^k(i,j,t) + \frac{w}{4}\Bigg[h^2\frac{\rho_V(i,j,t)}{\epsilon_0} \\ &\quad + V^k(i+1,j,t) + V^k(i,j+1,t) \\ &\quad + V^{k+1}(i-1,j,t) + V^{k+1}(i,j-1,t)\Bigg] \end{aligned} \tag{3.15}$$

The term $w$ is specific to the relaxation technique and is contained in the interval ]0,2[. The value I use is $w = 1.8$, which ensured the fastest convergence. The tolerance on the error between two successive values of the calculated potential $V^k$ and $V^{k+1}$ is $10^{-4}$.

### 3.5.4 Results

The potential can be calculated on several pixels and this for several times, using the values of volume charge density given by eq.(3.8). Fig. 3.14 presents the calculated potential in the region at the vertical of the central pixel at t = 0 s when there is no charge and at $t = 1$ ns just after the introduction of the point charge $Q = 200$ fC on the resistive layer as in fig. 3.13. $Q = 200$ fC corresponds to the charge created in a mixture of argon-isobutane by a 6 keV photon, assuming a piggyback amplification of 6000.
The introduction of the point charge creates a drop in the potential

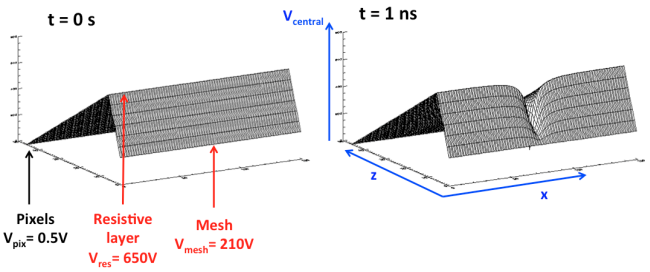


Figure 3.14: *Calculated potential with the finite difference method in the region at the vertical of the central pixel at t=0 s and t=1 ns, just after the introduction of the point charge. The introduction of the point charge Q = 200 fC, corresponding to the charge created by a 6 keV photon in a piggyback with an amplification of 6000, creates a drop of the potential in the region of the resistive layer considered. This pulse on the resistive layer is applied at the entrance of the capacitance formed by the resistive layer and the pixels of the Caliste, and creates a charge on the pixels.*

in the resistive layer. Fig. 3.15 presents the variation with time of the absolute value of potential difference between the initial potential of the resistive layer $V_{res} = 650$ V and the potential calculated in the region facing the central pixel. It is presented in absolute value. The introduction of the point charge creates a voltage difference of more than 100 V in the resistive layer. After 1 $\mu$s this potential difference is equal to 0.1 V and the potential in the region considered is then back to its initial value of 650 V.
This potential difference on the resistive layer is perceived by the Caliste electronics like a potential pulse at the entrance of the capacitance formed between the resistive layer and the pixels. This creates a charge at the entrance of the Caliste pixels and is then responsible of the creation of the signal registered by the pixels.
The potential difference created by the charge creates an electric field going from the charge to the edge of the resistive layer. Under this self induced electric field, the charges spread as presented in fig. 3.16. This motion of the charges under the electric field they created is what I call *diffusion* in this manuscript. This model is a simple case and does not represent the exact geometry of the detector, but it allowed me to understand why and how the charges diffuse in the resistive layer.

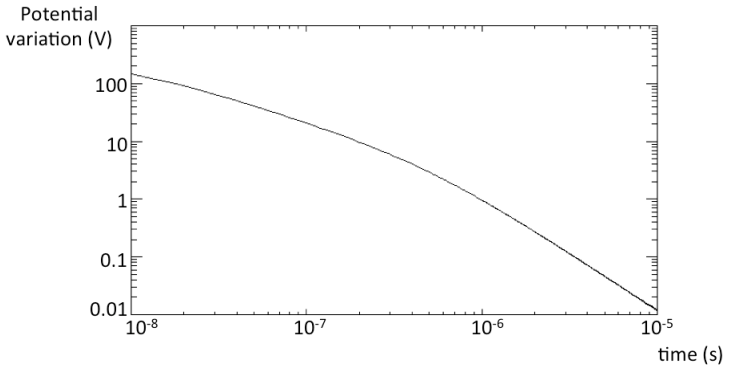


Figure 3.15: *Time variation of the potential on the resistive layer in the region facing the central pixel. The potential indicated is the absolute value of the difference between the potential in the region and the initial potential value of the resistive layer. At 1 ns, the potential difference is higher than 100 V. After 1 µs the potential on the region is almost back to its initial value.*

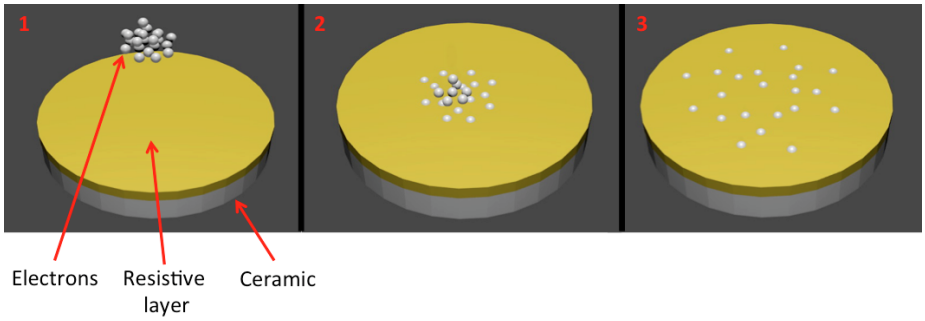


Figure 3.16: *The diffusion phenomenon in the resistive layer. 1: The cloud of amplified charges migrates toward the resistive layer. 2: The charges start to diffuse in the resistive layer toward the contact ring which surrounds the resistive layer. This diffusion is a self induced motion caused by the drop of potential created by the charges themselves. 3: The charges continue their migration toward the contact ring where they are evacuated. During their diffusion on the resistive layer, the charges create a signal on the pixels of the Caliste under them, hence the wide size of the events registered.*

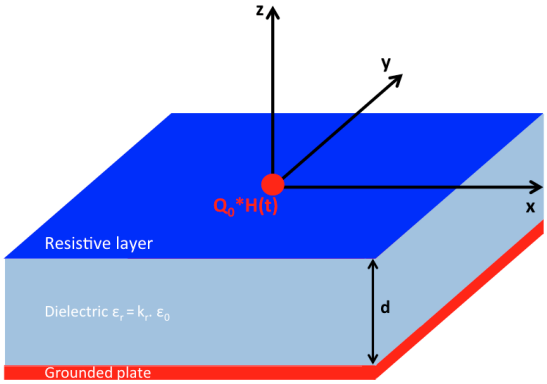


Figure 3.17: *Model of infinitely extended resistive layer parallel to a grounded plate. The grounded plate represents the pixel readout.*

## 3.6 Diffusion in a resistive layer parallel to a grounded plate

### 3.6.1 The model

The model of diffusion in a resistive layer parallel to a grounded plate (RLPGP) is presented in fig. 3.17. It is a model closer to the Caliste-MM geometry than the infinitely extended resistive layer as it takes into account the presence of the pixels. Here again, the dimensions in the $(x,y)$ plane are considered infinitely extended. In this geometry, the surface charge density created by a point charge $Q$ inserted at $(x{=}0,y{=}0)$ at $t{=}0$ in the resistive layer is [7]:

$$\rho(r,t) = \frac{Q}{d^2\pi}\frac{1}{8t/T}\ \mathrm{e}^{-\frac{r^2}{8d^2t/T}} \tag{3.16}$$

with $d$ the distance between the resistive layer and the Caliste and $T = 2d\epsilon_r R$ where $R$ is the resistivity of the resistive layer expressed in $\Omega/\square$.

If we note $\overrightarrow{E}(x,y,t)$ the electric field in the resistive layer at the coordinate $(x,y,t)$, the current density $\overrightarrow{j}$ in the resistive layer is given by $\overrightarrow{j} = \overrightarrow{E}/R$. $\overrightarrow{j}$ is the current density in the resistive layer considered infinitely thin, and is then expressed in A.cm$^{-1}$ instead of A.cm$^{-2}$. Noting $\rho(x,y,t)$ the charge density, we also have $\overrightarrow{\nabla}.\overrightarrow{j} = -\frac{\partial q}{\partial t}$.

This gives, using $\overrightarrow{E}$ = -$\overrightarrow{\nabla}$V:

$$\frac{\partial \rho}{\partial t} = \frac{1}{R}\Delta V = \frac{1}{R}(\frac{\partial^2 V}{\partial x^2} + \frac{\partial^2 V}{\partial y^2}) \tag{3.17}$$

Setting $\rho = C_S V$ with $C_S$ the surface capacitance, I derive

$$\frac{\partial \rho}{\partial t} = \frac{1}{RC_S}\Delta \rho = \frac{1}{RC_S}(\frac{\partial^2 \rho}{\partial x^2} + \frac{\partial^2 \rho}{\partial y^2}) \tag{3.18}$$

This equation is a diffusion equation, called the second Fick's law, with a diffusion coefficient $D = \frac{1}{RC_S}$. The charges move under the electric field they have created, so this process is different from the standard processes of diffusion like heat transfer as the motion of particles is not free but self induced. Nevertheless, in the approximation used, the equation governing the charge density is a diffusion equation.

### 3.6.2 The transmission line model

The diffusion equation (3.18) can be found by using the transmission line model. At first I consider the case of 1D motion of charges in the resistive layer. The resistive layer can be modeled by elementary linear portions of electric line as in fig.3.18 [9]. The presence of the capacitive element $C_l$ is caused by the capacitive coupling between the resistive anode and the Caliste's pixels, and between the anode and the mesh of the piggyback.

The system is controlled by the two differential equations

$$\begin{cases} \frac{\partial V}{\partial x}(x,t) = -R_l.I(x,t) \\ \\ \frac{\partial I}{\partial x}(x,t) = -C_l.\frac{\partial V}{\partial t}(x,t) \end{cases} \tag{3.19}$$

Solving this system gives the equation:

$$\frac{1}{R_l C_l}\frac{\partial^2 V}{\partial x^2} = \frac{\partial V}{\partial t} \tag{3.20}$$

The charge density $\rho$ is linked to the voltage $V$ by the Poisson equation: $\Delta V = -\frac{\rho}{\epsilon_0}$, where $\epsilon_0$ is the vacuum permittivity and

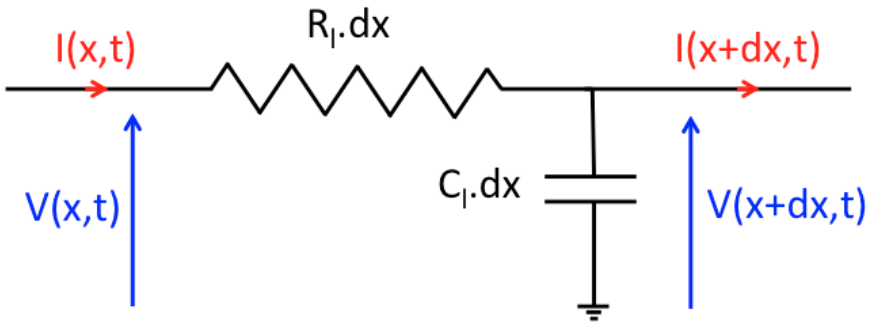


Figure 3.18: *Model of an elementary portion dx of the resistive layer for electrons motion in the 1D case. $C_l$ represents the linear capacitance, and $R_l$ is the linear resistivity.*

$\Delta$ is the laplacian operator. As I am considering the 1D case, I have the equivalence $\Delta = \dfrac{\partial^2}{\partial x^2}$. I then get from eq. (3.20):

$$-\frac{\rho}{\epsilon_0 R_l C_l} = \frac{\partial V}{\partial t} \tag{3.21}$$

Finally, by differentiating each member of eq. (3.21) by $\dfrac{\partial^2}{\partial x^2}$ I obtain

$$\frac{1}{R_l C_l}\frac{\partial^2 \rho}{\partial x^2}(x,t) = \frac{\partial \rho}{\partial t}(x,t) \quad \text{or} \quad \frac{1}{R_l C_l}\Delta\rho(x,t) = \frac{\partial \rho}{\partial t}(x,t) \tag{3.22}$$

The model can be generalized in 2 dimensions to give

$$\frac{1}{R_\square C_S}\Delta\rho(x,y,t) = \frac{\partial \rho}{\partial t}(x,y,t) \quad \text{or} \quad D\Delta\rho(x,y,t) = \frac{\partial \rho}{\partial t}(x,y,t) \tag{3.23}$$

with $R_\square$ the square resistivity of the resistive layer, $C_S$ the surface capacitance seen from the resistive layer and $D = \dfrac{1}{R_\square C_S}$ the analog of a diffusion coefficient. By this method using a modelization of the resistive layer, I find the same equation as eq.(3.18) which has been obtained by considering the charge spreading in a physics point of view.

### 3.6.3 Solution of the diffusion equation

The solution of (3.23) to a Dirac of charge in the resistive layer at ($x$=0,$y$=0,$t$=0) is [10]:

$$\rho_\delta(x,y,t) = \frac{Q}{(2\sqrt{\pi t D})^2}\ \mathrm{e}^{-\frac{x^2+y^2}{4tD}} \tag{3.24}$$

The initial cloud of charge is not a $\delta$ function. Its shape can be closely approximated by a Gaussian function which width depends on the transverse diffusion of the charges in the gas [10]. To obtain the expression of the charge density I perform a convolution between $\rho_\delta$ and a Gaussian of amplitude $Q_{tot}$ and variance $\sigma^2 = w^2$ (with $w$ the width of the cloud). $Q_{tot}$ is the absolute charge carried by the electron cloud. For a cloud of N electrons, $Q_{tot} = Nq$ with $q = 1.6\mathrm{e}^{-19}$ C the elementary charge.This gives:

$$\rho(x,y,t) = \frac{Nq}{2\pi(2\pi Dt + w^2)}\ \mathrm{e}^{-\frac{x^2+y^2}{2(2Dt+w^2)}} \tag{3.25}$$

$$= \frac{Nq}{2\pi(2\pi Dt + w^2)}\ \mathrm{e}^{-\frac{x^2+y^2}{2\sigma^2}} \tag{3.26}$$

with $\sigma = \sqrt{2Dt + w^2}$. Because of capacitive coupling, if the charge density in the resistive layer at the vertical of a pixel is $\rho(x,y,t)$, then the charge density at the pixel is -$\rho(x,y,t)$. From eq.(3.26) it is then possible to calculate the charge developed at the entrance of each pixel of the Caliste by integrated the charge density over the surface of the pixels.

## 3.7 Charge calculation and event simulation

### 3.7.1 Expression of the charge at the surface of the resistive layer

From the expression of the charge density $\rho$ given by eq. (3.23) coming from the RLPGP model it is possible to calculate the charge Q in any region of the resistive layer at any time. If ($x$=0,$y$=0) corresponds to the position of the center of the primary cloud charge, the

charge located in any squared area $S$ delimited by the coordinates $(x_1, x_2, y_1, y_2)$ with $x_2 > x_1$ and $y_2 > y_1$ is

$$Q_S = \frac{Nq}{4}[\mathrm{erf}(\frac{x_2}{\sqrt{2}\sigma}) - \mathrm{erf}(\frac{x_1}{\sqrt{2}\sigma})] \times [\mathrm{erf}(\frac{y_2}{\sqrt{2}\sigma}) - \mathrm{erf}(\frac{y_1}{\sqrt{2}\sigma})] \quad (3.27)$$

with the erf the error function defined as $\mathrm{erf}(x) = \frac{2}{\sqrt{\pi}} \int_0^x e^{-t^2} \mathrm{d}t$.
From this expression it is possible to compute the charge created by the diffusing charges in the various regions of the resistive layer facing each pixels of the Caliste, and then the charge created on the Caliste.

In theory, a convolution between this result and the arrival time distribution of the cluster on the resistive layer should be performed. This arrival time-spread is caused by the longitudinal diffusion of the charges and has a Gaussian profile: $L(t) = \frac{1}{\sigma_L \sqrt{2\pi}} \mathrm{e}^{-\frac{t^2}{2{\sigma_L}^2}}$. The standard deviation $\sigma_L$ is of the order of the nanosecond [1] which is very short compared to the other time values acting in the diffusion process. It can then be neglected and I consider in the following that all charges of the cloud arrive at the same time $t = 0$ on the resistive layer.

### 3.7.2 Estimation of the surface capacitance

At first it is necessary to compute the estimated surface capacitor seen by the charges on the resistive layer. I model an elementary surface of the resistive layer as in fig.3.19. The capacitance $C_{pix}$ is formed by two stacked dielectrics: the ceramic of relative permittivity $\epsilon_{cer} = 12$ and the air layer of relative permittivity $\epsilon_{air} = 1$.
I then have:

$$C_S = \frac{2\epsilon_{cer}\epsilon_{air}}{\epsilon_{cer} + \epsilon_{air}} \times \frac{\epsilon_0}{d_{cer} + d_{air}} \quad (3.28)$$

with $d_{cer} = 500$ $\mu$m and $d_{air}$ the size of the air layer which can be tuned. With an air layer of 500 $\mu$m I calculate $C_S = 8.85$ nF.m$^{-2}$. The capacitance between a pixel and the corresponding surface of the resistive layer is $C_{pix} = C_S{}^* S_{pix}$ with $S_{pix}$ the surface of a pixel. With the version of Caliste used, $S_{pix} \approx 500$ $\mu$m$^2$. So $C_{pix} = 2.21$ fF.

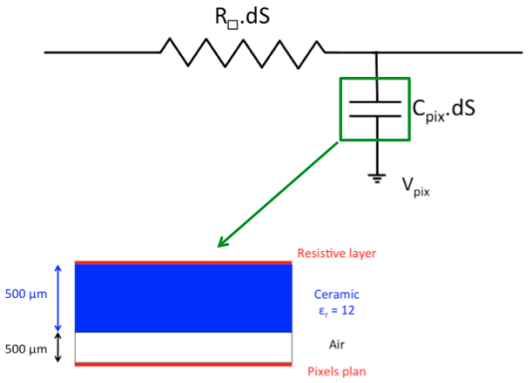


Figure 3.19: *Model of an elementary surface dS of the resistive layer.*

### 3.7.3 Charge profile on each pixel

It is now possible to calculate the charge transiting in front of each pixel. Fig.3.20 presents the evolution of the charge with time, for several pixels located at various distances from the center of the cloud charge arriving on the resistive layer. The parameters of the calculation are the real size of pixels of the Caliste. The total charge reaching the anode has been estimated considering a 6 keV photon being converted in a mixture of argon-isobutane (95% - 5%), and a gain of the piggyback of 6000 (corresponding to an amplification field of 33 kV.cm$^{-1}$, see fig.3.3). The distance $d_{air}$ has been taken equal to 500 $\mu$m.
The effect of the diffusion of electrons on a pixel is clearly visible. At first the charges arrive which creates an increase of the signal. Then a maximum is reached and the signal goes down as the charges moved away from the pixel.

### 3.7.4 The influence of $R_\square$ and $C_S$

One interesting thing to notice is that the maximum on the central pixel does not depend on the value of $R_\square$ or $C_S$. In fact, the maximum is reached at $t = 0$ and is equal to $Nq \times \mathrm{erf}(\frac{L_{pix}}{2w\sqrt{2}})^2$ where $L_{pix}$ is the length of one pixel and $w$ the standard width of the cloud charge. But the gain of the Caliste-MM detector changes with $d_{air}$, hence with $C_S$, and with $R_\square$. This is caused by the influence of $C_S$ and $R_\square$ on the diffusion speed of the charges, as they both take part in the diffusion coefficient $D = \frac{1}{R_\square C_S}$.

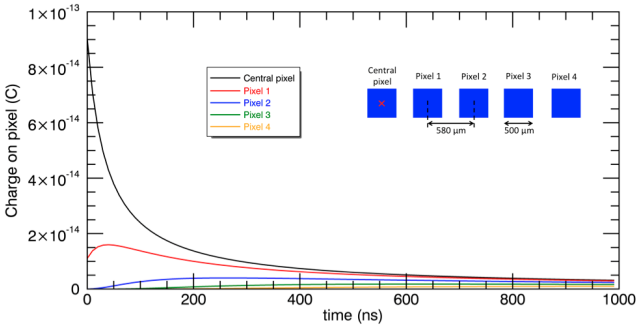


Figure 3.20: *Charge profile simulated on various pixels. The red cross indicates the center of the incoming cloud of charges. The parameters are:* $d_{air}$ *= 500* $\mu m$*,* $d_{cer}$ *= 500* $\mu m$*, for an incoming photon of 6 keV in a mixture of argon-isobutane (95% - 5%) and a piggyback gain of 6000 corresponding to an amplification field of 33* $kV.cm^{-1}$*.*

Fig.3.21 shows the charge profile on the central pixel for various distance between the ceramic and the air layer. As the distance increases, $C_S$ decreases thus $D$ increases and the charges diffuse faster. The same behavior happens when $R_\square$ is changed.

It is important to notice the high propagation speed of the charges, especially on the central pixel. In less than 100 ns the signal is divided by a factor of 4, then the decrease is slower. This is too fast for the pixel to record correctly the signal. I did not have time to simulate completely this process during my PhD. Such a study by simulation implies to be very precise on calculations of surface capacitance and the voltage profile on the resistive layer. To get those value I would have needed to make a model of the detector RLPGP to obtain the charge density equation and solve it with the finite difference method.
With the equations coming from the model of infinitely extended resistive layer parallel to a grounded plate, I found that the behavior of the model fits the measurements if I consider that the Caliste is able to read the signal properly only after 250 ns. If the charges spread faster, the recorded signal will then be lower because of this rising time effect of the electronics. This explains the change in gain of the Caliste-MM detector when increasing the distance between the Caliste readout and the ceramic, or when using a piggyback of other resistivity.

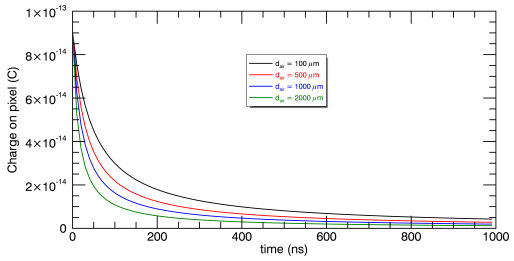


Figure 3.21: *Charge profile on the central pixel for various distances $d_{air}$ in an argon mixture and a piggyback gain of 6000. As the distance increases, the charges spread faster.*

### 3.7.5 Simulation

From this it is possible to simulate the shape of an event that would be recorded by the Caliste-MM detector. In a mixture of argon-isobutane (95% - 5%), a 6 keV photon produces 236 electrons [11]. At a given amplification field corresponds a gain of the piggyback alone, which can be obtained by making gain curves like that shown on fig. 3.3. Hence the number of charges $N$ arriving on the anode at a fixed amplification field can be estimated correctly. With eq. (3.27), it is then possible to calculate the charge profile on each pixels like in fig. 3.20. Then I take the maximum of the charge arriving on each pixel and convert it into the electronics value. Finally, I multiply the obtained signal by a factor in order to have the maximum of the event fitting the mean maximum of measured events in the same conditions. This factor is 0.2. It comes from the response time of the Caliste electronics. I did not study it in details as it needs a modelization more precise than the RLPGP which I did not have time to perform.
Fig.3.22 presents a real event recorded by the Caliste-MM detector (as in fig.4.22). It is an event corresponding to the conversion of a 6 keV photon in a gaseous mixture of argon-isobutane (95% - 5%) with an amplification field of 37 kV.cm$^{-1}$. The maximum of the recorded signal is normalized to 1. The bottom of fig.3.22 is the figure obtained when using the previous results on charge dispersion to calculate the charge transiting on each pixels in the case of such a conversion. The maximum of the charge his recorded. Thanks to a calibration made by applying a known voltage at the entrance of a known capacitance, it is possible to convert an injected charge from fC to electronics units used by the Caliste-MM detector. The

| Parameter | Value |
|---|---|
| Gaseous mixture | argon - isobutane (95% - 5%) |
| Drifting gap | 0.5 cm |
| Amplification gap | 128 $\mu$m |
| Bias voltage in the amplification gap | 410 V to 500 V |
| Amplification field | 32 kV.cm$^{-1}$ to 39 kV.cm$^{-1}$ |
| Resistive ayer material | $RuO_2$ |
| Resistive layer thickness | 20 $\mu$m |
| Resistive layer resistivity | 100 M$\Omega/\square$ |
| Ceramic material | $Al_2O_3$ 96% |
| Ceramic thickness | 300 $\mu$m |
| Air layer thickness | 500 $\mu$m |
| Pixel size | 500 $\mu$m |
| Pixel pitch | 580 $\mu$m |
| Pixels disposition | 16×16 matrix |

Table 3.2: *Caliste-MM standard parameters.*

maximum of the obtained simulated signal is normalized to 1.

## 3.8 Summary

The piggyback is a Micromegas-based detector, with a resistive layer as the anode. Its characteristics in term of gain and energy resolution are standard for a Micromegas-based on the bulk technology.

The Caliste-MM detector uses the piggyback for the conversion of photons into electrons and the amplification of the signal. But there are no electronics inside the gaseous detector. The electronics is outside, facing the ceramic of the piggyback, and read the signal thanks to capacitive coupling. The readout electronics used is called Caliste.

The standard parameters for the Caliste-MM detector are presented in table 3.2.

With this new concept of gaseous detector using a readout electronics outside the gaseous medium and in a contactless configuration, it is possible to detect 6 keV photons.

The shape of the detected events is due to the diffusion of the charges inside the resistive layer. Analytical calculations have been performed in order to understand this phenomenon.

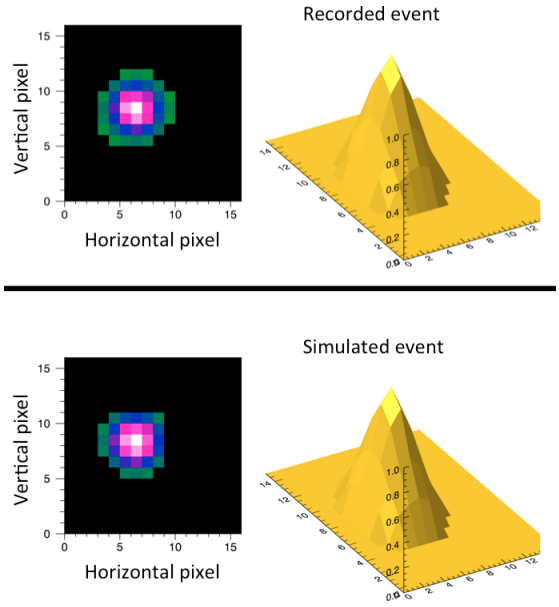


Figure 3.22: *Top: a real event recorded by the Caliste-MM detector. It corresponds do the detection of a 6 keV photon in a gaseous mixture of argon-isobutane (95% - 5%) with an amplification field of 37 $kV.cm^{-1}$. The signal is normalized to have its maximum equal to 1. The event is fit in order to recover the position of its centroid.*
*Bottom: simulation of the 6 keV event in the same gaseous mixture and amplification field, with its centroid at the position determined by the fit of the real event. The signal on each pixel corresponds to the maximum of the charge transiting on it calculated in the RLPGP model. This charge is then converted into electronics units thanks to calibration. The signal is normalized to have its maximum equal to 1.*
*The deviation between the measured and the simulated event is of 7.8% maximum. The mean error is 3.6%.*

# Bibliography


[1] D. Attié et al., *Piggyback resistive Micromegas*, Journal of Instrumentation **8** C11007 (2013)

[2] A. Meuris et al., *Caliste HD: A new fine pitch Cd(Zn)Te imaging spectrometer from 2 keV up to 1 MeV*, in 2011 IEEE Nuclear Science Symposium conference Record

[3] O. Limousin, *The story of Caliste: CdTe based pixel detectors for Hard X-Ray astronomy in space*, Habilitation à Diriger les Recherches, 2016

[4] A. Michalowska et aI., *Imaging X-ray detector front-end with high dynamic range: IDeF-X HD*, Nuclear Instruments and Methods in Physics Research Section A, Special Issue NDIP, 20 I I.

[5] A. Meuris, *Etude et optimisation du plan de détection de haute énergie en Cd(Zn)Te de la mission spatiale d'astronomie X et gamma Simbol-X*, PhD thesis (2015)

[6] http://www-hep.phys.saga-u.ac.jp/ILC-TPC/gas/

[7] W. Riegler, *Electric fields, weighting fields, signals and charge diffusion in detectors including resistive materials*, Journal of Instrumentation, **11** (2016)

[8] S. Dubos, *Nouveau spectro-imageur CdTe à très haute résolution spatiale et spectrale pour l'astronomie X et gamma*, PhD thesis

[9] M. S. Dixit, J. Dubeau, J. P. Martin and K. Sachs, *Position sensing from charge dispersion in micro-pattern gas detectors with a resistive anode*, Nuclear Instruments and Methods in Physics Research Section A, **518** (2004), 721-727

[10] M. S. Dixit and A. Rankin, *Simulating the charge dispersion phenomena in Micro Pattern Gas Detectors with a resistive anode*, Nuclear Instruments and Methods in Physics Research Section A, **566** (2006), 281-285

[11] http://xdb.lbl.gov/

# Chapter 4

# The Caliste-MM setup: calibration and measurements

# Contents

## Contents

# 4.1 Introduction

In this chapter I present the characterization of the Caliste-MM detectors, and compare them to simulations. I insist on the behavior of the detector with the change of specific parameters such as the resistivity of the anode or the distance between the Caliste readout and the piggyback's ceramic. I also present results using the detector in various special conditions in order to get good polarimetric performances: change of readout electronics, change of gas (using neon and helium instead of argon) and change of the piggyback amplification gaps.

# 4.2 The Caliste-MM detector: standard characterizations

## 4.2.1 Gain curve

The new concept of detection, using a piggyback and a contactless readout electronics, is proved: with the Caliste-MM detector, I am able to detect photons and see on the electronics how they are converted into the detector. The behavior of the detector with the variation of the various parameters needs to be characterized.

The first characterization is about the gain of the detector, as it is a very important parameter for gaseous detectors. One of the tunable parameters that plays an important role on the gain is the amplification field. Fig. 4.1 shows the gain of the Caliste-MM detector as a function of the amplification field. The configuration for the detector is the following : argon-isobutane mixture in $95\% - 5\%$ proportions, a resistivity of the resistive layer of 100 M$\Omega/\square$ and the

Caliste readout at a distance of 500 $\mu$m from the ceramic. This distance has been chosen as it allows the largest dynamic range in terms of amplification field. At shorter distances the electronics saturate at field higher than 33.6 kV.cm$^{-1}$ which prevents a full characterization of the detector gain. Fig 4.1 also shows on the same graph the gain curve of the piggyback alone which has already been presented in fig. 3.3.
To make the gain curve of the Caliste-MM detector, I added the charge registered on each pixel of each event, even the part due to the diffusion of charges in the resistive layer. In fact, the gain represents the total signal recorded compared to the signal created by the photon (here, the $\approx 230$ primary electrons created by the 6 keV photon in the gas), and the signal created by the diffusion is a part of the total signal registered.
Fig. 4.2 shows a histogram obtained when summing the entire signal created on the Caliste electronics. The detected photons have an energy of 6 keV, the gas used is a mixture of argon-isobutane (95%-5%), the amplification field used is 38 kV.cm$^{-1}$, the resistivity of the resistive layer is 100 M$\Omega/\square$ and the distance between the Caliste and the ceramic is 500 $\mu$m. The main peak is fitted by a gaussian function. The error on the gain measurement is the $1\sigma$ error estimates of the mean. In fig. 4.2, the estimated gain by the fit is 2142, and the $1\sigma$ error estimates of the mean is 10.2. It is an error of less than 0.5%. The estimation of the gain is then very small and can be neglected. It is then not indicated in the figures about gain measurement.
The other errors on the gain come from the dispersion of the gain of the various piggybacks. At a fixed amplification field, the gain between piggybacks of the same characteristics can vary by 30% because of differences in the fabrication process. To study those errors in more detail I would have needed a high number of piggybacks and compare their gains under the same conditions. The time to order and receive piggybacks from CERN being quite long, I concentrated my efforts on testing the behavior of the detector with the various characteristics of the piggyback such as amplification gap or resistivity, and not on testing a large sample of piggybacks with the same characteristics. Hence I did not measure this error.

Fig. 4.1 shows that the behavior of the Caliste-MM detector is similar to the one of the piggyback alone, the gain curves being parallel. But the gain of the Caliste-MM detector is lower than the one of the piggyback alone. This is due to the attenuation caused

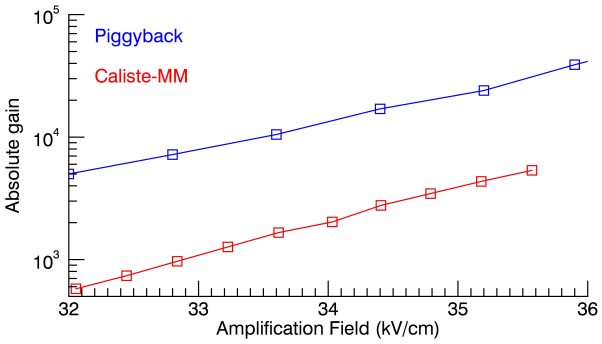


Figure 4.1: *Gain curve of the Caliste-MM detector (red) in a mixture of Ar - $iC_4H_{10}$ with the Caliste at 500 µm from the ceramic. It is the detectable charge, calculated by adding the signal created on each pixel of the Caliste readout. The blue curve is the gain of the piggyback only and is used to calculate the number of charges reaching the resistive anode. The behavior of the Caliste-MM detector is the same than the piggyback alone, but the signal is attenuated due to the design of outer and contactless electronics.*

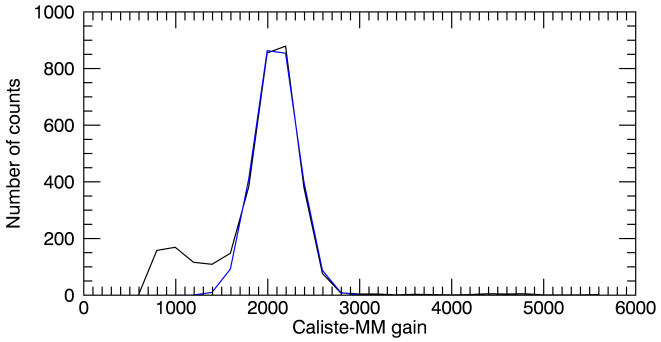


Figure 4.2: *Histogram of the values of the total signal recorded on the Caliste for each interaction of 6 keV photons. The gas used is a mixture of argon-isobutane (95%-5%), the amplification field used is 38 $kV.cm^{-1}$, the resistivity of the resistive layer is 100 MΩ/□ and the distance between the Caliste and the ceramic is 500 µm. The blue line is a gaussian fit of the main peak. The error bars indicated on the measured gain in the figures correspond to the 1σ error on the mean of the fit. Here, the estimate of the mean is 2142 and the 1σ error on this estimate is 10.2: it is an error of less than 0.5% on the estimate.*

by the ceramic and the air layer in the capacitive coupling of the Caliste and the Piggyback.
Fig. 4.3 presents the curve of the Caliste-MM gain as a function of the piggyback gain, for simulated and real data. The gain curve has been obtained by simulating events with the Infinitely Extended Resistive Layer Parallel to a Grounded Plate (IEPGP) model, for different amplification fields, giving different piggyback gains. For each amplification, the total signal simulated on the Caliste is taken and converted into number of charges. Taking the fraction between the number of charges simulated on the Caliste and the 236 electrons created by a 6 keV photon in argon gives the simulated gain. The deviation between the simulation and the measurement is of 24% maximum. At high piggyback gains, the deviation between the simulation and the measurement is less than 1%.

### 4.2.2 The influence of the air layer

In the Caliste-MM detector, the amplification field is not the only parameter to play an important role on the detector, as the distance between the Caliste and the electronics is also important. Fig. 4.4 shows the evolution of the gain of the Caliste-MM detector for distance varying from 200 $\mu$m to 1.7 mm, for an amplification field of 37.5 kV.cm$^{-1}$. The influence of the distance, and then of the thickness of the air layer left between the readout and the electronics, is very strong, as going from 500 $\mu$m to 1 mm reduces the gain by more than a factor of 2.
In the case of a varying distance, the number of charges created in the detector and diffusing in the anode layer does not change. The change of potential on the resistive layer is the same, but the capacitance coupling between the Caliste and the ceramic is lower. Hence the induced charge on the Caliste is lower. The strong variation of gain comes from the fact that the capacitive coupling varies strongly with the distance and is quickly lost.

This drop of gain with the distance between the ceramic and the readout electronics comes from the fact that changing this distance changes the surface capacitance seen by the charges when they diffuse in the resistive layer. Increasing the distance makes the charge diffuse faster. The electronics does not see the whole pulse developed on each pixel. Especially it does not see the maximum arriving on the pixels facing the center of the cloud charge and recover only the tail of the signal as shown in fig. 4.5. Hence, if the charges

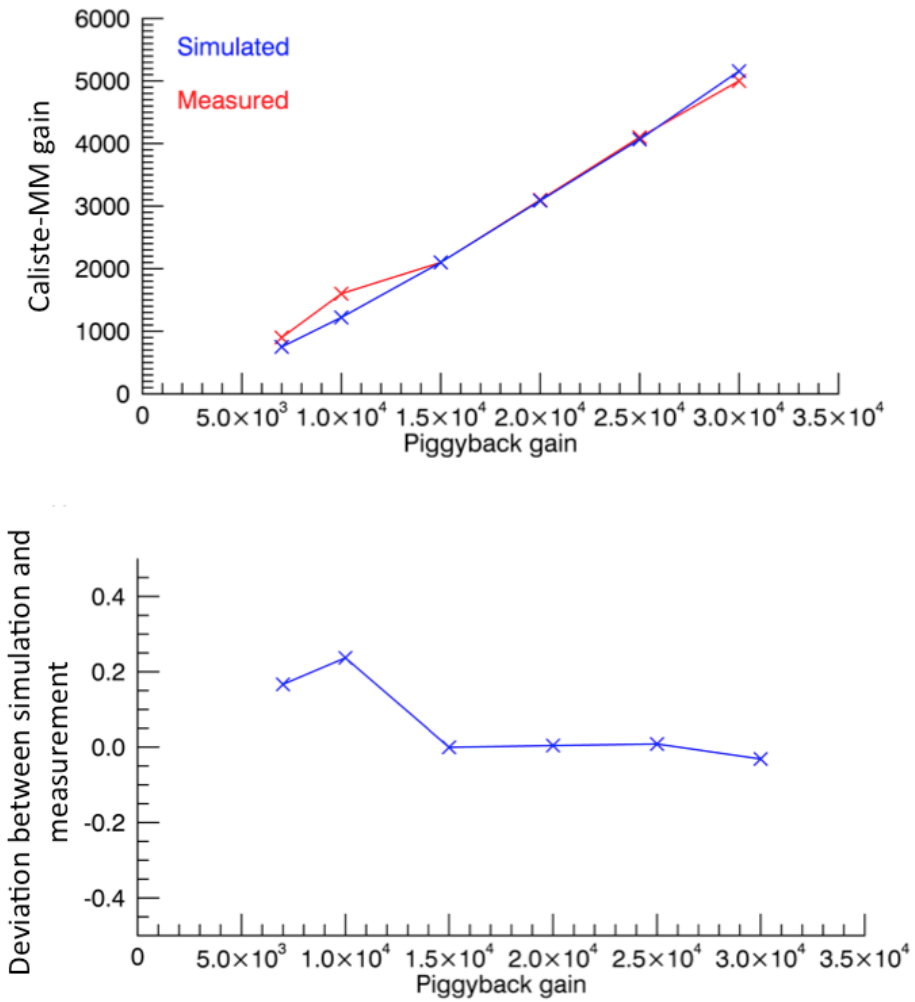


Figure 4.3: *Top: Gain of the Caliste-MM detector as a function of the piggyback gain. The red curve presents real measurements and the blue curve corresponds to analytical simulations coming from the infinitely extended resistive layer parallel to a grounded plate model. Bottom: deviation between the measurements and the model. At low piggyback gains the simulation deviates from the measurements up to 24%. At high piggyback gains the deviation between the simulation and the measurement is less than 1%.*

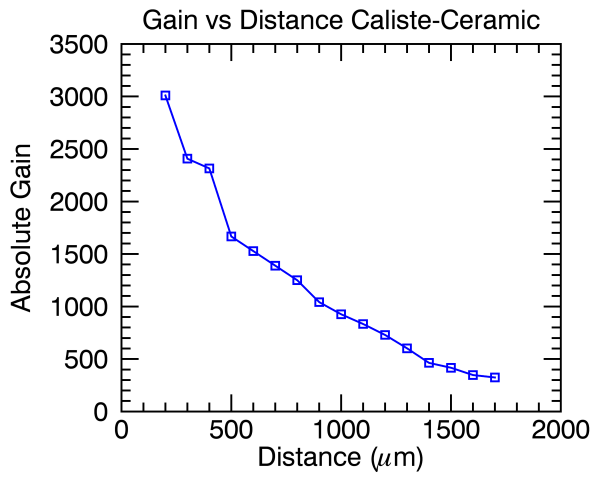


Figure 4.4: *Gain of the Caliste-MM detectors as a function of the distance separating the pixels of the Caliste and the ceramic of the piggyback. The influence of this distance is very strong as the gain drops quickly when the distance is increased, in a non linear way.*

spread faster, the recorded signal is lower.

### 4.2.3 The influence of the anode resistivity

Another parameter which influences the gain strongly is the resistivity of the anode layer. The resistivity influences the speed of the charges when diffusing in the resistive layer: if the resistivity is lower, the charges move faster. The signal developed on the pixel is faster, and if it is too fast the electronics is not able to record its maximum and will take only a fraction of it. The intensity of the signal registered will then be lower, even if the number of charges diffusing in the resistive layer is the same.
The shaping time of the electronics then plays an important role. But to be able to see those differences, the shaping time needs to be lower than the $\mu$s. For the Caliste readout, the shaping time ranges from 1 $\mu$s to 10 $\mu$s, and no change on the events shape was oberserved when this parameter varied. If the shaping time can be reduced down to few tens of ns, the rising time of 50 ns of the Charge Sensing Amplifier of each Caliste channel is another limitation.

Fig. 4.6 shows the variation plot of the gain of the Caliste-MM detectors for different resistivities of the anode layer: the top presents the gain curve for piggybacks using different resistive layers,

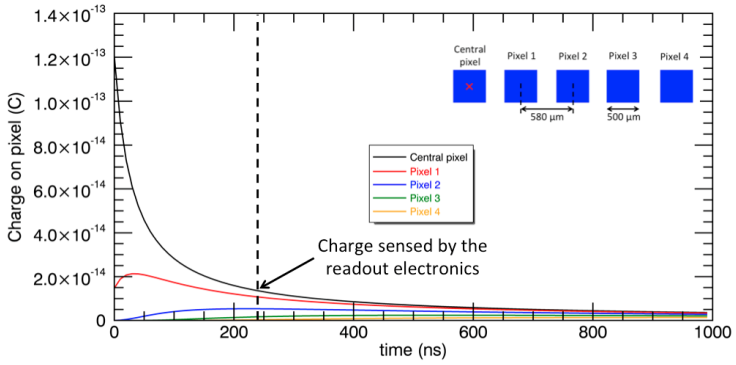


Figure 4.5: *Simulation of charge developed on pixels located at various distance from the center of the cloud charge. The piggyback gain is 8000, the distance between the Caliste and the ceramic is 500 µm, the resistivity of the resistive layer is 10 MΩ/□.*
*The beginning of the signal on the central pixels is developed too fast for the electronics to be recovered and only a part of it is taken into account. If the charges spread faster, the recorded signal is then lower. The value of 240 ns for the electronics to recover properly the signal has been found manually: using the signal developped only after 240 ns gave the best results in the simulation of events shape and gain. A proper estimation of this value would need a model more accurate than the IEPGP, and I did not have time to develop it.*

with a distance between the Caliste and the ceramic of 500 $\mu$m. The bottom is the variation of the gain with the resistivity, for a distance between the Caliste and the ceramic of 500 $\mu$m and an amplification field of 38 kV.cm$^{-1}$. The gain clearly drops when the resistivity is reduced.

This phenomenon is shown in fig. 4.7 which presents the simulated variation of the Caliste-MM gain with the resistivity of the anode layer. The simulation uses the IEPGP model in a mixture of argon-isobutane (95%-5%), with a fixed piggyback gain of 15000 and a distance between the Caliste and the ceramic of 500 $\mu$m. At each resistivity value, the gain is calculated in the same way than in fig. 4.3.

When the resistivity increases, the gain increases. To obtain a higher gain, it is then better to have a greater resistivity. However, the increase of the curve is very sharp for low values of the resistivity and almost flat at higher values. Trying to reach very high resistivity such as 400 M$\Omega/\square$ does not grant a much better gain. And if the gain is higher for high resistivity it is because of the slower evacuation of the charges in the resistive layer. Increasing the resistivity increases the evacuation time of the charges, and then reduces the flux that the detector can handle before facing pile-up events (2 different photons arriving in the detector, but being detected as one single event by the electronics). Choosing the resistivity then depends on the expected flux received and the gain aimed at. For our application a high rate is not needed, and to perform polarimetry a high gain is essential.

The value of 100 M$\Omega/\square$ for the resistivity that I used was appropriate in terms of gain, and presented the advantage of coming directly from a commercial paste that is spread by screen printing technique on the piggyback. The resistivity value is then precise. A resistivity of 200 M$\Omega/\square$ would have been better but CERN, which fabricates the piggyback detectors, did not have a commercial paste of 200 M$\Omega/\square$. This value could have been achieved by mixing paste of several resistivities, but it would have been an approximated value. And most of all, it would have been very hard to obtain 2 times the same value of resistivity, which is not ideal: if another piggyback is needed and its resistivity changes, all the characterizations have to be done again. For this reason I decided to keep the value of 100 M$\Omega/\square$ for the resistivity of the piggyback.

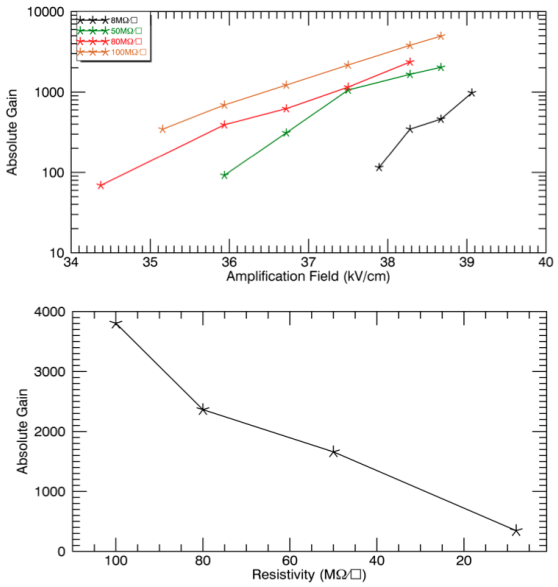


Figure 4.6: *Variation of the gain of the Caliste-MM detector with the resistivity of the anode layer. Top: gain curve of piggybacks using different resistivity, with a distance between the Caliste and the ceramic of 500 $\mu m$. Bottom: Variation of the gain with the resistivity of the piggyback, with a distance between the Caliste and the ceramic of 500 $\mu m$ and an amplification field of 38 $kV.cm^{-1}$. The gain drops when the resistivity is lowered, because the charges in the resistive layer move faster and the Caliste is not fast enough to recover the maximum of the developed signal on its pixels.*

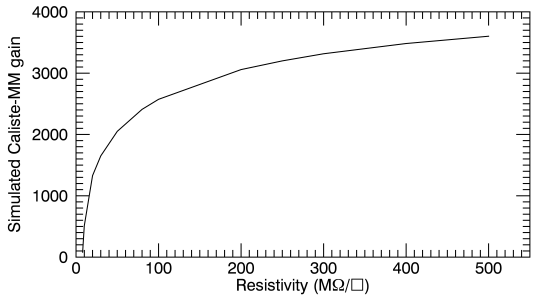


Figure 4.7: *Simulation of the variation of the Caliste-MM gain with the anode layer resistivity, a fixed distance of 500 $\mu$m between the Caliste and the ceramic and a piggyback gain of 6000. It shows the drop of the gain for low resistivity because of a faster diffusion of the charges.*
*The increase of the curve is very sharp for low resistivity, and almost flat at higher values.*

## 4.3 Optimizing events multiplicity

In this section I study the variation of the multiplicity, that is, of the number of selected pixels in an event after a threshold has been applied, as a function of a number of detector or beam parameters. There are two categories of parameters that can influence the multiplicity. The parameters which change the number of charges created, such as the energy of the detected photons or the amplification field. And the parameters which change the gain but not the number of charges created: the distance between the Caliste and the ceramic, and the resistivity.

### 4.3.1 Multiplicity dependence with amplification field

Fig. 4.8 shows a histogram of the event multiplicity for 6 keV photon detection in a mixture of argon-isobutane (95%-5%) with a distance between the Caliste and the ceramic of 500 $\mu$m, a resistivity of 100 M$\Omega/\square$ and an amplification field of 38 kV.cm$^{-1}$. The threshold on the pixels is fixed to 3600 electrons. Under this configuration of the Caliste-MM detector, a threshold of 3600 electrons on the pixels of the Caliste allows the detection of a photon of minimum 700 eV. The obtained histogram is fitted with a Gaussian profile. In the

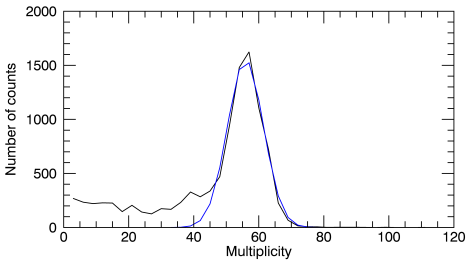


Figure 4.8: *Histogram of event multiplicity for 6 keV photon detection in a mixture of argon-isobutane (95%-5%) with a distance between the Caliste and the ceramic of 500 $\mu$m, a resistivity of 100 M$\Omega/\square$ and an amplification field of 38 kV.cm$^{-1}$. The blue line represents a gaussian fit performed on the histogram. The FWHM of this fit is used in the following figures to represent the repartition of the multiplicity around the mean value obtained by the gaussian fit. Here, the FWHM is equal to 16.2 pixels.*

following figures using multiplicity, the error bars used to represent the repartition of the multiplicity corresponds to the FWHM of the fitted Gaussian profile.
Fig. 4.9 shows typical 6 keV events registered on the electronics for various amplification fields, with a fixed distance between the Caliste and the ceramic of 500 $\mu$m. On the surface map it is possible to see the effect of the amplification field on the intensity of the signal. On the color map the change of the multiplicity of the events can be seen. This change of multiplicity is shown in fig. 4.10, which presents the variation of the mean multiplicity of the events as a function of the amplification field and of the variation of the Caliste-MM gain.

Showing curves using the Caliste-MM gain as variable is important, as when using a different piggyback for the photon conversion and amplification. Fig. 4.11 presents the gain variation of the Caliste-MM gain when using two different piggybacks, in the same conditions: argon-isobutane (95% - 5%), resistivity of 100 M$\Omega/\square$ , distance between the Caliste and the ceramic of 500 $\mu$m. The difference of the Caliste-MM gain is up to 50% at low amplification fields and around 30% at higher amplification fields. Hence using the gain instead of the amplification field to analyze the events is better.

This shows the importance of choosing a high amplification field:

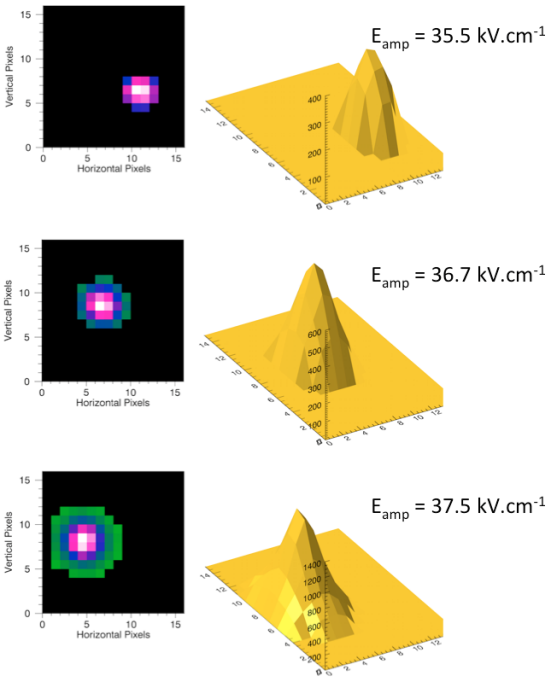


Figure 4.9: *Typical events registered by the Caliste electronics for a fixed threshold of 3600 electrons and a fixed distance of 500 µm between the Caliste and the ceramic when the amplification field is varied. The surface map allows to see the gain variation with the amplification field, which has been studied in fig. 4.1. The color map shows clearly the variation of the multiplicity with the amplification field. If the field is too low (event at the top of the figure), its reconstruction becomes harder.*

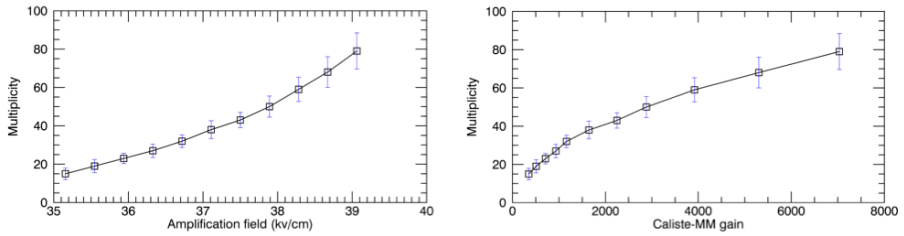


Figure 4.10: *Variation of the mean multiplicity of the events with the variation of the amplification field (left) and the variation of the Caliste-MM gain (right). The detected X-rays have an energy of 6 keV. The distance between the Caliste and the ceramic is 500 µm. The gas used is a mixture of argon-isobutane (95% - 5%) and the resistivity of the resistive layer is 100 MΩ/□. The multiplicity varies strongly with the amplification field, being multiplied by more than a factor 3 for small variations of the field. This is of importance as a high multiplicity goes with a better reconstruction and then a better spatial resolution, but a too high amplification field degrades the energy resolution. The amplification field has then to be chosen carefully depending on the application.*

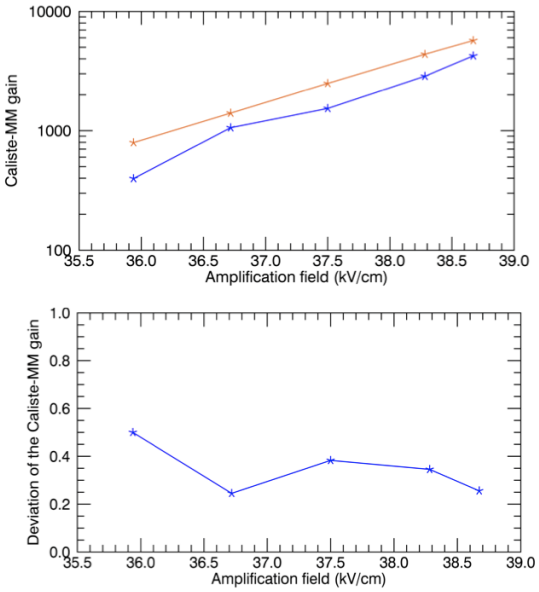


Figure 4.11: *Gain deviation of the Caliste-MM detector when two different piggybacks are used. The conditions of the measurements are: 6 keV photon detection in a mixture of argon-isobutane (95%-5%) with a distance between the Caliste and the ceramic of 500 µm and a resistivity of 100 MΩ/□. The deviation is up to 50% at low amplification fields, and around 30% at higher amplification fields.*

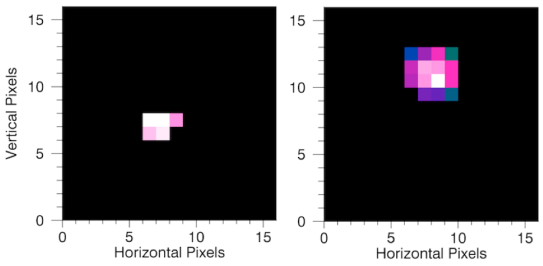


Figure 4.12: *Impact of the threshold value on the detection of 6 keV photons with the Caliste-MM detector. The gas used is a mixture of argon - isobutane (95%-5%), the distance between the Caliste electronics and the ceramic is 500 µm, the amplification field is 34.4 keV.cm$^{-1}$. Left: Threshold of 3600 electrons. Right: Threshold of 1440 electrons. The multiplicity is higher when a lower threshold is used.*

it is not just a matter of having a high gain, but also a matter of having a high multiplicity. Because a high multiplicity implies a better position reconstruction and so a better imaging capability. And to reconstruct the photoelectron's track, having a high multiplicity allows to use the transverse diffusion in the resistive layer to perform a better reconstruction of the track.

At low amplification field, it is possible to lower the threshold of the Caliste electronics. The minimum threshold to avoid triggering on the noise is 360 electrons. Fig. 4.12 shows the difference, at low amplification field, between a threshold of 3600 electrons and 1440 electrons. For a lower threshold, the multiplicity is higher, going from 2 to 15. For even lower amplification field, it is possible to detect events with a low threshold that are not detected with a threshold of 3600 electrons. This allows to detect events for Caliste-MM gain lower than 100. For gain higher than 100, the difference in the deposited energy on the Caliste-MM detector between the highest threshold of 3600 electrons and the minimum threshold of 360 electrons is of the order of 5%, and the size of events is increased by just one pixel in radius. Hence, because of this low difference, for standard measurements using high Caliste-MM gain I always use the threshold of 3600 electrons in order to reduce as much as possible the impact of the noise that can be created in the detector.

Unfortunately, a high multiplicity implies a higher acquiring time of the electronics, so a slower rate. In addition, a high multiplicity goes with a high amplification, which, as shown in fig. 3.3, can

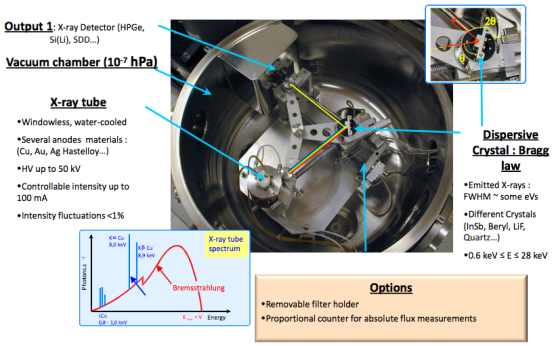


Figure 4.13: *The Solex facility. A wide range of X-ray energies are produced by an X-ray tube. The beam is reflected by a dispersive crystal. Thanks to Bragg law, the reflected beam is a monochromatic one, with an energy depending on the crystal used and of its orientation.*

degrade the energy resolution. This parameter is then a sensitive one and cannot simply be set at the maximum tolerated by the detector.

### 4.3.2 The Solex facility and multiplicity dependence with photons energy.

I had the opportunity to test the behavior of the Caliste-MM detector at different soft X-ray energies at the Solex facility [2, 3]. It uses a refracting or diffracting crystal to produce monochromatic soft X-ray beam from the Bremsstrahlung radiation of an X-ray tube. Thanks to the Bragg law, depending on the crystal used and the angle of incidence on the crystal, the output is a soft X-ray beam of monochromatic energy. The energies produced range from 0.6 keV to 28 keV, with a FWHM of few eV only. Fig. 4.13.

Fig. 4.14 the variation of the multiplicity for different photon energy. For this experiment I used a mixture of argon-ethane mixture (in proportion 90%-10%). This mixture is different from the classic argon-isobutane mixture (95% - 5%) because for this experiment I could only use a quencher from a short list of authorized gas in the facility, and isobutane was not among them. Among the list, ethane was the gas which allowed to reach the best possible gain, hence the choice. The detector is placed at a distance of 2 cm of the output of the beam. This air layer reduces the flux, but it was not possible to put the detector closer to the output because of its geometry. The

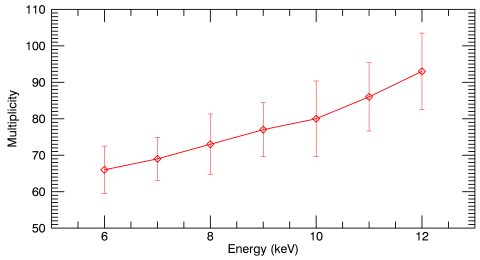


Figure 4.14: *Mean multiplicity of the registered events for various detected photons energy in a mixture of argon-ethane (90% - 10%), for a fixed distance between the Caliste and the ceramic of 500 $\mu$m, a resistivity of 100 M$\Omega/\square$ and an amplification field of 45 kV.cm$^{-1}$. The multiplicity changes quite strongly, because the number of primary electrons created by the ejected photoelectron is greater.*

distance between the Caliste and the ceramic was 500 $\mu$m, and the amplification field is 45.7 kV.cm$^{-1}$. The gain of a gaseous detector when using ethane as a quencher instead of isobutane is lower, which explains the higher amplification field used. In this mixture at this amplification field, the Caliste-MM gain is $2\times10^3$.
The multiplicity changes strongly with energy, and depending on the energy band of the detected light, the amplification field will have to be chosen carefully in order to have a high enough multiplicity for low energy photons, and this by still keeping a gain low enough in order to avoid sparks caused by photons of higher energy.

### 4.3.3 Multiplicity dependence with the thickness of the air layer

Fig. 4.15 shows typical 6 keV events registered by the Caliste electronics for a fixed amplification field when the distance between the Caliste and the ceramic is varied. Fig. 4.16 shows the variation of the mean multiplicity of the events for an amplification field of 35 kV.cm$^{-1}$ and a distance varying between 200 $\mu$m and 1600 $\mu$m. The decrease in multiplicity comes from the fact that the signal created by the diffusion on the pixels of the edge of an event eventually goes under the threshold when the distance increases. If the threshold of the pixels is lowered, the signal on the pixel on the edge can be recovered. Hence if a distance higher than 500 $\mu$m between the Caliste and the ceramic is needed in an application, lowering the threshold

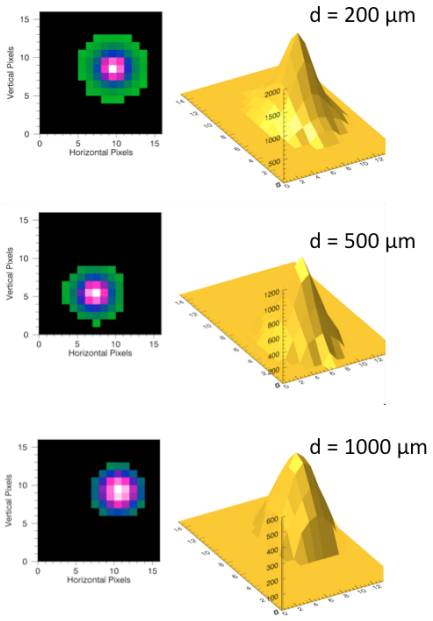


Figure 4.15: *Typical events registered on the Caliste electronics for an amplification field of 35 kV.cm$^{-1}$ and a varying distance between the Caliste and the ceramic. The multiplicity does not change significantly, while on the surface map it is clear that the gain drops when the distance increases, as shown in fig. 4.4*

.

of the pixels will allow to get a signal spread on several pixels and keep a good imaging capability. But it will not compensate the loss of gain observed in fig. 4.4.

Fig. 4.17 shows the evolution of the multiplicity of the detected events with the resistive layer. The conditions of the measurements are: mixture of argon-isobutane (95% - 5%), 6 keV photons, amplification field of 38.2 kV.cm$^{-1}$ and distance between the Caliste and the ceramic of 500 $\mu$m. The multiplicity goes down when the resistivity is lower. But the influence is not strong: for a resistivity of 8 MΩ/□ the mean multiplicity is 18 while for a resistivity of 100 MΩ/□ the mean multiplicity is 60. Multiplying the resistivity by 12.5 only multiplies the multiplicity by 3.

## 4.4 Energy resolution

### 4.4.1 Influence of the diffusion in the resistive layer

After the gain and the topology of the events, it is important to study the energy resolution of the Caliste-MM detector. There are several ways to treat the events: adding the signal of each pixels,

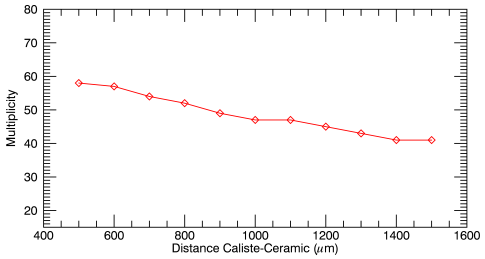


Figure 4.16: *Variation of the mean multiplicity of the events for a varying distance between the Caliste and the ceramic. The multiplicity changes but with way less significance than for a variation of the gain or the energy. Here, the number of charges created is not changed, and the variation of multiplicity happens when the signal caused by the diffusion on the pixels of the edge of the event goes under the pixel threshold: because this diffusion signal on the pixel of the edge of the event varies slowly with the distance (see chapter on simulation), the multiplicity varies slowly too.*

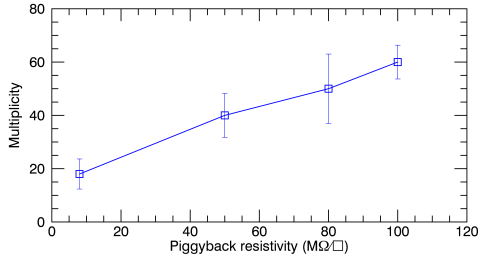


Figure 4.17: *Variation of the mean multiplicity of the events for a varying resistivity. When the resistivity increases, the size of the recorded events increases.*

taking only the maximum of the registered signal, fit the event by an adapted function and and take the maximum, the total or just a portion of the fit. Fig. 4.18 shows spectra obtained by the detector for 6 keV photons, for the exact same set of data, but with different ways to treat the signal. The conditions were: mixture of argon-isobutane (95%-5%), an amplification field of 38 kV.cm$^{-1}$, a distance between the Caliste and the ceramic of 500 $\mu$m and a resistivity of 100 M$\Omega/\square$.
The top image corresponds to the spectrum obtained by summing the signal registered on every pixel. For the two other spectra the signal has been fit by a 2D Gaussian function. The middle image is a spectrum obtained by taking simply the maximum of this fit. The bottom image is the spectrum obtained by fitting the events with a 2D Gaussian fit, and taking the signal contained inside the FWHM of the fit.

In every spectrum two peaks can be seen: the highest one in the main peak, the lowest one in the so called escape peak. The escape peak is due to the fluorescence events: a part of the energy of the incident photon is radiated as a photon with not enough energy to be detected, and then escape the detector. Only a fraction of the incident energy is then detected, which creates a second peak at lower energy. For 6 keV events in argon, the escape peak is located at 2.8 keV, and the main peak at 6 keV.

This escape peak is very helpful to see the effect of the data treatment that are used. The Caliste electronics has been calibrated, and it is linear with the energy. So without any treatment the signal created by the escape peak should have an energy equal to half the signal of the main peak. Fig. 4.18 shows that this is not always the case.

If the spectrum is obtained by summing the signal of every pixel (fig. 4.18, 1), the main peak has its mean at an energy more than twice the mean of the escape peak. This is due to the fact that by using the signal of every pixel, I include the diffusion inside the resistive layer, which means that the charges are counted more than once. For the escape events, there are less charges created, so the diffusion phenomena creates a less intense signal and the multiplicity of the event is lower. When summing the signal of all pixels, the influence of the diffusion will then be relatively low. For the main events which recover the missing energy thanks to the Auger electron, the diffusion phenomena generates a strong signal because of the higher number of charges diffusing in the resistive anode. If I

sum the signal of every pixel, the influence of this diffusion will be stronger than in the case of escape events. It results in a main peak having its mean at an energy higher than twice the mean energy of the escape events.

When taking only the maximum of the fit (fig. 4.18, 2), it is the reverse phenomena that happens. By taking only the maximum of the signal, the part due to the diffusion in the resistive layer is removed, but so is a part of the signal caused by the cloud of charges. For the escape events, the size of the cloud of charges reaching the anode is small, and by taking the maximum of the signal only a small part of the signal caused by the cloud of charges is lost. For the main events, the size of the cloud of charges is higher and by taking only the maximum of the signal a large part of the signal caused by the cloud of charges is lost. This results in a main peak having its mean at an energy less than twice the mean energy of the escape peak.

The spectrum fig. 4.18 (3) is done by fitting the event by a 2D Gaussian fit and taking the volume of the signal of the event contained in the FWHM of the fit. The FWHM of the fit depends on the multiplicity of the event, and then on the photon energy, amplification field, distance and resistivity of the Caliste-MM detector. By performing this kind of data analysis, the signal created only by the diffusion inside the resistive layer is partly removed, while all the signal created by the cloud of charges reaching the anode is taken into account. Building a spectrum with this method then gives a main peak at a mean energy twice larger than the mean energy of the escape peak.

This proves the strong influence of the diffusion phenomenon, which should be taken into account when building an energy spectrum. The methods used and their advantages are sumarized in tab.4.1 When building an energy spectrum I will always use the last method: taking the part of the signal only caused by the cloud of charges reaching the anode. It happens that this is the method which also gives the best results in term of energy resolution.

### 4.4.2 Background reduction with events topology

To reduce the background in the detector, it is possible to use the topology of the event. It allows to discard only partially detected

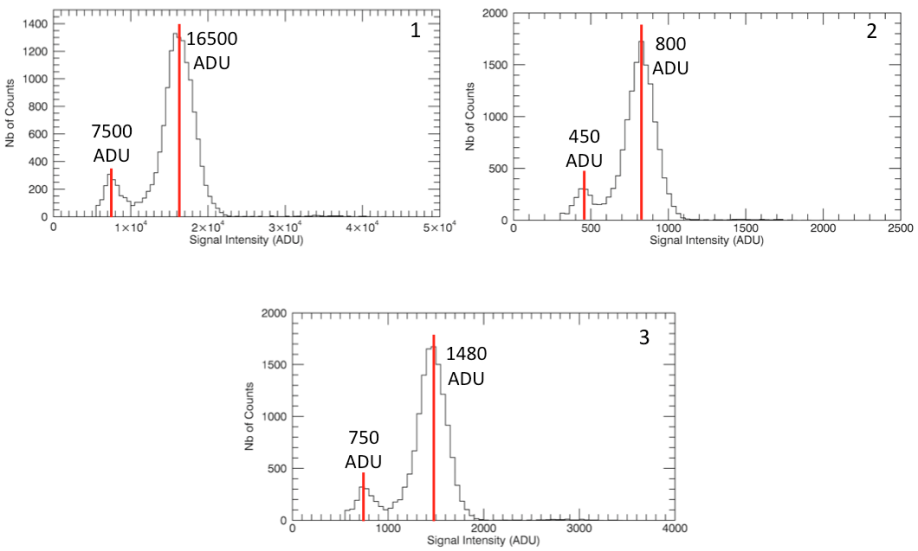


Figure 4.18: *Energy spectrum for 6 keV photons. The conditions were: mixture of argon-isobutane (95%-5%), an amplification field of 38 kV.cm$^{-1}$, a distance between the Caliste and the ceramic of 500 $\mu$m and a resistivity of 100 M$\Omega/\square$.*
*The spectrum are performed in 3 different manners. 1: the signal of every pixels is summed. The diffusion in the resistive is taken into account, meaning that the charges are counted more than once. It results in a main peak at a mean energy more than twice the energy of the escape peak.*
*2: each event is fit by a 2D gaussian function, and the spectrum is done by taking the maximum of the fit. The diffusion in the resistive is removed, but a part of the signal caused by the cloud of charges reaching the anode is lost. This results in a main peak at a mean energy less than twice the mean energy of the escape peak.*
*3: each event is fit by a 2D gaussian function, and only the signal contained under the FWHM of the fit is taken. It results in a main peak at a mean energy twice higher than the mean energy of the escape peak, as it should be when looking at 6 keV events (the escape peak being at 3 keV).*

| Method used | Advantage | Disadvantage |
|---|---|---|
| Summing signal of each pixel | Used for gain calculation | Some charges are counted twice because of the diffusion in the resistive layer |
| Taking the maximum of the signal | | Signal partly lost Lower energy resolution |
| 2D gaussian fit | Signal of diffusion partly removed Best energy resolution | Longer treatment time |
| Summing signal in the volume under FWHM | | |

Table 4.1: *The treatment methods used and their advantages.*

events, cosmic rays events, electronic noise which switched on a small number of pixels, etc... By a simple criterion on the multiplicity, the noise can be reduced to negligeable levels. Fig. 4.19 shows the difference in the noise when putting different trigger on the multiplicity (greater than 0, greater than 20, greater than 45 and greater than 55). The measurements have been performed using 6 keV photons converted in a mixture of argon-ethane (in a proportion of 90% - 10%). This is the same gaseous mixture used for the Solex experiment as I performed this analysis on the data taken at Solex. The Caliste-MM gain is equal to 2230 and the distance between the Caliste and the ceramic is 500 $\mu$m. With a trigger on the multiplicity, it is possible to even isolate the main peak from the escape peak, without using any other criterion. Knowing the incident energy, the amplification field and the distance between the Caliste readout and the ceramic, it is possible to estimate the multiplicity of the events and put a simple trigger to get the best possible spectrum.

### 4.4.3 Variation of the energy resolution with the amplification field

The energy resolution being a fundamental parameter, it is important to understand how it changes with the amplification field. Fig. 4.20 shows the variation of the energy resolution at 6 keV with the amplification field, for a distance between the Caliste and the ceramic of 500 $\mu$m and using a gaseous mixture of argon-isobutane in proportions of 95%-5%. This distance has been chosen in order

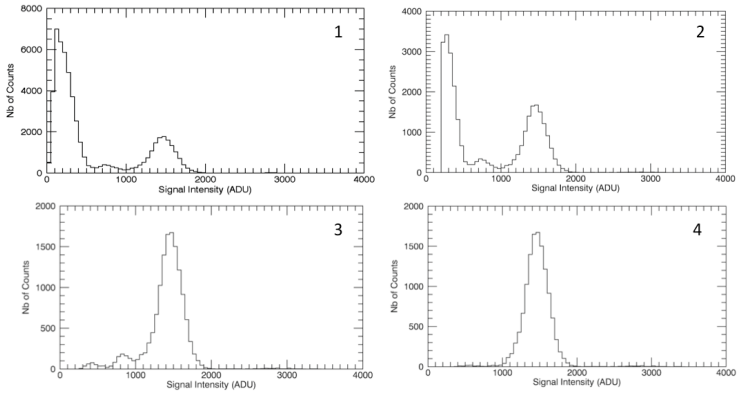


Figure 4.19: *Spectrum obtained on the same set of data than fig. 4.18, with different triggers on the multiplicity. The noise comes from partly registered events. 1: no trigger at all, the noise is very important. 2: spectrum for events of multiplicity greater than 20: the noise is reduced but is still here. 3: spectrum for events of multiplicity greater than 45: the noise almost disappeared. 4: spectrum for events of multiplicity greater than 55: the noise completely disappeared, so did the escape peak. This is very convenient to treat the main peak and estimate the energy resolution.*

to be able to vary the amplification field in a relatively wide range before reaching the saturation of the electronics, by still being able to recover signal created when a low amplification field is used.
The behavior of the Caliste-MM detector is the same than the behavior of the piggyback alone for the signal read on the mesh (as presented in fig. 3.3). There is an optimal amplification field that allows to reach the best energy resolution of the detector. This best energy resolution depends on the gaseous mixture used and on the piggyback itself, as from one detector to another a high difference in energy resolution can be observed, depending on the quality of the fabrication process.

### 4.4.4 Best energy resolution and perspectives for improvement

Fig. 4.21 shows a spectrum obtained on the Caliste-MM detector. The measurements has been performed in a mixture of argon-isobutane (95%-5%), a distance between the Caliste and the ceramic of 500 $\mu$m, a resistivity of 100 M$\Omega/\square$ and a Caliste-MM gain of 2500. This spectrum exhibits a resolution of 17% FWHM at 6 keV. This

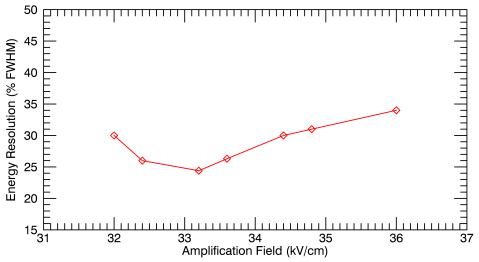


Figure 4.20: *Energy resolution of the Caliste-MM detector as a function of the amplification field for 6 keV photons, in argon-isobutane (95%-5%) with the Caliste at 500 µm from the ceramic. The resolution is expressed in % Full Width Half Maximum. The behavior is similar to the one presented in fig. 3.3: there is an amplification field which is optimum for the energy resolution. This parameter is then to be chosen carefully in order to get the best energy resolution by still having a gain high enough for the signal to be red by the Caliste through the ceramic.*

is the expected resolution when using the bulk technology. It means that using a resistive anode with a readout electronics outside the gaseous medium reading the signal through an air layer and a ceramic, does not degrade the energy resolution. Or at least in such a detector the energy resolution is not limited by the use of a piggyback.

If a better energy resolution is needed, it is necessary to change the gaseous part of the Caliste-MM detector. A possibility is to change the woven mesh into a flat mesh. It improves the electric field lines around the holes of the mesh and allows a better passing of the electrons through it. It also guarantees a better uniformity in the size of the amplification gap, which means a more uniform amplification and then a better overall energy resolution.
This idea of using a flat mesh has been used with the previously mentioned microbulk detectors, which could reach an energy resolution of 11% FWHM at 6 keV. In a microbulk detector, the starting piece is a polyimide foil with a thin copper layer on each side. The copper is chemically etched on both side, one side to form the mesh and the other side to form the anode. As the piggyback detectors use a resistive layer as the anode, spread on a ceramic plate, the process cannot be adapted for the piggyback detectors.
The other solution is to use a thin and flat electroformed mesh to

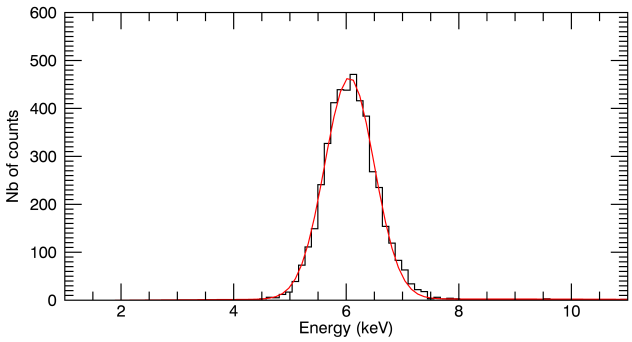


Figure 4.21: *Spectrum performed with the Caliste-MM detector, for 6 keV photons in a gaseous mixture of argon-isobutane (95%-5%) with a distance between the Caliste and the ceramic of 500 µm. The escape peak has been filtered out thanks to a multiplicity triggered as shown in fig. 4.19. The red curve corresponds to the gaussian fit performed on the data. The spectrum exhibits an energy resolution of 17% FWHM at 6 keV, as expected when using the bulk technology. The new concept of detection of the Caliste-MM detector does not degrade the energy resolution, which is ideal to perform spectrometry.*

replace the classical woven mesh. But this goes with higher costs and more fragile detectors because of the fragility of the electroformed mesh. However it is a way to improve the spectrometry that should be kept in mind for further improvements of the Caliste-MM detector.

## 4.5 Towards polarimetry

### 4.5.1 The problem in argon based mixtures

To perform polarimetry, it is necessary to recover the ejection direction of the photoelectron, and then to recover the track (or at least the beginning of the track) left by the the photoelectron through ionization of the atoms of the gas. And in an argon based mixture the events registered like in fig. 4.22 are almost symmetrical, and recovering the photoelectron's track is impossible. This is because of the very short range of the photoelectron's in argon: a 6 keV photon creates through photoelectric effect a K-shell photoelectron of

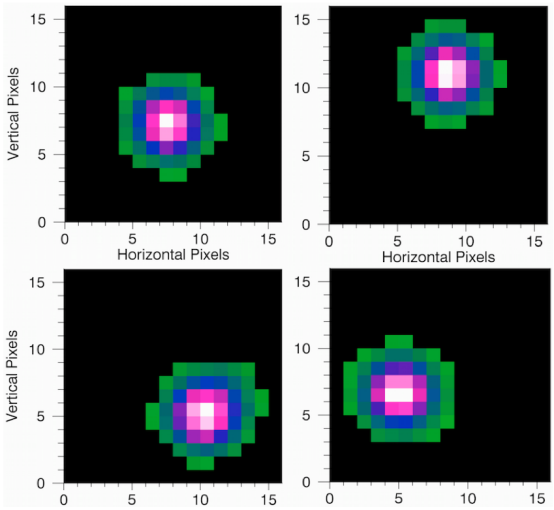


Figure 4.22: *Events registered in the Caliste-MM detector in an argon based mixture.*

2.8 keV as 3.2 keV are necessary to eject the photoelectron. And a 2.8 keV electron in argon has a mean freepath of 500 $\mu$m. It means that in the best case of ejection with a polar angle of 90 degrees and without multiple scattering, which would make the photoelectrons change their direction, the length of the track left by the photoelectron is of the order of 500 $\mu$m. The pixels of the Caliste having a pitch of 580 $\mu$m, the track is then impossible to recover and the detected events are symmetrical. Polarimetry cannot be performed in this configuration.

### 4.5.2 Results with helium based mixtures

Fortunately, several things can be done to get a polarimetric capacity. The first idea is to change the gaseous mixture used, and to replace argon by another gas such as helium. Fig. 4.23 presents 6 keV events in a mixture of helium-$CO_2$ (in proportion 95% - 5%) recorded by the Caliste electronics. The events are not symmetric anymore, allowing a partial reconstruction of the photoelectron's track. On the events presented, the maximum of deposited energy (the white part of the event) corresponds to the Bragg peak and therefore corresponds to the end of the track. The beginning of the track, which is the part I am interested in, has a lower intensity and is then harder to recover and reconstruct. The signal created by the

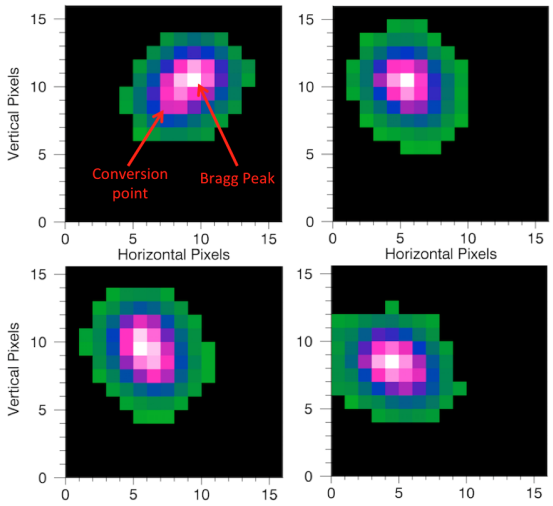


Figure 4.23: *6 keV events in a helium based mixture recorded by the Caliste-MM detector. The events are not symmetric as they were in fig. 4.22, and it becomes feasible to reconstruct the photoelectron's track and perform polarimetry. The region with the more intense signal (white pixels) corresponds to the Bragg peak and is the end of the track. The beginning of the track is less intense and harder to recognize.*

diffusion in the resistive layer has to be filtered out, but can help for the reconstruction as it increases the dissymmetry of the event. The various reconstruction methods that can be used will be detailed in the next chapter of this thesis.

6 keV photons in helium create a non symmetric signal recorded on the pixels, but recovering a track events such as those presented in fig. 4.23 is very hard as the track is still to short to see the ejection direction of the photoelectron. When I increase the energy of the incoming photons, the tracks become longer and reconstruction possible. Fig. 4.24 and 4.25 present events recorded by the Caliste-MM detector in a helium based gaseous mixture, for incoming photons of energy of 8 keV, 10 keV, 12 keV and 15 keV in the Soleil synchrotron facility. When the energy increases, the tracks become larger and the ejection direction is clearly visible. The reconstruction of the track is easier and polarimetry can be performed.

By increasing the energy of the incoming photon, I prove the polarimetric capacity of the Caliste-MM detector: photoelectrons

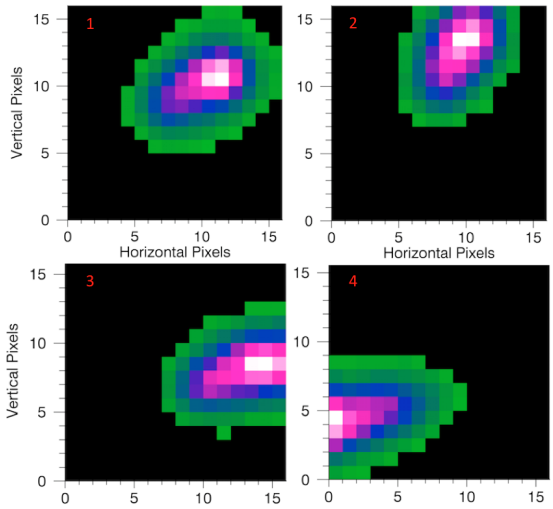


Figure 4.24: *Events recorded in the Caliste-MM detector for incoming photons of 8 keV (1 and 2) and 10 keV (3 and 4). The tracks are larger than the one created by 6 keV photons (fig. 4.23) and polarimetry is easier to perform.*

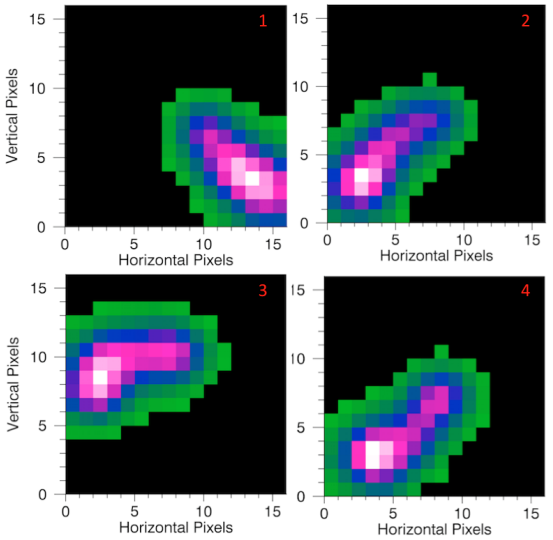


Figure 4.25: *Events recorded in the Caliste-MM detector for incoming photons of 12 keV (1 and 2) and 15 keV (3 and 4). The tracks are larger than the one recorded for 8 keV and 10 keV photons (fig. 4.24) and polarimetry can be performed nicely.*

tracks can be recorded in the detector and can be reconstructed. But increasing the energy too much presents several problems. First, as the energy increases, the Compton effect becomes more probable than the photoelectric effect. Fig. 4.26 presents the cross section of the photoelectric and the Compton effect in helium for energies from 1 keV to 20 keV. At 10 keV, the cross sections are already equally important, and when the energy increases the Compton effect becomes predominant, and the way to perform polarimetry changes (Cf Chap.1).

As shown on fig. 4.25, for high energy the tracks become very long, and quite a large fraction of it is not contained in the Caliste readout plane. This is not important when trying to perform polarimetry as I am only interested in the beginning of the track. But it is a critical point when trying to perform spectroscopy, as most of the energy information is contained in the Bragg peak at the end of the track. If the Bragg peak is out of the readout field of view, the energy information is lost. This is where the 3D architecture of the Caliste readout shows another advantage. In fact, the Caliste has been designed to be surrounded by other Caliste in order to build a matrix of several Caliste readouts and increase widely the field of view. Having large tracks is then not a problem as it is possible to increase the field of view without changing anything else on the detector, thanks to the Caliste-MM concept of non-coupled readout electronics. This is a part of the future improvements that has to be done on the Caliste-MM detectors.

Finally, the detector is supposed to be sensitive in the whole soft X-ray range, including 6 keV as it is the K-$\alpha$ ray of iron and is very interesting for the study of black holes as explained in chapter 1. Being sensitive to perform polarimetry at 6 keV is then a critical point.

### 4.5.3 The interest of a readout with smaller pixels

Even in helium, with the classical configuration of Caliste-MM does not allow to perform polarimetry with 6 keV photons, or at least to perform it efficiently because the ejection direction of the photoelectron on events like those in fig. 4.23 . One solution to overcome this problem is to change the readout electronics and use one with smaller pixels. This has been done and the Caliste has been replaced by the $D^2R_1$ electronics, presented in fig. 4.27. Like the Caliste elec-

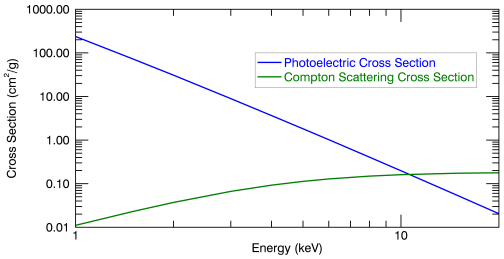


Figure 4.26: *Cross section of the photoelectric and the Compton effect in helium. At 10 keV, the cross sections are equivalent. When the energy increases, the Compton effect becomes largely the predominant effect.*

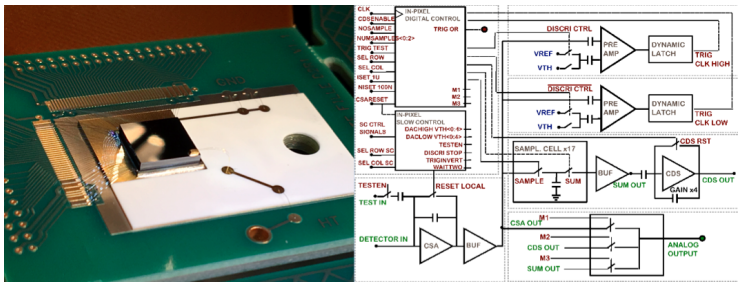


Figure 4.27: *$D^2R_1$ electronics [4]. Right: the electronics with a CdTe crystal on it. Right: one pixel block diagram. An incoming signal is converted into voltage by the Charge Sensing Preamplifier, and the output values of the CSA are sampled. The sampled output of the CSA are averaged before and after an event detection, and the difference of those two values represent the signal height of the detected event.*

tronics, the $D^2R_1$ electronics has been developed at CEA initially for semiconductor detectors [4]. The working principle of the $D^2R_1$ electronics is different than the Caliste's one. The signal arriving on each pixel is converted into voltage by a Charge Sensing Amplifier and a Multi Correlated Double Sampling is performed: the output of the CSA are sampled. The samples of the CSA output are averaged before and after an event detection and the difference of those two values gives the signal height of the detected event.

The important point relevant for this study is the smaller of size of the pixels of the $D^2R_1$ electronics. $D^2R_1$'s pixels have a pitch

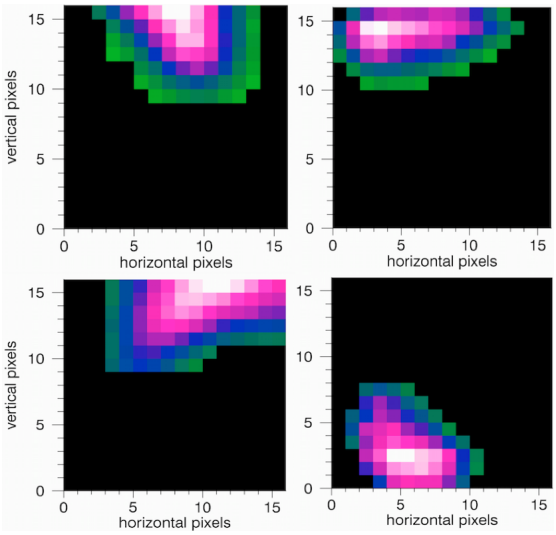


Figure 4.28: *6 keV events in a helium based mixture recorded by the $D^2R_1$-MM detector. The track left by the photoelectron is clearly visible and can be treated in a way more efficient way than the 6 keV tracks registered by the Caliste-MM detectors shown in fig. 4.23.*

of 300 $\mu$m, making them 4 times smaller in area than the Caliste's ones.

Thanks to the concept of non-integrated electronics of the Caliste-MM detector, it has been easy to change the Caliste to the $D^2R_1$ readout. This version of the detector, called $D^2R_1$-MM detector, has been tested with 6 keV photons and a helium-isobutane mixture (90% - 10%). Fig. 4.28 presents some events that are registered by the $D^2R_1$-MM detector. The tracks are more visible than the one recorded by the Caliste-MM detector in fig. 4.23. It must be kept in mind that the tracks are not larger: they are the same than those on fig. 4.23. Because the pixels of the $D^2R_1$ readout are 4 times smaller the spatial resolution is better, and the tracks can be reconstructed in a more efficient manner.

This test proves two things: it is possible to perform polarimetry nicely in the detector if the pixels are smaller. Moreover the concept of non integrated and contactless electronics works perfectly. In fact replacing the Caliste electronics with the $D^2R_1$ electronics was simple. It allows to think of a more adapted electronics for the experiment without thinking on its integration on the detector.

### 4.5.4 The drawbacks of using helium

Performing polarimetry with the Caliste-MM detector seems then possible using a helium based mixture. However, the use of helium has several problems. First it is a not suitable gas for spectrometry, as its Fano factor is high compared to the one of argon: 0.29 for helium when using in proportion 90%-10% with a quencher, compared to 0.177 for argon in the same condition [5]. It is also very transparent to soft X-rays: for 6 keV photons crossing 5 mm of gas the absorption is lower than 1‰. This adding to the predominancy of Compton scattering over the photoelectric effect makes helium a very unadapted gas for our purpose. Finally, the helium is an extremely light gas: this is an advantage for the length of the tracks, but the drawback is that it is extremely hard to contain. This is not a problem when the detector is used for characterization in a laboratory, but it can be a complication when sending the detector to space.

### 4.5.5 Use of neon based mixture in low pressure conditions an spectro-polarimetry measurements

Helium allowed to prove the polarimetric capacity of the detector, but is not a long term solution. In order to obtain longer tracks, there are different options: to use a neon based mixture or an argon based mixture, at low pressure. When lowering the pressure, the amplification field dynamic allowing to reach a high gain before entering the discharge region is smaller. Because of the low pressure of the gas, the avalanche will be larger (in size) and a spark between the anode and the mesh can happen for low amplification field. This reduces drastically the gain that can be reached before entering the discharge region of the piggyback. A compromise must then be found between a low enough pressure to be able to recover the photoelectrons tracks and a high enough pressure to be able to reach a proper amplification and read the signal on the electronics.

With standard piggybacks of amplification gap of 128 $\mu$m and resistivity of 100 M$\Omega/\square$ this has not been possible, as for a pressure low enough to get a visible track on the Caliste (less then 250 mbar) the amplification was to low to recover the track. But with a neon based mixture it has been possible. Fig. 4.29 presents some events registered by the Caliste electronics when using a neon based

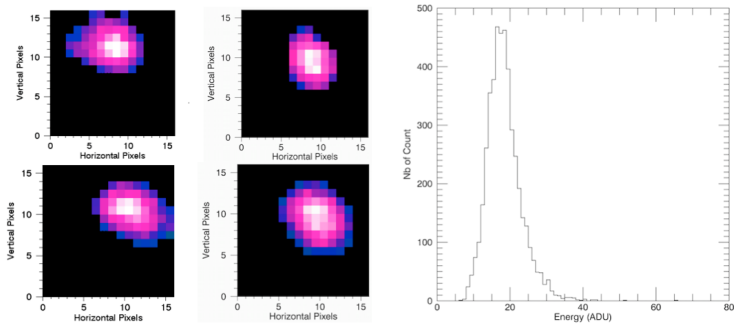


Figure 4.29: *Left: 6 keV events in a neon based mixture. The tracks are less visible than in helium, but given a proper reconstruction algorithm they can be reconstructed, and polarimetry can be performed. Right: energy spectrum. The energy resolution is of 30% FWHM at 6 keV. It is the first time that spectrometry and polarimetry can be performed on the same set of soft X-ray events.*

mixture (neon-ethane-$CF_4$) at a pressure of 375 mbar with 6 keV events. The gain is low and the tracks are less clear than the one in fig. 4.24 or fig. 4.25, but 6 keV events are visible.

Furthermore, it is possible to perform a spectroscopic measurements on those events. The spectrum obtained is presented in fig. 4.29 (right) and exhibits an energy resolution of 30% FWHM at 6 keV. This energy resolution is not very attractive. But this spectrum has been obtained from the tracks of fig. 4.29. It means that, given an optimized reconstruction algorithm, it is possible to perform spectro-polarimetry with the Caliste-MM detector. Even if the results can be improved, it is still the first time that soft X-ray spectrometry and polarimetry can be performed in the same gaseous mixture.

A way to improve the gain of the detector when used in low pressure condition is to use a piggyback with larger amplification gap. In fact, with a larger amplification gap, it will be possible to reach a higher gain before entering the discharge region, as the avalanche can be developed on a larger path before sparks happen. fig. 4.30 shows the gain obtained by the Caliste-MM detector when using amplification gap of 128 $\mu$m (standard value), 196 $\mu$m and 254 $\mu$m. The gas used is argon-isobutane (95%-5%), the resistivity is 100 M$\Omega/\square$, the distance between the Caliste and the ceramic is 500 $\mu$m. Attempts have been made to build piggybacks with 512 $\mu$m amplification gap but the fabrication process was not adapted

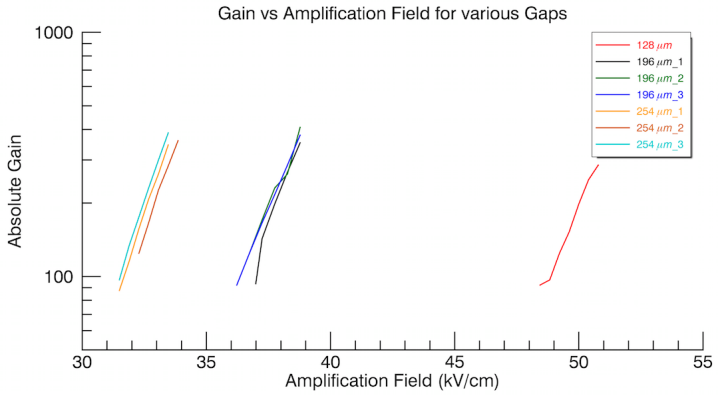


Figure 4.30: *Gain curve for the Caliste-MM detector using piggybacks with different amplification gap. For gap as high as 254 µm, it is possible to reach a high gain at lower amplification field as the avalanche is developed on a larger path.*

and the uniformity of the gap was extremely bad, degrading the energy resolution. With the various gaps used, it is possible to recover the same gain as with standard gap piggybacks, and this for lower amplification fields as the avalanche can be developed on a larger path. Tests using piggyback with larger amplification gap in a neon base mixture in low pressure conditions have yet to be performed but represent a promising axis of improvement of the Caliste-MM detector if coupled with the use of smaller pixels.

### 4.5.6 The use of a mixture of two noble gases

One way to improve the detector would be to use helium, but to add a small fraction (around 10%) of a heavy noble gas in it such as argon, krypton or xenon. The cross-section of the photoelectric effect with those gases is way larger than the one of helium. Fig. 4.31 presents the cross section of the photoelectric effect for the different noble gases (data from the NIST database [4]). In the soft X-ray energy band (from 1 to 20 keV) the cross-section of helium can be $10^6$ times lower than the one of argon or xenon. So even if added in a very small proportion, they would increase the efficiency of the gas by an important factor. But thanks to the large proportion of helium, the gaseous medium will still be light enough to let the photoelectron recoil. It would recoil less than when using only helium, mainly because the energy of the photoelectron would be that of the

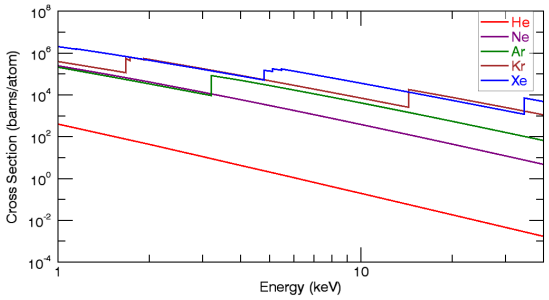


Figure 4.31: *Total photoelectric cross section in various noble gases [4]. The one of helium is way lower than the one of argon, krypton or xenon (fact which is responsible of the differences between the absorption coefficients presented in the previous chapter).*

incident photon minus the energy needed for the K-shell ionization of argon (or L-shell ionization of Xenon) which is around 3 keV. So smaller pixels would still be needed, but combined with this it could be a good track toward spectro-polarimetric measurements, and tests have to be performed in the future.

## 4.6 The need of a 100% polarized source

In term of polarimetry, several improvement directions have been found. In particular, the concept of using new electronics with smaller pixels, or reducing the pressure of the gas used to obtain longer tracks have been proven. But before going further it is possible to estimate the polarimetric capacity of the present version of the detector. To perform this, using helium is enough as it allows to recover the photoelectron's track. From data in helium, it is possible to develop various reconstruction methods that will help to recover the polarimetry of the signal. To do this, it is necessary to detect the signal from a 100% polarized source. A radioactive source such as the $^{55}$Fe source used in laboratory is not polarized, so it is necessary to bring the detector to a synchrotron facility which produces a signal naturally 100% polarized.
The reconstruction algorithms and the results obtained in the Soleil synchrotron facility are the topic of the next chapter of this manuscript.

## 4.7 Summary

The Caliste-MM detector has been fully characterized and its behavior with the different parameters (resistivity, distance, amplification field, ...) studied in depth. The behavior of the Caliste-MM detector in term of gain and multiplicity variations has been compared to the simulations using the infinitely extended resistive layer parallel to a grounded plate.

Performing polarimetry requires to use a helium based mixtures, which allows to recover properly the various photoelectrons' tracks. Other ways to improve the polarimetric capacity have been studied: using a readout electronics with smaller pixels or using a neon based gaseous mixture in low pressure conditions. Both concepts have been proven and a measurement of spectro-polarimetry on the same set of data has been performed.

Before going into further development, it is necessary to measure the polarimetric capacity of the Caliste-MM detector. To do this, the detector has to be brought in a synchrotron facility. The next chapter will present the experiment made with the Caliste-MM detector at the Soleil synchrotron facility, and the polarimetry results obtained.

# Bibliography


[1] http://www-hep.phys.saga-u.ac.jp/ILC-TPC/gas/

[2] C. Bonnelle, et al., *SOLEX : a tunable monochromatic X-ray source in the 1-20 keV energy range for metrology.* Nuclear Instruments and Methods In Physics Research A, **516** (2004), 594-601

[3] Y. Menesguen, *SOLEX: a comprehensive tool for X-ray detectors characterization*, 6e Conférence internationale sur les nouveaux développements en photodétection, (NDIP 2011), Lyon, France, 4-8 juillet 2011.

[4] A. Michalowska, *Studies and development of a readout ASIC for pixelated CdTe detectors for space applications*, PhD., Université Paris Sud - Paris XI, 2013

[5] S.F Biagi, D. Duxbury and E. Gabathuler, *Experimental results from a microdot detector overcoated with a semiconducting layer*, Nuclear Instruments and Methods In Physics Research A, **419**, 438-443 (1998), 594-601

[6] http://physics.nist.gov/cgi-bin/Xcom/xcom2

# Chapter 5

# Polarimetry measurements

# Contents

## Contents

## 5.1 Introduction

This chapter presents the polarimetry measurements performed with the Caliste-MM detector at the Soleil synchrotron facility. The Soleil facility and the Caliste-MM integration with the beam are presented with the various parameters of the experiment. Various events are presented to exhibit the difference between the photoelectric events and the Compton events. Then the reconstruction method to recover the ejection angle of the photoelectron is explained, and the modulation factors measured in various conditions are presented.

## 5.2 The Soleil synchrotron facility

In order to characterize the Caliste-MM detector as a polarimeter, it is important to measure its modulation factor, as explained in Chapter 1. To do this, a 100% polarized source is needed. For soft X-rays the best possible 100% polarized source is the light produced by a synchrotron beam.

The Caliste-MM detector has been installed at the Soleil synchrotron facility located at Saclay in France. Fig.5.1 shows the main building of the facility, where the synchrotron accelerator is located, and fig.5.2 [1] presents the working principle of the Soleil facility.
First, a beam of electrons is created and the electrons are accelerated up to 100 MeV by a Linear Accelerator. The electrons are then directed into a circular accelerator called Booster, where they are brought to their nominal energy of 2.75 GeV. Next the electrons are injected into a storage ring of 354 m of circumference.
At various places of the storage ring, dipoles (bending magnets), undulators or wigglers are placed in order to deviate or make undulate the electrons trajectory. This change of trajectory, which corresponds to an accelerated motion of the electrons, is accompanied by an emission of energy under the form of radiation called synchrotron light. This light is guided toward several light lines where the different experiments can be performed.

I brought the Caliste-MM detector to the light line called Metrologie [2]. The synchrotron light of this line is produced by a bending magnet, and can have a monochromatic energy between 100 eV and 40 keV. The size of the beam can range between few hundreds of micrometers and several millimeters. The flux produced is of few $10^9$ photons/s/mm$^2$. The beam is also 100% linearly polarized at each energy, which makes it perfectly suitable for the calibration of

Figure 5.1: *The Soleil Synchrotron Facility. The electron's accelerator is located inside the circular building.*

the Caliste-MM detector as a polarimeter.

## 5.3 The Caliste-MM setup at the Soleil facility

### 5.3.1 Experimental parameters

The Soleil synchrotron, and more specifically the Metrologie beam line, suits the requirements needed to evaluate the polarimetric capabilities of the Caliste-MM detector. Thus I installed the detector at the Metrologie beamline in order to perform the measurements needed. The detector was installed at the output of the beamline on a moving platform allowing x-y-z shifts with a micrometric precision as can be seen in fig. 5.3. The distance between the detector and the beamline was of 20 cm. This distance is big and most of the beam is absorbed in the air layer between the output and the entrance window of the detector. But it is not a problem thanks to the very high flux of the beam.
The gas used was a mixture of helium-i$C_4H_{10}$ (90% - 10%). The use of an helium-based mixture allows to get photoelectron's tracks long enough to be reconstructed. The drawback is a low efficiency. The distance between the Caliste readout and the ceramic was of 200 $\mu$m, the voltage on the mesh of 140 V and the voltage on the resistive layer of 660 V, creating an amplification field of 40.5 kV.cm$^{-1}$ for a gain of about $3\times10^3$.

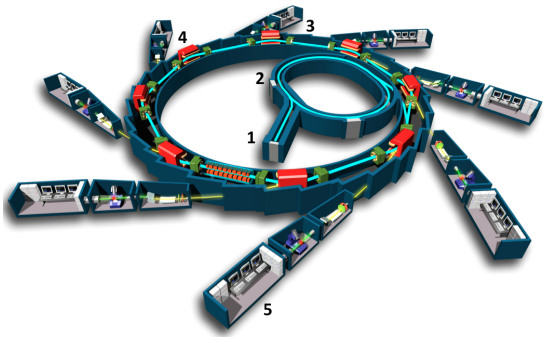


Figure 5.2: *The Soleil synchrotron scheme. 1) Electrons are created and accelerated by a linear accelerator up to 100 MeV. 2) The electrons directed into the Booster (circular accelerator) are accelerated to reach their nominal energy of 2.75 GeV. 3) The electrons are injected into a storage ring where they turn for several hours. 4) Several magnetic devices are located on the storage ring. There are bending magnets, undulators or wigglers, which will deviate or make oscillate the electrons so that they can produce the synchrotron light. 5) The synchrotron light is sent into various light lines, where the experiments take place.*

The size of the beam spot was controlled in order to deliver a high flux, but low enough to be supported by the detector. In fact, the charges must have enough time to be evacuated from the resistive layer, and the electronics must have enough time to read the signal, shape it and be ready for the next occurring event. Depending on the energy, the size of the beam had to be changed, but it was always of the order of magnitude of a rectangle of 14 $\mu$m length and 10 $\mu$m width. This very small size of spot ensures that the detected photons are those from the center of the beam, where the light is 100% polarized: the light coming from the edges of the beam may have a lower degree of polarization because of its interaction with the optical devices that bring the light in the beam line. It also ensures that the location of the photon interaction in the detector is perfectly known.

### 5.3.2 Run conditions

I took data at energies of 6 keV, 8 keV, 10 keV and 12 keV, and this for two different orientations of the detector: flat as in fig.5.3,

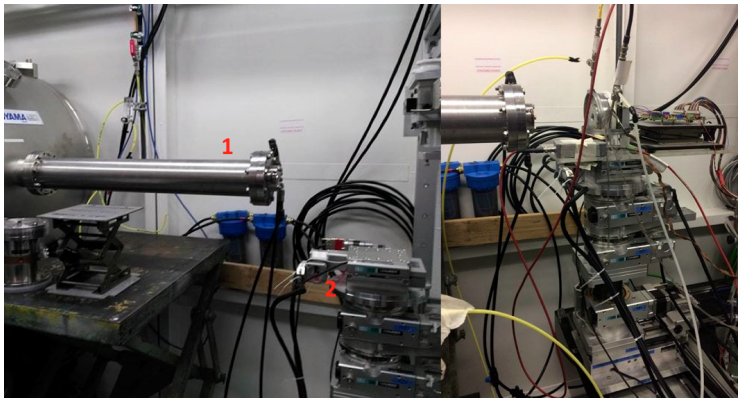


Figure 5.3: *Left: the output of the Metrology line. 1) Beam output. 2) 3D moving platform. The detector is fixed on this platform and can be perfectly centered with the output beam. Right: The Caliste-MM detector at the Soleil facility.*

and rotated by an estimated angle of $50^o$. These two orientations will allow the comparison between the polarimetric data. The two histograms of the ejection directions of the photoelectrons should both exhibit a sinus square structure as explained in the first chapter, but with the peaks and valleys shifted by the amount of the tilted angle. This will ensure that the result is not dominated by systematic effects.

## 5.4 Data analysis and Compton treatment

### 5.4.1 The photoelectric and Compton events

The photoelectric events in helium exhibit the shape of fig.5.4. It is their reconstruction which allows to perform polarimetry measurements. But they are not the only events that occur in the gas. In helium from energies greater than 6 keV the Compton effects become more probable and at 10 keV its probability is equal to the probability of the photoelectric interaction, as shown in fig. 5.5).

Performing polarimetry using Compton events is possible in theory with a gaseous detector, and the method used would be similar to the one used by semiconductor experiments, such as in [3]. But this method implies to be very precise on the measurement of the energy of the scattered photon. In fact, the polarization of the

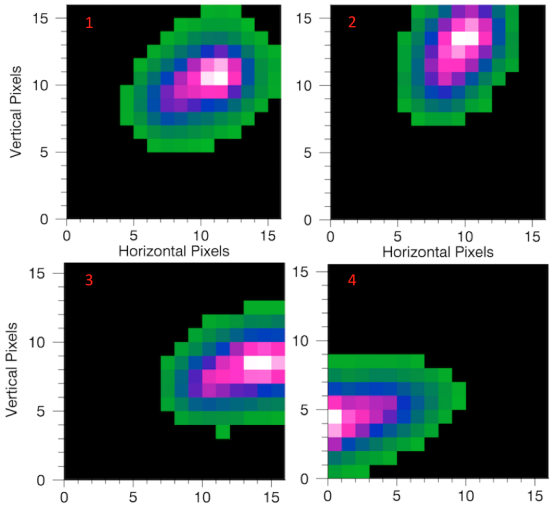


Figure 5.4: *Events recorded in the Caliste-MM detector for incoming photons of 8 keV (1 and 2) and 10 keV (3 and 4).*

detected light can be measured on Compton events where the secondary photon has been ejected with a high polar angle, as shown in fig.5.6. If the polar angle of the scattered photon, or its energy, as the polar angle and the energy of the scattered photon are linked, is not measured precisely, and performing polarimetry becomes very hard. And in the current configuration, the Caliste-MM detector is not suited to perform such a measurement as its energy resolution when using helium is of the order of 35%.
On top of that, to perform proper polarimetric measurement it is necessary to use only the Compton events with a scattered photon of high polar angle, and the scattered photon have to be absorbed in helium. Those conditions are rarely met, and using Compton events to perform polarimetry with the Caliste-MM detector is then inefficient. The Compton events have then to be discarded, even if they represent a non negligible part of the registered events.

### 5.4.2 The various Compton possibilities

The Compton events can take several shapes, which are presented in fig.5.8, depending on the various scenarii. The scheme of the Compton effect is recalled in fig.5.7. The Compton effect involves two photoelectrons: the first will be detected very close from the impact point of the beam, the second will be further. Depending on the splitting of the energy between the photoelectrons, several cases

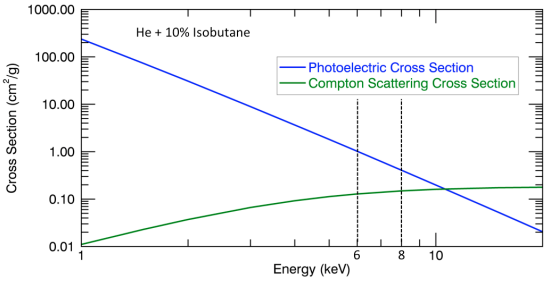


Figure 5.5: *Cross section of photoelectric and Compton effects in a gaseous mixture of helium and isobutane (in proportions of 90% - 10%). The photoelectric effect is the dominant one up to energies of 10 keV, but the Compton effect still have a high influence, especially at 8 keV. This reduces the efficiency as the detector has not been optimized to perform polarimetry on Compton events.*

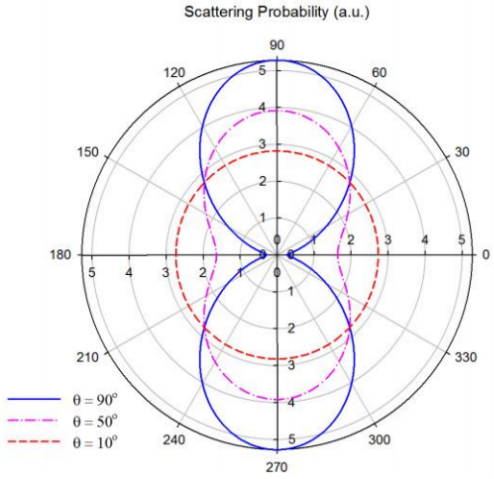


Figure 5.6: *Azimuthal scattering probability for the scattered photon of a Compton event for an incoming light polarized at a direction of 0°. Depending on the polar angle θ of the scattered photon, the probability changes. It makes it very hard to perform polarimetry measurements on Compton events if we can't measure precisely the polar angle of the scattered photon (or its energy as they are directly linked). The Caliste-MM detector is not suited to perform polarimetry on Compton events.*

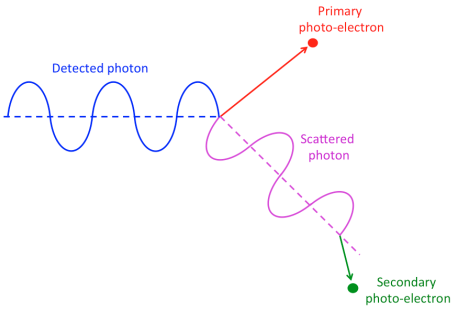


Figure 5.7: *Scheme of the Compton effect. It implies two photons: the incoming and the scattered one; and two photoelectrons. Depending on the escaping of the scattered photon, and on the detection of one or two of the photoelectrons, the registered events will have a different shape.*

can appear. If the secondary photoelectron escapes the detector, only the first will be detected. If the first photoelectron has a low energy, it is possible that it is not detected and only the secondary photoelectron is measured, far from the impact point of the beam. Or both photoelectrons can be detected.

The image at the bottom right of fig.5.8 presents a specific case that can be observed in the Caliste-MM detector. In this case, only the secondary photoelectron is observed. But this photoelectron had enough energy and had been ejected in a polar angle which made it leave a track very similar to a track left by the classic photoelectric effect. If we have no knowledge of the impact point of the beam, such an event will be impossible to differentiate from a photoelectric effect. Fortunately, they are very rare (because of all the conditions that have to be met in order for them to happen) and would participate weakly to the background.

Fig.5.9 presents another problem of the Compton effect: the difficulty to distinguish it with short photoelectric effect, even when the impact point is known. In the events presented it is impossible to know if it corresponds to a photoelectric effect which left a short track, to a Compton effect where only the first photoelectron has been detected, or even to a Compton effect where only the secondary photoelectron has been detected. Because of this uncertainty, those events have to be rejected.

### 5.4.3 The impact of Compton effect on efficiency

Most of the Compton events can be discarded by topology and spectrometry (in case of low energy deposition or double detection, such as in fig.5.8 Top and Bottom Left), and the other events are rare

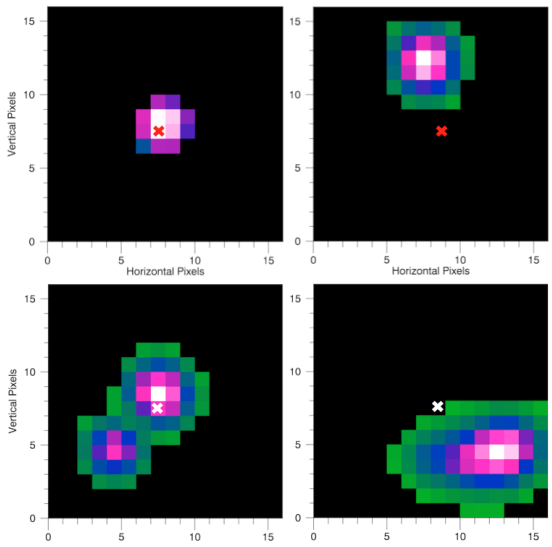


Figure 5.8: *Various type of Compton events registered in the detector. The crosses indicate the impact point of the beam. Top Left: Only the first photoelectron is detected, the secondary photon escaped the detector. Top Right: Compton event happening somewhere else than in the gas, for instance on the mesh or on the entrance window. The first photo electron escaped the detector, and only the secondary photoelectron is detected. Bottom Left: the first and secondary photoelectrons are detected. Bottom Right: The first photoelectron has not been detected (like in event Top Right), the secondary photoelectron has been ejected in a direction parallel to the readout plane and left a track. This track looks closely to a classic track left after a photoelectric effect and has not to be mistaken with it.*

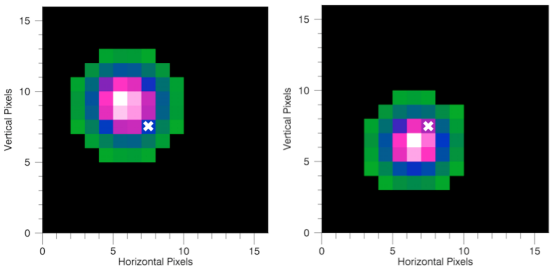


Figure 5.9: *Events recorded in the Caliste-MM detector. It is hard to say if they correspond to a short photoelectric event, or to a Compton event where only the first photoelectron has been recorded and left a short track while the secondary photoelectron escaped the detector.*

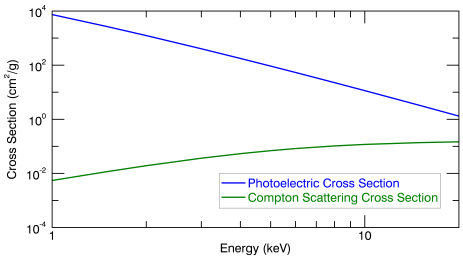


Figure 5.10: *Photoelectric and Compton cross section in neon. In the soft X-range, the Photoelectric effect is more than 100 times more probable than the Compton effect. Neon appears to be the good gas to reduce the impact of the Compton effect.*

enough to be confused with photoelectric events without strong consequences on the polarimetry measurement. The main problem from the Compton events come from the fact that it reduces by almost half the efficiency of the detector (which is already quite inefficient because of the transparency of helium at the considered energy).

A solution, as mentioned in the previous chapter, would be to use neon in low pressure conditions, as the Compton effect is much lower in it. Fig.5.10 presents the photoelectric and the Compton cross section in neon. At 10 keV, the photoelectric effect is still around 100 times more probable than the Compton effect.
The other solution could be to add a small proportion of argon or xenon, in which the Compton effect at the energies aimed at are almost inexistent. The drawback is that for those gases, the ionization potential are high: 3.2 keV for the argon K-shell, and 5.4 keV for the xenon L shell. When trying to detect 6 keV photons (which is the aimed energy to perform black holes spin study as explained in chapter 1), the resulting photoelectron will have an energy of around 3 keV if we use argon, and 600 eV if you use xenon. Even if the main component of the mixture is helium, the photoelectrons tracks will be short because of their low energy, and this is not a solution in the current configuration of the detector as smaller pixels would be needed.

### 5.4.4 The use of Compton events

Despite the problems mentioned before, the Compton events still present a major advantage: as they happen often, with the increased

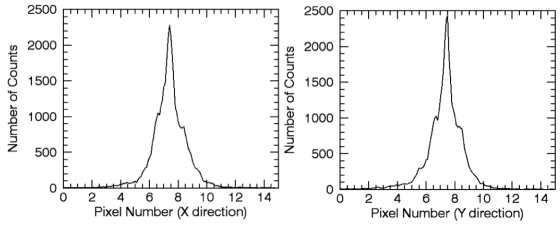


Figure 5.11: *The histogram of the two coordinates of the registered position of the Compton events. The bin used is of 0.1 pixel. A peak is clearly visible and allows to measure the position of the incoming beam with a precision of 60 $\mu m$.*

probability of ejecting the photoelectron at low polar angles $\theta$, they can help to measure with a subpixel resolution the position of the beam.

The procedure to select the Compton events as the one in fig. 5.8 is the following. First only events with a multiplicity lower than 25 are selected. I fit each event by a 2D gaussian fit. The fit estimates the main axis of the event. It estimates the standard deviation in the main axis direction of the fit and in the perpendicular axis. If the event is round the standard deviations have similar values. If it is elliptic these parameters have values sensitively different. If the deviation between these standard deviations is lower than 10% the event is selected.
The two coordinates of the position of the centroid of the fit are recovered. Then I make a histogram of the recovered position for each coordinate, and I obtain the curve presented in fig.5.11. The bin used is 0.1 pixel pitch (less than 60 $\mu$m), and the peak is still extremely clear. The position of this peak gives the position of the beam with a much better resolution than a pixel.

## 5.5 Reconstruction at 8 keV of a photoelectron track

The reconstruction method used consists in several steps, presented in fig.5.12. At first I filter the Compton events to keep only the photoelectric events. Then the effect of the diffusion in the resistive layer is partly removed, until the total of the energy left is equal to 70% of the initial value. This value has been chosen as it is the one which gives the best polarimetry results. Then the Bragg peak is

cut, in order to leave only the beginning of the track. I calculate the weighted barycenter of this beginning of track. This barycenter is expected to be on the trajectory followed by the photoelectron. I know with a precision of 50 $\mu$m the impact point of the beam, so the starting position of the photoelectron. The line linking the starting position of the photoelectron and the barycenter of the track's beginning is a good approximation of the 2D projection of the ejection direction of the photoelectrons. By recovering the angle of this line with respect to a fixed reference axis, I obtain an estimate of the azimuthal angle of this ejection direction.

Fig.5.13 shows the result of this reconstruction method on several tracks. It is efficient for all kind of tracks, straight or bent because of multiple scattering.

## 5.6 Polarimetry results at 8 keV

### 5.6.1 Modulation curve

The photoelectric events are reconstructed with the method explained before, and from the reconstructed ejection direction the various azimuthal ejection angles are recovered. Fig.5.14 shows the histogram of the reconstructed azimuthal angle for a 8 keV run with an estimated orientation of $50^o$. The red curve is the fitted function A + B$\times\cos^2(\phi$-$\phi_0)$, with A, B and $\phi_0$ free parameters representing respectively the offset, the amplitude and the polarization direction. The error bars are the statistical errors $\sqrt{n}$, where $n$ is the number of counts in each bin.

As the incoming source is 100% polarized, from the parameters of the fit it is possible to calculate the modulation factor of the detector $\mu = \frac{B}{2A+B}$ (see first chapter). It gives a modulation factor $\mu = 92\%$. This factor is extremely high, despite the relatively big size of pixels used. This is due to the diffusion inside the resistive layer: it spreads the signal over several pixels, which helps to reconstruct the barycenter of the beginning of the track in a more efficient way and gives a high precision on the reconstruction.

### 5.6.2 The algorithm efficiency

To get the curve obtained in fig.5.14, only long tracks have been taken into account. By long track I mean that the maximal length edge to edge is greater than 7.5 pixels. Those tracks need to have a

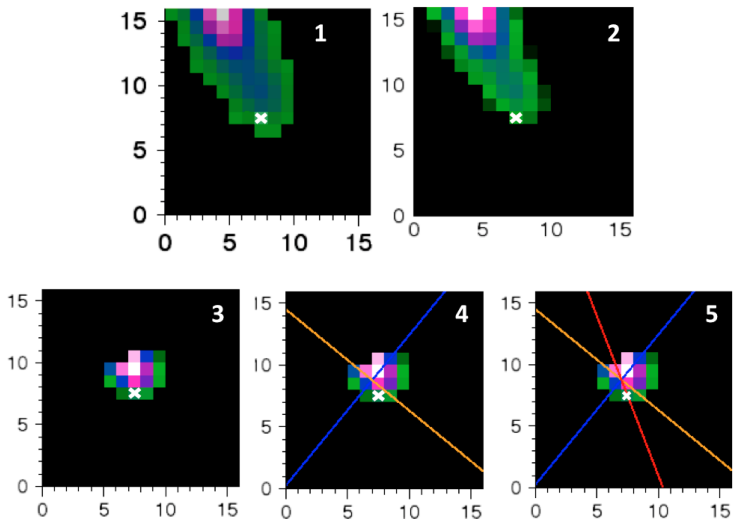


Figure 5.12: *The reconstruction method used. The cross shows the impact point of the beam.*
*1) The photoelectric tracks are filtered from the Compton events.*
*2) The effect of the diffusion inside the resistive layer is partly removed by a simple threshold, until the energy of the remaining event is lower than 70% of the total energy. This value has been chosen experimentally as it is the one which gives the best results in term of energy resolution.*
*3) The Bragg peak is cut until 30% of the energy of the track after step 2 is left. This value has been chosen experimentally to provide the best results.*
*4) I calculate the barycenter of this beginning of track. The position of the barycenter is given by the intersection of the two lines seen on the picture.*
*5) The red line is the line passing by the impact point and the barycenter of the beginning of the track. It corresponds to the projection of the ejection direction of the photoelectron.*

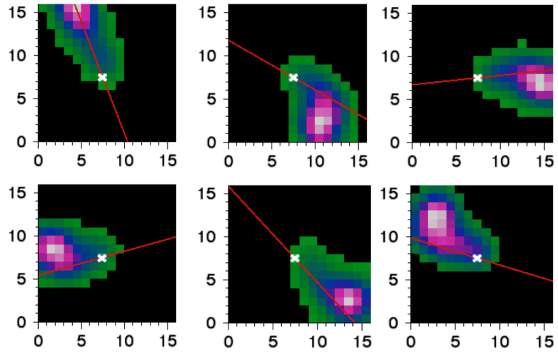

Figure 5.13: *The reconstruction method performed on several tracks. It shows its efficiency, no matter if the track is a straight line or if it turns at the end due to multiple scattering of the photoelectron.*

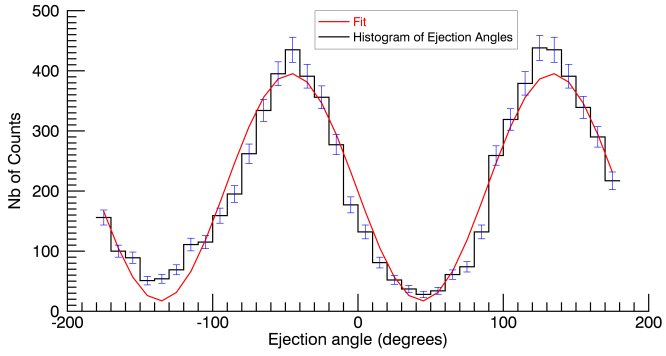


Figure 5.14: *Histogram of the reconstructed azimuthal ejection direction, and the fitted function $A + B \times cos^2(\phi\text{-}\phi_0)$ corresponding to the theoretical distribution. The modulation factor calculated from the parameters of the fit gives $\mu$=92%. These are the best results obtained with the Caliste-MM detector.*

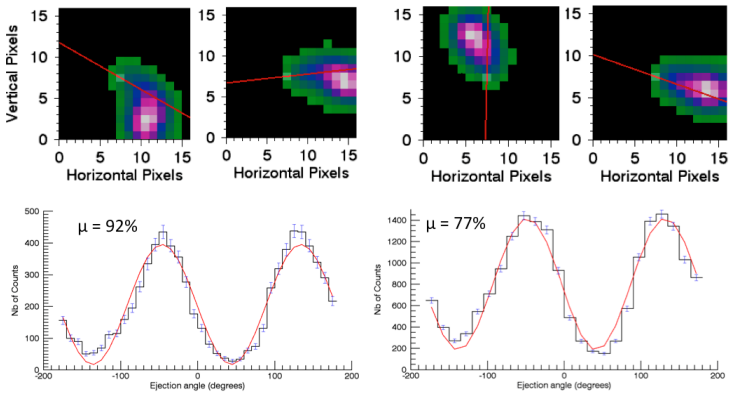


Figure 5.15: *Modulation curves obtained when various track lengths are accepted. Left: track of a minimum length of 7.5 pixels from the impact point. Right: track of a minimum length of 6.5 pixels from the impact point. When the accepted tracks get shorter, the modulation factor reduces.*

photoelectric effect produced with a polar angle of $90^o$. Moreover, the multiple scattering experienced by the electron has to be in the plane parallel to the readout place. Those events are quite rare and make the detector less efficient.

Fig.5.15 and 5.16 show the shortest tracks accepted with the estimated ejection direction and the modulation curve obtained when running the reconstruction on those tracks. As shown, when the tracks get shorter their reconstruction becomes less clear even by eye. And because of the large size of pixels the reconstruction of the ejection direction is less precise. This is responsible for the drop of the modulation factor $\mu$: when accepting tracks 2 pixels shorter (around 1 mm shorter), the modulation factor goes from $\mu = 92\%$ to $\mu = 57\%$. It still satisfies the requirements of a medium-class science space mission of $\mu = 30\%$. But a higher modulation factor allows a better Minimum Detectable Polarization with a lower number of photons.

Fig.5.17 shows an example of tracks that are too short to be reconstructed properly and the modulation curve obtained when taking them into account. The modulation factor drops down to 45% which is still acceptable, but the fitting of the curve A + B $\cos^2(\phi\text{-}\phi_0)$ is not good anymore, which proves that there are some systematic errors that I do not understand yet. I strongly suspect that they come from the fact that the impact point of the beam is measured precisely, but not perfectly. This error in the measurement

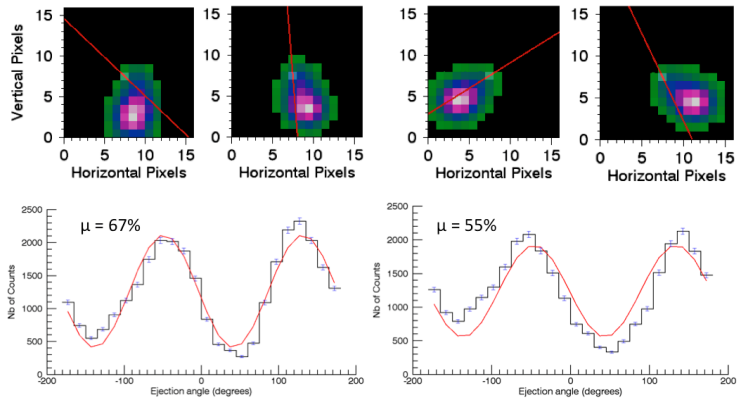


Figure 5.16: *Modulation curves obtained when various track lengths are accepted. Left: track of a minimum length of 6 pixels from the impact point. Right: track of a minimum length of 5.5 pixels from the impact point. When the accepted tracks get shorter, the modulation factor reduces and goes down to 55%.*

has a very small effect on large tracks but becomes important when the tracks are shorter, and might be responsible of this less good fitting.

Fig.5.18 shows the variation of the measured modulation factor for different accepted track lengths. Because of the more imprecise reconstruction on shorter tracks, the modulation factor drops when the accepted tracks get shorter. Fig. 5.19 shows how varies the ratio of reconstructed events with the various filters compared to the total number of track. The reconstruction which gives the best modulation factor unfortunately rejects a large number of tracks. This is understandable, as in order to be properly reconstructed the tracks have to be ejected with a polar angle $\theta$ close to $90^o$ and have to experience almost no multiple scattering which reduces the size of the track in the anode plane. Those events are then quite rare but their reconstruction is the most efficient.

An important parameter of a polarimeter is the quality factor $Q = \mu\sqrt{\epsilon}$ where $\epsilon$ is the efficiency of the detector. To calculate the efficiency I first estimate an efficiency of detection of photons of 1% in the mixture of helium-isobutane. I multiply this efficiency with the efficiency of the reconstruction algorithm presented in fig. 5.19. Fig.5.20 presents the value of the quality factor of the detector for various track length accepted in the reconstruction.

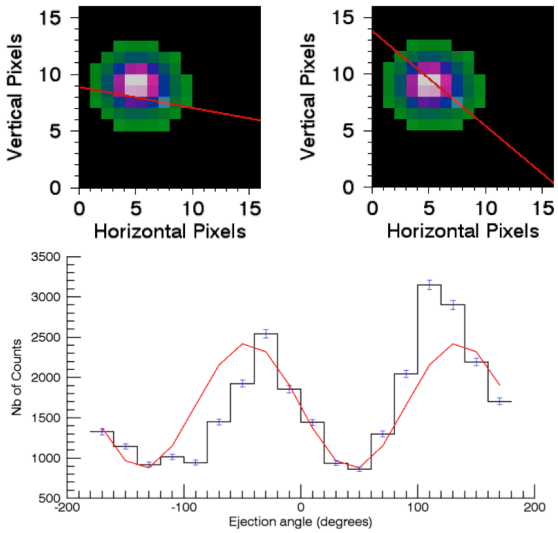


Figure 5.17: *Examples of very short tracks with length lower than 5.5 pixels from the impact point. It is hard to make a difference between them and a Compton event where only the secondary photon has left a signal. The modulation curve obtained when taking those tracks into account gives a modulation factor of 45%. The fit of the theoretical curve $A + B\ cos^2(\phi - \phi_0)$ is not good anymore, which proves that there are some systematic effects that I do not understand yet.*

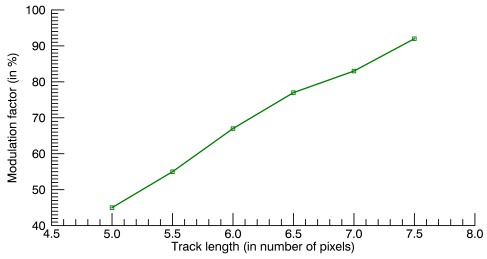


Figure 5.18: *Modulation factor measured for various accepted track length. When the accepted tracks get shorter, the reconstruction is less precise and the modulation factor drops.*

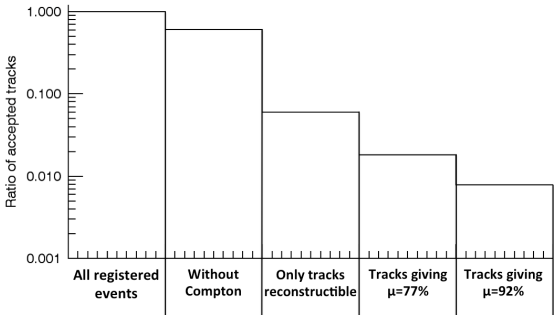


Figure 5.19: *Ratio of accepted tracks at 8 keV for the reconstruction compared to the total number of events (including Compton). The ratio of photoelectric events compared to Compton events is of around 65%.*
*To obtain a proper reconstruction, a trigger has to be implemented to keep only the tracks with a length greater than 5.5 pixels from the impact point as in fig. 5.16. With this trigger only 7.5% of the registered events are kept.*
*Increasing the selection on the track length to get a better modulation factor reduces drastically the number of accepted tracks: 2% of accepted events when taking those longer than 6.5 pixels from the impact point, 1% of accepted events when taking those longer than 7.5 pixels from the impact point.*

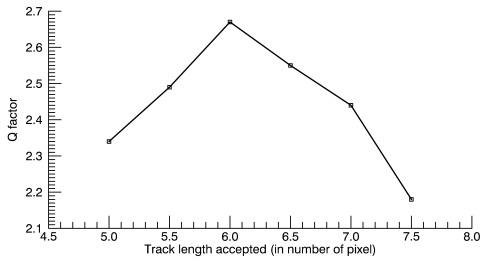


Figure 5.20: *Q factor of the detector for different track length accepted (size expressed in number of pixels). It is always higher than 20 and reaches 26.5 as its best.*

The quality factor is contained between 2 and 3. This value is low and it mostly comes from the low detection efficiency. In fact, assuming that 100% of tracks can be reconstructed with a detection efficiency of 1% and a modulation factor of 92%, the Q factor calculated is 9, which is still low. Improving the detection efficiency of the gaseous detector is then essential.

### 5.6.3 The problem of low efficiency

Several ways to improve the efficiency of the detector exist. First the used mixture is not efficient for absorption of X-rays. Helium is highly transparent in the soft X-ray range. The addition of a small proportion of isobutane as quencher improves the efficiency of conversion by a factor of 4, as a large part of the conversion will be performed in isobutane, but even with this high improvement the efficiency remains quite low.

Fig.5.21 shows the attenuation coefficient of helium alone and a mixture of helium and isobutane in proportions of 90% - 10%. The addition of the quencher increases the efficiency of detection as a good part of the events will be converted in the isobutane. But the attenuation coefficient is still very low and the absorption of soft X-rays in 5 mm of this mixture is of less than 0.5%. To compare this to a goal value, the ESA's requirement in term of efficiency of detection is 1%. This is an achievable goal if the conversion space is increased or if the gas is changed to add a small proportion of argon or xenon as explained in the previous chapter.

The second problem is that at those energies the Compton effect happens often. Fig.5.5 presents the cross-sections for the Compton

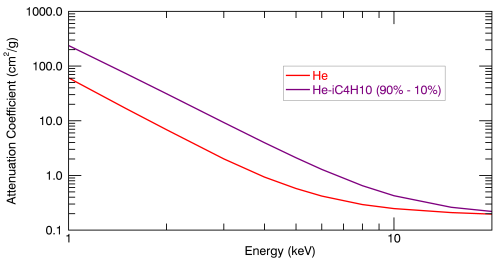


Figure 5.21: *Attenuation coefficient in the soft X-ray range in helium alone and in a mixture of helium and $iC_4H_{10}$ (isobutane). The addition of 10% of isobutane increases the efficiency of conversion as a good part of it will be done in the isobutane (and essentially in the Carbon atoms).*

effect and the photoelectric effect in the used mixture (data from the XCOM database of the NIST [4]).

### 5.6.4 Improvements possibilities

In order to improve this, several things can be envisioned. First it is possible to use a readout electronics with smaller pixels, as it gives a much better spatial resolution on the detector as shown in the previous chapter with the use of the $D^2R_1$ electronics.

Another way to improve the reconstruction is to use electronics with a good timing resolution: this would transform the detector into a TPC and allow to get information on the third spatial coordinate. Thanks to this, it would be possible to reconstruct properly photoelectron's tracks even for photoelectrons ejected with a low polar angle, or for those which undergo multiple scattering. This is commonly used in TPC for high energy physics or rare event detection such as in [5]. However, the photoelectrons tracks of few mm are probably too short to use properly the TPC approach.

Finally, using a gas with a small proportion of argon or xenon will also help. In those cases, the Compton events almost never happen: in the energy range of 1 keV to 20 keV, the photoelectric effect is 1000 times more probable than Compton scattering in argon, and 10000 times more probable in xenon. Each photon will then be detected thanks to the photoelectric effect. As we can see in fig. 5.19, removing the Compton events at 8 keV is responsible for the loss of 35% of the events: having only photoelectric events in the

detector would then automatically increase the number of accepted tracks.

### 5.6.5 Measurements with an other detector orientation

I also performed measurements at 8 keV with an orientation of the detector estimated at 5 degrees. Unfortunately, for these measurements the pixels at the edges of the electronics had been cut as they were noisy. The length of the accepted tracks had then to be reduced and corresponds to the tracks shown in fig.5.16 (left).

Fig.5.22 shows the curve obtained with such a measurement. The peaks do not have exactly the same width for unknown reasons and this problem is under investigation but it is highly probable that it comes from a reconstruction problem: for these measurements, the center of the beam is slightly shifted by 200 $\mu$m from the center of the pixel, and because of the large size of the pixels and the square geometry of the pixels matrix, this might introduce a systematic error during the reconstruction that has not been fixed yet.

However, despite this asymmetry, the peaks position clearly shifted with the orientation of the detector, proving the capability of the Caliste-MM detector to reconstruct properly the polarization direction of the detected X-rays.

## 5.7 Reconstruction at other energies

Measurements have been performed at energies of 6, 8, 10 and 12 keV, and fig.5.23 presents the modulation curves obtained. The reconstruction used is the same than the one presented in fig. 5.12. The triggers on the track length are: 7.5 pixels from the impact point minimum for 8, 10 and 12 keV, and 6 pixels from the impact point minimum for 6 keV. The trigger is not the same for 6 keV events as tracks longer than 7 pixels for 6 keV photons does not exist. The modulation factor at 6 keV is low as the track length is very short and the reconstruction is then not very efficient.

At energies above 8 keV, the modulation factor is always greater than 80%. At 12 keV, the modulation factor is good but exhibits the same asymmetry as in fig.5.22, for it seems the same reasons of the beam shifted from the center of a pixel.

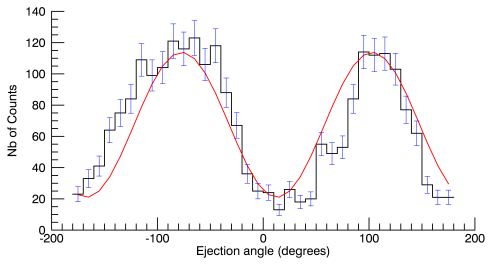


Figure 5.22: *Modulation curves obtained for an orientation of the detector estimated at 5 degrees. The red curve is the fitted function A + B×cos²(ϕ-ϕ₀). The accepted tracks are short as the pixels on the edges had been cut during the measurement. The modulation factor is of 67%, which is consistent with the track lengths accepted. The fit gives an angle of polarisation at 7.8 degrees. This is consistent with the estimated orientation of 5 degrees of the detector.*
*The function A + B×cos²(ϕ-ϕ₀) does not fit perfectly the histogram and the peaks are asymmetric. This problem is under investigation.*

The modulation at 10 keV is in good agreement with the estimated model, but the modulation factor is lower than the one for 8 keV data, whereas a modulation factor at least as good can be expected. This comes from the fact that Compton events becomes predominant at 10 keV (see fig.5.5). Those Compton events can participate to background as they can leave tracks in the detector that can be mistaken with a photoelectric event.
Fig.5.8 (bottom right) presented one of those events. Fig.5.24 present another kind of Compton events that fake photoelectric events: they are harder to recognize and can be easily be accepted by the filters of the reconstruction algorithm. Fig.5.25 shows a modulation curve obtained before filtering events like those in fig.5.24, and after.
The modulation curve factor goes from 65% to more than 80%, which proves that those events participate a lot on the background. Some of those cannot be filtered as they look very closely to photoelectric events and there is absolutely nothing to distinguish them from the photoelectric events. They will then participate on the background. Because Compton events are highly probable at 10 keV, they will then have a high influence on the background. This is the reason why the modulation factor at 10 keV is lower than the one at 8 keV, despite having larger tracks to get a better reconstruction.

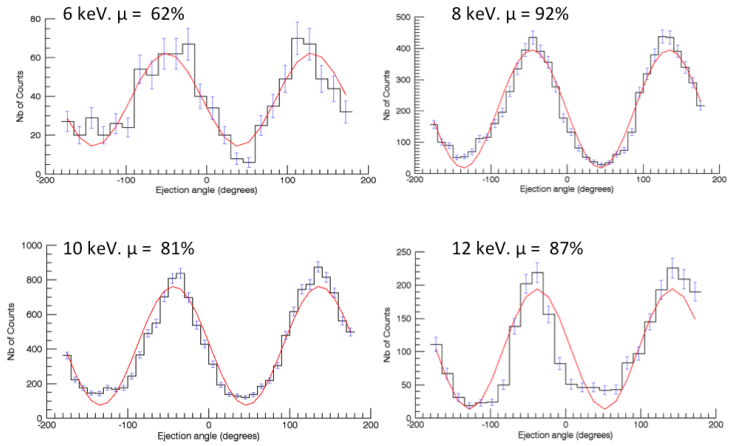


Figure 5.23: *Modulation curves obtained at various energies. The 6 keV events are short (the same size as in fig.5.16 right), which explains the lower modulation factor. The modulation factor is still above the 30% required by ESA for its M4 mission. The modulation factor is above 80% at the other energies.*

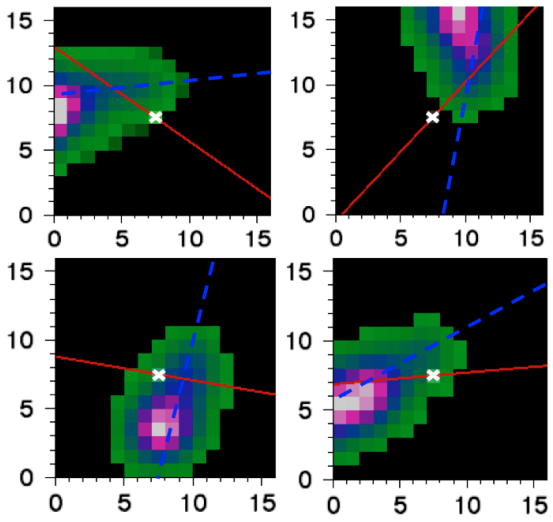

Figure 5.24: *Compton background events can be mistaken for photoelectric events. The white cross is the impact point of the beam, the red line is the reconstructed ejection direction by the algorithm while the dotted blue line is the real ejection direction. Those fake photoelectric events clearly participate to the background.*

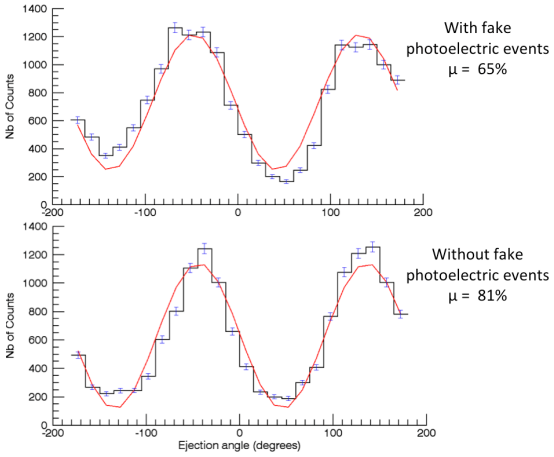


Figure 5.25: *Modulation curves at 10 keV obtained when taking into accounts the fake photoelectric events presented in fig.5.24 and when removing them. The modulation factor improves a lot.*

## 5.8 Summary

The Caliste-MM detector has been brought to the Soleil synchrotron facility which produces 100% linearly polarized soft X-rays, in order to characterize its polarimetric capability.
Runs had been taken using a mixture of helium and isobutane (in proportion 90% - 10%), at various energies and for various detector's orientations.
The modulation factor obtained at 8 keV is of 92%. It proves the capability of the Caliste-MM detector to measure the polarization fraction of the detected light. The dependence of the modulation factor has been studied as a function of track length and is higher than 60% for tracks longer than 6 pixels from the impact point.
The modulation curves obtained for various detector orientations exhibit a shift of the peaks position in agreement with what is expected, proving the high capability of the Caliste-MM detector to measure the polarization direction of the detected X-rays.
The modulation factor at different energies has been measured. The best modulation factor, of 92%, is obtained at 8 keV. At 6 keV the modulation factor decreases due to the short length of the tracks. At 10 and 12 keV the modulation factor is reduced as Compton scattering events are mistaken with photoelectric events.
The systematic errors are still under study.

# Bibliography


[1] https://www.synchrotron-soleil.fr/

[2] https://www.synchrotron-soleil.fr/en/beamlines/metrologie

[3] S. Antier et al., *Hard X-ray polarimetry with Caliste, a high performance CdTe based imaging spectrometer*, Experimental Astronomy 39 (2015) 233-258

[4] http://physics.nist.gov/cgi-bin/Xcom/

[5] I.G. Irastorza, F. Aznar, J. Castel, S. Cebrián, T. Dafni, J. Galán, J.A. Garcia, J.G. Garza, H. Gómez, D.C. Herrera, *Gaseous time projection chambers for rare event detection: results from the T-REX project. I. Double beta decay*, Journal of Cosmology and Astroparticle Physics (2016)

# Conclusion

Astrophysics is dedicated to the understanding of our universe and the objects that compose it. To get information about the various physical phenomenon implied, the observation of light is the most ancient and uberous. Observations can be performed on the whole electromagnetic spectrum, from radio waves to gamma rays, and four sciences can be performed on it: imaging, spectrometry, timing and polarimetry.

Those four sciences gave abundant results at every energy of the electromagnetic spectrum except polarimetry in the soft X-ray band (1 keV - 20 keV) which, for instrumental reasons, has not been performed properly yet. It is possible to use the photoelectric effect to perform polarimetry. In fact, the ejection direction of the photoelectron is modulated by the polarization direction and the polarized fraction of the detected light. By recovering the ejection direction of the photoelectron for each interaction and making a histogram of those direction, it is possible to recover those information. Because in gas the mean path length of a photoelectron is high, it leaves a track long enough to be measured by a pixelated electronics. Hence gaseous detectors are ideal candidates to build a polarimeter, and with the invention and improvements of the Micro Pattern Gaseous Detectors in the late 90's, the interest of the astrophysical community for soft X-ray polarimetry was renewed.

In this manuscript I presented the Caliste-MM detector. It is a new concept of gaseous detectors which uses a piggyback detector for photon conversion and signal amplification, and the Caliste readout electronics. Its particularity is that the electronics are completely uncoupled from the detectors. In fact, the anode of the piggyback is a simple resistive layer spread on a ceramic plate, which closes the gaseous chamber and makes it leak tight. The Caliste readout is outside the gaseous medium, facing the ceramic and reading the signal of the charges diffusing in the resistive layer by capacitive coupling.

Its characteristics have been presented in detail: shape of events, gain, energy resolution and behavior with the variation of the various parameters of the detector. Analytical simulation were presented to support the understanding of the physical phenomena intervening in the detector. The Caliste-MM detector exhibits standard performances in term of gain and energy resolution. With its innovative design, I measured a resolution of 17% FWHM at 6 keV, which is a classical value when using the bulk technology.

The Caliste-MM detector was brought to the Soleil synchrotron facility, in the Metrologie line which produces a 100% polarized monochromatic soft X-rays beam. With this experiment, it has been possible to perform polarization measurements at energies ranging from 6 keV to 12 keV. The reconstruction algorithm used is presented in detail, and results at various energies and with various triggers are presented. The detector exhibits a modulation factor up to 92% at 8 keV, proving the efficiency of the Caliste-MM detector as polarimeter.

Those results are very promising, especially considering the fact that the detector uses an outside and contactless electronics which can be changed easily to fulfil the requirements. Of course they are not perfect, and several points can be improved. First the imaging capacity of the detector has not been tested yet. Because of the use of a resistive layer as the anode spreading the signal on several pixels, the spatial resolution is better than the pixel pitch, and its limitation actually comes from the diffusion of the photoelectron in the gas used for the detection. It is of around 200 $\mu$m in Argon and up to 4 mm in Helium. This diffusion is very important for polarimetry and can be used for imaging if we are able to identify the impact point from the track left by the photoelectron. But to identify this impact point properly, it is necessary to have small pixels, and the pixels of the Caliste readout are too large to get a better spatial resolution than 200 $\mu$m in Argon.

The use of smaller pixels is also of importance as the detector needs to perform good polarimetric measurements in the range of 2 keV - 12 keV. In its current configuration, its performances are outstanding between 8 keV and 12 keV. At 6 keV the modulation factor drops to 62%, and the detector is inefficient at lower energies because of the low mean freepath of the photoelectrons. With smaller pixels this problem could be solved, and the fact that the electronics is completely uncoupled from the other part of the de-

tector makes it very easy to change. It has been briefly done when using the $D^2R_1$ readout electronics to read 6 keV events with a much better spatial resolution on the photoelectron's track, but it has to be done in more detail and measurements at energies below 6 keV have to be performed to validate the performances of the detector.

Another point to look at is the efficiency of the detector. This problem has been mentioned in the manuscript and can be improved in several ways. First the use of smaller pixels would allow more events to be reconstructed and makes the detector more efficient. The conversion efficiency has also to be improved. It can be done by using a larger conversion gap: in the current configuration the conversion gap (also called drift gap) is 0.5 cm thick. A gap of 2 cm would improve the conversion efficiency by a factor 4 without degrading the performances of the detector.
The efficiency can also be improved by using another gas than a Helium based one, as mentioned in the last chapter. Changing the gas goes with the use of the detector in low pressure conditions, in order to let the photoelectron recoil far enough for its track to be measured. Such measurements have been done and presented in the manuscript and they look promising, but they have to be coupled with the use of smaller pixels to give good results.

The use of another gaseous mixture than Helium is also very important for the energy resolution parameter. The Caliste-MM detector shows an energy resolution of 17% FWHM at 6 keV, which is good, but it is in Argon. In Argon, performing polarimetry is almost impossible because of the low energy of the photoelectron, as 3 keV are required to ionize the K-shell (which makes Argon impossible to use for low energy measurements). And the measurements giving a modulation factor of 92% have been performed in a Helium based mixture, and the associated spectrum exhibits an energy resolution of 35% FWHM at 6 keV which is far from the ESA's requirements. Using Neon would solve the problem. This, coupled to the use of piggyback using flat and thin mesh instead of standard woven mesh, would bring the energy resolution of the detector at a good level, by still allowing to perform good polarimetric measurements.

What emerge from those last remarks is that the future of this detector necessarily goes with the use of smaller pixels. In its current configuration the detector has outstanding performances which go far above the ESA requirements and makes it very competitive if compared to the XIPE or IXPE projects, but only in the energy band of 8 keV - 12 keV. Good performances at lower energies cannot

be obtained without smaller pixels, and it would be the principal axis to explore for further developments.

The Caliste-MM detector is a new concept of spectro-polarimeter, using an innovative design of outside and contactless readout electronics. Thanks to the use of a resistive anode, the electronics is protected from the sparks developed inside the gaseous detector. And thanks to this new design, the electronics are uncoupled from the anode and can be changed and developed independently from the gaseous detector in order to satisfy the requirements. Despite this new design, the performances reached by the detector are very good and its polarimetric capacity has been proven.

Soft X-ray polarimetry could be used outside of the scope of astrophysics. It could be used in a certain way to perform background reduction in dose measurements for medical imaging. For instance let's take the example of a fluorescent material mixed with human tissue, and the objective is to measure the dose of material in the tissue. The sample is hit by an X-ray source, and a detector is placed at an angle of 90 degrees and measures the radiations coming from the sample. Those radiations consist mainly of two parts: the fluorescence of the material, and the diffusion from the X-rays produced by the source. This diffusion is considered as background as it does not necessarily come from the material aimed at. If the X-ray source is 100% polarized, the diffusion will also be polarized, while the fluorescence will not be. By performing polarimetry measurements, it could be possible to reduce the background by identifying the polarized fraction (caused by the diffusion) and removing it, giving a much more efficient detector.

The concept of uncoupled electronics can be used in several applications as it is independent from polarimetry. In particle physics gaseous detectors are often used. Because of their high sensitivity to sparks, resistive anode strips are often used. When using the bulk technology, the anode and the mesh of the detector form one single entity. If one strip breaks, as it often happens, it is impossible to change it without changing the whole detector and having to calibrate it again. This problem is completely solved by the use of a piggyback detector: because the readout is not integrated to the detector, if one strip is broken it would be enough to simply use another PCB with the same strip design, without manipulating the rest of the detector and having to calibrate it again.

But having to search for other applications of the detector than

astrophysics is not necessary: soft X-ray polarimetry is a complete and challenging science by itself, and this is why it has never been performed properly up to now. The information that it would bring would strongly reinforce our knowledge of energetic objects in the universe.

# Résumé en français

Effectuer des mesures de polarimétrie des rayons X provenant de sources astrophysiques permettrait d'obtenir de nombreuses informations sur les objets émetteurs : géométrie des disques d'accrétion de pulsars, champ magnétique au cœur des restes de supernovae ou encore détermination du spin des trous noirs. Avant les années 2000, la polarimétrie dans la gamme d'énergie des rayons X mous (1 keV - 20 keV) reposait sur l'utilisation de deux phénomènes : la diffusion Thomson et la diffraction de Bragg. Malheureusement ces deux techniques présentent plusieurs défauts, notamment une très faible efficacité, et ce sur une dynamique d'énergie médiocre. Pour ces raisons instrumentales, seul le satellite OSO-8, lancé en 1975, a embarqué un polarimètre, produisant des résultats pionniers mais pouvant être améliorés. La polarimétrie X a ensuite été mise de côté compte tenu des progrès fulgurants en imagerie, spectrométrie et timing dans la gamme d'énergie X.
Cependant, il est possible d'utiliser un autre phénomène physique pour faire de la polarimétrie des rayons X mous : l'effet photo-électrique, qui apparaît comme une approche bien plus adaptée que l'utilisation de la diffraction de Bragg ou de la diffusion Thomson. La polarimétrie par le truchement de l'effet photo-électrique repose sur la mesure de la direction d'éjection du photo-électron, laquelle est modulée par la direction de polarisation de la lumière incidente. Il s'agit alors de construire un détecteur permettant un recul suffisant des photo-électrons afin de reconstruire leurs traces, et les détecteurs gazeux sont par nature des candidats idéaux. Or, les années 2000 ont vu l'avènement d'une toute nouvelle technologie de détecteurs gazeux : les Micro Pattern Gaseous Detectors. Inventés à la fin des années 1990, leur développements et améliorations successives ont permis de les rendre suffisamment performant pour qu'ils soient maintenant capables de mesurer une trace de photo-électrons de quelques centaines de microns, les rendant ainsi parfaitement adaptés à une mesure de polarimétrie.

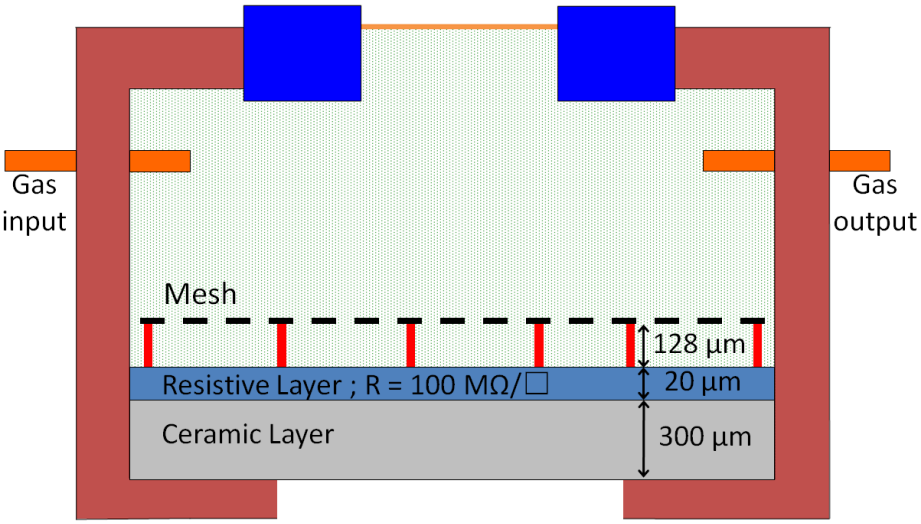


Figure 5.26: *Schéma du détecteur Caliste-MM. L'électronique de lecture Caliste est placée à l'extérieur du milieu gazeux et lit le signal développé dans le piggyback à travers la céramique. La couche résistive assure une protection de l'électronique contre les décharges qui peuvent avoir lieu dans le piggyback. Les parties détection et lecture sont entièrement découplées et peuvent donc être changées rapidement en fonction des besoins.*

Cette thèse traite du développement et de la caractérisation d'un spectro-polarimètre à rayons X-mous d'un genre entièrement nouveau : Caliste-MM. Il consiste en un détecteur gazeux appelé piggyback associé à une électronique de lecture miniature baptisée Caliste. Fig.5.26 présente un schéma de ce détecteur, et fig.5.27 présente le détecteur lui-même.

L'une des principales innovations de ce détecteur tient au fait que son électronique de lecture est située en dehors du milieu gazeux. Les charges créées dans le piggyback diffusent dans une couche résistive répandue sur une céramique venant fermer le détecteur gazeux. Le module électronique Caliste enregistre le signal qui se répand dans la couche résistive à travers la céramique et une fine lame d'air par couplage capacitif. Le détecteur est ainsi composé de deux parties complètement indépendantes : conversion de la lumière et amplification par le piggyback, et lecture du signal par le Caliste. Les deux peuvent alors être développées indépendamment l'une de l'autre, l'électronique étant protégée des étincelles développées dans

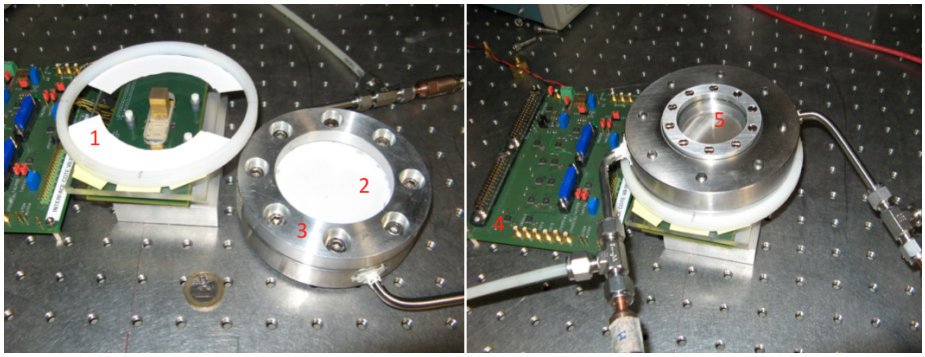


Figure 5.27: *Le setup du détecteur Caliste-MM. Gauche : Les deux parties du détecteurs sont séparées. 1: Les espaceurs permettent de contrôler la distance entre la céramique du piggyback et le Caliste. 2 : Céramique du piggyback. 3 : Enceinte contenant le gaz. Droite : Le Caliste-MM : le piggyback est simplement placé au dessus de l'électronique Caliste. 4 : Carte de conversion digitale vers analogique. 5 : fenêtre d'entrée transparente aux rayons X.*

le détecteur grâce à la couche résistive du piggyback.
J'ai d'abord étudié la topologie des évènements : ceux-ci, visibles en fig.5.28, ont une taille moyenne dans l'Argon de plusieurs millimètres, alors que la trace d'un photo-électron de 6 keV dans le même gaz laisse une trace de 200 $\mu$m. Afin de comprendre ce phénomène j'ai réalisé une simulation analytique, à l'aide d'une méthode des éléments finis. Celle-ci m'a permis de mettre en évidence l'impact de la diffusion des charges dans la couche résistive ainsi que son fonctionnement. En appliquant les paramètres du détecteur à la simulation, j'ai été capable de reproduire les évènements avec une erreur moyenne de 3.6%, comme présenté en fig.5.29.

J'ai ensuite étudié plusieurs caractéristiques du détecteur, à commencer par son gain, à savoir la fraction entre le nombre de charges mesurées sur l'électronique Caliste par rapport au nombre de charges crées dans le gaz (avant amplification) par le photo-électron. La courbe de gain du détecteur Caliste-MM est similaire à celle d'un détecteur MPGD standard. Le gain est compris entre $10^2$ et $10^3$, en dessous des performances d'un détecteur Micromegas standard, à cause de la présence de la lame d'air entre le Caliste et la céramique atténuant le signal.
J'ai aussi pu étudier la résolution spectrale du détecteur, qui atteint 18% FWHM à 6 keV, ce qui est un résultat standard pour un détecteur piggyback : utiliser un concept innovant d'électronique dé-

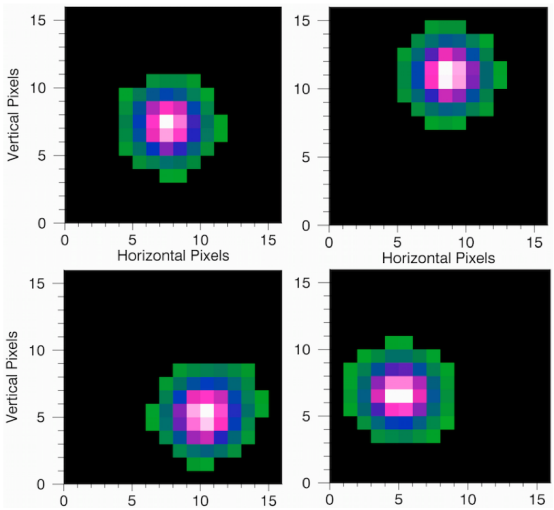


Figure 5.28: *Plusieurs évènements de 6 keV enregistrés par le détecteur Caliste-MM utilisant une mixture d'Argon-Isobutane (95%-5%). Chaque évènement représente la conversion d'un photon de 6 keV dans le détecteur, la migration des charges primaires dans l'espace d'amplification du piggyback, l'amplification des charges primaires, la diffusion des charges créées dans la couche résistive, et la lecture du signal à travers la céramique et la lame d'air.*

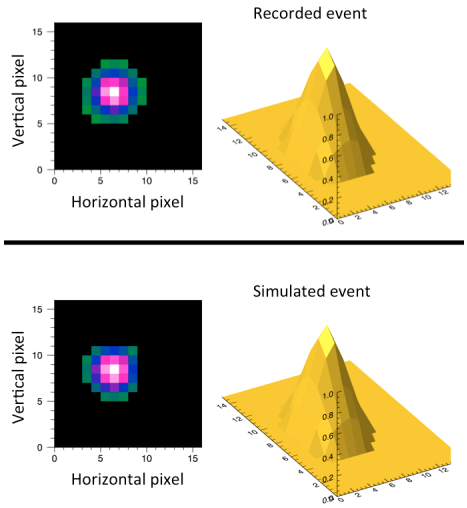


Figure 5.29: *Haut : évènement réel enregistré dans le détecteur Caliste-MM lors de la détection d'un évènement de 6 keV. Bas : simulation d'un évènement de 6 keV. Les signaux sont normalisés pour avoir leur maximum égal à 1. L'erreur moyenne de la simulation est de 3.6%.*

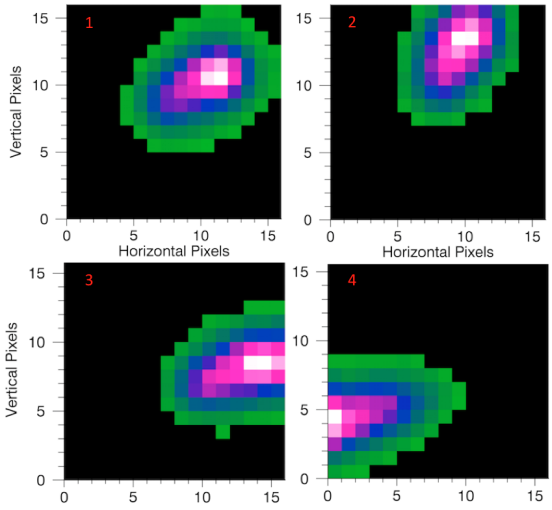


Figure 5.30: *Évènements enregistrés par le détecteur Caliste-MM pour des photons de 8 keV (1 et 2) et de 10 keV (3 et 4). Les traces laissées par le photo-électron ne sont plus isotropiques et il est possible d'effectuer des mesures de polarimétrie.*

couplée du détecteur gazeux ne dégrade donc pas les performances spectroscopiques, et le détecteur Caliste-MM peut effectuer de la spectrométrie.

Malheureusement, comme il est possible de le voir en fig.5.28, les évènements enregistrés semblent isotropiques, et il est difficile d'identifier la direction d'éjection du photo-électron : effectuer de la polarimétrie avec le détecteur Caliste-MM dans ses conditions standards est donc délicat. Les différentes méthodes pour obtenir une trace reconstructible issue de photo-électrons sont aussi étudiées : utilisation d'une électronique de lecture plus finement pixelisée (utilisant ainsi pleinement le concept d'électronique découplée), test en basse pression ou utilisation de gaz légers comme l'Helium ou le Néon.
L'utilisation d'Helium comme gaz de détection pour effectuer de la polarimétrie apparaît comme une solution idéale : les évènements enregistrés, présentés en fig.5.30, ne sont plus isotropiques et il est possible de reconstruire la direction d'éjection du photo-électron.

Enfin, grâce à des mesures effectuées sur le faisceau 100% polarisé de la ligne Métrologie du synchrotron SOLEIL, j'ai pu mesurer le facteur de modulation du détecteur à différentes énergies de 6 à 12 keV. Une mesure du facteur de modulation de 92% à 8 keV, présen-

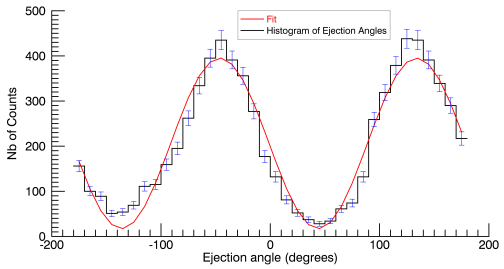


Figure 5.31: *Noir : Histogramme des directions d'éjection des photoélectrons à 8 keV. Rouge : fit de la courbe théorique* $A + B \times cos^2(\phi - \phi_0)$ *. Le facteur de modulation, calculé à partir des paramètres du fit, donne* $\mu = 92\%$.

tées en fig.5.31, prouve le grand potentiel de ce nouveau spectropolarimètre et l'intérêt de son concept innovant.

# Annexe

Published by IOP Publishing for Sissa Medialab

Received: *January 27, 2016*
Revised: *March 2, 2016*
Accepted: *March 14, 2016*
Published: *April 12, 2016*

# Caliste-MM: a spectro-polarimeter based on the micromegas concept for soft X-ray astrophysics

**P. Serrano,**[1] **D. Attié, D. Desforge, E. Ferrer Ribas, F. Jeanneau and O. Limousin**

*IRFU, CEA, Université Paris-Saclay,*
*F-91191 Gif-sur-Yvette, France*

*E-mail:* paul.serrano@cea.fr

Abstract: Performing X-ray polarimetry of astrophysical sources is a topic of growing interest, with only a few flying experiments dedicated to it so far. For soft X-rays sources detection from 1 keV to a few tens of keV, the best technique certainly consists in using the photoelectric effect, which is the dominant phenomenon at those energies in gaseous detectors. One of the main issues is the gaseous detector's reliability in space and the sensitivity to sparks of their associated front-end electronics caused by cosmic rays. To overcome this limitation, we investigate the opportunity of building a new spectro-polarimeter with outer and contactless radiation hard readout electronics, placed outside the gas chamber. In order to perform this, we use a Micromegas detector with a resistive anode spread on a ceramic plate. The signal is then transmitted by capacitive coupling to the outer electronics. The readout electronics in question, inherited from Caliste-HD, consists of a fine pitch 3D detector module developed at CEA initially designed for semi-conductor applications.

In this paper we present the different parts of our experimental setup as well as recent results obtained by illuminating our prototype with an $^{55}$Fe source. In addition to the optimization of the detector's parameters, we also present the first spectrum of a soft X-ray gaseous detector with outer and contactless electronics and photo-electron tracks obtained with the detector making a step forward in the field of soft X-rays spectro-polarimeter.

Keywords: Micropattern gaseous detectors (MSGC, GEM, THGEM, RETHGEM, MHSP, MICROPIC, MICROMEGAS, InGrid, etc); Polarimeters; Spectrometers; X-ray detectors

[1]Corresponding author.



doi:10.1088/1748-0221/11/04/P04016

2016 JINST 11 P04016

## Contents



## 1 Introduction

X-ray astronomy allows the observation of the most violent phenomena in our universe. Spectroscopy, imaging and photometry in soft X-ray energies (1 keV – 15 keV) are well mastered sciences performed by famous missions (Chandra, RXTE, XMM-Newton). But X-ray polarimetry is still missing: only a few pioneer dedicated experiments have been flying on board of rockets or satellites [1–4]. Because of the low sensitivity of the instruments based on Bragg diffraction and Thomson scattering the only positive detection was the polarization of the Crab Nebula [5].

Thanks to the improvement of gaseous detectors in the late 90s and the possibility to use the photoelectric effect to perform soft X-ray polarimetry, the interest for this scientific domain has been renewed. In fact, because polarimetry gives significant information on the magnetic field of the emitting X-ray source, it would give information on a wide variety of X-ray sources and allow the validation of theoretical models. Consequently, various missions are currently under development such as the XIPE [6], IXPE [7] and PRAXyS missions. Such applications are for instance [6] the observation of accelerating phenomena in supernovae remnants or pulsar wind nebulae by measuring the variation of the magnetic field inside the nebulae.

Polarimetry can be performed in a gaseous detector thanks to the photoelectric effect, where an incoming photon is converted in the gas into a photo-electron. The differential cross-section for this effect is given by the Heitler formula [8]:

$$\frac{d\sigma_{ph}}{d\Omega} = r_0^2 \alpha^4 Z^5 \left[\frac{m_e c^2}{E}\right]^{\frac{7}{2}} \frac{4\sqrt{2}\sin^2\theta\cos^2\phi}{(1-\beta\cos\theta)^4} \tag{1.1}$$

where $r_0$ is the classical radius of the electron and $\beta$ its velocity in units of the speed of light, $\alpha$ the fine-structure constant, $m_e$ the rest mass of the electron, E the energy of the incoming photon, Z the atomic number of the absorbing atom, $c$ the speed of light and $\theta$ and $\phi$ are respectively the polar angle and azimuthal angle of ejection as defined in figure 1. The ejection direction is modulated by $\cos^2\phi$ and is then directly linked to the polarization direction of the incident photon. By looking at the angular distribution of the azimuthal ejection direction of the incoming photons of an X-ray source, it is possible to derive the polarization direction of the source and measure its polarized fraction.



2016 JINST 11 P04016

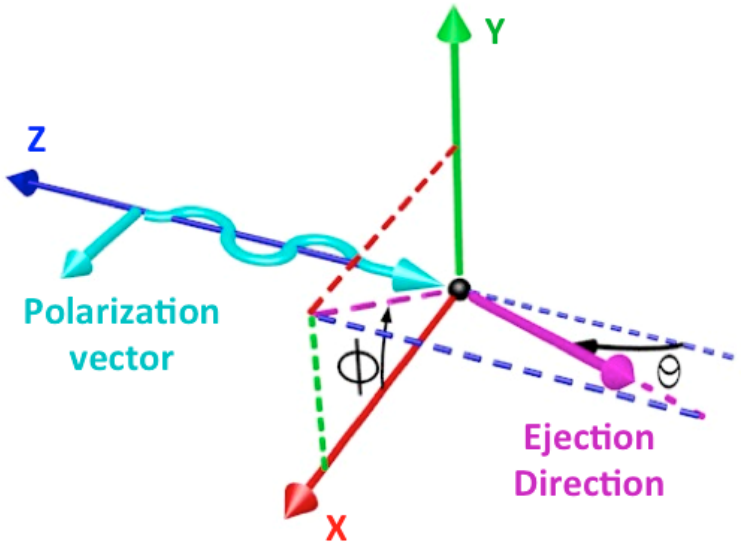


**Figure 1**. Photoelectric effect. The light blue arrow represents the electric vector, the purple line is the ejection direction of the photo-electron and the black point is the ejected photo-electron. $\theta$ and $\phi$ are respectively the polar and azimuthal angles. The ejection direction is modulated by $\cos^2\phi$.

## 2 The Caliste-MM system

Our new gaseous detector is based on the Micromegas concept presented in [9]. When considering a space-borne application, specific attention must be paid to the protection of the electronics from the sparks caused by cosmic radiation, which can easily damage the electronics, without sacrificing the performance. The classical solution is to use large protection cards: if the detector is to be used in orbit those protection cards would need to be space qualified and radiation hardened, which would inevitably bring a significant increase of the development costs and mass. A more original and convenient solution is to use a piggyback Micromegas [10]. Based on the bulk technology, the particularity of this detector is its anode, which is a resistive layer of sheet resistance of 100 MΩ/□ spread on a 300 $\mu$m thick ceramic plate. Figure 2 (left) shows the detector chamber with the piggyback inside: one of its face is not inside the gas and is directly in contact with the outside, so there are no electronics inside the detector. Figure 2 (right) shows a scheme of the piggyback and represents its mesh, amplification gap, resistive layer and ceramic plate. It is this ceramic plate which is directly in contact with the outside. The readout electronics are to be placed outside the detector, facing the ceramic to read the signal through it by capacitive coupling. It is then possible to have easily interchangeable and possibly contactless electronics and should provide a natural protection from the sparks, as the electronics being outside the gaseous medium.

Tests have been performed on a piggyback detector filled with argon-isobutane mixture (95% - 5%). The detector has been illuminated with an $^{55}$Fe source, producing 5.9 keV photons. Figure 3 is obtained by reading the signal developed inside the piggyback: the mesh and drift voltages are independently powered by a CAEN N471A module and the signal is read on the mesh by an electronics chain consisting of an ORTEC charge pre-amplifier with its output fed into a CANBERRA 2022 Amplifier and a multichannel analyzer AMPTEK MCA-8000A for spectra acquisition. The number



2016 JINST 11 P04016

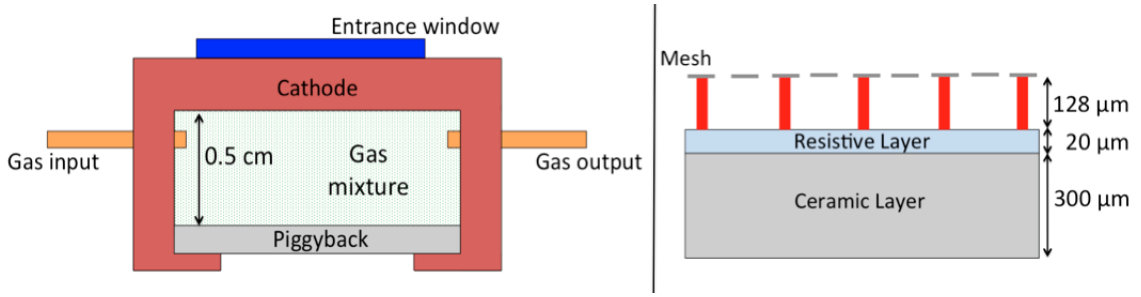


**Figure 2**. Left: the gaseous detector's chamber: there are no electronics inside the gaseous medium. Right: focus on the piggyback. Its resistivity is R = 100 MΩ/□.

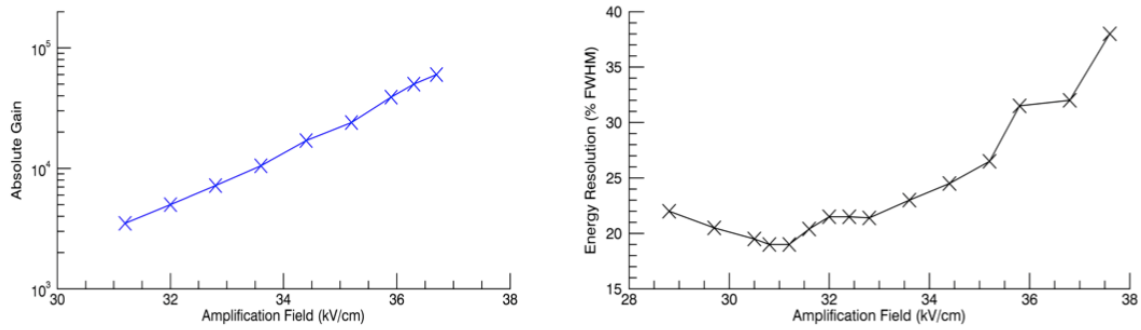


**Figure 3**. Gain and Energy resolution as a function of the amplification field. The performances are the expected ones for the bulk technology.

of charges collected is obtained from the ADC units of the MCA by calibrating the electronics chain. The absolute gain is determined by calculating the ratio between the charge collected at the mesh and the primary electrons' charge created by the incoming 5.9 keV photon. These results show expected performances for the bulk technology with an 128 $\mu$m amplification gap in terms of gain and energy resolution reaching 18 % FWHM at 6 keV. This limit on the resolution is due to the use of a 35 $\mu$m standard stainless mesh which degrades the electric field lines between the holes. Resolutions of 11.5% FWHM at 6 keV can be attained with Micromegas microbulk detectors using 5 $\mu$m thick meshes [11]. In the near future we plan to use a flat mesh on a piggyback to improve the energy resolution.

The readout electronics must have some specific qualities. It must be low noise and sensitive enough to be able to read the signal through the ceramic plate of the piggyback. It should be position sensitive and be finely pixelated to be able to recover the ejection direction of the photo-electrons in order to perform polarimetry. It should also be able to perform spectroscopy with good energy resolution to reach at least the resolution of the piggyback detector. Caliste electronics [12, 13] (figure 4 left), initially used for semiconductors hard X-Ray spectroscopy, present all those characteristics.

Caliste has in fact several interesting properties to read the signal of the piggyback, summarized in table 1. The electronic noise is very low, which makes it a perfect candidate to read the signal of the piggyback through the ceramic. Each channel of the electronics is a self-triggered spectroscopic chain presented in figure 4 (right), and the 256 pixels are multiplexed by 8 IDeF-X ASICs [14].



2016 JINST 11 P04016

**Table 1**. Caliste body main characteristics.

| | |
|---|---|
| 3D block: | $10 \times 10 \times 16.5$ mm$^3$ |
| 16x16 pixels: | 8 ASICs IDeF-X of 32 channels |
| Pixel diameter: | 450 $\mu$m |
| Pixel Pitch: | 625 $\mu$m |
| Consumption: | 850 $\mu$W/channel |
| Low Noise: | ENC = 50 e$^-$ rms |

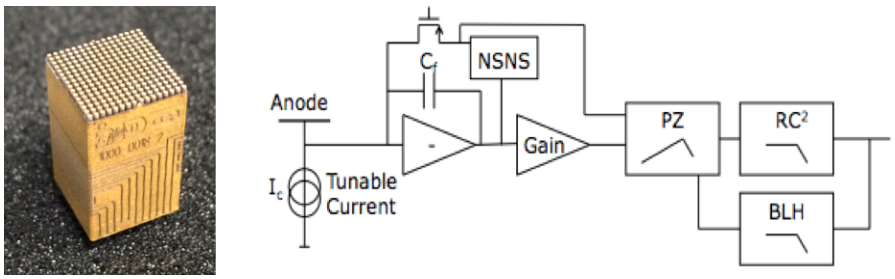


**Figure 4**. Left: the Caliste electronics. The dimensions are 1 cm$^2$ by 1.65 cm high. The 256 pixels, organized in an array of 16x16, can be seen on top of the electronics. Right: spectroscopic chain block diagram of one channel.

An incident charge on a pixel is converted into a pulse and its pulseheight measured. The signal is read out if it is above the preset threshold that is tunable for every channel. With the IDeF-X ASICs, it is possible to tune several parameters to optimize the reading of a gaseous detector instead of a semiconductor. In particular it is possible to optimize the shaping time, the dynamic, the charge preamplifier bias current and the controller frequency. Another advantage of the Caliste is its radiation hardness and space-qualification, which gives a tremendous asset toward the use of the detector in space-borne applications.

The Caliste is coupled to the piggyback detector in the setup shown in figure 5, called Caliste-MM. The Piggyback is placed on top of the Caliste and the system can be put in a contactless configuration where the electronics do not touch the ceramic. Preliminary characterization has been done by Attié et al. [15] in 2014. First tests have been done with a gaseous mixture of argon-isobutane (95%-5%) at atmospheric pressure, with a contactless configuration (Caliste at 500 $\mu$m from the ceramic) and an $^{55}$Fe source. Figure 6 shows some events read on the Caliste after the conversion of a photon inside the detector: the image represents the 2D pixels array of the Caliste, and the deposited energy is represented by the colormap. The events are round and their typical diameter is 6 mm. The large size of the events is mostly due to the diffusion inside the resistive layer of the piggyback. It is the first time that a gaseous detector has been readout by contactless electronics. The detector has been continuously tested for 4 months, experiencing frequent sparks but resulting in no observable damage to the detector, proving the merits of Caliste-MM and the resistive layer for electronics protection.



2016 JINST 11 P04016

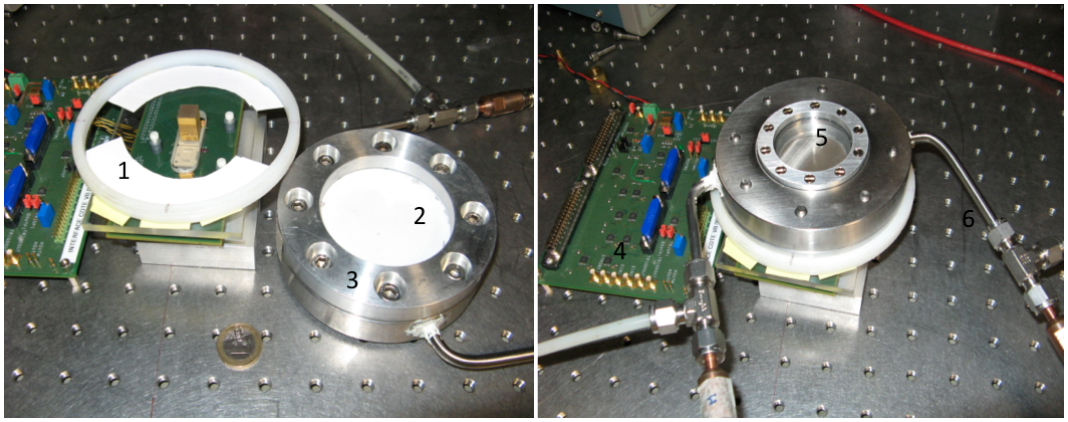


**Figure 5**. Left: setup with Caliste and Piggyback separated. Right: Caliste-MM setup. 1: 500 $\mu$m spacer. 2: piggyback's ceramic. 3: piggyback's chamber. 4: acquisition electronics. 5: entrance window. 6: gas tubes.

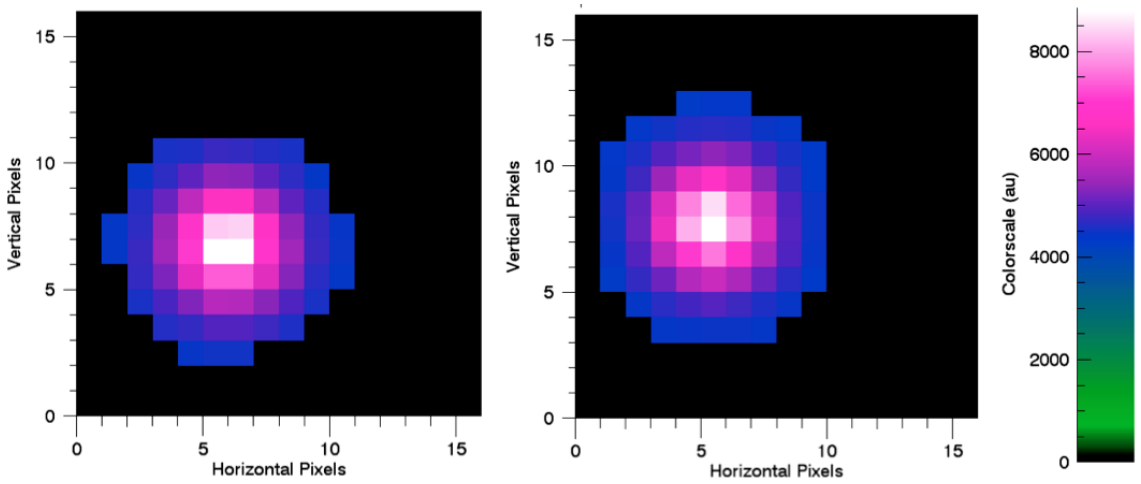


**Figure 6**. Photon conversion in argon-isobutane (95% - 5%) as read on the Caliste. The horizontal and vertical axes represent the pixel coordinates.

## 3 Results of the first prototype

The gain of the system as a function of amplification field is shown in figure 7 and compared to the gain of the isolated piggyback (already presented in figure 3). The voltages on the piggyback are provided independently by a CAEN N1471 module and the signal is read directly by the Caliste through the ceramic and the 500 $\mu$m air layer, this particular distance being chosen because of the higher precision of the 500 $\mu$m spacers. The absolute gain is determined by calculating the ratio between the charge collected on the Caliste and the primary electrons' charge created by the incoming 5.9 keV photon. The general behaviour of the piggyback is preserved. Reading the signal through the ceramic coupled to a layer of air decreases the gain. But it is still of the order of magnitude of $10^3$ which is large enough for soft X-ray applications when using a low noise and highly sensitive electronics such as Caliste. Another interesting parameter for the Caliste-MM



2016 JINST 11 P04016

detector is the distance between the Caliste and the ceramic, as it plays an important role on the induced signal on the detector. Figure 8 shows the variation of the gain of the detector versus this distance for an amplification field of 35 kV.cm$^{-1}$. When closer to the ceramic, the gain is up to 4 times more important which seems natural because of the narrowing of the air layer. The variations of the gain are more important for closer distances. These phenomena are currently under study with the development of an analytic model of the detector, but already indicate that they influence the gain of the system. If a greater gain is needed (to detect lower energies for instance) the Caliste can be placed closer to the ceramic, while keeping the amplification field at the value that optimizes the energy resolution. However, decreasing the distance too much can create some problems. A contact between the ceramic and the Caliste can mechanically damage the pixels of the electronics. The pixels do not all have exactly the same size and their height can vary by ±25 $\mu$m. This variation degrades the energy resolution of the system for distances closer than 400 $\mu$m. Finally, the quality of the used spacers is not equivalent. The 500 $\mu$m spacers are more trustworthy and easier to use, explaining why they have been used for most of our characterizations.

Figure 9 shows a spectrum of the events presented in figure 6 after a calibration of each pixel of the Caliste. Each event is fitted with a 2D gaussian function. Several methods have been tested to build a spectrum: histogram of the maximum deposited on a pixel for each event, of the maximum of a 2D gaussian fit, or of the total energy deposited by each event on the Caliste. But the best results are obtained by integrating the value of the fit within $1\sigma$ from its centroid. The spectrum is built from the resulting value. Performing a $1\sigma$ integral, instead of a $2\sigma$ or other, ensures that the main peak of the spectrum is at around twice the energy of the escaping peak, as it should be (main peak at 5.9 keV, escape peak at 2.8 keV). Any other method moves the two peaks away from one another, thus distorting the energy calibration. We strongly suspect that the $1\sigma$ integral limits the influence of the diffusion inside the resistive layer by taking only the created charges deposited on the detector. This is still a preliminary result and a full modelization of the detector has to be carried out to confirm this. The spectrum exhibits a good energy resolution of 17.7 % FWHM at 6 keV. Having external and contactless electronics does not degrade the energy resolution, as we are able to recover the minimum resolution of the piggyback alone (showed in figure 3).

Argon has however two disadvantages: its K-edge energy is high (3.2 keV) so a soft X-ray photon will create a low energy photo-electron, and it is a high Z gas so the photo-electron's track will be short. This makes an argon mixture at atmospheric pressure not well adapted to perform polarimetry as a photo-electron does not propagate far enough to leave a good track and allow the recovery of the ejection direction. It can be seen in figure 6 that recovering the ejection direction of the photons in argon is impossible as the events appear round. The gas has been replaced by helium - $CO_2$ (90 % – 10 %) at atmospheric pressure. Helium has the advantages of being a low K-edge and low Z gas. The results for 8 keV photons are presented in figure 10. This figure proves that helium is well suited for polarimetry, as photo-electrons can propagate far enough to leave a visible track. The blue pixels are due to the diffusion of the signal inside the resistive layer of the piggyback and the pink and white pixels correspond to the photo-electron's track: the fact that this track is visible makes polarimetry possible with the Caliste-MM. The maximum of the deposited energy in the conversion, represented by the white pixels in the picture, corresponds to the Bragg peak and is the end of the track. The ejection direction of the photo-electron can be recovered using the pixels at the beginning of the track. Without any data treatment, the ejection direction can be roughly estimated



2016 JINST 11 P04016

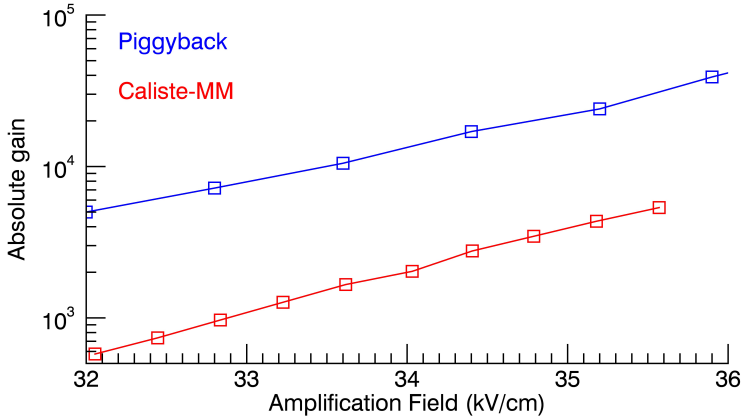


**Figure 7**. Comparison of gains as a function of amplification field for Caliste-MM and piggyback alone. The distance between Caliste and the ceramic is 500 $\mu$m. The behaviour is comparable, but due to the coupling through the ceramic plate and a layer of air, the gain of Caliste-MM is attenuated.

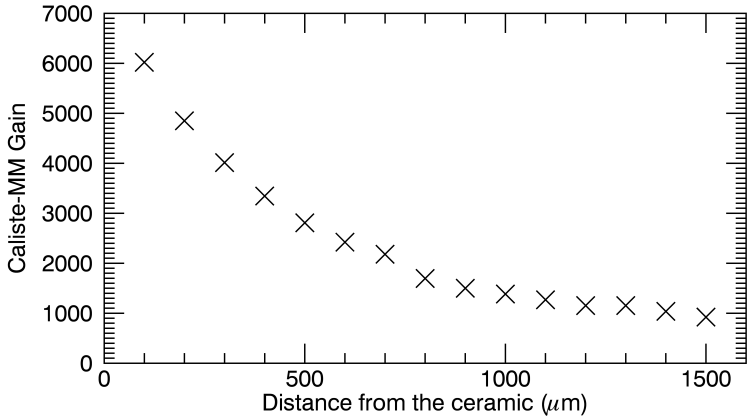


**Figure 8**. Absolute gain versus the distance between the electronics and the ceramic for an amplification field of 35 kV.cm$^{-1}$. When the distance is greater than 1 mm, the gain stabilises.

and seems to be horizontal going from the left to the right of the image. Data analysis will obviously give a better precision, but the fact that the track and the ejection direction can be estimated directly foresees good potential for the track reconstruction and polarimetry measurement.

## 4 Discussion

Caliste-MM can perform spectrometry or polarimetry using different gases, but its main objective is to perform both goals at the same time. For this using a neon or argon mixture at low pressure appears to be a good solution although the parameters of the detector will have to be optimized for spectro-polarimetry. To perform spectrometry it is important to use a specific amplification field



2016 JINST 11 P04016

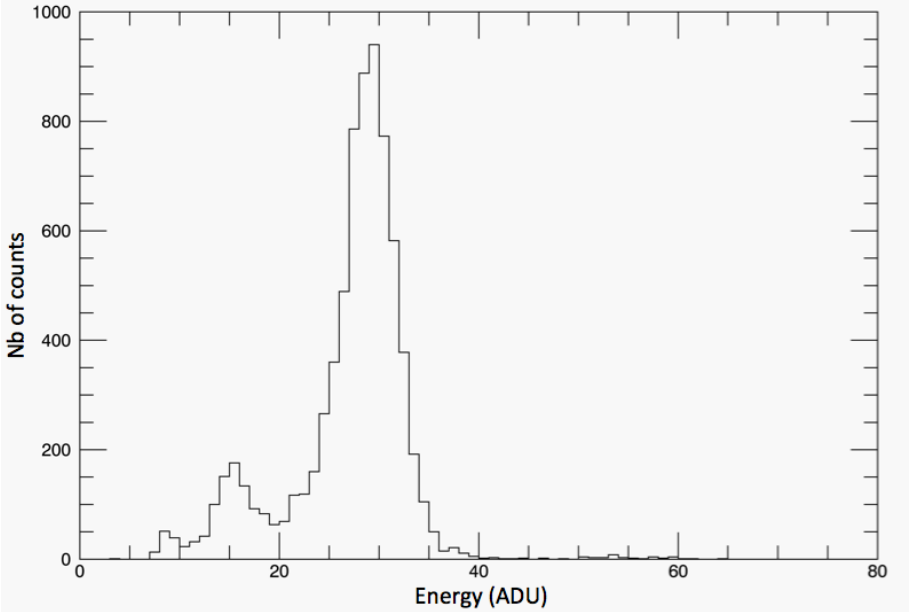


**Figure 9**. The $^{55}$Fe spectrum using Argon-Isobutane mixture. The energy resolution is 17.7% FWHM at 5.9 keV.

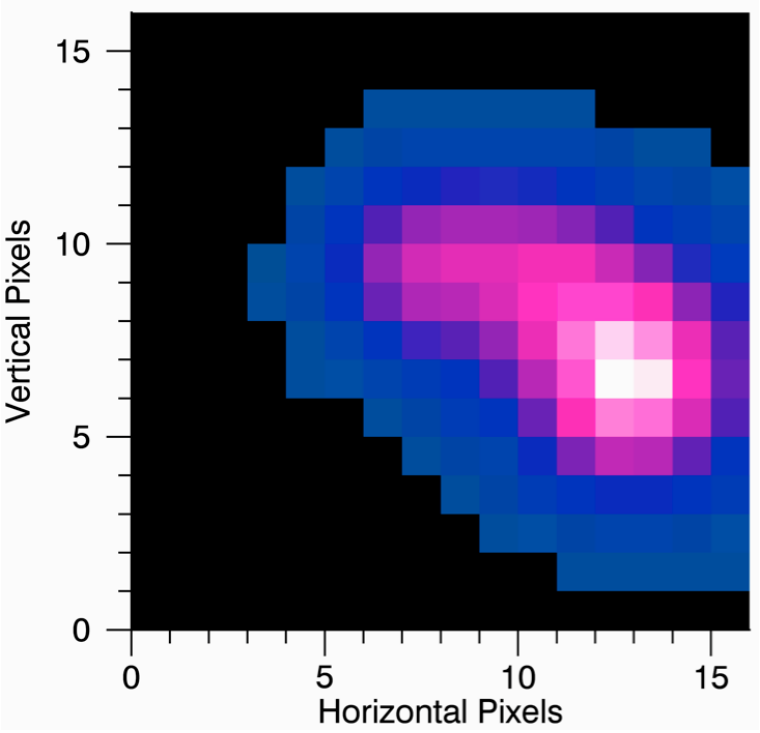


**Figure 10**. 8 keV photon conversion in helium: the photo-electron's track is visible and its ejection direction can be recovered.

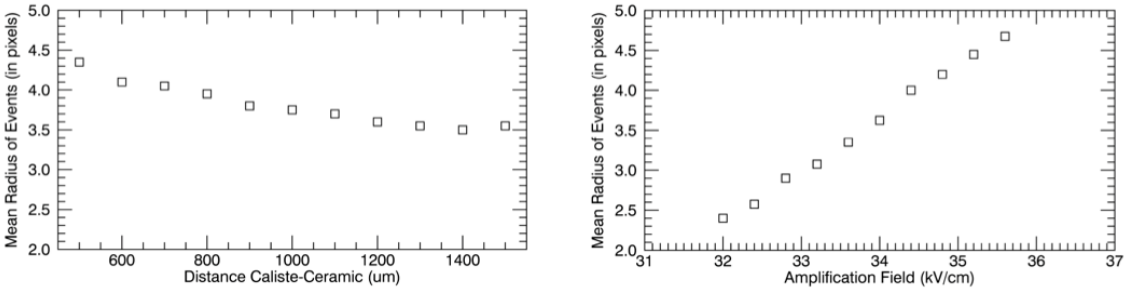


**Figure 11**. Left: size of the events versus the amplification field (distance Caliste-ceramic = 600 $\mu$m). Right: size of the events versus the distance between the ceramic and the Caliste (amplification field = 35 kV.cm$^{-1}$).

which gives the best energy resolution as shown by figure 3 (right). However, if the photo-electron leaves a track, as is expected for polarimetry, it is necessary to have a high gain in the detector in order to recover the entire length of it and especially the beginning. This can be done by decreasing the distance between the Caliste and the piggyback's ceramic as shown in figure 8, without changing the amplification field. Both amplification field and distance play a role in the size of the events and we need to ensure that the entirety of each event is recovered by the Caliste in order to treat the event for spectrometry. This influence is presented in figure 11. On the left is the variation of the mean radius of the events expressed in number of pixels versus the distance between the Caliste and the ceramic for an amplification field of 35 kV.cm$^{-1}$. On the right is the same variation versus the amplification field. These figures show that increasing the amplification field increases the size of the events, following what seems to be a linear relation. If a high amplification field is needed for energy resolution purposes at other energies than 6 keV a part of the event will not be detected by the electronics and the data treatment will be degraded. However, figure 11 left shows that increasing the distance between the Caliste and the ceramic reduces the event's size slightly. It may be a solution to compensate the influence of the amplification field when trying to keep events of various energy completely inside the Caliste for a better fit and analysis. This will, however, make the gain of the Caliste-MM lower and we might not be able to recover the begining of the track and perform polarimetry. Spectro-polarimetry finally needs optimization of the different parameters such as gain, distance between the Caliste and theceramic or gas mixture, and construction of an analytical model of Caliste-MM to help in this optimization. It must be noted that the figures presented in figure 11 will be very valuable in the validation of the analytical model.

## 5 Summary

Caliste-MM is a new detector developed to perform spectro-polarimetry in soft X-ray energies. It uses a Micromegas technology, called Piggyback, consisting of a resistive anode spread on a ceramic plate. The readout electronics, called Caliste, is placed outside the gaseous medium and the signal is read through the ceramic by capacitive effect, being then naturally protected from sparks. Several parameters of Caliste-MM have been characterized, such as its gain behaviour or the influence of the distance between the Caliste and the ceramic, which shows interesting properties that need to be studied in details. In Argon, the system also shows a good energy resolution of less than 18 % FWHM at 6 keV when using a specific 1$\sigma$ cut, which is the minimum resolution of the piggyback alone. Having outer and contactless electronics does not degrade the resolution of the detector.

The $1\sigma$ cut limits the influence of the diffusion inside the resistive layer and is the method which does not distort the energy calibration by giving the best energy resolution. When using helium the photo-electrons' tracks are visible as well as their ejection direction, making a measurement of polarimetry possible. Different parameters need to be optimized and further work will include an analytic modelization of Caliste-MM to help this optimization, tests with Neon based mixtures in low pressure condition to perform spectro-polarimetry, and tests in a 100% polarized beam in order to make a measurement of the modulation factor of our promising polarimeter.

## References


[1] M.C. Weisskopf et al., *A graphite crystal for stellar X-ray astronomy*, *Rev. Sci. Instrum.* **43** (1972) 967.

[2] M.C. Weisskopf et al., *Measurement of the X-ray polarization of the Crab nebula*, *Astrophys. J.* **208** (1976) L125.

[3] R. Novick et al., *Detection of X-ray polarization of the Crab nebula*, *Astrophys. J.* **174** (1972) L1.

[4] R.A. Gowen et al., *An upper limit to the linear X-ray polarization of SCO X*-1, *Mon. Not. Roy. Astron. Soc.* **179** (1977) 303.

[5] M.C. Weisskopf et al., *A precision measurement of the X-ray polarization of the Crab nebula without pulsar contamination*, *Astrophys. J.* **220** (1978) L117.

[6] P. Soffitta et al., *XIPE: the X-ray Imaging Polarimetry Explorer*, *Exper. Astron.* **36** (2013) 523 [arXiv:1309.6995].

[7] M.C. Weisskopf et al., *An imaging X-ray polarimeter for the study of galactic and extragalactic X-ray sources*, *Proc. SPIE* **7011** (2008) 70111I.

[8] W. Heitler, *The quantum theory of radiation*, Oxford University Press, Oxford U.K. (1954).

[9] Y. Giomataris, P. Rebourgeard, J.P. Robert and G. Charpak, *Micromegas: a high granularity position sensitive gaseous detector for high particle flux environments*, *Nucl. Instrum. Meth.* **A 376** (1996) 29.

[10] D. Attié et al., *A piggyback resistive Micromegas*, 2013 *JINST* **8** P05019 [arXiv:1208.6525].

[11] S. Andriamonje et al., *Development and performance of microbulk Micromegas detectors*, 2010 *JINST* **5** P02001.

[12] O. Limousin et al., *Caliste* 256*: CdTe imaging spectrometer for space science with a* 580 *μm pixel pitch*, *Nucl. Instrum. Meth.* **A 647** (2011) 46.

[13] A. Meuris et al. *Caliste HD: a new fine pitch Cd(Zn)Te imaging spectrometer from* 2 *keV up to* 1 *MeV*, in proceedings of *IEEE Nucl. Sci. Symp. Med. Imag. Conf. Rec.* (2011) 4485 Valencia Spain October 23–29 2011.

[14] A. Michalowska et al., *IDeF-X HD: a low power multi-gain CMOS ASIC for the readout of Cd(Zn)Te detectors*, in proceedings of *IEEE Nucl. Sci. Symp. Conf. Rec.* (2010) 1556, Knoxville U.S.A. October 30–November 6 2010.

[15] D. Attié et al., *R&D on a novel polarimeter spectro-imager with Micromegas detectors and a Caliste readout system*, in proceedings of *New Development In Photodetection*, Tour France June 30–July 4 2014 [*Nucl. Instrum. Meth.* **A 787** (2015) 312].


2016 JINST 11 P04016

ARTICLE IN PRESS

Nuclear Inst. and Methods in Physics Research, A ▮ (▮▮▮▮) ▮▮▮–▮▮▮

Contents lists available at ScienceDirect

Nuclear Inst. and Methods in Physics Research, A

journal homepage: www.elsevier.com/locate/nima

# Caliste-MM: Polarimetric measurements at the Soleil facility

P. Serrano [a], P. Da Silva [b], E. Ferrer-Ribas [a,*], O. Limousin [a], P. Mercere [b], F. Orsini [b]

[a] IRFU, CEA, Université Paris-Saclay, F-91191 Gif-sur-Yvette, France
[b] Synchrotron SOLEIL, L'Orme des Merisiers, Saint-Aubin, France

ARTICLE INFO

*Keywords:*
Polarimetry
Spectroscopy
Soft X-ray
Piggyback
Micromegas

ABSTRACT

Performing polarimetry in the soft X-ray range, from 1 keV to 15 keV, is a topic of high interest in the astrophysical community. However, for instrumental reasons, soft X-ray polarimetry has been performed only once so far by a mission on board the OSO-8 satellite in 1975. Since the early 2000's, thanks to the development of Micro Pattern Gaseous Detectors (MPGD), it is possible to perform polarimetry by measuring the azimuthal scattering anisotropy of the photoelectrons created during the detection of soft X-rays by photoelectric effect. The Caliste-MM detector is a gaseous polarimeter, using a novel design of contactless readout electronics to read the signal developed in the resistive anode of a piggyback micromegas detector.

In this paper we present polarimetry measurements obtained with the Caliste-MM detector at the Soleil synchrotron facility. Photoelectrons tracks obtained in the beamline are shown, and the reconstruction method to find the photoelectrons azimuthal angle is described. We conclude by presenting the modulation curve obtained at 8 keV, with a modulation factor of the detector reaching 88%.



## 1. Introduction

X-ray astronomy allows the observation of the most violent phenomena in our universe. Spectroscopy, imaging and timing in soft X-ray energies (1 keV–15 keV) are well mastered sciences performed by famous missions (Chandra, RXTE, XMM-Newton). But X-ray polarimetry is still missing: only a few pioneer dedicated experiments have been flying on board of rockets or satellites [1]. Because of the low sensitivity of the instruments based on Bragg diffraction and Thomson scattering the only positive detection is the polarization of the Crab Nebula [2] and soft X-ray polarimetry has been swept aside. And this despite the wide range of information that a soft X-ray polarimetry measurement could bring, from the measurement of black hole spins [3] to the composition of jets of low synchrotron peaked blazars [4].

Thanks to the improvement of gaseous detectors in the late 90's and the possibility to use the photoelectric effect to perform soft X-ray polarimetry, the interest for this scientific domain has been renewed. Various missions are currently under development such as the XIPE [5] or the IXPE [6] missions.

Polarimetry can be performed in a gaseous detector thanks to the photoelectric effect, where an incoming photon is converted in the gas into a photo-electron. The differential cross-section for this effect is given by the Heitler formula [7]:

$$\frac{d\sigma_{ph}}{d\Omega} = r_0^2 \alpha^4 Z^5 \left(\frac{m_e c^2}{E}\right)^{\frac{7}{2}} \frac{4\sqrt{2}\sin^2\theta\cos^2\phi}{(1-\beta\cos\theta)^4} \quad (1)$$

where $r_0$ is the classical radius of the electron, $\beta$ its velocity in units of the speed of light, $\alpha$ the fine-structure constant, $m_e$ the rest mass of the electron, $E$ the energy of the incoming photon, $Z$ the atomic number of the absorbing atom, $c$ the speed of light and $\theta$ and $\phi$ are respectively the polar angle and azimuthal angle of ejection as defined in Fig. 1.

The ejection direction is modulated by $\cos^2\phi$ and is then linked to the polarization direction of the incident photon. The histogram of the azimuthal angles measured for each interaction is called modulation curve. The position of the peaks gives the polarization direction. The amplitude gives the polarized fraction, as shown in Fig. 2.

## 2. The Caliste-MM detector

Performing polarimetry by using the photoelectric effect relies on the reconstruction of the photoelectrons tracks. The detection medium must then have a density low enough to let the photoelectron recoil. In a gaseous detector, a photoelectron created by a soft X-ray photon

* Corresponding author.
*E-mail addresses:* paul.serrano@cea.fr (P. Serrano), paulo.dasilva@synchrotron-soleil.fr (P. Da Silva), esther.ferrer-ribas@cea.fr (E. Ferrer-Ribas), olivier.limousin@cea.fr (O. Limousin), pascal.mercere@synchrotron-soleil.fr (P. Mercere), fabienne.orsini@synchrotron-soleil.fr (F. Orsini).

https://doi.org/10.1016/j.nima.2017.11.079
Received 8 November 2017; Received in revised form 21 November 2017; Accepted 23 November 2017
Available online xxxx
0168-9002/

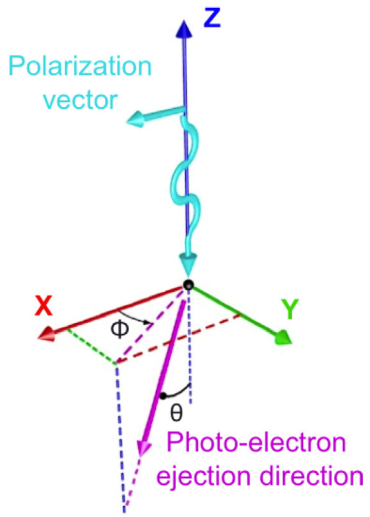


**Fig. 1.** The photoelectric effect. The differential cross section of the effect is modulated by $\cos^2\phi$. The histogram of the various azimuthal angles gives the modulation curve.

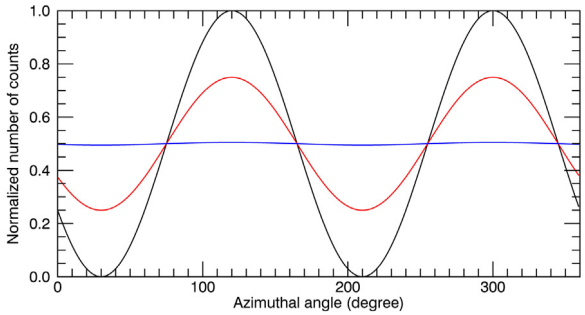


**Fig. 2.** Modulation curves in the case of the detection of black: 100%, red: 50% and blue: 0% polarized light. The position of the peaks gives the polarization direction, the amplitude gives the polarized fraction. (For interpretation of the references to color in this figure legend, the reader is referred to the web version of this article.)

ionizes the gas on its way and creates a track of primary electrons of few hundreds of μm. A 6 keV photon in helium at 1 bar creates a track of 146 primary electrons of length of 3 mm. To reconstruct the track, the readout electronics should then have a pitch of few hundreds μm.

The use of a MPGD allows to amplify the signal of the primary electrons and to reconstruct the photoelectron track. The Caliste-MM detector [8,9] is such a MPGD. It uses the architecture of the piggyback micromegas [10], derived from the micromegas architecture [11]. The anode of the detector is a resistive layer spread on a ceramic plate. There are no strips or pixels in the gaseous medium. The readout electronics used is the Caliste-HD readout [12], a space-qualified electronics consisting in a matrix of 256 pixels of pitch of 625 μm. It is placed outside the gaseous medium, facing the ceramic plate to read the signal of charges in the resistive layer. The signal is read by capacitive coupling. Changing the resistivity of the resistive layer or the distance between the Caliste and the ceramic, influence the propagation of the charges. The influence of these parameters on the signal is studied in detail in [8,9].

The scheme of the setup is presented in Fig. 3 and the actual setup is presented in Fig. 4. Such a novel design of detector presents various advantages. First the resistive layer protects the electronics from the sparks and discharges created in the gaseous detector that can damage it. Those sparks are caused by cosmic muons on ground and can be caused by protons and heavy ions in a space environment. The readout electronics is not integrated to the gaseous detector. It is then easy to change if one pixel is damaged or if a finer pitch or larger readout plane is needed. With the Caliste-MM detector, it is possible to detect photons

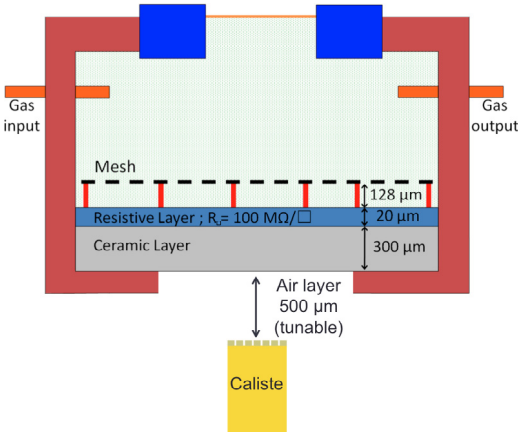


**Fig. 3.** The Caliste-MM scheme. It is composed of a piggyback detector which detects the photon and amplify the signal. The charges reach the anode made of a resistive layer spread on a ceramic plate. The Caliste readout electronics is placed outside the gaseous detector and read the signal in the resistive layer through an air layer and the ceramic plate.

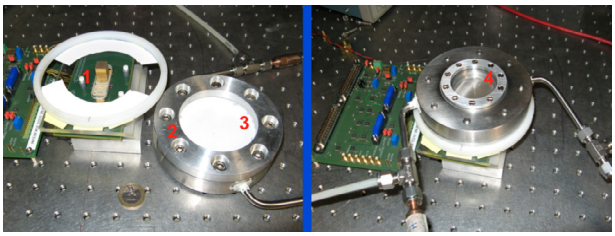


**Fig. 4.** The Caliste-MM setup. Left: Piggyback and readout separated. Right: Caliste-MM setup. The ceramic of the piggyback faces the Caliste electronics. 1: Caliste electronics. 2: Gaseous chamber. 3: Piggyback ceramic closing the gaseous chamber. 4: Entrance window.

from 1 keV to 20 keV and with an energy resolution of 18% FWHM at 6 keV when using an argon based mixture.

## 3. Polarimetry measurements

The Caliste-MM detector has been installed at the Soleil synchrotron facility in the *Metrologie* beamline [13], which produces a 100% polarized soft X-ray beam. Fig. 5 presents 8 keV events recorded by the detector when using a mixture of helium-isobutane (90%–10%), at a fixed amplification field of 40.5 kV cm$^{-1}$. The signal is spread on several pixels which allows its reconstruction in order to perform polarimetry.

The reconstruction method used is done in 5 steps. First the impact point of the beam is identified. To do this, a hitmap of the run is done, which gives Fig. 6 (left). Then a histogram is made in the $X$ and $Y$ directions, and the histograms are fitted by a Gaussian function, shown in Fig. 6 (right). The Gaussian fits give a reduced $\chi^2$ of 0.8 and are then in good agreement with the data. Their centroid give a $X$ and $Y$ coordinates that identify the impact point of the beam for the run considered.

After this identification we reconstruct the various tracks following the process explain in Fig. 7. The tracks are thresholded until 60% of the signal remains. This value has been optimized experimentally to give the best results for the reconstruction. Then the Bragg peak is removed: the pixel with the maximum signal is identified, and the signal is cut in a circle of increasing radius until 30% of the signal remains. The value of 30% has also been optimized experimentally. After the removal of the Bragg peak, only the beginning of the track remains and its barycenter is calculated. The line passing through the calculated barycenter and the impact point of the beam is the ejection direction of the photoelectron.



Please cite this article in press as: P. Serrano, et al., Caliste-MM: Polarimetric measurements at the Soleil facility, Nuclear Inst. and Methods in Physics Research, A (2018), https://doi.org/10.1016/j.nima.2017.11.079.

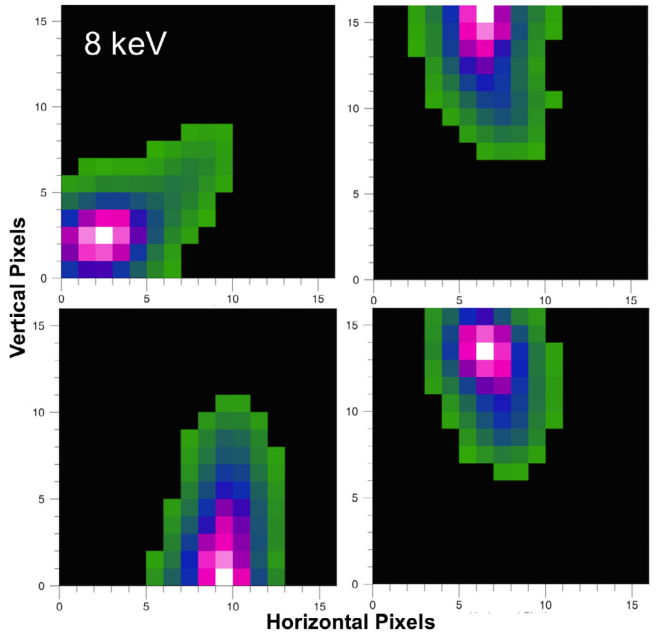


**Fig. 5.** 8 keV photons tracks recorded in the Caliste-MM detector at the Soleil synchrotron facility. The tracks are long enough to be reconstructed to perform polarimetry measurement.

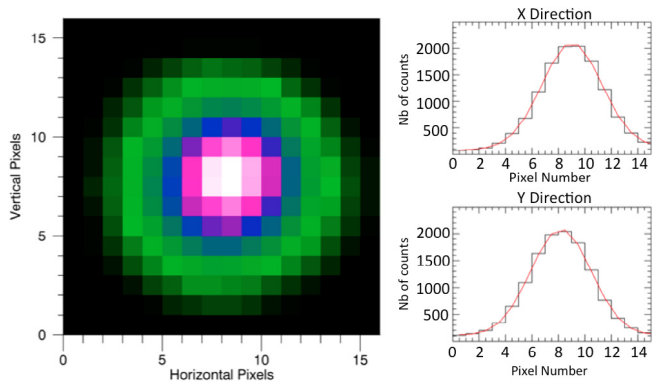


**Fig. 6.** Identification of the impact point of the beam. Left: hitmap of the run. The value in each pixels represents the number of time that the pixel has recorded signal. Right: histograms in the X and Y direction, fitted by a Gaussian function (red curve). The centroids of the fit give X and Y coordinates, identifying the impact point of the beam.

This reconstruction method is applied on the tracks of the run and allows to recover the azimuthal angles for each reconstructed interactions. Fig. 8 presents the result of the reconstruction of the ejection direction at 8 keV on various tracks, and the associated reconstructed azimuthal angle $\phi$. Making a histogram of the azimuthal angles gives the modulation curve in Fig. 9. The histogram is fitted with the theoretical distribution $A + B * \cos^2\phi$. The agreement between the data and the theoretical distribution is not very good (reduced $\chi^2 = 9$) and indicates that there might be systematic errors in the measurement or the reconstruction.

Fig. 10 presents the difference between the fit and the data. A structure is visible and proves the presence of systematic errors. The residual is fitted by a sinus function. The peaks of the sinus are in the ± 45° directions and the valleys are in the horizontal and vertical directions. The systematic errors might then come from the square geometry of the readout plane. Fig. 11 is the fit of the data when adding the sinus fit of the residual to the theoretical function $A + B * \cos^2\phi$. The agreement between the fit and the data is better, and gives a reduced $\chi^2 = 2$. The modulation factor is $\mu = 88\%$.

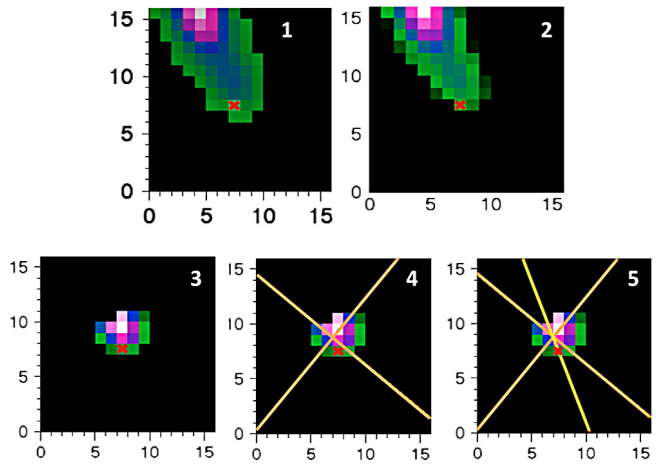


**Fig. 7.** Reconstruction method used. 1: Identification of the impact point of the beam, represented by the red cross on the images. 2: Threshold of the image until 60% of the track remains. 3: Cut of the Bragg peak until 30% of the signal remains. 4: Calculating the barycenter of the image. 5: The line passing through the impact point and the barycenter is the ejection direction of the photoelectron.

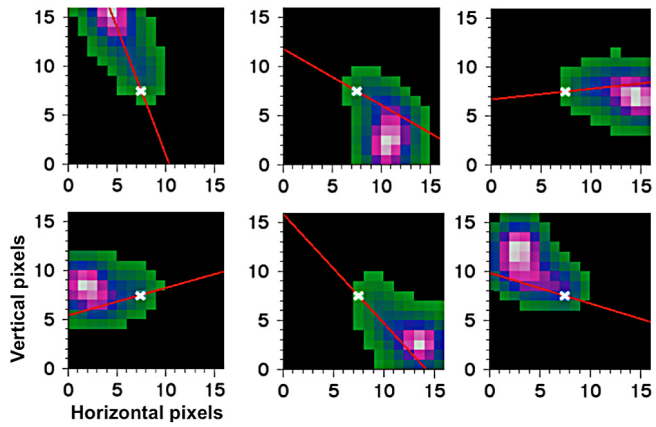


**Fig. 8.** The reconstruction method applied on several tracks. The red line represents the reconstructed ejection direction. From this direction the azimuthal angle of ejection direction can be calculated.

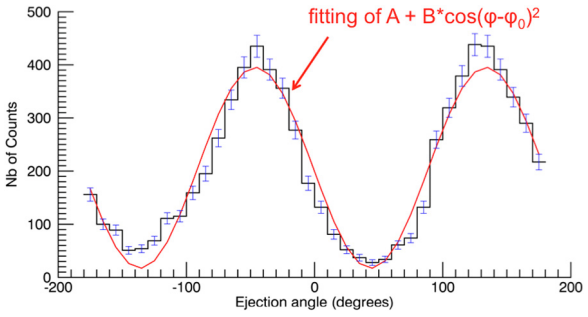


**Fig. 9.** Modulation curve obtained on a 8 keV run. The red curve is the fit of the theoretical distribution, the blue bars are the statistical errors. The measured modulation factor is $\mu$ = 92%.



Please cite this article in press as: P. Serrano, et al., Caliste-MM: Polarimetric measurements at the Soleil facility, Nuclear Inst. and Methods in Physics Research, A (2018), https://doi.org/10.1016/j.nima.2017.11.079.

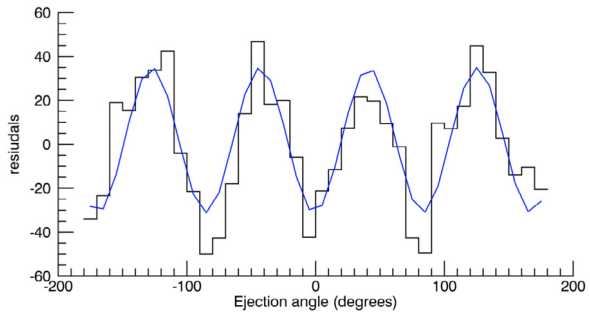


**Fig. 10.** Black: residual of the fit of the theoretical function $A+B*\cos^2\phi$ to the data. Blue: fit of a sinus function. A structure is visible. The peaks are in the $\pm 45°$ directions while the valleys are in the horizontal and vertical directions. This indicates that the systematic errors might come from the square geometry of the readout plane. (For interpretation of the references to color in this figure legend, the reader is referred to the web version of this article.)

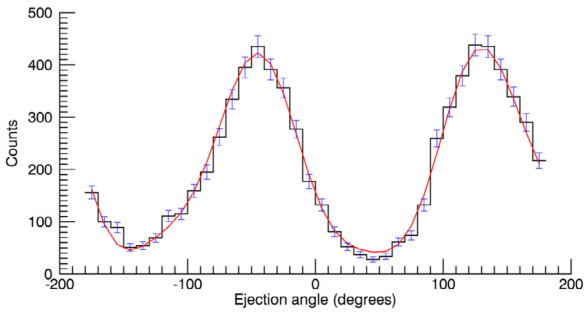


**Fig. 11.** Fit of the theoretical function $A + B*\cos^2\phi$ with the addition of the sinus fit of the residual. The agreement between the fit and the data is better, with a reduced $\chi^2$ is 2. The modulation factor obtained is $\mu = 88\%$.

## 4. Conclusion and prospects

The Caliste-MM detector exhibits good spectrometric performances in argon and good polarimetric performances in helium. To perform spectro-polarimetry, it is possible to use neon in low pressure conditions to get tracks long enough while keeping a good energy resolution. The use of a finer pitch readout electronics allows to get a better spatial resolution on tracks reconstruction and gives access to polarimetry measurement at lower energies, where the photoelectrons tracks are shorter. The use of neon at 250 mbar with a readout pitch of 200 μm will allow to have the same spatial resolution on the tracks at 4 keV than in helium at 8 keV, and then increase the energy band at which the detector is efficient.

## References

[1] M.C. Weisskopf, et al., A graphite crystal for stellar X-ray astronomy, Rev. Sci. Instrum. 43 (1972).
[2] M.C. Weisskopf, et al., A Precision measurement of the X-ray polarization of the Crab Nebula without pulsar contamination, ApJ 220 (1978).
[3] M. Dovciak, et al., Light-bending scenario for accreting black holes in X-ray polarimetry, ApJ 731 (2011).
[4] H. Zhang, M. Böttcher, X-ray and gamma-ray polarization in leptonic and hadronic jet models of blazars, ApJ 774 (2013).
[5] P. Soffitta, et al., XIPE: the X-ray imaging polarimeter explorer, Exp. Astron. 36 (2013).
[6] M.C. Weisskopf, et al., The Imaging X-ray polarimetry explorer (IXPE), Results Phys. 6 (2016).
[7] W. Heitler, The Quantum Theory of Radiation, Oxford University Press, 1954, p. 206.
[8] P. Serrano, et al., Caliste-MM: a spectro polarimeter based on the micromegas concept for soft X-ray astrophysics, JINST 11 (2016).
[9] P. Serrano, Caliste-MM: A New Spectro-Polarimeter for Soft X-Ray Astrophysics (Ph.D. thesis), Université Paris Saclay, 2017.
[10] D. Attié, et al., Piggyback resistive Micromegas, JINST 8 (2013).
[11] Y. Giomataris, et al., MICROMEGAS: a high-granularity position-sensitive gaseous detector for high particle-flux environments, NIMA 376 (1996).
[12] A. Meuris, et al., Caliste HD: A new fine pitch Cd(Zn)Te imaging spectrometer from 2 keV up to 1 MeV, in: IEEE Nuclear Science Symposium Conference Record, 2011.
[13] https://www.synchrotron-soleil.fr/fr/lignes-de-lumiere/metrologie.



Please cite this article in press as: P. Serrano, et al., Caliste-MM: Polarimetric measurements at the Soleil facility, Nuclear Inst. and Methods in Physics Research, A (2018), https://doi.org/10.1016/j.nima.2017.11.079.

université PARIS-SACLAY
ÉCOLE DOCTORALE
Astronomie et Astrophysique d'île-de-France

**Title :** Caliste-MM : a new spectro-polarimeter for soft X-ray astrophysics
**Key words :** *Astrophysics, Polarimetry, X-rays, Gaseous detectors*
**Abstract :** Performing X-ray polarimetry of astrophysical sources could provide precious insight into the properties of the emitting objects, for example the geometry of pulsars accretion disks, magnetic field inside the core of supernovae remnants or measurement of black holes spin. These fundamental observations are today impossible due to the missing performance of X-ray polarimeters.
The use of the photo-electric effect to perform spectro-polarimetry in the energy band of 1 keV to 15 keV appears to be like a much better approach than the use of Bragg diffraction or Thomson scattering. Performing polarimetry with the photo-electric effect relies on the measurement of the ejection direction of the photo-electron, which is modulated by the polarization direction of the incoming light. In order to reconstruct the photo-electron track, a detector allowing the photo electrons to recoil far enough is needed. Gaseous detectors are naturally perfect candidates. This PhD thesis focusses on the development and the characterization of a soft X-ray spectro- polarimeter of a completely new design : Caliste-MM. It consists of a gaseous detector called *piggyback Micromegas* associated with a miniature 3D readout electronics baptized Caliste. The main innovation of this detector comes from the fact that its readout electronics is located outside the gaseous medium. The charges created inside the piggyback diffuse in a resistive layer spread on a solid ceramic plate that closes the detector. The Caliste records the signal of the charges in the resistive layer through the ceramic and a small air layer by capacitive induction. The detector is composed of two completely independent parts : the piggyback where the X-ray conversion and amplification takes place, and the Caliste for the recording of the signal. These two parts can then be developed independently. Moreover the electronics are protected from sparks thanks to the resistive layer of the piggyback.
The detailed characteristics of the detector are studied such as the shape of the events, the gain and the energy resolution. Analytical models are compared to the obtained results in order to explain the physical phenomena responsible for the topology of the recorded events. Different strategies to improve the reconstruction of the photo-electrons are explored including for example finer pitched readout electronics, low pressure and the use of lighter gases such as Neon or Helium.
Finally, thanks to the measurements performed on the 100% linearly polarized beam of the Mtrologie line of the SOLEIL synchrotron facility, the modulation factor of the detector has been measured at different energies ranging from 6 keV to 12 keV. A measurement of the modulation factor of 92% at 8 keV proves the high potential of this new spectro-polarimeter and the interest into its innovative design.

**Titre :** Caliste-MM : un nouveau spectro-polarimètre pour l'astrophysique des rayons X mous
**Mots clés :** *Astrophysique, Polarimétrie, Rayons X, Détecteurs gazeux*
**Résumé :** Effectuer des mesures de polarimétrie des rayons X provenant de sources astrophysiques permettrait d'obtenir de nombreuses informations sur les objets émetteurs : géométrie des disques d'accrétion de pulsars, champ magnétique au coeur des restes de supernovae ou encore détermination du spin des trous noirs. Ces informations fondamentales sont pour l'instant inaccessibles à cause de l'absence de polarimètres X performants .
L'utilisation de l'effet photoélectrique pour effectuer de la mesure spectro polarimétrique des rayons X mous dans la bande d'énergie de 1 keV à 15 keV apparaît comme une approche bien plus adaptée que l'utilisation de la diffraction de Bragg ou de la diffusion Thomson. La polarimétrie par le truchement de l'effet photoélectrique repose sur la mesure de la direction d'éjection du photoélectron, laquelle est modulée par la direction de polarisation de la lumière incidente. Il s'agit alors de construire un détecteur permettant un recul suffisant des photoélectrons afin de reconstruire leurs traces, et les détecteurs gazeux sont par nature des candidats idéaux. Cette thèse traite du développement et de la caractérisation d'un spectro-polarimètre à rayons X-mous d'un genre entièrement nouveau : Caliste-MM. Il consiste en un détecteur gazeux, le *piggyback Micromegas* associé à une électronique de lecture miniature baptisée Caliste. L'une des principales innovations de ce détecteur tient au fait que son électronique de lecture est située en dehors du milieu gazeux. Les charges créées dans le piggyback diffusent dans une couche résistive répandue sur une céramique venant fermer le détecteur gazeux. Le module électronique Caliste enregistre le signal qui se répand dans la couche résistive à travers la céramique et une fine lame d'air par couplage capacitif. Le détecteur est ainsi composé de deux parties complètement indépendantes : conversion de la lumière et amplification par le piggyback, et lecture du signal par le Caliste. Les deux peuvent alors être développées indépendamment l'une de l'autre, l'électronique étant protégée des étincelles développées dans le détecteur grâce à la couche résistive du piggyback. Les caractéristiques détaillées du détecteur sont étudiées et présentées : forme des évènements, gain, résolution en énergie, ainsi que la variation de ces caractéristiques avec les différents paramètres du détecteur. Des modèles analytiques sont comparés aux résultats obtenus afin d'expliciter les phénomènes physiques responsables de la topologie des évènements enregistrés. Les différentes méthodes pour obtenir une trace reconstructible issue de photoélectrons sont aussi étudiées : utilisation d'une électronique de lecture plus finement pixelisée (utilisant ainsi pleinement le concept d'électronique découplée), test en basse pression ou utilisation de gaz légers comme l'Helium ou le Néon. Enfin, grâce à des mesures effectuées sur le faisceau 100% polarisé de la ligne Métrologie du synchrotron SOLEIL, le facteur de modulation du détecteur est mesuré et présenté à différentes énergies de 6 à 12 keV. Une mesure du facteur de modulation de 92% à 8 keV prouve le grand potentiel de ce nouveau spectro-polarimètre et l'intérêt de son concept innovant.

**Université Paris-Saclay**
**Espace Technologique / Immeuble Discovery**
**Route de lOrme aux Merisiers RD 128 / 91190 Saint-Aubin, France**